UNDERCOOLING AND RAPID SOLIDIFICATION OF FE-CR-NI TERNARY ALLOYS

by

Toshihiko Koseki

B. Eng., University of Tokyo, Japan (1981)
M. Eng., University of Tokyo, Japan (1983)

Submitted in partial fulfillment of the requirements
of the Degree of

Doctor of Science in Materials Engineering

at the

MASSACHUSETTS INSTITUTE OF TECHNOLOGY
April, 1994

Signature of Author _____
Department of Materials Science and Engineering
April 29, 1994

Certified by _____
Merton C. Flemings
Toyota Professor of Materials Processing
Head of Department of Materials Science and Engineering
Thesis Advisor

Certified by _____
Carl V. Thompson
Professor of Electronics Materials
Chairman, Departmental Committee on Graduate Students

UNDERCOOLING AND RAPID SOLIDIFICATION OF FE-CR-NI TERNARY ALLOYS

by

Toshihiko Koseki

Submitted to the Department of Materials Science and Engineering on April 29, 1994 in partial fulfillment of the requirements for the degree of Doctor of Science in Materials Engineering.

Abstract

Phase selection and subsequent microstructural evolution during rapid solidification were investigated with a series of Fe-Cr-Ni alloys of constant Fe (70 wt%). Three of the alloys have fcc as the primary phase upon equilibrium solidification, and two solidify with bcc as the primary phase. Melting and undercooling of samples were achieved using an electromagnetic levitation technique. Rapid solidification was subsequently obtained in a "containerless" condition in an inert gas flow (gas-cooled solidification) or by casting the melt onto a solid chill substrate or into a liquid metal bath.

Primary bcc solidification was found to be dominant during gas-cooled solidification from the undercooled melt, even for alloys which solidify as primary fcc upon equilibrium solidification. Evidence of metastable bcc solidification in bulk samples was explicitly obtained when Fe-17.5Cr-12.2Ni alloy samples were undercooled by about 20 K or more. The primary phase was identified by solute profiles of the quenched mushy region and by structural features in the final microstructures. Metastable bcc solidification was verified also in Fe-16Cr-14Ni and Fe-15Cr-15Ni through thermal analysis of the double recalescence behavior as well as solute profiles in quenched structures. It is concluded that the phase selection during gas-cooled solidification is determined by the preferential nucleation of bcc in the undercooled melt. Following primary metastable bcc solidification, stable fcc is formed in these alloys. When the formation of fcc occurs in the semi-solid condition, it proceeds in a peritectic manner, and is enhanced by the presence of a high fraction of bcc. Nucleation and growth of stable and metastable phases during gas-

cooled solidification are discussed and a nucleation phase diagram for Fe-Cr-Ni alloys is proposed.

In contrast to gas-cooled solidification, fcc solidification is dominant over bcc during the chill casting of undercooled melts, even for equilibrium primary bcc alloys. Fcc dendrites preferentially grow from the chill, but the vicinity of the metal/chill interface often reveals an apparent non-dendritic growth morphology. Small bcc dendrites are retained at the interface, which suggests nearly concurrent nucleation of bcc and fcc. The mechanism of preferential growth of fcc is discussed in terms of thermal and kinetic factors and the stability of the growth morphology. A dendrite growth model for chill casting is presented by assuming that heat evolution at the dendrite tip occurs both into the undercooled melt and through the growing solid. The effect of heat extraction rate on growth behavior during chill casting is discussed, and a diagram for the stability of growth morphology is presented.

In gas cooled solidification, bcc-to-fcc transformation occurs either in the semi-solid or the fully solid state after primary bcc solidification during gas cooling. The transformation mechanism becomes massive-like at higher initial undercoolings. The metallographic features of massive fcc are presented, and the effect of initial undercooling on the bcc-to-fcc transformation is discussed.

Thesis Supervisor: Merton C. Flemings
Titles: Toyota Professor of Materials Processing
Head of the Department of Materials Science and Engineering

TABLE OF CONTENTS

LIST OF FIGURES

Chapter II

initial undercoolings of (a) 33 K, (b) 51 K, (c) 138 K, and (d) 155K.

Figure 9 - Concentration distributions of Cr and Ni in the mushy region which was obtained using liquid metal quenching after the first recalescence, and measured by the computer-aided microprobe analyzer (CMA).

Figure 10 - Solidification structure obtained by free levitation with an initial undercooling of 18 K, which shows the mixed solidification of primary fcc and primary bcc; (a) the whole sample, (b) a region showing primary bcc solidification, and (c) a region showing primary fcc solidification.

Figure 11 - Microstructural changes with time after the first recalescence obtained by liquid metal quenching following free levitation; (a) 0.25 s after recalescence (ΔT=110 K), (b) 0.4 s after recalescence (ΔT=105 K), (c) 1.5 s after recalescence (ΔT= 116 K), and (d) 1.9 s after the first recalescence and 0.4 s after the second recalescence (ΔT=109 K).

Figure 12 - Concentration distributions of Cr and Ni in the vicinity of the growing interface of fcc, obtained by CMA.

Figure 13 - X-ray diffraction results from specimens quenched (a) before the second recalescence and (b) after the second recalescence.

Figure 14 - Stability of nucleating phase calculated as a function of wetting angle difference ($\theta_{fcc/sub.}$-$\theta_{bcc/sub.}$) in Fe-17.5Cr-12.2Ni, where $\theta_{fcc/sub}$ and $\theta_{bcc/sub}$ are the wetting angle for heterogeneous nucleation between fcc and a catalyst and between bcc and a catalyst, respectively. Two lines giving temperatures of nucleating phase transition were obtained using different free energy values as noted.

Figure 15 - A calculated nucleation phase diagram indicating preferentially nucleating phase as a function of temperature and composition, and plots of experimental observations of primary phases on the diagram.

Figure 16 - Growth velocities of fcc and bcc dendrites calculated as a function of melt temperature using the BCT model, and comparison of experimentally estimated velocities with the model results.

Figure 17 - Dendritic growth of stable fcc phase into the semi-solid after metastable bcc solidification with initial undercooling of 67 K.

Chapter III

pp. 109 - 129

Figure 1 - Pseudo-binary phase diagram of the Fe-Cr-Ni alloy system at 70 wt pct Fe calculated using Thermo Calc[10], and locations of the two alloy compositions used in the present study. Dashed lines are the extension of liquidus and solidus lines.

Figure 2 - Schematic diagram of apparatus for levitation melting and undercooling experiments.

Figure 3 - Typical recalescence curves observed in the solidification of Fe-16Cr-14Ni alloy with different initial undercooling. Transition from single to double recalescence was found at an initial undercooling of about 60 K.

Figure 4 - Typical recalescence curves observed in the solidification of Fe-15Cr-15Ni alloy with different initial undercooling. Transition from single to double recalescence was found at an initial undercooling of about 100 K

Figure 5 - Effect of initial undercooling on time for the first recalescence in Fe-16Cr-14Ni and Fe-15Cr-15Ni alloys.

Figure 6 - Effect of initial undercooling on time for the second recalescence in Fe-16Cr-14Ni and Fe-15Cr-15Ni alloys.

Figure 7 - Temperatures after the first recalescence and second recalescence in the solidification of Fe-16Cr-14Ni alloy

Figure 8 - Temperatures after the first recalescence and second recalescence in the solidification of Fe-15Cr-15Ni alloy

Figure 9 - Effect of initial undercooling and alloy composition on time between the first recalescence and second recalescence.

Figure 10 - Typical microstructures of Fe-16Cr-14Ni which were solidified with different initial undercooling (ΔT) and quenched into In-Ga liquid bath immediately after recalescence. (a) ΔT =12 K, (b) ΔT = 58 K, (c) ΔT = 101 K, and (d) ΔT = 176 K.

Figure 11 - Microstructures of Fe-16Cr-14Ni which were solidified with similar initial undercooling but with different plateau time, and quenched into an In-Ga bath immediately after the second recalescence. (a) ΔT = 66 K with a plateau time of 4 ms, and (b) ΔT = 70 K with a plateau time of 350 ms.

Figure 12 - X-ray diffraction results from specimens shown in Figure 11 (a) and (b). (a) ΔT = 66 K with a plateau time of 4 ms, and (b) ΔT = 70 K with a plateau time of 350 ms.

Figure 13 - Typical microstructures of Fe-15Cr-15Ni which were solidified with different initial undercooling (ΔT) and quenched into an In-Ga liquid bath immediately after recalescence. (a) ΔT = 60 K, (b) ΔT = 104 K, (c) ΔT = 205 K, and (d) ΔT = 306 K.

Figure 14 - Concentration profiles of Cr and Ni in a microstructure of Fe-15Cr-15Ni which was solidified with an initial undercooling of 60 K, and quenched after recalescence.

Figure 15 - Concentration profiles of Cr and Ni in a microstructure of Fe-16Cr-14Ni which was solidified with an initial undercooling of 101 K, and quenched after recalescence.

Figure 16 - Effect of composition and initial undercooling on the occurrence of double recalescence. The comparison of the effect with the nucleation diagram suggests that double recalescence is related to metastable bcc solidification.

Figure 17 - Effect of initial undercooling on solute profiles at dendrite cores plotted on the nucleation diagram.

Figure 18 - Growth velocities of fcc and bcc dendrites calculated as a function of melt temperature using the BCT model[11], and comparison of experimentally estimated velocities with the model results for Fe-16Cr-14Ni alloy.

Figure 19 - Growth velocities of fcc and bcc dendrites calculated as a function of melt temperature using the BCT model[11], and comparison of experimentally estimated velocities with the model results for Fe-15Cr-15Ni alloy.

Figure 20 - Effect of fraction solid after the first recalescence on the plateau time. It is suggested that plateau times are stable and composition-dependent when the fraction solid is more than 0.4.

Figure 21 - Calculation results of the nucleation temperature of fcc at various nucleation sites in the presence of the liquid and bcc.

Chapter IV

pp. 146 - 158

Figure 1 - Pseudo-binary phase diagram of the Fe-Cr-Ni alloy system at 70 wt pct Fe calculated using Thermo Calc[10]. The locations

of the two alloy compositions, A and B, used in the present study are indicated in the figure.

Figure 2 - Schematic diagram of apparatus for levitation melting. Undercooled melt samples were either solidified while levitated (gas-cooled solidification), or cast on a chill block made of various materials, or quenched into the liquid In-Ga bath.

Figure 3 - Solidification structures of alloy A (Fe-17.5Cr-12.2Ni): (a) developed by gas-cooled solidification with an initial undercooling of 51 K, (b) chill cast onto a copper substrate (ΔT= 71 K), (c) chill cast onto a ferritic stainless steel substrate (ΔT= 39 K), and (d) chill cast onto an alumina substrate (ΔT= 64 K).

Figure 4 - Bcc dendrites observed at the chill surface in the cast structure of alloy A: (a) cast onto an alumina substrate (ΔT= 64 K), and (b) cast onto a copper substrate (ΔT= 71 K).

Figure 5 - Microstructure of alloy A cast onto copper chill (ΔT= 71 K). The sporadic thin layer of bcc dendrites is followed by a region which seems non-dendritic in 20 μm from the chill.

Figure 6 - Solidification structures of alloy B (Fe-18.5Cr-11.3Ni): (a) developed by gas-cooled solidification with an initial undercooling of 60 K, (b) chill cast onto a copper substrate (ΔT= 78K), (c) chill cast onto a ferritic stainless steel substrate (ΔT= 49 K), and (d) chill cast onto an alumina substrate (ΔT= 64 K).

Figure 7 - Distributions of Cr and Ni in a solidification structure of alloy A cast onto copper chill (ΔT= 71 K).

Figure 8 - Solute-rich cores seen in fcc dendrites in the form of crosses: (a) alloy A cast onto a copper chill (ΔT= 71 K), and (b) alloy B cast onto a copper chill (ΔT= 78 K).

Figure 9 - Distributions of Cr and Ni in the solidification structure of alloy B cast onto a copper chill (ΔT= 78 K).

Figure 10 - Microstructure of specimens quenched into an In-Ga liquid bath from the undercooled liquid state: (a) alloy A (ΔT= 27 K), showing a fully fcc, fine cellular structure, and (b) alloy B (ΔT= 28 K), showing a fully fcc zone (bright) for about 100 μm from the surface, and an adjacent region of coarse bcc dendrites (dark).

Figure 11 - Structures of samples quenched into an In-Ga chill bath from the undercooled liquid state: (a) alloy A, ΔT= 105 K, (b) alloy B, ΔT= 98 K, (c) a typical structure of the region of bcc dendrites (alloy A, ΔT= 105 K), and (d) a typical structure of the region of fcc dendrites (alloy A, ΔT= 105 K).

Figure 12 - Boundary structure between the regions of bcc dendrites and fcc dendrites: (a) at low magnification and (b) at high magnification.

Figure 13 - Structure of an alloy A sample which cast onto a copper chill from the slightly undercooled liquid state ($\Delta T \approx 7K$).

Chapter V

pp. 181 - 191

Figure 1 - Schematic of the thermal field around a dendrite tip growing into an undercooled melt during chill casting

Figure 2 - Effect of melt temperature on the tip velocity of a bcc dendrite for two heat extraction conditions: no heat extraction (J=0) and a heat extraction rate J of 10^9 W m^{-2}.

Figure 3 - Effect of melt temperature on the tip radius of a bcc dendrite for different heat extraction conditions. Heat extraction rate J is varied from 0 to $3x10^{10}$ W m^{-2}.

Figure 4 - Effect of heat extraction rate and melt temperature on the growth morphology of fcc and bcc.

Figure 5 - Effect of heat extraction rate and growth velocity on the growth morphology of fcc and bcc, (a) evaluated by the present model, and (b) evaluated by the KGT model[10]

Figure 6 - Effect of heat extraction rate on the tip velocity of fcc and bcc dendrites at a given melt temperature: 1500 K, 1600 K, and 1650 K.

Figure 7 - Effect of heat extraction rate on the tip radius of fcc and bcc dendrites at a given melt temperature: 1500 K, 1600 K, and 1650 K.

Figure 8 - Effect of heat extraction rate on the tip temperature of fcc and bcc dendrites at a given melt temperature: 1500 K, 1600 K, and 1650 K.

Figure 9 - Relationship between the tip velocity of a bcc dendrite and thermal Péclet number for different heat extraction conditions. Heat extraction rate J is varied from 0 to 3×10^{10} W m^{-2}.

Figure 10 - Effect of the thermal conductivity of the liquid on the tip velocity of fcc and bcc dendrites

Figure 11 - Schematics of the thermal field around a dendrite tip and the solid/liquid interface for different growth situations.

Chapter VI

pp. 210 - 221

Figure 1 - Schematic of the thermal field around a dendrite tip growing into an undercooled melt during chill casting.

Figure 2 - Schematics of the thermal field around the solid/liquid interface during planar growth with the presence of thermal undercooling.

Figure 3 - Calculated nucleation temperatures of fcc and bcc during continuous cooling. Contact angles between fcc and the substrate ($\theta_{fcc/sub}$) and between bcc and the substrate ($\theta_{bcc/sub}$) were assumed to be equal, and calculations were made assuming contact angles of 30°, 45°, and 60°. The intersection of one of these calculated curves with a given cooling curve gives the nucleation temperature of the phase of interest for that particular situation.

Figure 4 - Schematics of cooling curves at a high cooling rate and a low cooling rate. If the cooling rate is sufficiently high, the melt could be supercooled to the fcc nucleation temperature a very short time after the bcc nucleation temperature is reached.

Figure 5 - The effect of heat extraction rate on tip velocities of fcc and bcc dendrites for Fe-18.5Cr-11.3Ni at various melt temperature: 1650 K, 1600 K, and 1500 K.

Figure 6 - The effect of melt temperature on tip velocities of fcc and bcc dendrites calculated for Fe-17.5Cr-12.2Ni at a heat extraction rate of 3×10^{10} W m^{-2}.

Figure 7 - The effect of melt temperature on tip velocities of fcc and bcc dendrites calculated for Fe-18.5Cr-11.3Ni at a heat extraction rate of 3×10^{10} W m^{-2}.

Figure 8 - The effect of melt temperature on tip velocities of fcc and bcc dendrites calculated for Fe-18.5Cr-11.3Ni at a heat extraction rate of 3×10^{8} W m^{-2}, showing the instability of fcc dendritic growth at small undercoolings.

Figure 9 - Schematic illustration of the growth of planar fcc preferentially to dendritic bcc.

Figure 10 - Comparison of the growth velocity between a bcc dendrite and fcc plane front. Heat extraction rate through bcc is 3×10^8 W m^{-2}, while that through fcc is varied from3×10^8 to 1×10^{10} W m^{-2}.

Figure 11 - The effect of heat extraction rate on thermal undercooling at the tip of fcc and bcc dendrites for Fe-18.5Cr-11.3Ni at various melt temperature: 1650 K, 1600 K, and 1500 K.

Figure 12 - The effect of dendrite tip temperature on the tip velocity of fcc and bcc dendrites at a heat extraction rate of 1×10^9 W m^{-2}.

Chapter VII

pp. 240 - 255

Figure 1 - Calculated pseudo-binary phase diagram of the Fe-Cr-Ni system at 70 wt pct Fe with the extension of liquidus and solidus lines and the locations of the alloy compositions: alloys A, B and E.

Figure 2 - Structure of Fe-18.5Cr-11.3Ni (alloy B) after gas-cooled solidification with an initial undercooling of (a) 14 K and (b) 150 K.

Figure 3 - Structures observed at the core region of the sample of Fe-18.5Cr-11.3Ni (alloy B) after gas-cooled solidification with an undercooling of 150 K: (a) aligned fcc blocks along lacy bcc, and (b) grain boundary allotriomorphs and platelets of fcc.

Figure 4 - X-ray diffraction results obtained from samples of Fe-18.5Cr-11.3Ni (alloy B) solidified with an initial undercooling of

(a) 14 K and (b) 150 K, which correspond to the structures shown in Figures 2(a) and 2(b), respectively.

Figure 5 - Thermal histories of samples solidified with an initial undercooling of 14 K and 150 K, which correspond to the structures shown in Figures 2(a) and 2(b), respectively.

Figure 6 - Effect of initial undercooling on the onset temperature of the bcc-to-fcc transformation in a levitated Fe-18.5Cr-11.3Ni (alloy B). The transformation temperature was determined by the onset of the exothermic reaction or the change of the slope of the cooling curve.

Figure 7 - Structure of Fe-19.7Cr-10.3Ni (alloy E) after gas-cooled solidification with an initial undercooling of (a) 22 K and (b) 128 K.

Figure 8 - X-ray diffraction results obtained from samples of Fe-19.7Cr-10.3Ni (alloy E) solidified with an initial undercooling of (a) 22 K and (b) 128 K, which correspond to the structures shown in Figures 7(a) and 7(b), respectively.

Figure 9 - Micro X-ray diffraction results obtained from (a) lacy bcc mixed with fcc and (b) a single coarse grain in the sample of Fe-19.7Cr-10.3Ni (alloy E) with an initial undercooling of 128 K.

Figure 10 - Concentration profiles of Cr and Ni in the sample of Fe-19.7Cr-10.3Ni (alloy E) with an initial undercooling of 128 K.

Figure 11 - Thermal histories of samples solidified with an initial undercooling of 22 K and 128 K, which correspond to the structures shown in Figures 7(a) and 7(b), respectively.

Figure 12 - Effect of initial undercooling on the onset temperature of the bcc-to-fcc transformation in a levitated Fe-19.7Cr-10.3Ni (alloy E).

Figure 13 - Structures of samples of Fe-19.7Cr-10.3Ni (alloy E) which were quenched into In-Ga immediately after recalescence from different undercooling levels: (a) 25 K and (b) 125 K.

Figure 14 - Structure of Fe-17.5Cr-12.2Ni (alloy A) after gas-cooled solidification with an initial undercooling of (a) 51 K and (b) 155 K.

Figure 15 - X-ray diffraction obtained from samples of Fe-17.5Cr-12.2Ni (alloy A) solidified with an initial undercooling of 155 K, which corresponds to the structure shown in Figure 14(b).

Figure 16 - Thermal history of the sample solidified with an initial undercooling of 155 K, which corresponds to the structure shown in Figure 14(b).

LIST OF TABLES

Chapter VI

Chapter VII

LIST OF APPENDICES

Acknowledgments

Since I came to MIT in the fall of 1990, many people helped me pursue my studies on various occasions and in various ways. I would like to take this opportunity to recognize these people. My special thanks are due:

To my thesis supervisor, Professor Merton C. Flemings, for his warm direction and support throughout my studies at MIT. Whenever I encountered difficulty, he always encouraged me, and spent many hours discussing my research with me despite his tight schedule. I have obtained a great deal of advice and insight from these discussions, and also learned a lot from him about general attitude and approach to research as a material scientist and engineer.

To my thesis committee members, Professor Samuel M. Allen and Professor Andreas Mortensen, for their useful advice through discussions and careful review of the draft of this thesis.

To Dr. John M. Vitek, who is one of my thesis committee members from Oak Ridge National Laboratory and spent many hours with me discussing my research progress whenever he came up to Boston. I appreciate his plentiful advice and help with the electron beam welding of my alloys.

To Professor Kenneth C. Russell for a number of valuable discussions on the nucleation theory and its application.

To Professor Harold D. Brody and Professor Theodoulos Z. Kattamis for their helpful suggestions and continuing encouragement.

To Dr. Thomas J. Piccone, who helped me a great deal at the beginning of this thesis work. His availability for discussions on experiments and theoretical work is gratefully acknowledged.

To John E. Matz, who has been my nearest neighbor in Rm. 8-436 in the last few years, and patiently proofread all the drafts of this thesis correcting my English and technical errors in writing. His friendliness is really appreciated.

To Dr. Yanzhong Wu and Dr. Qi Zhao for their suggestions and help with the levitation experiment.

To the students and visiting researchers in the Solidification and Metal Matrix Composites Processing Group: Dr. Nancy F. Dean, Dr. Tamila Jonas, Yoshiro Ito, Peter Grasty, Yoshiaki Kajikawa, Ittipon Diewwanit, Masahiko Nakade, Hua Shen, Takeshi Ohkuma, Tetsuya Nukami, Arvind Sundarrajan, Douglas Matson, and Shoichi Honjo. Although some of them interacted me only for a short time, I have learned a lot from technical and non-technical discussions with them.

To Ms. Hilda N. Pierce and Ms. Kathy R. Farrell, who helped me communicate with professors and people outside of MIT. They were very efficient at making appointments, sending mails and fax, and typing and forwarding memos between professors and me.

To Vicken Dekermendjian and Ms. Maria Wehrle-Due, whose competent technical help with equipment and materials is acknowledged.

To Nippon Steel Corporation, Japan, which provided me this great opportunity to study abroad and has fully supported me during the stay. I am especially grateful to Professor Tasuku Fuwa, Mr. Takuo Kitamura, Dr. Tetsuro Ohashi, and Dr. Nobutaka Yurioka. Without their understanding and support, this work would not have been completed. Thanks are also extended to Mr. Hiroshige Inoue and Dr. Tadao Ogawa for all their technical help including CMA analyses, Dr. Tooru Matsumiya, Dr. Yoshio Ueshima and Dr. Takashi Tanaka for their advice and encouragement, and Mr. Hidehiro Endo for his various help and friendliness.

To Dr. Yuh Shiohara at the Institute of Superconducting Technology and Professor Takateru Umeda at the University of Tokyo, for their valuable comments on the theoretical approach to the rapid solidification of Fe-Cr-Ni alloys. Professor Umeda also provided many results from his published and unpublished research to me.

To the family of Professor Flemings and the family of Professor Teiichi Ando for their great hospitality on many occasions. I and my family really appreciate those wonderful times.

To my wife, Masako, my son, Hiroaki, and my daughter, Julia, for the atmosphere they made for me and their understanding, affection, patience, and encouragement.

Chapter I - Introduction

1. Background

1.1 Rapid Solidification of Alloys

Rapid solidification is characterized by high growth rates of the solid (i.e., high solidification rates) which are several orders of magnitude greater than those in conventional solidification. These high growth rates are attained either by high undercooling or by rapid cooling or quenching of the liquid. The former is achieved by methods such as levitation melting and the glass slag technique. Since nucleation of the solid is more difficult due to the absence of a mold and other nucleation catalysts in those techniques, the liquid can be cooled to temperatures far below the liquidus temperature. Once solidification starts in this highly undercooled melt, the growth of the solid is almost instantaneous due to a strong thermodynamic driving force for crystallization. On the other hand, rapid solidification can also be attained by rapid cooling in processes such as substrate quenching, and by high-speed laser or electron-beam welding. In those cases, the rapid movement of the solid/liquid interface is mainly brought about by the high heat extraction rates.

The high growth rate of the solid often leads to a departure of the solid/liquid interface from an equilibrium state[1-3]. As the solidification rate increases, complete rearrangement of atoms at the interface during crystallization is less likely to occur due to the limited time available. As a result, a number of microstructural changes are imparted to rapidly solidified materials:

- refinement of microstructure
- increased solid solubility
- improvement of chemical homogeneity
- new metastable structures and phases

Because of these microstructural characteristics of rapidly solidified materials, a variety of rapid solidification processes have been developed for the purpose of fabricating materials with improved or unique structure and performance. Examples are the fabrication of amorphous materials, fine alloy powders, and fine alloy fibers. In these fabrication processes, rapid solidification is performed by cooling the liquid alloys at a rate of 10^4 to 10^6 K/s Also, rapid solidification processing is used to modify surface structure and properties of existing materials as a post-manufacturing process. This modification is achieved by surface melting and alloying using high-energy density beams[4,5] and by plasma spraying. Direct thin strip casting and high speed welding by laser and electron beams are included in the category of rapid solidification processing. Many other potentially interesting applications of rapid solidification processing are also being developed.

1.2 Metallurgical Aspects of Rapid Solidification

Although some rapid solidification processes are already past the development stage, many metallurgical aspects of rapid solidification are still under investigation. These are primarily related to:

- evolution and stability of growth morphology
- selection and stability of solidifying phase

An important growth morphology in rapid solidification is the dendrite because of the effectiveness of this morphology in redistributing heat and mass.[1,8] Dendrite growth models[8-11] were developed for both constrained and unconstrained growth by combining the extended planar front instability criteria[6-8] with the analytical work by Ivantsov[12]. In addition to heat and mass transport at the tip of an isolated dendrite, capillary effects, kinetic effects and nonequilibrium interface conditions have also been incorporated. Calculated results, such as the dendrite growth stability,

tip radius, and growth velocity, have been experimentally examined in various rapid solidification processes. Several important research efforts were undertaken at MIT[13-15]. Dendrite growth velocity was determined by the use of high-speed cinematography and pyrometry, and compared with the results obtained from models.[13,14,16,17] Changes in grain structure and the coarsening of dendrites were also studied.[15] However, such experimental approaches have so far been conducted mainly on binary alloys, and the number of investigations on ternary or higher multicomponent alloys is still limited.

Phase selection and microstructural stability has been one of the primary interests of rapid solidification research. The problem has been discussed based on nucleation theory and the equilibrium phase diagram with metastable liquidus and solidus line extensions.[18-24,56] This approach was reasonable for small-volume systems such as gas-atomized powders, but its validity is still unclear for large volume or rapidly quenched systems; experimental verification for bulk samples is quite lacking. On the other hand, growth-controlled phase selection was observed in laser and electron beam surface melting in the absence of a nucleation barrier.[19, 25, 26]

1.3 Previous work on the Fe-Cr-Ni System

One of the multicomponent alloy systems in which rapid solidification has been most actively investigated is the iron-chromium-nickel (Fe-Cr-Ni) alloy system. In addition to the practical importance of this alloy system as the basis for stainless steel, it has several features which make it ideal for rapid solidification research. Firstly, the solidification behavior of stainless steel has been determined according to composition and solidification conditions in recent years.[27-31] Secondly, during the early stages of the research, interesting metallurgical features of rapid solidification were noted in this system. Finally, the equilibrium phase diagram and thermodynamic data for Fe-Cr-Ni have been well investigated through both experiments and thermodynamic calculations[32-38].

Although phase chemistry is likely to be non-equilibrium in rapid solidification, thermodynamics is still important for the discussion of solidification behavior and phase stability, as was demonstrated in the research on binary alloys.

Solidification modes of Fe-Cr-Ni alloys are strongly composition-dependent, and are generally classified as follows [28, 29]:

- A mode : Fully fcc solidification.
- AF mode : Primary fcc, plus eutectic reaction (fcc+bcc) at the terminal stage.
- FA mode : Primary bcc, plus eutectic reaction (bcc+fcc) at the terminal stage.
- F mode : Fully bcc solidification.

Bcc, if formed during solidification, generally undergoes solid state transformation to fcc on post-solidification cooling. Thus, the final microstructural characteristics in the as-solidified condition are not always identical to microstructural characteristics immediately after solidification. However, the solidification mode is still dominant in determining the final microstructure. In single phase solidification via A and F modes, solute distribution profiles during solidification are retained in the final dendritic microstructure[28,39]. In the case of AF and FA solidification modes, morphologies, distributions and contents of ferrite and austenite also reflect the solidification mode well[28-31]. Microstructural features and solute profiles resulting from each solidification mode are described in detail in the next chapter.

While the solidification modes were being established, research on rapid solidification of the Fe-Cr-Ni alloys was begun using high-energy density beams such as laser and electron beams for welding.[40-46] Fcc solidification was found to be dominant as the welding speed (i.e., solidification speed and cooling rate) increased. Obviously, solidification in welding is controlled by growth with a positive temperature gradient in the liquid and solid, and it was concluded that rapid constrained dendritic growth favored the fcc

phase rather than the bcc phase.[55] The trend of preferential fcc solidification was also found in chill casting and splat cooling experiments.[45,47] Unlike laser and electron beam welding, solidification is controlled not only by growth but also by nucleation at the substrate in those processes. In addition, the melt was substantially undercooled by the substrate prior to solidification.[47]

In contrast to the above results, primary metastable bcc solidification became dominant with decreasing particle size, i.e., with increasing undercooling of the melt and solidification rate, in gas atomization of type 303 stainless steel.[22,23] Calculations using classical nucleation theory supported the experimental result showing the preferential nucleation tendency of bcc at increased undercooling. The prediction that bcc is favored over fcc as a primary phase was also made for Fe-Ni alloys[14,20,24,48,50], but microstructural verification by experiment was limited to fine particles [20,49]. Some droplet experiments produced a two-step recalescence behavior in the solidification of hyper-peritectic Fe-Ni alloys in a deeply undercooled condition [14,50,51]. The first recalescence was considered to be a result of metastable bcc solidification. However, corresponding microstructural evidence was not presented.

2. Objective and Approach

The overall objective of the present research is to obtain a better understanding of the rapid solidification of Fe-Cr-Ni ternary alloys. Although a number of rapid solidification research projects have been carried out on this alloy system, many aspects still remain controversial and poorly understood. Among these, the phase selection problem mentioned above is certainly an important issue.

This study tries to gain a consistent understanding of the phase selection behavior and subsequent solidification sequence both

theoretically and experimentally. The results from droplet experiments are so far not consistent with results from chill casting and high speed laser and electron beam welding. These processes exhibit some differences in the pertinent variables such as the nucleation barrier and temperature gradient; however, it is not clear why this leads to a difference in phase selection. The different phase selection behavior should be explained on a common basis: nucleation and growth. The mechanism of the phase selection and factors controlling it should be metallurgically ascertained as well. Changes in microstructure during and after solidification also need to be clarified; the change of metastable primary phase is of particular interest.

A rapid solidification experiment using a levitation technique is a promising experimental method for fulfilling the above objectives. In fact, unconstrained dendrite growth into an undercooled melt, which is commonly encountered in many rapid solidification processes, has not been investigated well in the Fe-Cr-Ni alloy system. One of the drawbacks of laser and electron beam melting experiments and gas-atomization experiments is a lack of actual information about the thermal history of the sample during rapid solidification. On the other hand, a levitation experiment with a high speed pyrometry system can provide quantitative information on temperature and heat evolution and dissipation as a function of time during rapid solidification[14,15,51]. The solidification sequence can be interrupted by quenching a sample into a liquid metal bath[15] for microstructural observation at various stages of solidification. Also, high cooling rate can be obtained in the solidification of undercooled melts by quenching onto chill substrate. This can be used for examining the effect of heat flow conditions by changing the chill material.

3. Overview of the Following Chapters

The following consists of six major chapters (Chapter II to Chapter VII). Each chapter has the style of an independent paper, containing its own introduction, objective, results, discussion, and conclusions. However, there is a consistent overall objective throughout the six chapters as mentioned above. Each chapter's introduction is more detailed than this chapter in providing background information pertinent to each subject.

Chapter II is entitled "Metastable Bcc Solidification of A Primary Fcc Fe-Cr-Ni Alloy". Nucleation-controlled solidification of a primary fcc Fe-17.5Cr-12.2Ni alloy is investigated using containerless, gas-cooled solidification by a levitation technique. Three major results are noted in this chapter. First, metastable bcc solidification in bulk samples, which was unclear in the past in spite of predictions[20], is explicitly shown. Metallographic evidence of metastable bcc solidification is presented. Second, using nucleation theory and a growth model, it is shown that the nucleation process is dominant over the growth process in determining the primary phase to solidify. A nucleation phase diagram for Fe-Cr-Ni alloys is proposed. Finally, the decomposition of the metastable bcc phase is analyzed, and a peritectic like semi-solid process is identified as well as the solid-state bcc-to-fcc transformation process.

Chapter III is entitled "Double Recalescence and Double Dendrite Formation in the Solidification of Primary Fcc Fe-Cr-Ni Alloys". Solidification of Fe-16Cr-14Ni and Fe-15Cr-15Ni alloys are analyzed based on recalescence behavior and quenched structures. The following three findings form the core of this chapter. First, double recalescence is demonstrated in Fe-Cr-Ni alloys for the first time, and is shown to result from metastable bcc solidification and subsequent formation of the stable fcc phase. This result is confirmed by the "nucleation phase diagram" obtained in Chapter II. It is shown that fcc formation follows metastable bcc solidification during the inter-recalescence plateau and the second recalescence, and the formation of

fcc is enhanced by the presence of a high fraction of bcc solid. Finally, the internal dendritic core within each dendrite and solute profiles are correlated to the recalescence behavior. The double recalescence[14,50,51] and solute-rich core[52-54] were treated separately in the past, but a relationship between these two are suggested in this chapter.

Chapter IV is entitled "Effect of Heat Extraction Rate on Dendrite Growth into Undercooled Melt in Fe-Cr-Ni Alloys". The solidification of Fe-17.5Cr-12.2Ni and Fe-18.5Cr-11.3Ni during chill casting was investigated using various chill materials, and this chapter describes the experimental results. It is shown that fcc solidification becomes dominant in these alloys, which is in contrast to the dominance of bcc in gas-cooled solidification. It is suggested that the high heat extraction rate achieved by the chill causes the preferential fcc solidification. The growth morphologies of fcc and bcc in chill casting are also discussed.

Chapter V is entitled "Rapid Dendrite Growth during Chill Casting". In connection with the previous chapter, a dendrite growth model for chill casting is proposed. It is assumed that a dendrite tip grows into the undercooled liquid and heat evolution at the dendrite tip occurs both into the undercooled melt and through the growing solid towards the chill. The effect of heat extraction through the solid is incorporated into the BCT model[10]. Dendrite growth behavior in the presence of this heat extraction is discussed. Particular emphasis is placed on the stability of dendrite growth in the presence of heat extraction through the solid.

Chapter VI is entitled "Preferential Fcc Solidification in Fe-Cr-Ni Alloys during Chill Casting". This chapter tries to explain the preferential fcc solidification found in the chill casting described in Chapter IV. Calculations are conducted using nucleation theory and the dendrite growth model developed in Chapter V. The calculations show that bcc nucleation is always favored, but it is suggested that a high heat extraction rate at the chill can cause nearly concurrent nucleation of bcc and fcc. Preferential fcc growth is discussed with reference to

the thermal effect, kinetic effect, and the stability of the growth morphology.

Chapter VII is entitled "Bcc-to-Fcc Transformation after Rapid Solidification in Fe-Cr-Ni Alloys". This chapter describes the bcc-to-fcc transformation behavior during the gas-cooled solidification of three different alloys. The occurrence of a massive transformation is shown in samples solidified with large initial undercoolings. The metallographic features of massive fcc are presented, and the effect of initial undercooling on the formation of the massive fcc is discussed.

Finally, some suggestions for future work in this field are given in Chapter VIII.

References

1. W. J. Boettinger and S. R. Coriell: *Science and Technology of the Undercooled Melt*, eds. P. R. Sahm, H. Jones, and C. M. Adam, Martinus Nijhoff Publ., Dordrecht, 1986, p.81
2. M. J. Aziz: *J. Appl. Phys.*, 1982, vol. 53, p. 1158
3. M. J. Aziz: *Mater. Sci. Eng.*, 1988, vol. 98, p. 369
4. S. C. Gill, M. Zimmermann, and W. Kurz: *Acta metall.*, 1992, vol. 40, p. 2895
5. M. Gremaud, M. Carrard, and W. Kurz: *Acta metall.*, 1990, vol. 38, p. 2587
6. W. W. Mullins and R. F. Sekerka: *J. Appl. Phys.*, 1964, vol. 35, p. 444
7. R. Trivedi and W. Kurz: *Acta metall.*, 1986, vol. 34, p. 1663
8. J. Lipton, W. Kurz, and R. Trivedi: *Acta metall.*, 1987, vol. 35, p. 957
9. J. Lipton, M. E. Glicksman, and W. Kurz: *Mater. Sci. Eng.*, 1984, vol. 65, p. 57
10. W. J. Boettinger, S. R. Coriell, and R. Trivedi: *Rapid Solidification Processing: Principles and Technologies*, eds. R. Mehrabian and P. A. Parrish, Claitor's Publ. Div., 1988, p. 13

11. W. Kurz, B. Giovanola and R. Trivedi: *Acta metall.*, 1986, vol. 34, p. 823
12. G. P. Ivantsov: *Dokl. Akad. Nauk S.S.S.R.*, 1947, vol. 58, p. 567
13. Y. Wu: Sc. D. Thesis, MIT, 1986
14. T. Piccone: Sc. D. Thesis, MIT, 1990
15. Q. Zhao: Sc. D. Thesis, MIT, 1992
16. Y. Wu, T. J. Piccone, Y. Shiohara, and M. C. Flemings: *Metal Trans. A*, 1987, vol. 18A, p. 915
17. T. J. Piccone, Y. Wu, Y. Shiohara, and M. C. Flemings: *Metal Trans. A*, 1987, vol. 18, p. 925
18. J. H. Perepezko: *Mater. Sci. Eng.*, 1984, vol. 65, p. 125
19. D. M. Follstaedt, P. S. Peercy, and J. H. Perepezko: *Mat. Res. Soc. Proc.*, 1988, vol. 100, p. 573
20. D. J. Thoma and J. H. Perepezko: *Metall. Trans. A*, 1992, vol. 23A, p. 1347
21. N. Saunders and P. Tsakiropoulos: *Mater. Sci. Tech.*, 1988, vol. 4, p. 157
22. T. F. Kelly: Ph. D. Thesis, MIT, 1982
23. T. F. Kelly, M. Cohen, and J. B. Vander Sande: *Metall. Trans. A*, 1984, vol. 15A, p. 819
24. T. F. Kelly and J. B. Vander Sande: *Int'l. J. Rapid Solidification*, 1987, vol. 3, p. 51
25. J. A. Juarez-Islas, H. Jones, and W. Kurz: *Mater. Sci. Eng.*, 1988, vol. 98, p.123
26. H. Jones: *Metall. Sci. Tech.*, 1989, vol. 17, p. 63
27. J. C. Lippold and W. F. Savage: *Weld. J.*, 1979, vol. 58, p. 362s
28. T. Takalo, N. Suutala, and T. Moisio: *Metall. Trans. A*, 1979, vol. 10A, p. 1173
29. N. Suutala, T. Takalo, and T. Moisio: *Metall. Trans. A*, 1980, vol. 11A, p. 717
30. J. A. Brooks, J. C. Williams, and A. W. Thompson: *Metall. Trans. A*, 1983, 14A, p. 23
31. J. A. Brooks, J. C. Williams, and A. W. Thompson: *Metall. Trans. A*, 1983, 14A, p. 1271
32. V. G. Rivlin and G. V. Raynor: *Int'l. Met. Rev.*, 1980, vol. 248, p. 21

33. Y.-Y. Chuang and Y. A.-Chang: *Metall. Trans. A*, 1987, vol. 18, p. 733
34. M. Hillert and C. Qiu: *Metall. Trans. A*, 1990, vol. 21A, p. 1673
35. M. Hasebe and T. Nishizawa: *Applications of Phase Diagram in Metallurgy and Ceramics*, ed. G. C. Carter, NBS, 1978, p. 911
36. A. Yamada, T. Umeda, M. Suzuki, G. Aragane, H. Kihara and Y. Kimura: *Tetsu-to-Hagane*, 1987, vol. 73, p. 1676
37. A. Yamada, T. Umeda, and Y, Kimura: *Tetsu-to-Hagane*, 1990, vol. 76, p. 2137
38. E. Schürmann and J. Brauckmann: *Arch. Eisenhüttenwes.*, 1977, vol. 48, p. 3
39. T. Ogawa and T. Koseki: *Weld. J.*, 1989, vol. 68, p. 181s
40. L. C. Lippold: *Weld. J.*, 1985, vol. 64, p. 127s
41. M. Bobadilla, J. Lacaze, and G. Lesoult: *J. Cryst. Growth*, 1988, vol. 98, p. 531
42. Y. Nakao, K. Nishimoto, and W.-P. Zhang: Proc. *4th Int'l. Colloq. on Welding and Melting by Electron and Laser Beams*, eds. M. Contré and M. Kuncevic, French Inst. of Welding, 1988, p. 673
43. J. W. Elmer: Sc. D. Thesis, MIT, 1988
44. J. W. Elmer, S. M. Allen, and T. W. Eagar: *Metall. Trans. A*, 1989, vol. 20A, p. 2117
45. J. M. Vitek, A. Dasgupta, and S. A. David: *Metall. Trans. A*, 1983, vol. 14A, p. 1833
46. S. A. David, J. M. Vitek, and T. L. Hebble: *Weld. J.*, 1987, vol. 66, p. 289s
47. H. Mizukami, T. Suzuki, and T. Umeda: *Tetsu-to-Hagane*, 1991, vol. 77, p. 134
48. M. R. Libera and Y. Shiohara: *MRS Int'l. Mtg. on Adv. Mats.*, 1989, vol. 3, p. 573
49. H.-M. Lin, Y.-W. Kim, and T. F. Kelly: *Acta metall*, 1988, vol. 36, p. 2537
50. Q. Zhao, T. J. Piccone, Y. Shiohara, and M. C. Flemings: *MRS Int'l. Mtg. on Adv. Mats.*, 1989, vol. 3, p. 597
51. D. M. Herlach, B. Feuerbacher, and E. Schleip: *Mater. Sci. Eng.*, 1991, vol. A133, p. 795
52. T. Z. Kattamis: *Z. Metallkde*, 1970, vol. 61, p. 856

53. T. Z. Kattamis and R. Mehrabian: *J. Mater. Sci.*, 1974, vol. 9, p. 1040
54. A. Munitz and G. J. Abbaschian: *Adv. Materials & Manufacturing Processes*, 1988, vol. 3, p. 419
55. J. M. Vitek and S. A. David: To be published
56. W. P. Allen and J. H. Perepezko: *Metall. Trans. A*, 1991, vol. 22A, p. 753

Chapter II - Metastable Bcc Solidification of A Primary Fcc Fe-Cr-Ni Alloy

Abstract

Rapid solidification of a primary fcc ferrous alloy, Fe-17.5 wt pct Cr-12.2 wt pct Ni, was investigated using a levitation melting and undercooling technique. Metastable bcc solidification was obtained in bulk specimens when they were undercooled by about 20 K or more in the process used. The primary phase was identified by solute profiles of the quenched mushy region as well as the structural features in the final microstructures.

Models of nucleation and growth were applied for comparison with experimental results. It is concluded that metastable bcc solidification is caused by nucleation, while the effect of growth on the phase selection is not significant. A nucleation phase diagram is proposed by combining experimental observation and nucleation theory for Fe-Cr-Ni alloys.

Formation of the fcc phase following metastable bcc solidification was observed by quenching the levitated specimens into a liquid metal bath at various times after recalescence. It occurs in the semi-solid condition at lower levels of undercooling, where the transformation is peritectic-like, involving solute transport across interdendritic liquid paths. At higher undercoolings, the transformation of bcc to fcc is primarily by solid state transformation, and likely to become massive-like as undercooling increases.

1. Introduction

1.1 Previous Work on Phase Selection in Ferrous Alloys

Phase selection and microstructural stability have been primary issues in rapid solidification research.[1,2] Many experimental instances of metastable phase solidification have been identified in various alloy systems by using different rapid solidification techniques. Obtaining and controlling metastable phases is important practically if novel materials are to be produced. From the scientific point of view, an understanding of phase selection behavior and its mechanism is also of interest, in connection with understanding microstructural evolution during rapid solidification.

In ferrous alloys, selection between bcc (ferrite) and fcc (austenite) during rapid solidification has been studied for many years. It has been examined particularly in the Fe-Ni alloy system since metastable bcc solidification was first reported by Cech[3] in Fe-29.5 wt pct Ni powders. The potential for metastable bcc solidification was also indicated theoretically in hyperperitectic Fe-Ni alloys undercooled below the liquidus line extension of the bcc phase.[4] A good summary of previous experimental work on phase selection in Fe-Ni alloys is available in ref. [5].

Despite many studies, only limited experimental evidence of metastable bcc solidification has been reported[3,6]. In addition, nearly all of the evidence has been limited to the solidification of fine powders. In bulk solidification of hyperperitectic alloys, two-step recalescence behavior has been observed, suggesting metastable bcc solidification in the first recalescence.[7-9] However, corresponding microstructural evidence was not obtained.

The potential for metastable bcc solidification was also investigated in the Fe-Cr-Ni alloy system.[9-11] Kelly *et al.* [9] reported that primary bcc solidification became dominant with decreasing particle size, i.e., with increasing undercooling, in the gas atomization

of type 303 stainless steel. They also performed a calculation based on nucleation theory, and showed the preferential nucleation tendency of bcc at increased undercooling. MacIsaac *et al.*[10] also reported a change from fcc to bcc with decreasing particle size for the solidification of type 316 stainless steel droplets.

As noted above, observation of metastable bcc structures has only been made in fine powders. However, nucleation of bcc is also expected to be favored over fcc in bulk undercooled melts. As stated by Thoma and Perepezko[5], the metastable bcc is likely to be retained in the final structure of rapidly-cooled fine powders but unlikely in the final structure of slowly-cooled bulk specimens, thus making it difficult to develop a full understanding of the solidification process in Fe-Ni alloys. They therefore considered both the solidification pathway and subsequent solid-state transformations, and concluded metastable bcc solidification occurred in specimens of a range of different sizes in their study.

The approach of Thoma and Perepezko is valid but not sufficient to explain the full range of phase selection behavior reported in the literature. For example, the preferential fcc formation observed in substrate quenching of both Fe-Ni alloys[12] and Fe-Cr-Ni alloys[13] can not be explained by their analysis, despite the fact that initial melt undercooling and post-solidification cooling rate in substrate quenching are comparable to fine powder solidification.

1.2 Solidification Behavior of Fe-Cr-Ni Alloys

Solidification of Fe-based Fe-Cr-Ni alloys in conventional casting and welding has been classified into four modes depending on the primary phase and subsequent solid-state transformation.[14-18] Reviewing those overall solidification modes is useful for the interpretation of rapidly solidified structure as discussed in the previous section.

Figure 1 is the pseudo-binary phase diagram of 70wt%Fe-Cr-Ni, which is of interest in the present study. Extended liquidus and solidus lines are also included as dashed lines. The diagram was obtained by thermodynamic calculation using Thermo-Calc[19] as described later. The equilibrium primary phase to solidify (for alloys in this section of the ternary diagram) is either fcc or bcc depending on composition. Bcc near the eutectic composition becomes unstable as temperature decreases, and undergoes transformation to fcc. Although the actual solidification follows a 3-dimensional path, the following solidification modes are intuitively understandable based on the pseudo-binary phase diagram. The schematics of four solidification modes of Fe base-Cr-Ni alloys (or austenitic stainless steel) are shown in Figure 2.[14]

A and AF modes solidify as primary fcc.[14,16,18] The liquid is enriched in Cr (i.e., the partition ratio of Cr, $k_{Cr}<1$) and partitioning of Ni is insignificant (i.e., the partition ratio of Ni, $k_{Ni}\approx1$) during fcc solidification. While the A mode is fully fcc solidification, the AF mode involves the (fcc+bcc) eutectic reaction in interdendritic regions as the Cr concentration increases in the interdendritic liquid. The eutectic has a divorced morphology. The amount of bcc decreases slightly on post-solidification cooling by diffusional bcc-to-fcc transformation, but some is stabilized by solute partitioning, and is retained in the final structure. The concentration of Cr is further increased and that of Ni is decreased in the bcc after the transformation. As a result, the final structure of the A mode is fully fcc, and that of the AF mode is fcc cell/dendrite with interdendritic bcc.

The FA mode solidifies as primary bcc.[15, 17,18] In contrast to primary fcc solidification, the liquid is enriched in Ni ($k_{Ni}<1$) and partitioning of Cr is insignificant ($k_{Cr}\approx1$) during bcc solidification. The (fcc+bcc) eutectic reaction occurs in interdendritic regions as the Ni concentration increases in the liquid. The primary bcc shrinks by bcc-to-fcc transformation, yet remains at the core of dendrites to give vermicular/skeletal and/or lacy morphologies which are

surrounded by fcc. The dendritic structure is still identifiable from the morphology of bcc in the final structure. It is noted that the concentration of Cr is increased and that of Ni is decreased in the bcc as a consequence of the solid state transformation.

The F mode is fully bcc solidification.[15] The bcc-to-fcc transformation starts from a fully bcc structure after the solidification. It results in the development of Widmanstätten fcc or lath-like fcc plates, primarily initiating from prior bcc grain boundaries. Therefore, the original dendritic structure is barely visible in the final structure. Relatively fast homogenization of solutes in the fully bcc sample prior to transformation also assists in the dissipation of the original solidification structure. In the final microstructure, the bcc is enriched in Cr and the fcc is enriched in Ni.

1.3 Objectives of This Study

The question of what determines phase selection in the rapid solidification of ferrous alloys has not heretofore been resolved. The potential for metastable bcc formation from an undercooled melt has been predicted by many researchers using nucleation theory; however, evidence has been limited. In addition, there is experimental evidence showing that phase selection is not determined by nucleation alone. The preferential fcc solidification seen in substrate quenching was already described as an example, and it will be seen later in this work that there is a strong effect of heat extraction rate on the phase selection. Selective fcc growth was also found in primary bcc stainless steels when surface-melted using laser and electron beams.[21-23] In this case, there is no nucleation barrier to solidification, and so phase selection must be growth-controlled.

The objective of this chapter is to show the occurrence of metastable bcc solidification in bulk specimens of a primary fcc Fe-Cr-Ni alloy and to determine the criteria governing it. A levitation melting technique was used to achieve various undercooling levels

and subsequent rapid solidification. Metallographic features showing evidence of metastable bcc solidification are presented. In an effort to identify the criteria governing the phenomenon, the effect of undercooling on phase selection was evaluated using nucleation theory. Finally, the decomposition of the metastable bcc phase and the subsequent evolution of the stable fcc phase are discussed, based on the observation of structural changes in the mushy zone with time.

2. Experimental

2.1 Material

The Fe-Cr-Ni alloy used in this study was 17.5 wt pct Cr - 12.2 wt pct Ni - bal. Fe. The location of the alloy on the isoplethal section of the Fe-Cr-Ni ternary phase diagram at 70 wt pct Fe is indicated by an arrow as "alloy A" in Figure 1. The composition is on the primary fcc side of the eutectic composition, Fe-18.1 wt pct Cr-11.9 wt pct Ni. The alloy was vacuum-melted using pure materials, and cast into a 7 kg ingot. It was then hot-forged, hot-rolled, and finally hot-drawn into 5-mm dia. rod. Finally, the product was solution-annealed at 1323 K for 1800 s followed by a water-quench. Those processes essentially eliminated all microsegregation of solutes in the starting material. Chemical analysis revealed that the purity of the ternary alloy was more than 99.96 wt pct with the remaining impurities (< 0.04 wt pct) mainly consisting of carbon (0.003 wt pct), silicon (< 0.01 wt pct), manganese (< 0.01 wt pct), nitrogen (0.001 wt pct) and oxygen (0.008 wt pct).

The equilibrium solidification mode of the alloy, primary fcc, was verified using induction melting. The alloy rod was placed in an induction coil, and a part of the rod was melted and slowly solidified in an inert atmosphere as in zone-melting. A typical equilibrium solidification structure is shown in Figure 3. The solidification was AF

mode, displaying dendrites of fcc (bright) with interdendritic bcc (dark). The solidification mode was also verified by autogenous welding using conventional gas-tungsten arc welding and low-speed electron beam welding.

2.2 Levitation Experiment

A schematic diagram of the experimental apparatus is shown in Figure 4. The apparatus included a levitation melter and a temperature measuring system. The levitation melter consisted of a high frequency power supply (10 kW, 450 kHz), capacitor banks, and a levitation coil. The coil used in the experiments had an inner diameter of 13 mm and was configured with five lower primary turns and two upper reverse turns. A quartz tube was inserted inside the coil and connected to a vacuum chamber below, so that the levitation atmosphere and the stream of cooling gas could be controlled. A liquid metal bath was placed about 50 mm below the levitated specimen when quenching was desired.

In a given experiment, an alloy specimen of mass 0.5 g (±0.05 g) was electro-magnetically levitated and induction-heated in an atmosphere of argon and 4 vol pct hydrogen until completely melted. Then, cooling was accomplished by flowing high-purity (99.9996%) helium, eventually causing nucleation to occur at a certain undercooled temperature with accompanying rapid recalescence. Some samples were solidified while levitated, and this process is hereafter referred to as "gas-cooled solidification". Other specimens were quenched from the semi-solid state into a Ga-25 pct In liquid bath at specified times after recalescence, in order to "quench in" the structure existing at different times during solidification.

The thermal history of levitated specimens was measured using a two-wavelength pyrometer which was connected to a two-channel digital data acquisition and storage system. Two data sampling rates were assigned simultaneously in order to measure the entire thermal history with low resolution and rapid recalescence

with high resolution; 200 Hz (5 ms per point) was typically employed for the former purpose, and 200 kHz (5 μs per point) for the latter. Calibration of the thermal measurements for Fe-Cr-Ni alloys was performed prior to the experiments in the same way as detailed in previous studies [23,24]. The linear signal ratio-temperature relationship was evaluated through more than sixty calibration experiments, and based upon that, the accuracy of undercooling measurement was estimated to be within ±7%.

2.3 Metallography

The microstructures of the specimens were observed by optical microscopy. Specimens after levitation were spherical, with a diameter of approximately 5 mm. They were cut into halves, and then mounted so as to observe the cross section. Of major interest in the observation is the region in the vicinity of the specimen surface, since the pyrometric temperature measurement was performed at the surface. In order to reveal the microstructure, the sample was electrolytically etched at 4 V for 5 to 10 s in an aqueous solution of 10 vol pct sulfuric acid. The etching delineated the relative difference of Ni concentration as well as the phase boundaries; regions of low Ni concentration such as bcc were selectively stained dark, while regions of high Ni concentration such as fcc were relatively bright in the duplex structures. The coloration could not be used to determine the structure in a single-phase region or a partitionless region, however.

Concentration profiles of Cr and Ni in solidification structures were measured using computer-aided microprobe analysis (CMA)[25]. Two-dimensional step-scanning was conducted over the area of interest on as-polished cross-sections of the samples. Operating conditions of the CMA were: an acceleration voltage of 15 kV, a beam current of 1 μA, a spot size (i.e., beam diameter) of 1 μm, and beam irradiation time of 20 ms per point.

X-ray diffractometry (XRD) was used to identify the phase balance in the structure of interest. Measurement was conducted on the as-polished cross section of a sample (approximately, 20 mm^2) with the diffraction angle, 2θ, varying from 30° to 100°. Operating conditions of the XRD were: an acceleration voltage of 60 kV and a current of 300 mA for the X-ray source using a copper target, a divergence slit of 1° and a receiving slit of 0.3° for the diffractometer.

3. Calculation

3.1 Thermodynamic Properties of Fe-Cr-Ni Alloys

Phase diagrams and thermodynamic properties such as free energy, enthalpy etc. were calculated using Thermo Calc, a software and database package for the calculation of phase diagrams developed by Sundman *et al.*[19] Thermodynamic data from the SGTE (Scientific Group of Thermodata, Europe) database of Thermo Calc version J were applied to those calculations after comparing the portion of calculated phase diagram of interest with that by Chuang *et al.*[26] and that by Hasebe *et al.*[27] The isoplethal section of the Fe-Cr-Ni ternary phase diagram shown in Figure 1 was one of the calculation results. All the thermodynamic properties necessary for the following numerical analyses were calculated to maintain correspondence between the numerical results and the phase diagram.

3.2 Nucleation

Classical nucleation theory[28-30] is applied to evaluate the phase selection during nucleation. Heterogeneous nucleation at the specimen surface is assumed. Although the nature of the catalyst (substrate) is not known in the present experiment, the liquid/gas

interface can be a good nucleation site. Following the classical nucleation theory, surface nucleation rate, I_s, is given by

$$I_s = \frac{k_s}{\eta} \exp\left[-\frac{\Delta G^*}{kT}\right] \qquad (1)$$

where k_s is the kinetic parameter for surface nucleation[28,30], η is the viscosity of the liquid, ΔG^* is the critical free energy of the formation of a nucleus, k is the Boltzmann constant, and T is the absolute temperature. η can be estimated for metallic systems by using[29,30]

$$\eta = 10^{-4.3} \exp\left[\frac{3.34}{T_r - T_{rg}}\right] (N\ s\ m^{-2}) \qquad (2)$$

where T_r is a reduced temperature ($=T/T_L$), and T_{rg} is the reduced glass transition temperature. In the case of planar catalytic sites and incoherent nuclei, the critical free energy ΔG^* is given by

$$\Delta G^* = \frac{16\pi}{3} \frac{\gamma_{S/L}^3}{\Delta G_v^2} f(\theta) \qquad (3)$$

where $\gamma_{S/L}$ is the interfacial energy between the solid and the liquid, ΔG_v is the free energy for the formation of the solid from the liquid (per unit volume), and $f(\theta)$ is a catalytic potency factor which is a function of the wetting angle θ between the nucleus and the substrate given as $f(\theta)=(2-3\cos\theta+\cos^3\theta)/4$.

In the calculation, ΔG_v and $\gamma_{S/L}$ are critical parameters affecting the final results. Two cases are considered for ΔG_v:

(i) maximum free energy change (i.e., thermodynamic driving force), ΔG_{max}, as an upper bound for ΔG_v.[31]
(ii) free energy change for massive (i.e., composition invariant) transformation, $\Delta G_{massive}$, as a lower bound for ΔG_v.

Schematic representations of these quantities on the free energy diagram are given in Appendix 1. Both were calculated as a function of temperature using Thermo Calc, the results (absolute values) of which are also shown in the Appendix 2. Those two ΔG_v's are realistic extreme cases in terms of the composition of nuclei; ΔG_{max} corresponds to full partitioning and $\Delta G_{massive}$ to partitionless situation. The interfacial energy between the solid and the liquid, $\gamma_{S/L}$, is estimated with the following equation[32,33]:

$$\gamma_{S/L} = \frac{\alpha_{S/L} \Delta H_{S/L}}{(N\bar{V}^2)^{1/3}} \qquad (4)$$

where $\alpha_{S/L}$ is a dimensionless interfacial energy parameter, $\Delta H_{S/L}$ is the enthalpy difference between the solid and the liquid, N is Avogadro's number, and $\bar{V}$ is the molar volume. Corresponding to each case of (i) and (ii), $\Delta H_{S/L}$ is also calculated as a function of temperature by Thermo Calc.

Nucleation rate, I_S, is a function of T and θ, and thereby, nucleation temperature, $T_N(\theta)$, during continuous cooling is determined by integrating the nucleation rate,[29]

$$\int_{T_N(\theta)}^{T_L} \frac{I_s S}{dT/dt} dT = 1 \qquad (5)$$

where S is the surface area and dT/dt is the cooling rate of the specimen. The implication of Eq. (5) is that the number of nuclei becomes one when the temperature reaches the nucleation temperature, $T_N(\theta)$, during continuous cooling. It is known that $T_N(\theta)$ will not change significantly even if the number of the RHS is changed.[4,9] Two independent functions, $T_{N,\,fcc}(\theta_{fcc/sub})$ and $T_{N,\,bcc}(\theta_{bcc/sub})$, are obtained from Eq. (5), where $\theta_{fcc/sub}$ and $\theta_{bcc/sub}$ are wetting angles between fcc and substrate and between bcc and substrate, respectively. $T_N(\theta)$ is a one-to-one function monotonously decreasing with θ. If the two functions, $T_{N,\,fcc}(\theta_{fcc/sub})$ and $T_{N,\,bcc}(\theta_{bcc/sub})$,

are plotted together on the θ-T coordinate, a given transition temperature, T_t, can specify a unique difference of wetting angles, $\Delta\theta$ ($=\theta_{fcc/sub}-\theta_{bcc/sub}$). At the same time, the reverse is also true. In other words, a given $\Delta\theta$ can specify a unique value of T, and thus, $\Delta\theta$ and T_t have a one-to-one correspondence. Therefore, if a value of $\Delta\theta$ is assumed in advance, one can uniquely determine the corresponding transition temperature at which fcc nucleation and bcc nucleation have the same likelihood, without knowing either $\theta_{fcc/sub}$ or $\theta_{bcc/sub}$. In actual calculation, the following combinations are searched numerically with a given $\Delta\theta$:

$$T_{N,\,fcc}(\theta_{fcc/sub}) = T_{N,\,bcc}(\theta_{bcc/sub}) \qquad (6\text{-}1)$$

and

$$\theta_{fcc/sub} = \theta_{bcc/sub} + \Delta\theta \qquad (6\text{-}2)$$

Numerical data used in the calculation are listed in Table 1.

3.3 Growth

Dendrite tip models were called upon to evaluate the effect of phase stability on the growth. The Boettinger-Coriell-Trivedi (BCT) model[34] was employed. In Fe-Cr-Ni alloys, equilibrium partition ratios indicated that distinct partitioning occurred only with one of the two solute elements for each primary phase to solidify. Pseudo-binary approximation of the alloy system and linear approximation of the liquidus and solidus lines were found to be reasonable, and the BCT model was applied under these assumptions. The details of the model itself are not described here, but can be found in refs. [34, 35]. Numerical data used in the calculation are given in Table 2.

4. Experimental Results

4.1 Thermal History

Figure 5 shows a typical cooling curve observed during a levitation experiment. The melt was initially superheated by about 100 K, then cooled at a rate of approximately 100 K/s. At a certain undercooled temperature, T_N, the melt started to rapidly solidify with recalescence. Undercooling, ΔT (= T_L-T_N), obtained in this study ranged from 12 K to 160 K. The recalescence time, a time from T_N to T_R, was a function of undercooling, decreasing with increasing undercooling as shown in Figure 6. The effect of initial undercooling on the recalescence temperature, T_R, was not as clear in this study as reported before[24,35]. This was probably due to the narrow freezing temperature range of the alloy. After reaching T_R, the temperature decreased slowly while the specimen was in the semi-solid state.

During most levitation experiments with the present alloy, a secondary recalescence from T_N' to T_R' was observed about 0.5 to 2 s after the first recalescence. The onset temperature, T_N', decreased as the initial undercooling increased, as shown in Figure 7. The time between the first recalescence and the second recalescence did not show any distinct dependency on initial undercooling. The specimen became fully solid after the second recalescence, and then cooled at a rate of 100 to 150 K/s. Significance of the marked temperatures and times are to be discussed in the following sections.

4.2 Metastable BCC Solidification from the Undercooled Melt

Figure 8 shows typical solidification structures obtained by gas-cooling solidification with initial undercoolings from 33 K to 155 K. In the micrographs, bcc is stained dark, and fcc bright. Microstructures varied with initial undercooling; however, as detailed below, features of primary metastable bcc solidification were commonly observed in each structure.

Figure 8(a) is for an initial undercooling of 33 K. Dendrites are elongated from the specimen surface towards the inside for 100 to 200 μm, and seem to be interconnected to one another; however, dendrites beyond these are rather globular and appear to be isolated. Bcc phase (dark) is retained at the core region of each dendrite with skeletal or vermicular morphologies; skeletal bcc is more evident at the cores of the elongated dendrites. The location and morphology of the retained bcc are typical of FA solidification mode[15,17,18] as illustrated in Figure 2.

Figure 8(b) is for an initial undercooling of 51 K. Retained bcc near the specimen surface is denser than that in Figure 8(a), yet dendrite boundaries are clear, outlined by fcc (bright). The morphology of retained bcc varies from a lacy appearance to skeletal and vermicular appearances as it goes from the surface to the inside. As compared with Figure 2, those morphologies at the core region of dendrites are characteristic features indicating FA mode solidification.[15]

Figure 8(c) is for an initial undercooling of 138 K. No dendritic structure is seen near the specimen surface; in its place is large-scale plate-like fcc. This implies that a bcc-to-fcc diffusional transformation occurred after fully bcc solidification (F mode), forming a plate-like (or Widmanstätten) structure of fcc from bcc grain boundaries. At intermediate undercoolings between 51 K and 138 K, structures appropriate for mixtures of FA mode and F mode were observed.

Figure 8(d) is for an initial undercooling of 155 K. The structure near the surface of the specimen was fully fcc and did not contain any retained ferrite. The structure was considered to be achieved by massive transformation following fully bcc solidification. This conclusion was based on the temperature of the bcc-to-fcc transformation, and changes in structures, solute profiles, and X-ray diffraction before and after the transformation, as discussed later. In

fact, the inside of the specimen clearly retained the final structure produced by primary bcc solidification.

In order to confirm the above conclusion microstructurally, solidification was interrupted immediately after recalescence by liquid metal quenching, and the solute distribution in the mushy zone was measured. Figure 9 shows a quenched structure and corresponding concentration maps of Cr and Ni. The specimen was initially undercooled by 33 K, and quenched into the In-Ga liquid bath approximately 0.3 s after recalescence. Dendrite morphology is elongated near the surface and globular inside, which is analogous to structural features shown in Figure 8(a). The fraction solid seems to be slightly higher near the surface than inside at the moment of quenching. The interdendritic regions (showing fine cellular structure) were liquid prior to the quench. No significant partitioning of Cr is seen between the solid and the liquid, but partitioning of Ni is considerable. Ni is depleted in the solid, and enriched in the interdendritic liquid. The composition profiles indicate that the solid existing in the mushy zone is bcc, and thereby confirm that the primary solidification product is metastable bcc phase. This was supported by similar tests on other quenched specimens made with different undercoolings.

Both primary fcc and primary bcc solidification were found to coexist in a specimen when the initial undercooling was small. An example appears in Figure 10, which was undercooled by 18 K prior to solidification. Nearly half of the specimen surface is covered with retained bcc having a skeletal morphology, and the remainder with fcc dendrites with interdendritic bcc. The former indicates primary bcc solidification growing toward the inside from the surface, and the latter primary fcc solidification; however, the growth of the metastable bcc was limited to near the surface. It should be noted that the growth direction of retained bcc is different from that of nearby fcc. The mixed solidification of primary bcc and fcc suggests that the transition of the primary phase from stable fcc to metastable bcc occurs at about this undercooling level.

4.3 Structural Change after Metastable Bcc Solidification

Microstructural changes during gas cooled solidification were observed through liquid metal quenching experiments, and they revealed that the second recalescence is associated with the formation of fcc phase. Figure 11 shows changes in microstructure with time after the first recalescence. Specimens which were similarly undercooled but quenched into In-Ga bath at different times after the first recalescence were selected. The initial undercooling of every specimen was similar: around 110 K.

Fine dendrites of primary bcc were uniformly distributed within the entire specimen at 0.15 s after the first recalescence (Figure 11(a)). This suggests that the temperature distribution within a specimen during and immediately after the recalescence was uniform, and that the assumption of adiabatic conditions during recalescence is reasonable. In the specimen levitated and cooled 0.4 s before quenching, more notable dendrite thickening is apparent in the outer region, as well as dendrite coarsening (Figure 11(b)). The distribution of fraction solid suggests slightly lower temperature at the surface than at the center. In the specimen held 1.5 s before quenching, the outer region appears to have been nearly fully solid and largely homogenized while the inside was still semi-solid (liquid+bcc) with substantial coarsening occurring there (Figure 11(c)).

In all experiments, fcc was observed in the structure only after appearance of the second recalescence. The formation of fcc is seen in Figure 11(d) which was obtained at 1.9 s after the first recalescence and 0.4 s after the second recalescence. The growth interface of fcc, proceeding toward the center, is seen at about 1.2 mm inside from the specimen surface in the figure. A mixture of fcc and bcc (which is close to the final structure in samples fully solidified by gas cooling) is observed behind the interface, while the mixture of liquid and primary bcc remains ahead of the interface.

Figure 12 shows the solute profile of Cr and Ni in the vicinity of the growth interface of the fcc. The profiles in the liquid are basically the same as those in Figure 10; Ni is notably partitioned between the primary bcc and the liquid while the partitioning of Cr is insignificant. On the other hand, Cr is largely depleted in growing fcc and enriched in both bcc and interdendritic regions behind the interface. The concentration of Ni in fcc is slightly lower than that in the liquid, and much higher than that in bcc. The bcc-to-fcc transformation is also characterized by the shrinkage of the Ni-depleted region in the fcc. In summary, the solute profiles obviously indicate fcc growth into the (liquid+bcc) semi-solid region with solute redistribution.

Figure 13 shows X-ray diffraction results from the structures quenched before and after the second recalescence, corresponding to the structure shown in Figure 11(a) and 11(d), respectively. Peaks indicating fcc in Figure 13(a) probably resulted from the previously liquid region which presumably solidified to fcc through quenching, or from the bcc-to-fcc transformation during quenching. A clear difference between Figures 13(a) and 13(b) is that the (111) peak of fcc significantly increased in the latter. This indicates that the second recalescence can be attributed to the formation of fcc which has a preferred orientation.

5. Discussion

5.1 Effect of Nucleation on Phase Selection

Calculated temperatures for the fcc-to-bcc transition in Fe-17.5Cr-12.2Ni alloy are plotted in Figure 14 as a function of wetting angle difference, $\Delta\theta(=\theta_{fcc/sub}-\theta_{bcc/sub})$. The figure shows that fcc is favored as a nucleating phase at relatively high temperature but that stability is reversed as temperature decreases. The two lines are

based on the two different free energy changes, ΔG_{max} and $\Delta G_{massive}$, used in the calculation. Liquidus lines for fcc and metastable bcc are also included in the figure. Preferential fcc nucleation is expected above the transition temperature, and bcc nucleation below it.

The calculated transition temperatures in Figure 14 are in general agreement with the tendency of the phase selection observed in levitation experiments. The line obtained from the use of ΔG_{max}, and the line from $\Delta G_{massive}$ show similar dependencies on $\Delta\theta$ ($=\theta_{fcc/sub}-\theta_{bcc/sub}$); the former approaches the liquidus of bcc at the high end of $\Delta\theta$, and the latter to the bcc-T_0. Experimentally, both primary fcc and primary bcc were found to coexist at undercoolings around 18 K, and thereby, the transition in nucleating phase was considered to be at those undercooling levels. Since massive nucleation is more likely at lower temperatures, the transition temperature calculated by using ΔG_{max} is probably suitable for comparing calculation results with observation at small undercooling. Thereby, the difference of the wetting angles is deduced from the line using ΔG_{max} to be close to zero for gas-cooled solidification, although its physical significance is not clear due to the unknown nature of the "substrate". On the other hand, the line using $\Delta G_{massive}$ is probably suitable for comparing calculation results with observation at large undercoolings.

Using the assumption $\theta_{fcc/sub}=\theta_{bcc/sub}$ (i.e., $\Delta\theta=0$), a diagram indicating preferential nucleating phase (a nucleation phase diagram) was constructed as shown in Figure 15. Extended liquidus lines of fcc and bcc are included by dotted lines, and experimental observations of primary phases are also plotted in the figure. Fcc is a dominant nucleating phase in the region above the transition line, and bcc nucleation is dominant otherwise. The transition temperature decreases as Cr content decreases, or as the composition goes to the side where fcc is stable. At lower temperatures, bcc nucleation is always dominant, even in equilibrium primary fcc compositions. This is primarily due to its smaller liquid/solid interfacial energy. In fact, the nucleation phase diagram is applicable to experimental results

obtained with the more fcc-stable Fe-15Cr-15Ni alloy, as described in the following chapter. It is interesting to note that the transition temperature is below the liquidus temperature of the bcc phase, and the difference between the two temperatures becomes larger in the region of fcc stability; this implies that the liquidus extension of an alternate phase may not indicate the onset of the nucleation of the alternate phase despite the common practice of using it for this purpose[2].

5.2 Growth of Primary Phase during Recalescence

Figure 16 shows the calculated result of dendrite tip velocity from fcc and bcc versus melt temperature. Since the growth velocities of both phases are close to each other at all undercoolings, it appears that either phase can grow as long as its nuclei exist. In other words, The growth model does not indicate a growth preference of either fcc or bcc, and growth is not expected to be critical to phase selection in this system.

Growth velocities were experimentally estimated from measured recalescence time, and correlated with the result of the model also in Figure 16. Since undercoolings attained in the present study were small to intermediate as compared with the unit undercooling, $\Delta H_f/C_{pL}$ (ΔH_f, latent heat of fusion, and C_{pL}, specific heat of the liquid), multiple nucleation could occur during nucleation and growth stages. Temperature was measured through pyrometry at the specimen surface. Therefore, the observed recalescence time, Δt_R, could be related to the growth velocity, V, assuming that recalescence represents site saturation by nucleation and growth at the specimen surface. In other words, measurement of recalescence results from the decrease of undercooled regions by the formation and growth of high temperature dendrites, and the measurement of its termination corresponds to the overlapping of thermal diffusion fields around growing dendrites. The two-dimensional Johnson-Mehl-Avrami equation[36] was applied to relate V and Δt_R:

$$V = 4.4\,(I_S)^{-0.5}\,(\Delta t_R)^{-1.5} \qquad (7)$$

where I_S is the surface nucleation rate at the nucleation temperature. In the calculation of nucleation in the previous section, I_S always fell between 10^6 and 10^7 ($m^{-2}\ s^{-1}$) at the nucleation temperature, and thus, $I_S = 10^7$ was assumed in the above equation. As seen in Figure 16, velocities obtained by Eq. (7) show good agreement with the model results. Inversely, this implies that the assumptions of steady state dendrite growth and recalescence controlled by nucleation and growth are acceptable.

5.3 Formation of Secondary, Stable Fcc Phase

In Figures 11 and 12, it is apparent that the transformation of bcc to fcc in the semi-solid regions occurs by diffusion of solvent through the liquid, according to the peritectic-like reactions:

$$L + \text{bcc} \rightarrow \text{fcc}\ (+\ \text{bcc}) \qquad (8)$$

The association of the liquid phase provides a relatively rapid transport mechanism for the bcc-to-fcc transformation, and accounts for the relatively rapid temperature rise of the second recalescence. In fact, as shown in Figure 7, most of the onsets of the second recalescence are in the liquid/bcc two-phase region, and the nucleation and growth of fcc occurs at those temperatures. The distribution of Ni shown in Figure 12 indicates that the liquid is the most enriched in Ni, bcc is the least, and fcc is intermediate, which is in accord with the mass balance of the peritectic reaction in Eq. (8). Another typical example is shown in Figure 17, which was obtained by quenching after metastable bcc solidification with relatively small undercooling (ΔT= 67 K). The fraction of primary bcc is relatively small, and dendritic growth of secondary, stable fcc is clearly seen to proceed into the semi-solid.

As seen in Figure 7, the onset temperature of the second recalescence was relatively low when initial undercooling was large; it was close to the fcc solvus in some specimens. As the temperature decreases, microstructure prior to the transformation is likely to be fully bcc with extensive solute homogenization, rather than the semi-solid. Under those conditions, i.e., in nearly fully solid situation, the mechanism of the bcc-to-fcc transformation can be either diffusional for Widmanstätten structures or perhaps even massive in the extreme case[38]. Typical consequences were shown in Figures 8(c) and 8(d). In summary, the formation of stable fcc after the metastable bcc solidification occurs both in the semi-solid and in the fully solid state. The former is likely when the initial undercooling is relatively small so that semi-solid is present for long times after the first recalescence. On the other hand, the latter becomes dominant when initial undercooling increases and less remaining liquid is available at the transformation time.

6. Conclusions

Phase selection and microstructural evolution during the rapid solidification of Fe-17.5 wt pct Cr-12.2 wt pct Ni alloy was investigated. The equilibrium solidification mode of the alloy was primary fcc. Undercooling and rapid solidification of bulk samples of the alloy were achieved using a levitation technique. Conclusions obtained are:

(1) Metastable bcc solidification in bulk specimens, which was not clear in the past in spite of predictions, occurs at initial undercoolings of 20 K to 160 K. The bcc solidification is identified by the final microstructures and by solute distributions in mushy regions; the microstructures show retained bcc typical of primary bcc solidification mode, and the solute profiles exhibit the distinct depletion of Ni and insignificant partition of Cr in growing solid which is also specific to bcc solidification.

(2) Nucleation and growth calculations were made using classical nucleation theory and the BCT (Boettinger-Coriell-Trivedi) dendrite growth model. Bcc nucleation is favored over fcc nucleation for undercoolings greater than 20 K. Growth shows little preference for a specific phase to grow in an undercooled condition in the present system. Therefore, it is concluded that nucleation is the process governing primary phase selection.

(3) A nucleation phase diagram was constructed based on experimental observation and theoretical calculation assuming no difference of wetting angles of fcc and bcc for heterogeneous nucleation. The diagram shows which of the two phases nucleates in an undercooled condition for a range of Cr-Ni-70 wt pct Fe alloys.

(4) When the primary phase to solidify is metastable bcc, subsequent recalescence occurs 0.5 to 2 s after the original recalescence. This is attributed to the formation of fcc. At lower undercooling levels, it takes place by peritectic-like transformation in the semi-solid condition involving solute transport across interdendritic liquid paths. At higher undercoolings, it is essentially by the solid state bcc-to-fcc transformation, and likely to be massive as undercooling increases.

Appendix 1

Schematic Representations of ΔG_{max} and $\Delta G_{massive}$ on the Free Energy Diagram

Schematic representations of ΔG_{max} and $\Delta G_{massive}$ on the free energy diagram are shown below, where ΔG_{max} is the maximum free energy change or thermodynamic driving force and $\Delta G_{massive}$ is the free energy change for composition invariant transformation. In the figure, C0 and C* are the nominal composition and the solid composition giving thermodynamic driving force, respectively.

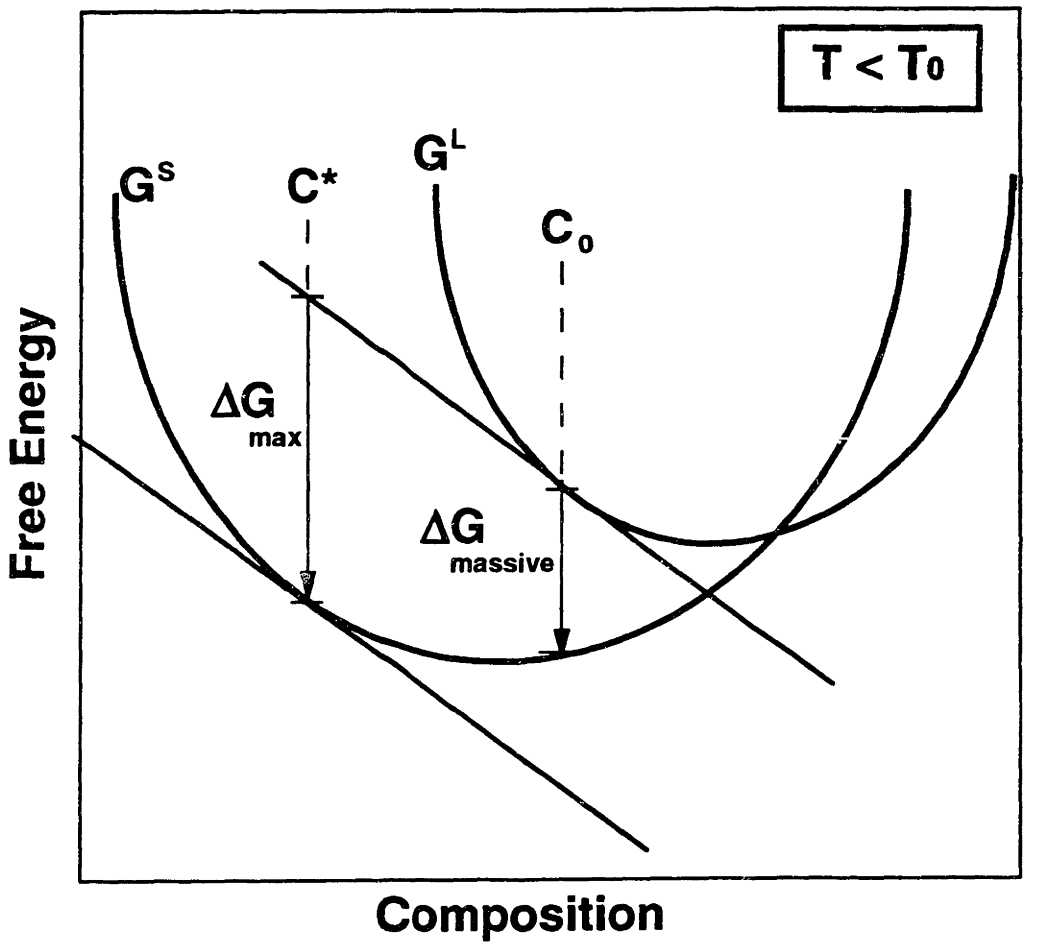

Appendix 2 - ΔG_{max} and $\Delta G_{massive}$ calculated for fcc and bcc as a function of temperature using Thermo Calc[19].

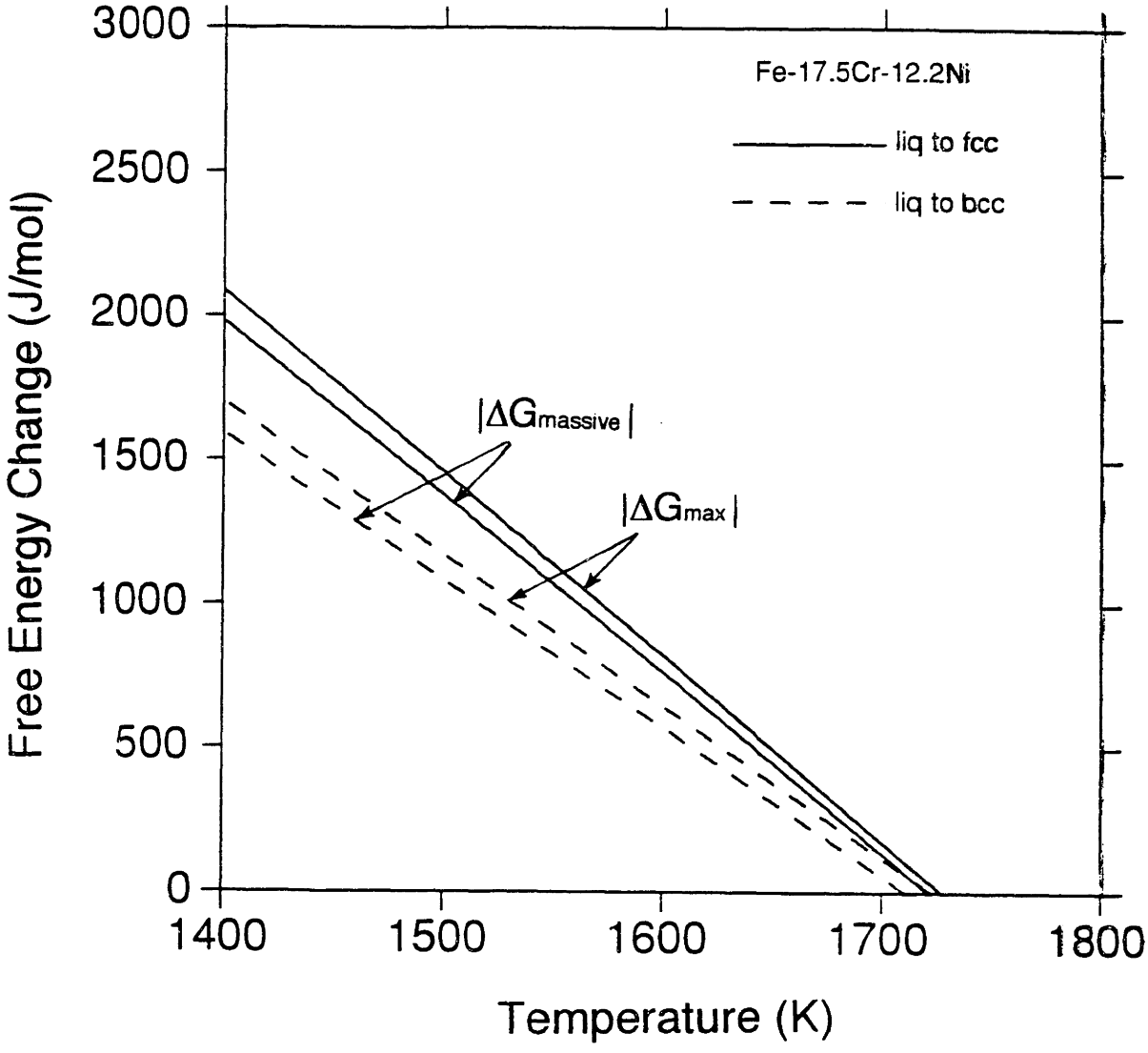

References

1. H. Jones: *Metall. Sci. Tech.*, 1989, vol. 7, p.63
2. J. H. Perepezko and W. J. Boettinger: *Mat. Res. Soc. Symp. Proc.*, 1983, vol. 19, p. 223
3. R. E. Cech: *Trans. AIME*, 1956, vol. 206, p. 585
4. T. F. Kelly and J. B. Vander Sande: *Int'l. J. Rapid Solidification*, 1987, vol. 3, p. 51
5. D. J. Thoma and J. H. Perepezko: *Metall. Trans. A*, 1992, vol. 23A, p. 1347
6. Y.-W. Kim, H.-M. Lin, and T. F. Kelly: *Acta Metall.*, 1988, vol. 36, p. 2525
7. Q. Zhao, T. J. Piccone, Y. Shiohara, and M. C. Flemings: *MRS Int'l. Mtg. on Adv. Mats.*, 1989, vol. 3, p. 597
8. D. M. Herlach, B. Feuerbacher, and E. Schleip: *Mater. Sci. Eng.*, 1991, vol. A133, p. 795
9. T. F. Kelly, M. Cohen, and J. B. Vander Sande: *Metall. Trans. A*, 1984, vol. 15A, p. 819
10. D. G. MacIsaac, Y. Shiohara, M. G. Chu, and M. C. Flemings: *Proc. Conf. on Grain Refinement in Castings and Welds*, G. J. Abbaschian and S. A. David, eds., TMS-AIME, Warrendale, PA, 1983, pp. 87
11. W. Löser and D. M. Herlach: *Metall. Trans. A*, 1992, vol. 23A, p. 1585
12. T. Z. Kattamis, W. F. Brower, and R. Mehrabian: *J. Cryst. Growth*, 1973, vol. 19, p. 229
13. H. Mizukami, T. Suzuki, and T. Umeda: *Tetsu-to-Hagane*, 1992, vol. 78, p. 1369
14. T. Takalo, N. Suutala, and T. Moisio: *Metall. Trans. A*, 1979, vol. 10A, p. 1173
15. N. Suutala, T. Takalo, and T. Moisio: *Metall. Trans. A*, 1980, vol. 11A, p. 717
16. J. A. Brooks, J. C. Williams, and A. W. Thompson: *Metall. Trans. A*, 1983, vol. 14A, p. 23
17. J. A. Brooks, J. C. Williams, and A. W. Thompson: *Metall. Trans.* A, 1983, vol. 14A, p. 1271

18. T. Koseki, T. Matsumiya, W. Yamada, and T. Ogawa: To be published in *Metall. Trans. A*
19. B. Sundman, B. Jansson, and J.-O. Andersson: *CALPHAD*, 1985, vol. 9, p. 153
20. J. M. Vitek, A. Dasgupta, and S. A. David: *Metall. Trans. A*, 1983, vol. 14A, p. 1833
21. M. Bobadilla, J. Lacaze, and G. Lesoult: *J. Cryst. Growth*, 1988, vol. 89, p. 531
22. J. W. Elmer, S. M. Allen, and T. W. Eagar: *Metall. Trans. A*, 1989, vol. 20A, p. 2117
23. Q. Zhao: Sc. D. Thesis, MIT, 1992
24. T. J. Piccone, Y. Wu, Y. Shiohara, and M. C. Flemings: *Metall Trans. A*, 1987, 18A, p. 925
25. I. Taguchi and H. Hamada: *Analytical Sci.*, 1985, vol. 1, p. 119
26. Y.-Y. Chuang and Y. A.-Chang: *Metall. Trans. A*, 1987, 18A, p. 733
27. M. Hasebe and T. Nishizawa: *Applications of Phase Diagram in Metallurgy and Ceramics*, G. C. Carter, ed., NBS, 1978, p. 911
28. D. Turnbull and J. C. Fisher: *J. Chem Phys.*, 1949, vol. 17, p. 71
29. D. Turnbull: *Contemp. Phys.*, 1969, vol. 10, p.473
30. F. Spaepen and D. Turnbull: *Rapidly Quenched Metals II*, N. J. Grant and G. B. Giessen, eds., MIT Press, Cambridge, MA, 1976, p. 205
31. C. V. Thompson and F. Spaepen: *Acta metall.*, 1983, vol. 31, p. 2021
32. F. Spaepen and R. B. Meyer: *Scr. metall.*, 1976, vol. 10, p. 257
33. C. V. Thompson: Ph. D. Thesis, Harvard University, 1981
34. W. J. Boettinger, S. R. Coriell, and R. Trivedi: *Rapid Solidification Processing: Principles and Technologies IV*, R. Mehrabian and P. A. Parrish, eds., Claitor's Publ. Div., Baton Rouge, LA., 1988, p. 13
35. M. Suzuki, T. J. Piccone, M. C. Flemings, and H. D. Brody: *Metall. Trans. A*, 1991, vol. 22A, p. 2761
36. J. W. Christian: *Theory of Transformation in Metals and Alloys*, Pergamon Press, Oxford, 1975, p.19
37. Y. Ono: *The Properties of Liquid Metals*, S. Takeuchi, ed., Taylor and Francis, London, 1973, p. 543

38. J. Singh, G. R. Purdy, and G. C. Weatherly: *Metall. Trans. A*, 1985, vol. 16A, 1363
39. W. J. Boettinger, S. R. Coriel, and R. F. Sekerka: *Mater. Sci. Eng.*, 1984, vol. 65, p.27

Table 1 : Parameter values used for nucleation calculation (other than ΔG_{max}, $\Delta G_{massive}$ and corresponding $\Delta H_{S/L}$s).

paprameter		value		ref.
T_L	liquidus temperature (K)	1726.19	(fcc)	
		1721.88	(bcc)	
$\alpha_{S/L}$	dimensionless interfacial energy parameter (-)			
		0.86	(fcc/liq)	[32]
		0.71	(bcc/liq)	[33]
$\bar{V}$	molar volume (m^3 mol^{-1})	7.71×10^{-6}	(liq)	
		7.71×10^{-6}	(fcc)	
		7.71×10^{-6}	(bcc)	
k_s	kinetic parameter for surface nucleation ($N m^{-4}$)			
		1×10^{29}		[28,30]
T_{rg}	reduced glass transition temperature (-)	0.25		[29]
S	surface area of specimen (m^2)	7.85×10^{-5}		
dT/dt	cooling rate ($K s^{-1}$)	100		

Table 2: Parameter values used for the calculation of the dendrite tip model.

parameter		value		ref.
T_L	liquidus temperature (K)	1726.19	(fcc)	
		1721.88	(bcc)	
ΔH_f	enthalpy of fusion (J mol^{-1})	11332.44	(fcc)	
		8947.16	(bcc)	
ΔS_f	entropy of fusion (J $mol^{-1}K^{-1}$)	6.5552	(fcc)	
		5.6766	(bcc)	
k_{Cr}	partition ratio of Cr	0.8630	(liq/fcc)	
k_{Ni}	partition ratio of Ni	0.7692	(liq/bcc)	
m_L	slope of liquidus (K $wt\%^{-1}$)	-4.1248	(fcc)	
		-6.6133	(bcc)	
C_{pL}	specific heat of liqiud (J $mol^{-1}K^{-1}$)	43.7468		
$\overline{V}$	molar volume (m^3 mol^{-1})	7.71×10^{-6}	(liq)	
		7.71×10^{-6}	(fcc)	
		7.71×10^{-6}	(bcc)	
D_{Cr}	diffusivity of Cr in liquid (m^2 s^{-1})			
	D_0 diffusion constant (m^2 s^{-1})	2.67×10^{-7}		[37]
	Q activation energy (J mol^{-1})	6.69×10^4		[37]
D_{Ni}	diffusivity of Ni in liquid (m^2 s^{-1})			
	D_0 diffusion constant (m^2 s^{-1})	4.92×10^{-7}		[37]
	Q activation energy (J mol^{-1})	6.77×10^4		[37]
α	thermal diffusivity in liquid (m^2 s^{-1})	5.4×10^{-6}		[21]
V_0	sound velocity in liquid (m s^{-1})	2000		[34]
a_0	interatomic distance in liquid (m)	1×10^{-9}		[39]

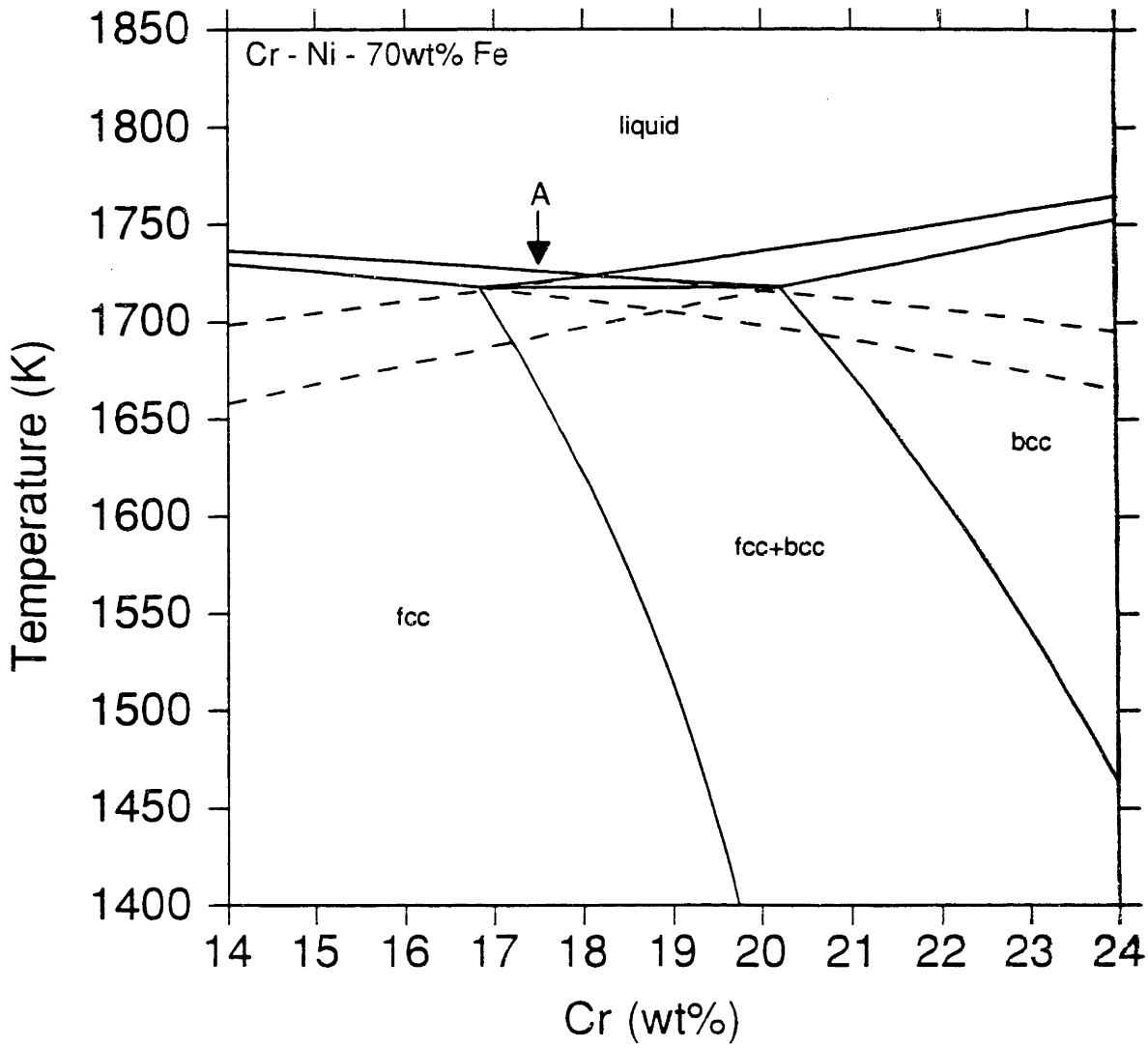

Figure 1 - Calculated pseudo-binary phase diagram of the Fe-Cr-Ni system at 70 wt pct Fe with the extension of liquidus lines and the location of the alloy composition used in the present study.

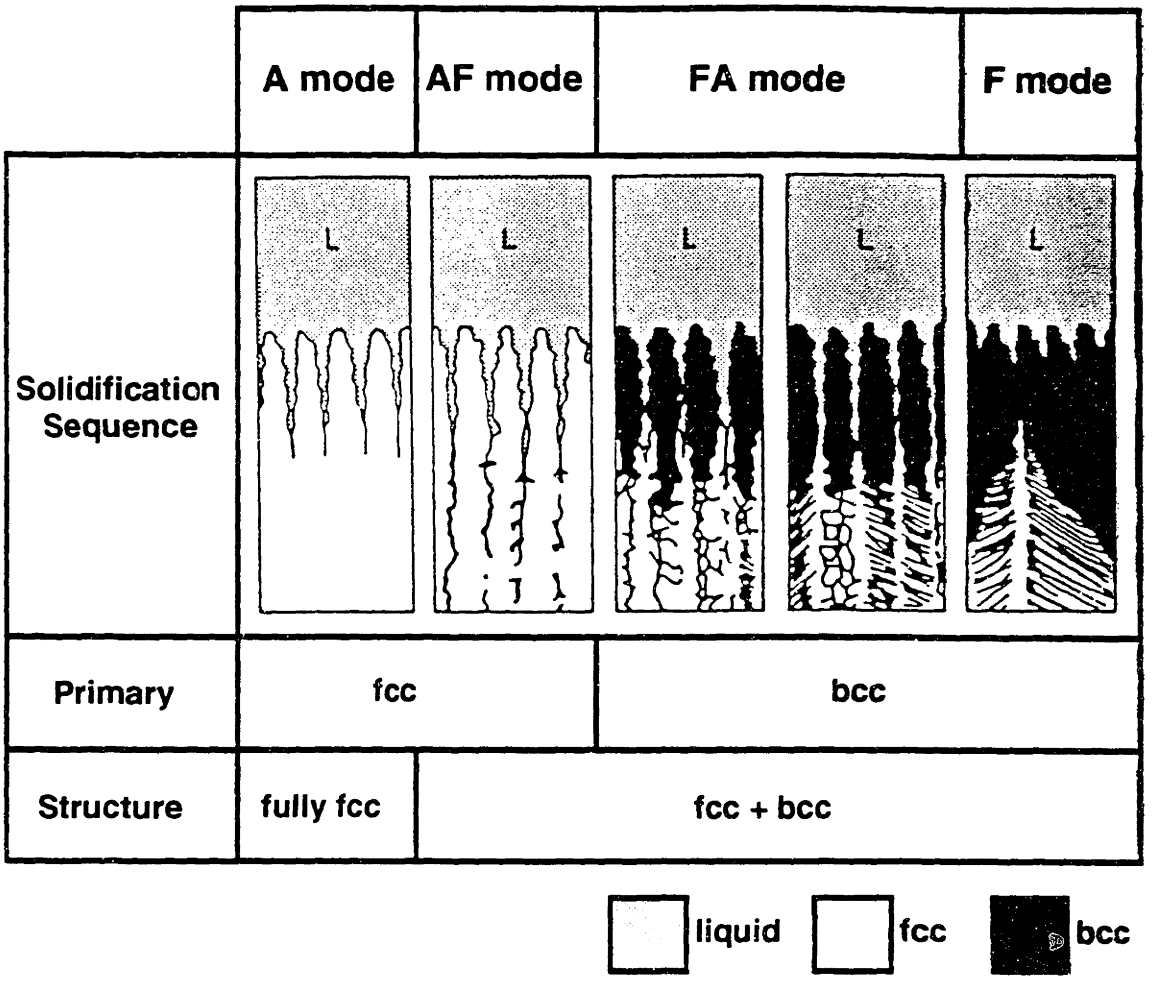

Figure 2 - Schematics of solidification modes of Fe-base-Cr-Ni alloys and austenitic stainless steels observed in conventional casting processes.

Figure 3 - Solidification structure of the Fe-17.5Cr-12.2Ni alloy obtained by zone melting.

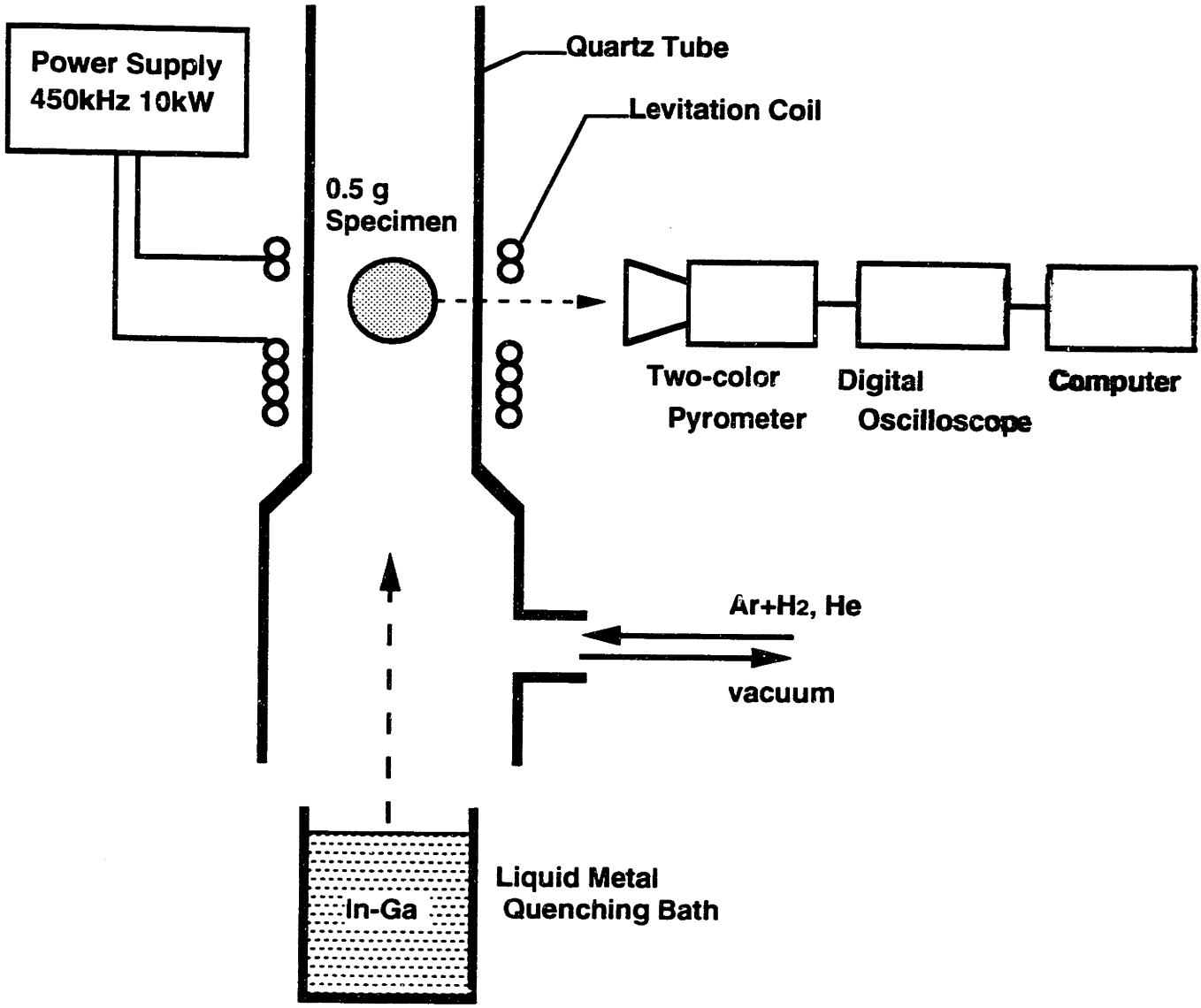

Figure 4 - Schematic of apparatus for levitation melting and undercooling experiments.

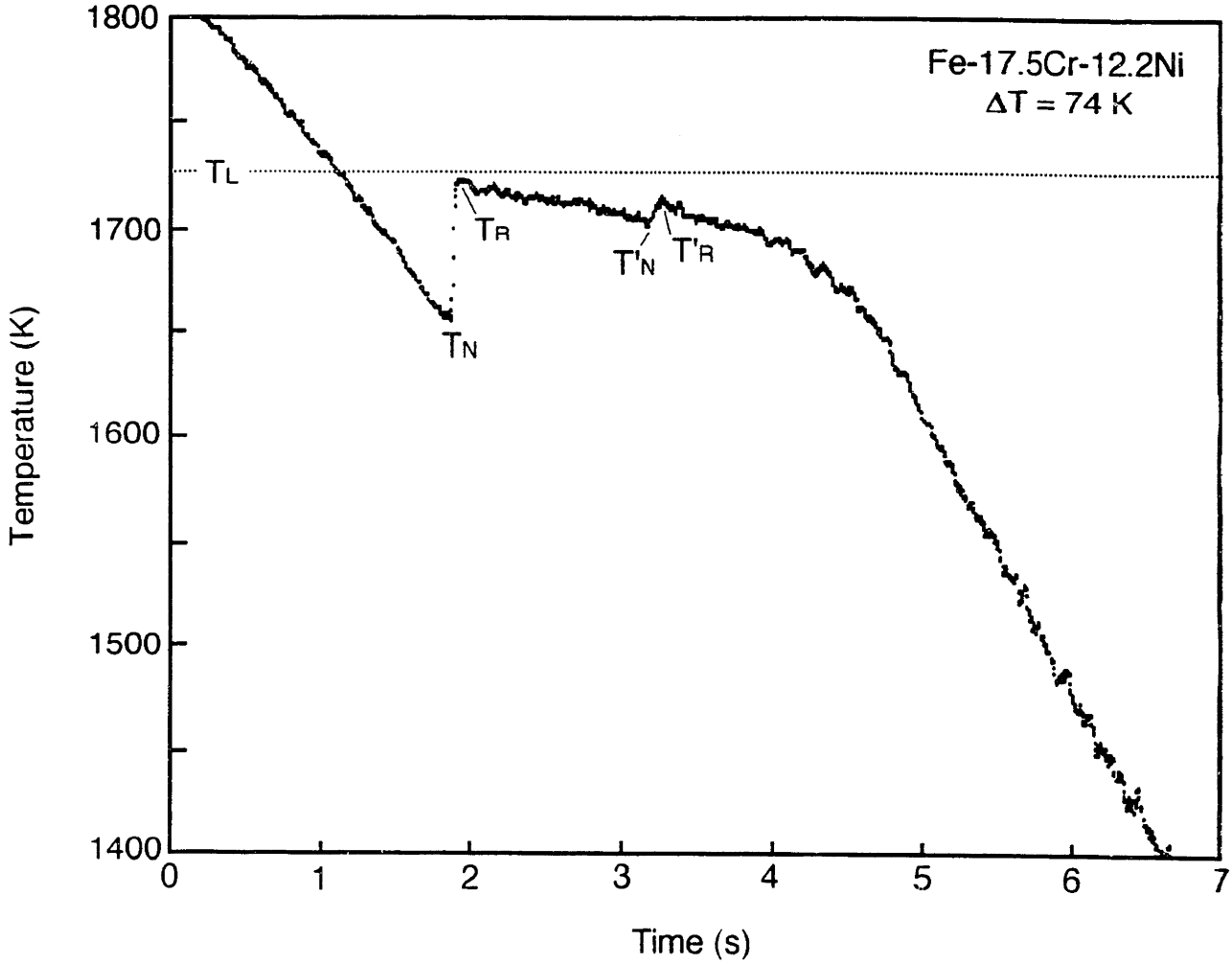

Figure 5 - A cooling curve obtained during gas-cooled solidification with an initial undercooling of 74 K. T_L is the liquidus temperature, T_N and T_R are the onset and termination temperatures of the first recalescence, respectively, and T'_N and T'_R are the onset and termination temperatures of the second recalescence, respectively.

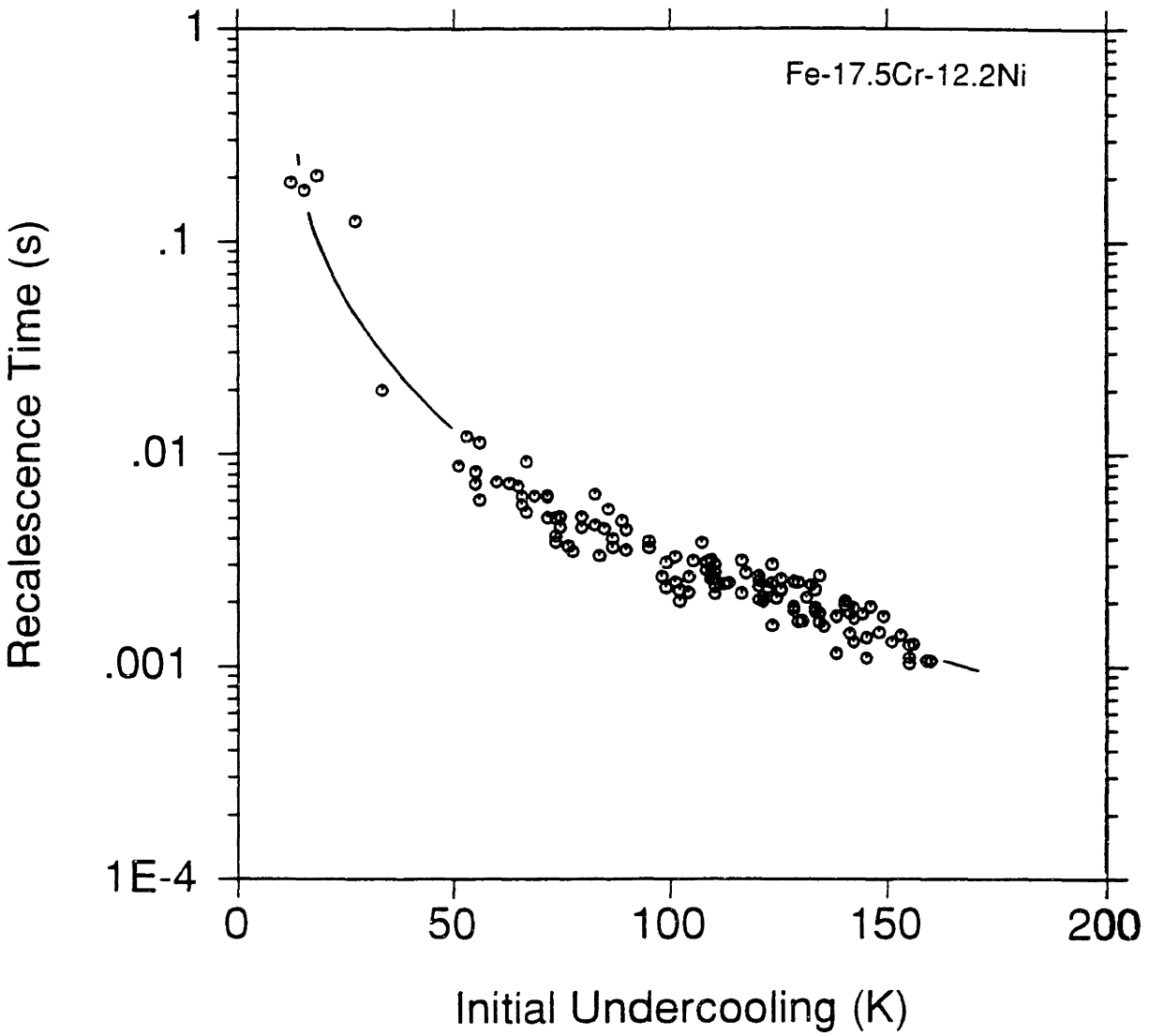

Figure 6 - Effect of initial undercooling on time for the first recalescence.

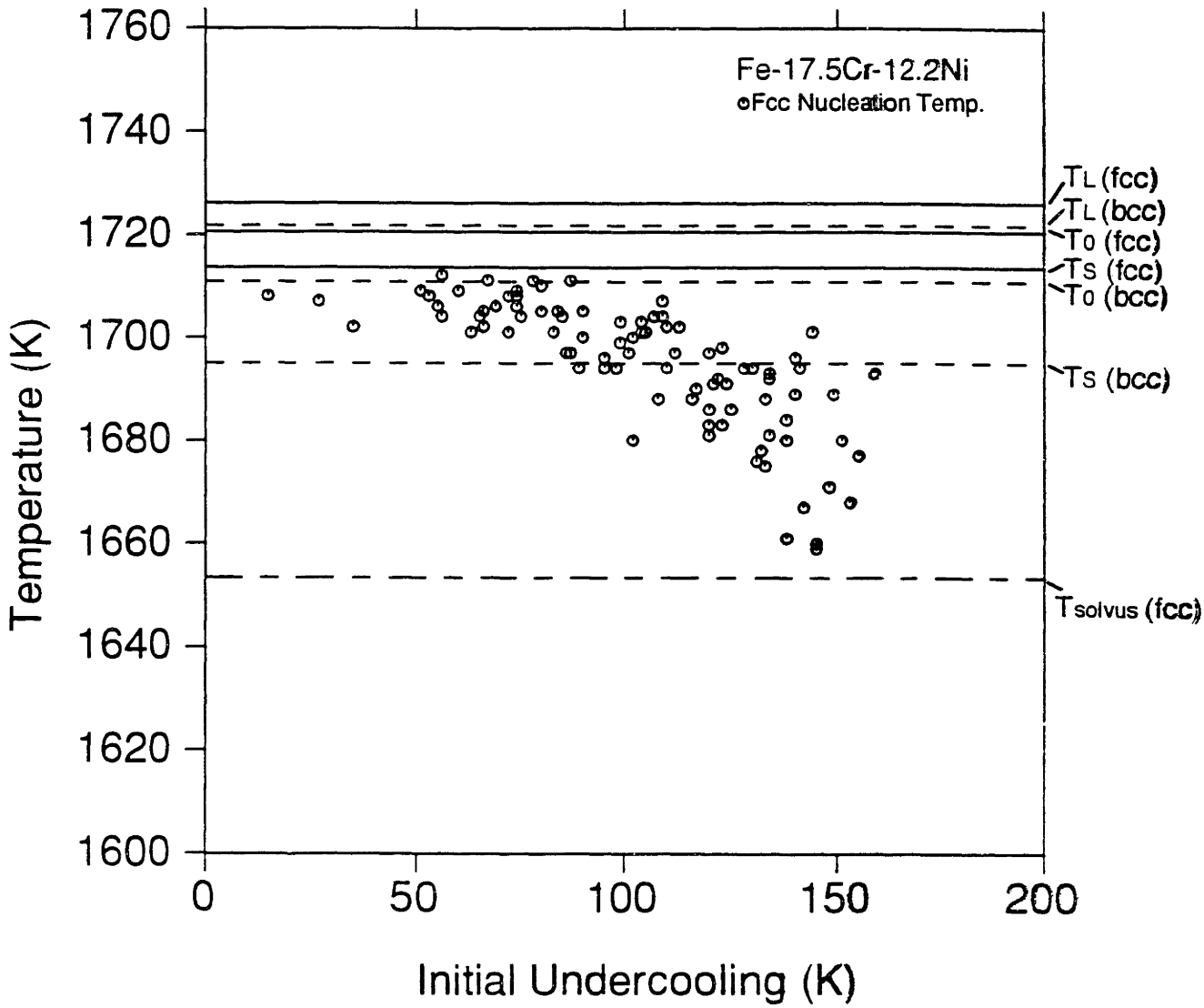

Figure 7 - Effect of initial undercooling on the onset temperature of the second recalescence.

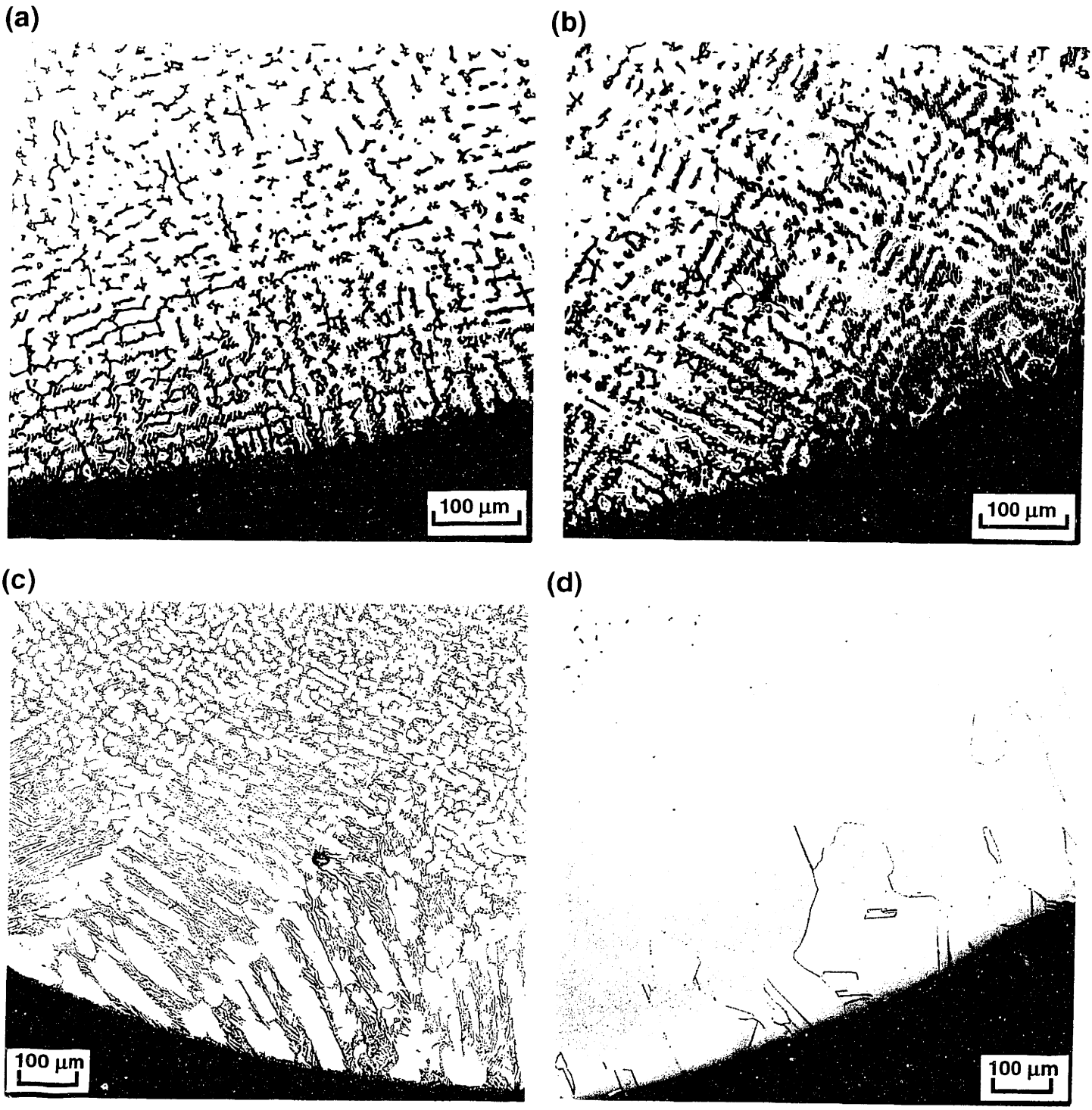

Figure 8 - Solidification microstructure in the vicinity of the specimen surface, obtained by gas-cooled solidification with initial undercoolings of (a) 33 K, (b) 51 K, (c) 138 K, and (d) 155K.

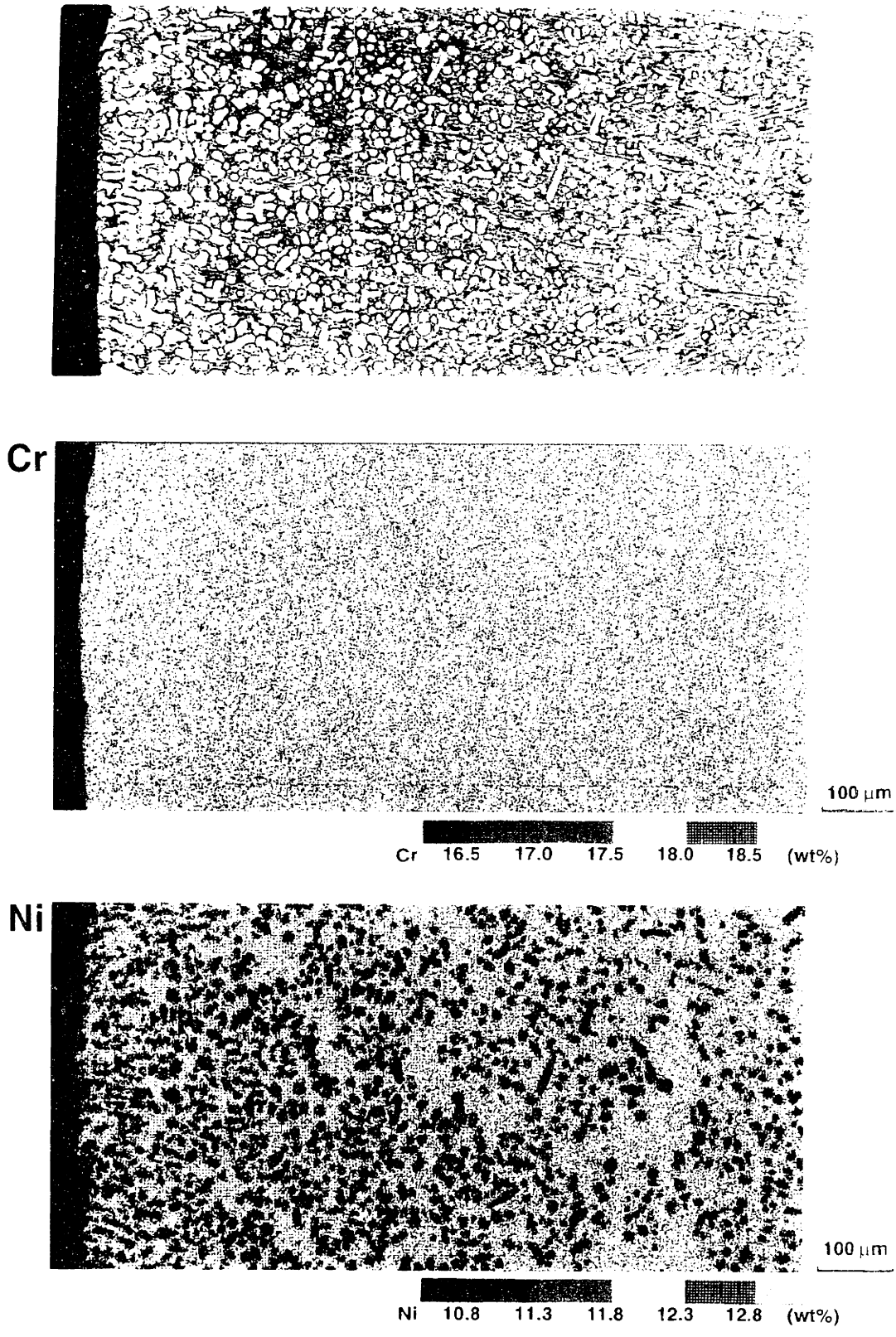

Figure 9 - Concentration distributions of Cr and Ni in the mushy region which was obtained using liquid metal quenching after the first recalescence, and measured by the computer-aided microprobe analyzer (CMA).

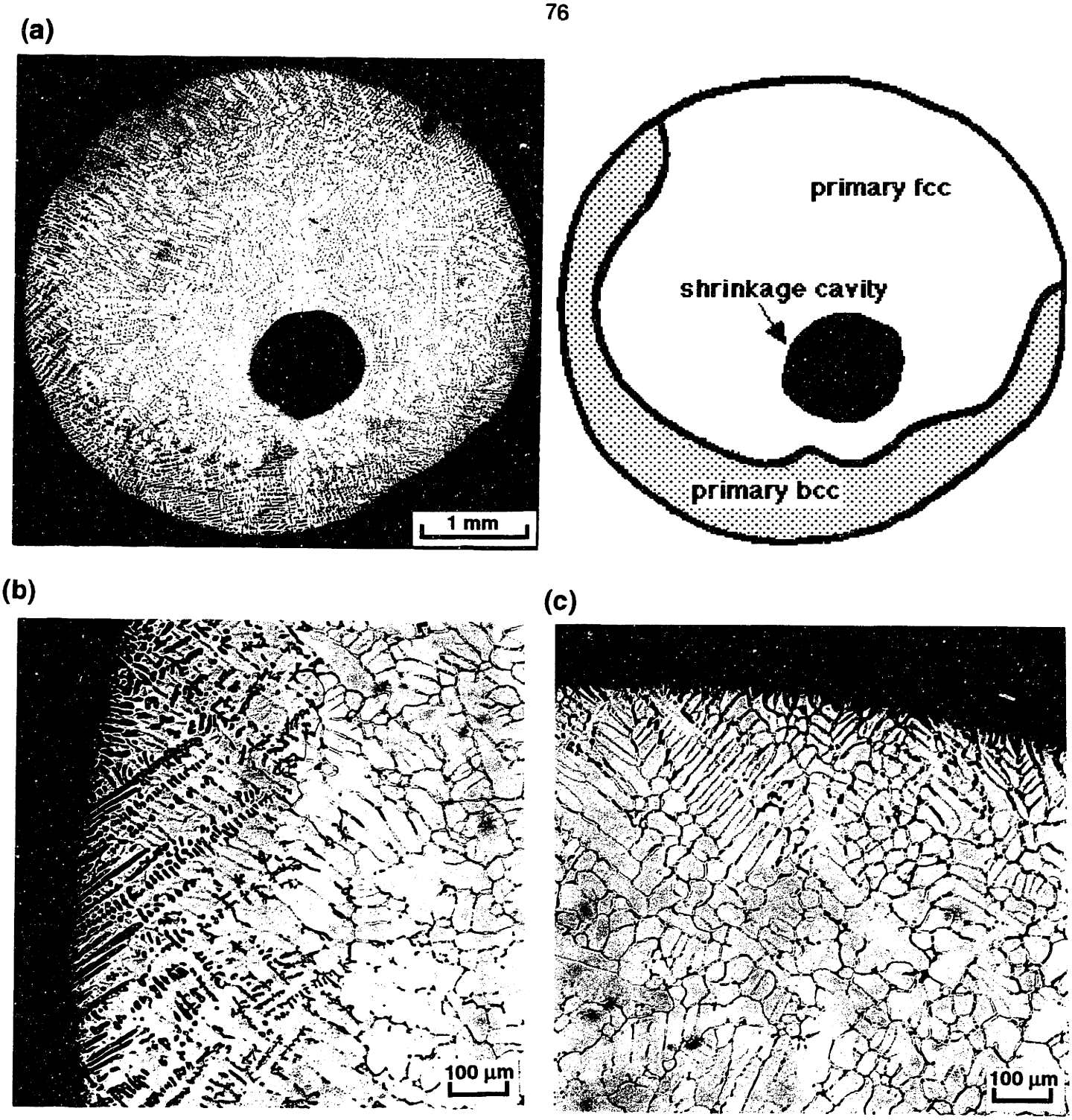

Figure 10 - Solidification structure obtained by free levitation with an initial undercooling of 18 K, which shows the mixed solidification of primary fcc and primary bcc; (a) the whole sample, (b) a region showing primary bcc solidification, and (c) a region showing primary fcc solidification.

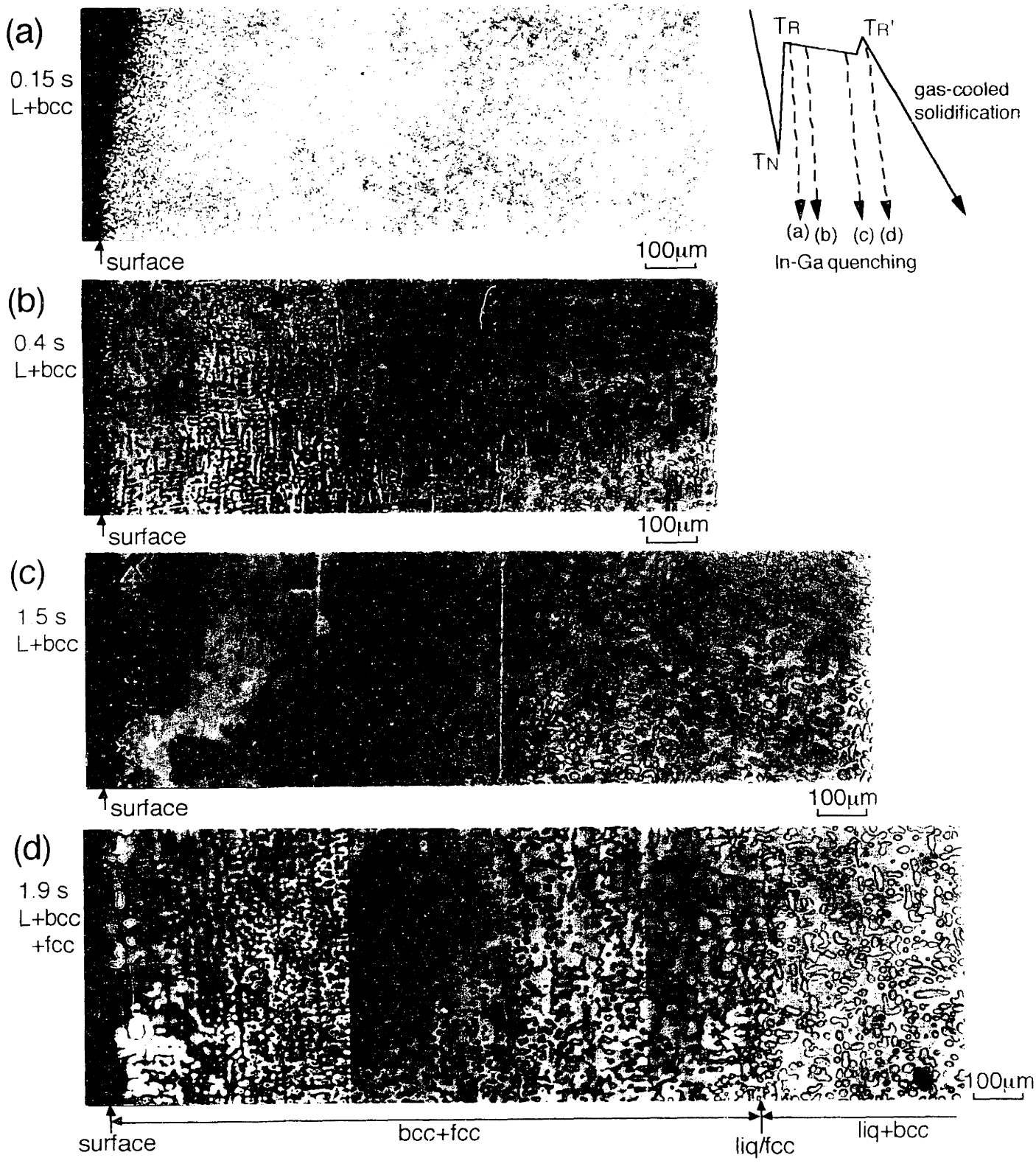

Figure 11 - Microstructural changes with time after the first recalescence obtained by liquid metal quenching following free levitation; (a) 0.25 s after recalescence (ΔT=110 K), (b) 0.4 s after recalescence (ΔT=105 K), (c) 1.5 s after recalescence (ΔT= 116 K), and (d) 1.9 s after the first recalescence and 0.4 s after the second recalescence (ΔT=109 K).

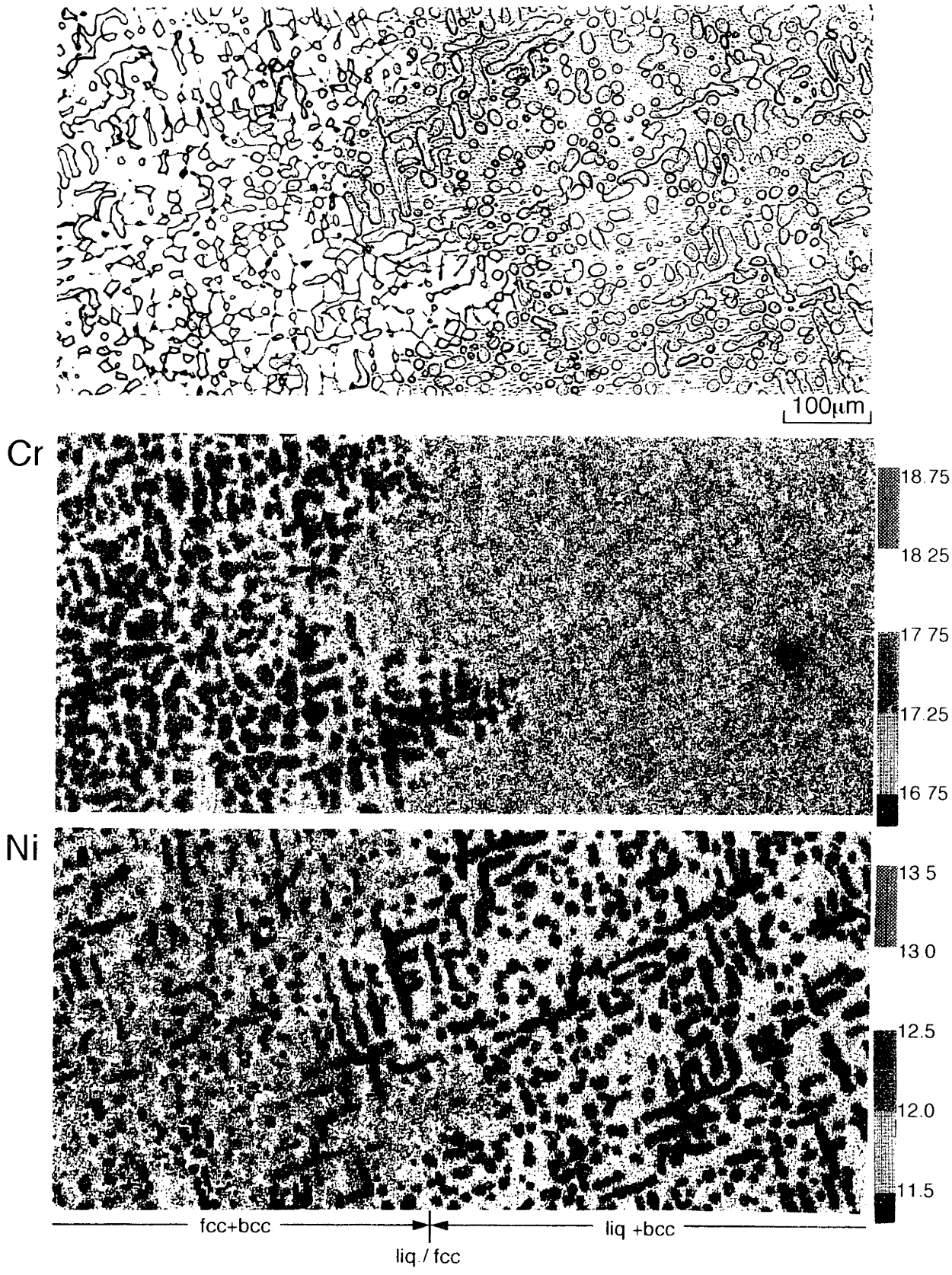

Figure 12 - Concentration distributions of Cr and Ni in the vicinity of the growing interface of fcc, obtained by CMA.

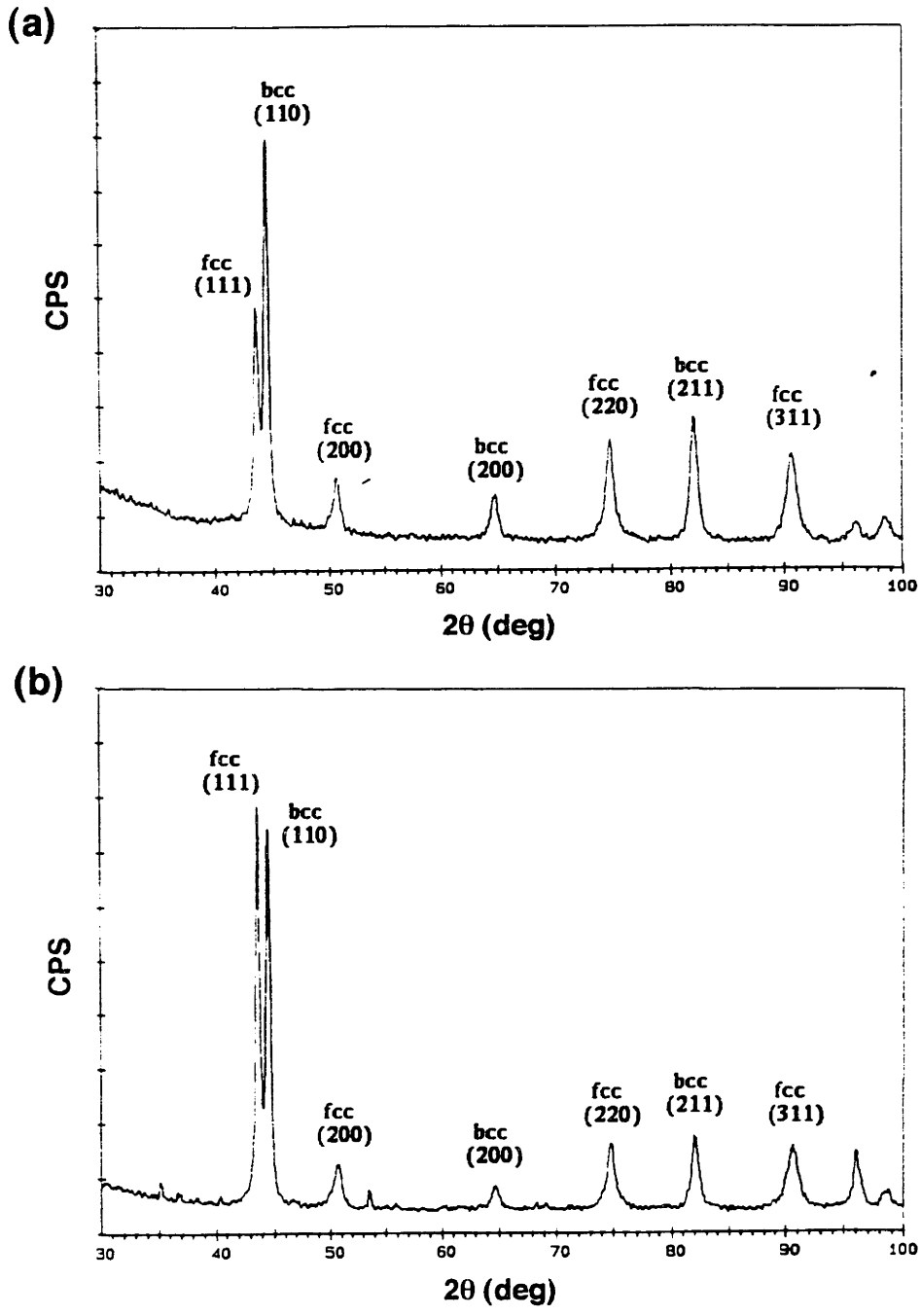

Figure 13 - X-ray diffraction results from specimens quenched (a) before the second recalescence and (b) after the second recalescence.

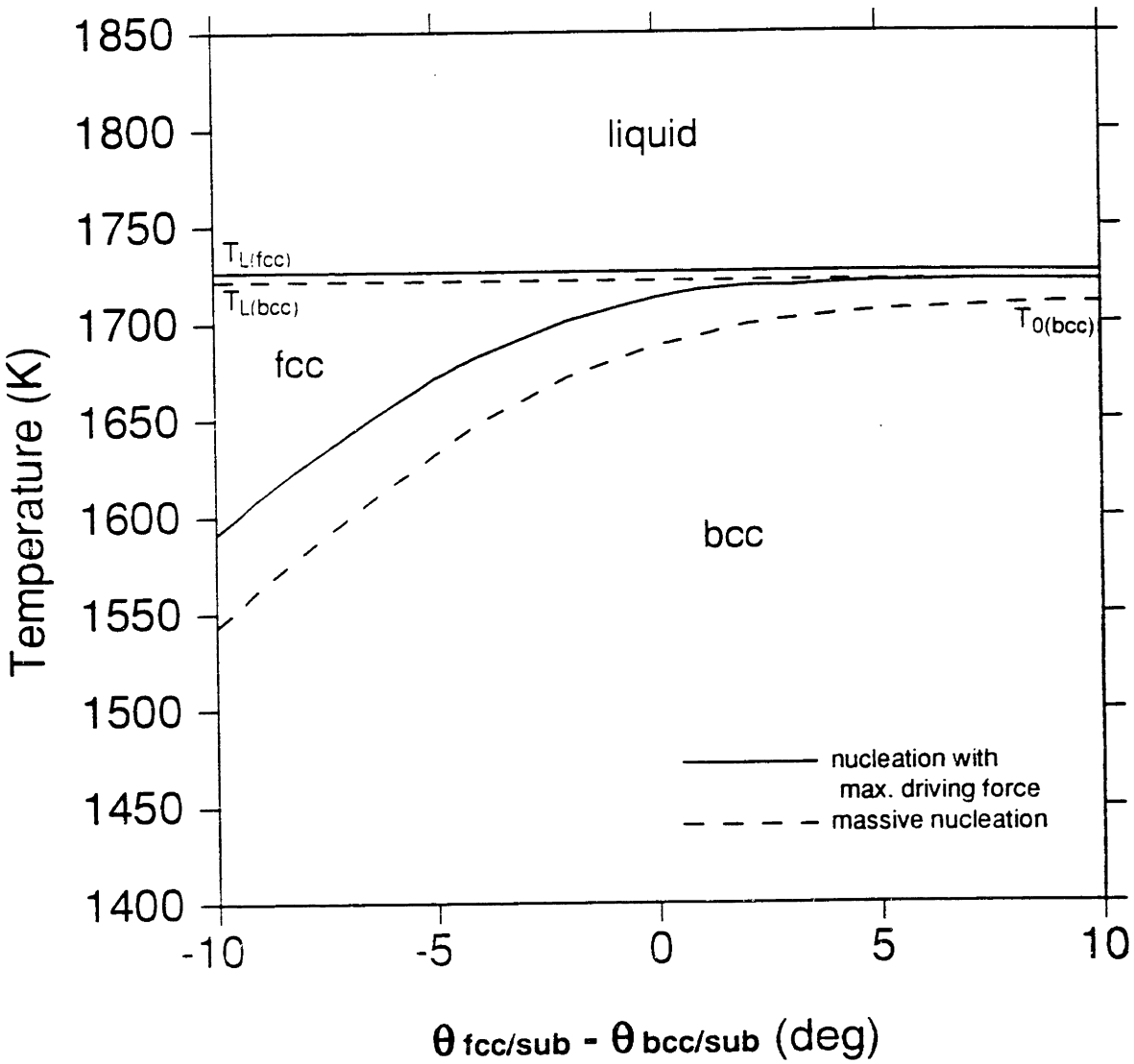

Figure 14 - Stability of nucleating phase calculated as a function of wetting angle difference ($\theta_{fcc/sub.}$-$\theta_{bcc/sub.}$) in Fe-17.5Cr-12.2Ni, where $\theta_{fcc/sub}$ and $\theta_{bcc/sub}$ are the wetting angle for heterogeneous nucleation between fcc and a catalyst and between bcc and a catalyst, respectively. Two lines giving temperatures of nucleating phase transition were obtained using different free energy values as noted.

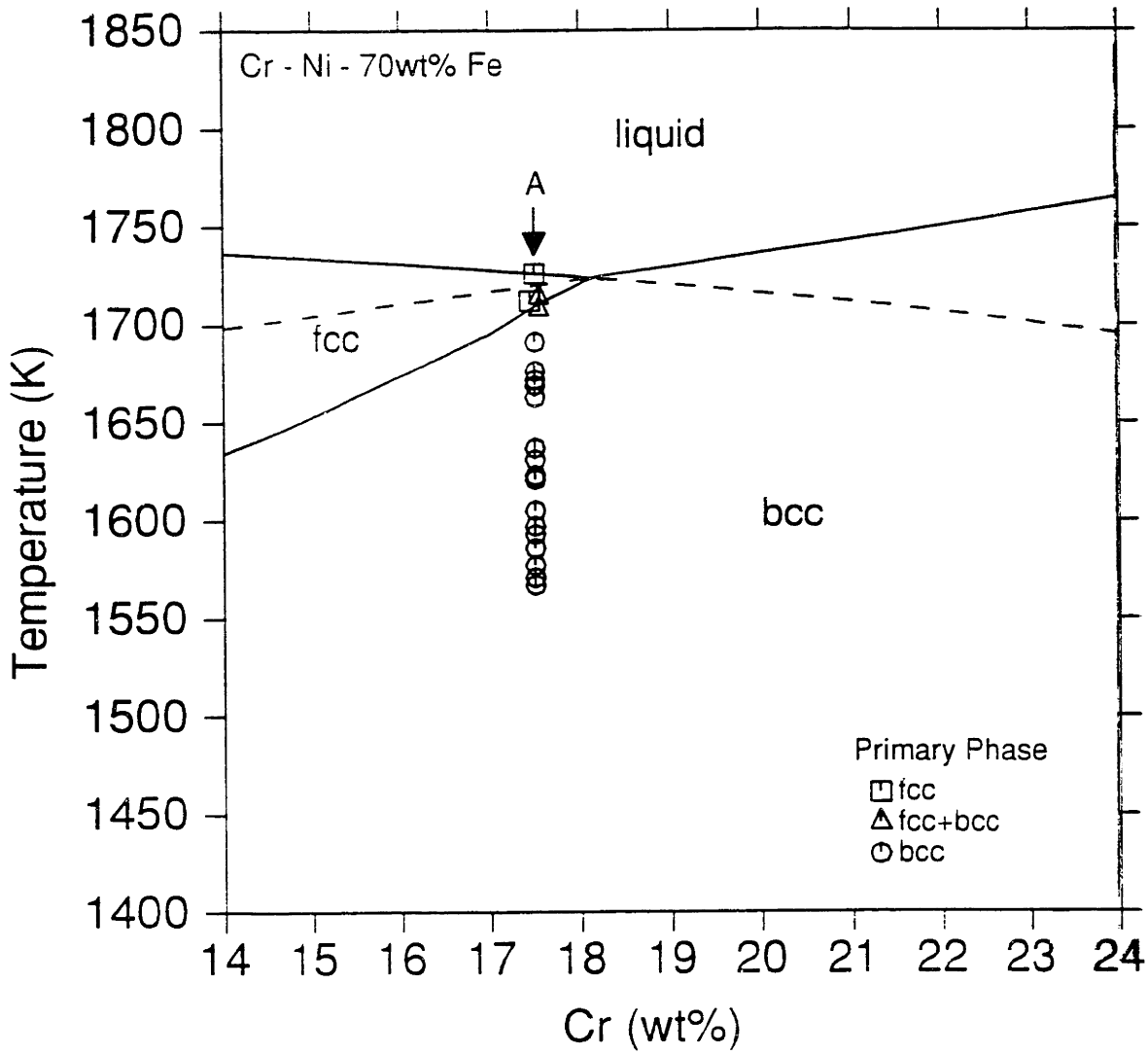

Figure 15 - A calculated nucleation phase diagram indicating preferentially nucleating phase as a function of temperature and composition, and plots of experimental observations of primary phases on the diagram.

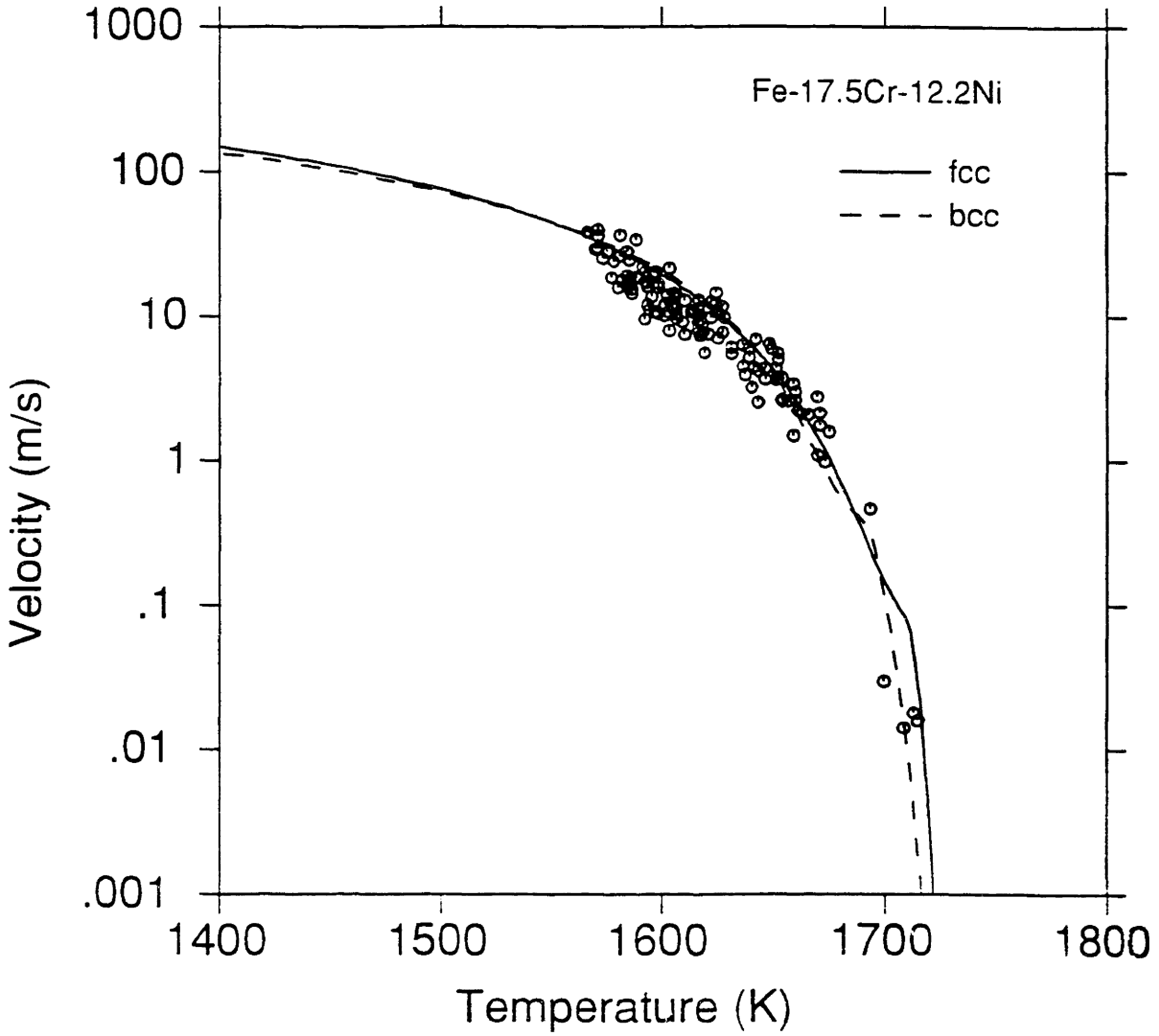

Figure 16 - Growth velocities of fcc and bcc dendrites calculated as a function of melt temperature using the BCT model, and comparison of experimentally estimated velocities with the model results.

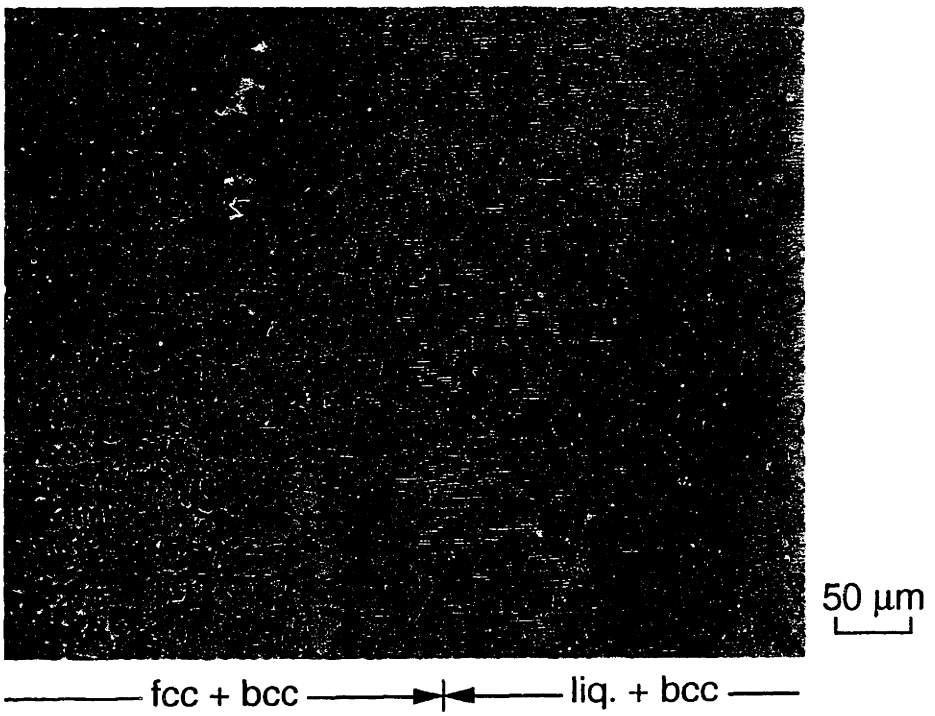

Figure 17 - Dendritic growth of stable fcc phase into the semi-solid after metastable bcc solidification with initial undercooling of 67 K.

Chapter III - Double Recalescence and Double Dendrite Formation in the Solidification of Primary Fcc Fe-Cr-Ni Alloys

Abstract

The rapid solidification behavior of two primary fcc Fe-Cr-Ni alloys, Fe-16Cr-14Ni and Fe-15Cr-15Ni, was investigated by using a levitation technique.

Double recalescence was observed in both alloys for initial undercoolings greater than a certain level specific to each alloy composition. Comparison with a "nucleation diagram" indicates that the first recalescence is attributable to metastable bcc solidification. This was supported by other data: recalescence temperatures, solute profiles, and X-ray diffraction. It is concluded that the inter-recalescence plateau is an incubation period for the formation of fcc, which causes the second recalescence. Analyses of the lengths of the plateau and second recalescence suggest that a high fraction of bcc solid enhances the stable nucleation of fcc, and that the growth of fcc into bcc is massive-like when the initial undercooling is large.

An internal dendritic structure was observed at the core of each dendrite in microstructures obtained by quenching immediately after recalescence. Those core structures are brought about by either fcc solidification with non-equilibrium partitioning or by metastable bcc solidification. Solute profiles at the core structures reflect the primary phase to solidify. Both Cr- and Ni-enriched cores are obtained when the primary phase is fcc, while Cr-enriched but Ni-depleted cores are found when the primary phase is metastable bcc. Those profiles are peculiar to rapid solidification.

1. Introduction

The use of high-speed pyrometry has made it possible to analyze rapid recalescence during solidification from the undercooled melt. Time and temperatures for the recalescence have been measured with high resolution in various alloy systems.[1-6] Verification of theoretical models such as dendrite tip models and coarsening models have been attempted by comparing those thermal measurements with model results.[1-6]

Double recalescence was found in the course of some of those rapid solidification studies using high speed pyrometry; it was found in hyper-peritectic Fe-Ni alloys,[3,6,7] and also in hyper-peritectic Fe-Co and Fe-Cu alloys.[7] Double recalescence consisted of three stages: the first recalescence from the undercooled melt, the second recalescence to the final maximum recalescence temperature, and an isothermal plateau between the two recalescence events. Piccone[7] considered that those three stages were respectively attributed to metastable bcc solidification, subsequent fcc solidification, and an incubation time for the nucleation of fcc. Therefore, it was stated that double recalescence was evidence of metastable bcc solidification in bulk samples of the above ferrous binary alloys. However, no metallographic features corresponding to the recalescence behavior were presented in that research, and metastable bcc solidification was proposed only on the basis of thermal measurements.

Munitz and Abbaschian[8] quenched hyper-peritectic Fe-Ni alloys from the undercooled liquid state, and found dendrite cores to be enriched in solute in solidified specimens. Solute-rich regions were observed in the form of crosses at dendrite cores when the undercooling prior to the quench was below the T_0 for fcc but above the T_0 for bcc. It was concluded that solute-rich crosses resulted from the partitionless solidification of fcc at the initial stage of dendritic solidification, and therefore, they were not formed when specimens were undercooled below the T_0 for bcc because they solidified with metastable bcc. However, since nucleation occurred while the

undercooled specimen was in the quenching medium, precise thermal measurement could not be made. In particular, the actual nucleation temperature and the thermal behavior of the recalescence were not identified.

The above observations provide useful clues for investigating metastable bcc solidification, but thermal measurements and metallographic observations have not been correlated. In addition, double recalescence has not been previously analyzed in detail, and determination of the metastable bcc primary phase has been by inference.

Phase selection in the Fe-Cr-Ni alloy system during rapid solidification has a similarity to that in the Fe-Ni alloy system, but neither double recalescence nor solute-rich dendrite cores have been reported thus far. In the previous chapter, it was shown that metastable bcc solidification occurs in bulk undercooled specimens of Fe-17.5Cr-12.2Ni alloy, a primary fcc alloy. In that case, two separate recalescences were found to occur during solidification, corresponding to primary bcc formation and subsequent fcc formation. However, the recalescence behavior was quite different from the double recalescence previously reported in Fe-Ni alloys.[3,6,7] The time between the first and second recalescences was several orders of magnitude larger in the Fe-Cr-Ni alloy of the previous chapter than in the earlier work. In addition, the system was not isothermal between the first and second recalescence in the Fe-Cr-Ni alloy; instead, the temperature decreased down to the nucleation temperature of fcc. In contrast, there was an isothermal plateau between the two recalescences in the earlier work, implying that the double recalescence occurred under adiabatic conditions.

In this chapter, the solidification behavior and resultant microstructures of two primary fcc Fe-Cr-Ni alloys were investigated. The alloys employed were Fe-16Cr-14Ni and Fe-15Cr-15Ni; fcc is more stable in these alloys than in the previously studied Fe-17.5Cr-12.2Ni. In both alloys, double recalescence and structures showing

the appearance of solute-rich cores were obtained. Analyses of these two observations are presented, and their mechanism, the relationship between them, and the factors governing their occurrence are discussed.

2. Experimental

Two Fe-Cr-Ni alloys were used: Fe-16Cr-14Ni (alloy C) and Fe-15Cr-15Ni (alloy D); the locations of both alloy compositions are indicated on the pseudo-binary phase diagram of the Fe-Cr-Ni system at 70 wt pct Fe shown in Figure 1. It is obvious that the stability of fcc in both alloys is improved over that in the Fe-17.5Cr-12.2Ni alloy which was investigated in the previous chapter. The purity of those ternary alloys is more than 99.9 wt pct as indicated by the chemical analyses listed in Table 1. The preparation of the starting materials was the same as described in the previous chapter.

The equilibrium solidification modes of the materials were verified by slow zone melting in an inert atmosphere and low-speed (4.2×10^{-3} m s^{-1}) electron beam welding, both of which are also described in the previous chapter. Both alloys solidified as primary fcc and produced fully fcc microstructures in these equilibrium solidification processes.

Figure 2 shows a schematic diagram of the apparatus for the levitation experiment. An alloy specimen of mass 0.5 g (±0.05g) was levitated within the coil and melted in an atmosphere of argon and 4% hydrogen. Then, it was cooled by flowing high-purity helium, and solidified from a certain undercooled temperature with rapid recalescence. Some samples were completely solidified while levitated in the cooling gas (gas-cooled solidification), while others were quenched into a Ga-25%In liquid bath immediately after recalescence to quench in the mushy-zone structure. The thermal history of a levitated specimen was measured using high-speed

pyrometry. Two data sampling rates were used to measure both the whole thermal history and rapid recalescence event simultaneously; a sampling rate of 200 Hz was employed for the former purpose, and sampling rates of 100 to 200 kHz for the latter. The accuracy of undercooling measurements was within ±7%.

Microstructures were observed by optical microscopy. As-solidified spherical samples approximately 5 mm in diameter were cut into halves and then mounted so as to observe the cross section. Regions near the specimen surface were primarily examined since the temperature measurement was performed at the surface. The microstructure was revealed by the use of electrolytic etching in an aqueous solution of 10 vol pct sulfuric acid. Concentration distributions of Cr and Ni were measured using computer-aided microprobe analysis (CMA)[9]. Two-dimensional profiles were obtained by x-y step-scanning over the area of interest on the as-polished cross-section of a sample. Operating conditions of the CMA were: an acceleration voltage of 15 kV, a beam current of 1 μA, a beam size (also the distance of each step scan) of 1 μm, and beam irradiation time of 20 ms per point. X-ray diffractometry (XRD) was used to identify phases existing in the structure of interest. Measurements were conducted on the as-polished cross section of a sample. Operating conditions of XRD were: an acceleration voltage of 60 kV and a current of 300 mA for the X-ray source using a copper target, a divergence slit of 1° and a receiving slit of 0.3° for the diffractometer, and a diffraction angle, 2θ, from 30° to 100°.

3. Results

3.1 Thermal History

Typical recalescence curves measured during the levitation of Fe-16Cr-14Ni and Fe-15Cr-15Ni are shown in Figures 3 and 4, respectively. Double recalescence was observed as the initial

undercooling (ΔT) increased, exhibiting three stages: the first recalescence from an originally undercooled melt, the second recalescence to the final recalescence temperature, and an isothermal plateau linking the first and second recalescence. The phenomenon became distinct when the initial undercooling was greater than approximately 60 K in the former alloy, and greater than approximately 100 K in the latter alloy. Specimens which were undercooled around the "transition temperature" did not clearly show the plateau, but showed a brief stay at an intermediate temperature during the temperature rise, as seen in the recalescence curve of ΔT = 114 K in Figure 4.

The behavior of the first recalescence was directly related to initial undercooling; the temperature rise became steep with increasing initial undercooling, as seen in Figures 3 and 4. The effect of the undercooling on the time for the first recalescence, which is the time during which the temperature rises from the maximum undercooling to the plateau temperature, is plotted for both alloys in Figure 5. Undercooling obtained in the present study ranged from 12 K to 244 K for Fe-16Cr-14Ni alloy, and from 40 K to 312 K for Fe-15Cr-15Ni alloy. Times decreased with increasing initial undercooling, and the time-undercooling relationship in both alloys seems identical.

Time for the second recalescence, which is the time during which the temperature rises from the plateau temperature to the maximum recalescence temperature, was also a function of initial undercooling, as shown in Figure 6; it decreases with increasing initial undercooling. The recalescence time in Fe-16Cr-14Ni is longer than that in Fe-15Cr-15Ni; the former ranges from approximately 1 ms to 10 ms, while the latter from 0.2 ms to 2 ms. In the figure, data points of 10 ms for Fe-16Cr-14Ni alloy were measured at the 200 Hz sampling rate since times between the first and second recalescence were so long in those samples that a high sampling rate (100 kHz) was not available at the moment of the second recalescence.

Therefore, the actual times for those data points are somewhere between 5 ms and 10 ms.

Figures 7 and 8 show temperatures after the first and second recalescences in Fe-16Cr-14Ni and Fe-15Cr-15Ni alloys, respectively. In the figure, temperatures of the liquidus and solidus were calculated using Thermo Calc [10] (ver. J). In both alloys, temperatures after the first recalescence are close to the liquidus temperature of metastable bcc, while temperatures after the second recalescence are approximately the solidus temperature of fcc. The effect of initial undercooling on those recalescence temperatures are insignificant. It is interesting to note that undercooling at the plateau is about 30 K or less, with respect to the fcc liquidus, and therefore, times for the second recalescence shown in Figure 6 are relatively small for their undercooling level, as compared with times in Figure 5.

Figure 9 plots times between the first and second recalescence (hereafter, referred to as plateau time) against initial undercoolings in both alloys. Plateau times in Fe-16Cr-14Ni alloy are generally longer than those in Fe-15Cr-15Ni alloy. In the former alloy, plateau times are mostly stable between 1 ms and 5 ms when initial undercoolings are approximately more than 100 K. For undercoolings less than that, plateau times spread over longer duration up to 700 ms. On the other hand, plateau times in Fe-15Cr-15Ni alloy are between 0.2 and 0.9 ms regardless of undercooling. In summary, except for the scatter in Fe-16Cr-14Ni alloy at lower undercooling levels, the effect of initial undercooling on plateau times is insignificant, but the effect of alloy composition is noticeable.

3.2 Microstructure

Figure 10 shows microstructures of Fe-16Cr-14Ni alloys which were solidified with different initial undercooling and quenched approximately 0.3 s after recalescence (after the second recalescence, if applicable). The quenching was effective in retaining not only dendrites, but also their internal structures.

Figure 10(a) is for an initial undercooling of 12 K. Double recalescence was not observed at this undercooling level. Bright "crosses" are seen at the cores of dendrites. Interdendritic regions showing a fine cellular structure were liquid prior to the quench.

Figure 10(b) is for an initial undercooling of 58 K. This undercooling level is close to the "transition", but double recalescence was not clearly recognized in this specimen. Within a dendrite, another internal dendritic structure is present; it is more obvious on the longitudinal section of the dendrites. It is interesting to note that the outer boundary to the dendrites reveals a smooth solid/liquid interface without any significant perturbation, while the internal dendrites retain well-developed, very fine secondary branches.

Figure 10(c) is for an initial undercooling of 101 K. Distinct double recalescence was observed. The quenched structure is similar to the structure shown in (b) with an initial undercooling of 58 K. It seems that secondary branches of internal dendrites were somewhat ripened as compared with those in (b).

Figure 10(d) is for an initial undercooling of 176 K. Double recalescence was obvious during the solidification. Some of the dendrites are in the process of coalescing, and more than one core structure is often seen within a unit after coalescence.

The effect of plateau time on solidification structure was examined in Fe-16Cr-14Ni alloy. Figure 11 compares two microstructures which exhibited similar initial undercoolings but different plateau times during their solidification; Figure 11(a) is for an initial undercooling of 66 K and plateau time of 4 ms, and Figure 11(b) is for 70 K and 350 ms. Both microstructures were obtained by quenching the samples immediately after the second recalescence into an In-Ga liquid bath. It appears that the shorter plateau time brought about dendritic internal structures, while the longer plateau time resulted in a rather spherodized, blocky internal structure

without secondary branches. The volume of internal phase seems larger in the case of longer plateau time. Figures 12(a) and 12(b) are X-ray diffraction results for the two microstructures shown in Figure 11(a) and 11(b), respectively. Larger bcc diffraction peaks were obtained from the structure with a longer plateau time than from that with a shorter plateau time.

Figure 13 shows microstructures of Fe-15Cr-15Ni alloys quenched approximately 0.3 s after recalescence. Figures 13(a) and (b), which were obtained with initial undercoolings of 60 K and 104 K, respectively, show similar structures to Figures 10(a) and (b). The internal structures in the 60 K undercooled sample are rather cellular/dendritic, while those in the 104 K undercooled sample are dendritic with developed secondary branches. On the other hand, as the initial undercoolings become even larger, the internal dendritic structures become indistinct. Coalescence and coarsening of dendrites are pronounced, as seen in Figures 13(c) and (d). This is probably a result of the higher fraction solid after recalescence with higher initial undercooling.

3.3 Solute Profile in Quenched Specimen

Solute profiles in quenched microstructures were measured in selected specimens using CMA, and the following three patterns were observed regarding profiles at dendrite cores:

(1) enriched in both Cr and Ni
(2) enriched in Cr but depleted in Ni
(3) no measurable enrichment in Cr and Ni

Figure 14 shows profiles of Cr and Ni measured on the quenched microstructure shown in Figure 13(a). The sample solidified with an initial undercooling of 60 K and did not show double recalescence. Concentrations of both Cr and Ni are higher at dendrite cores than the surrounding areas, which is typical of pattern (1). Concentrations of both Cr and Ni at the core are close to the

nominal contents, while concentrations in the surrounding are 0.5 to 1.0 wt pct lower. Interdendritic regions which were liquid prior to the quench are enriched in both Cr and Ni.

Figure 15 displays profiles of Cr and Ni in the microstructure shown in Figure 10(c). The sample solidified with an initial undercooling of 101 K and showed a distinct double recalescence. The profiles are representative of pattern (2). Cores are enriched in Cr, but depleted in Ni with respect to the neighboring dendrite area. The enrichment of Cr is close to the nominal content, while Ni is more than 1 wt pct below the nominal content.

The pattern (3) was measured in structures which solidified with high undercoolings. Profiles seem uniform within dendrites, being slightly depleted in both solutes. Interdendritic regions are enriched with both solutes, but the extent of segregation was smaller than in previous patterns.

4. Discussion

4.1 Occurrence of Double Recalescence

The relationship between initial undercooling and the occurrence of double recalescence was compared with the "nucleation phase diagram" which was determined in the previous chapter. Results are shown in Figure 16. Calculation of the diagram was described in the previous chapter. It appears from this plot that the occurrence of double recalescence corresponds to bcc nucleation. That is, experiments in which moderate or distinct double recalescence was observed lie at or below the calculated line for the transition from fcc nucleation to bcc nucleation.

Two calculated lines for the transition are provided in the nucleation diagram: one is for partitioned nucleation driven by

maximum driving force, and the other for partitionless (massive) nucleation. From this analysis, it is difficult to determine which transition line is more applicable, since the observations showed rather broad transitions for both alloys. The actual transition appears to be between the two lines, and the transition in recalescence behavior also seems to be in agreement with this.

The relation between the observation of double recalescence and the "nucleation phase diagram" is consistent with discussions in the previous chapter. Double recalescence results from metastable bcc solidification, and its occurrence is therefore controlled by nucleation. Inversely, the validity of the "nucleation phase diagram" which was proposed in the previous chapter is supported by the present observations.

Metastable bcc solidification during the first stage of double recalescence is also supported by recalescence temperature and X-ray diffraction results. Despite some scatter, Figures 7 and 8 suggest that the temperature after the first recalescence is approximately the liquidus temperature of bcc and the temperature after the second recalescence is between the fcc liquidus and solidus temperatures. The implication is that the first recalescence can be attributed to bcc formation, and the second recalescence to the formation of fcc. Bcc diffraction peaks were obtained from a quenched structure having a higher fraction of core structure, as shown in Figure 11(b). Those bcc peaks are considered to result from dendrite cores, and therefore, suggest metastable bcc solidification during the first stage of double recalescence.

4.2 Relationship between Double Recalescence and Microstructure

Internal dendritic structures were found within dendrites in samples quenched after recalescence, but these internal structures can not readily be related on the basis of morphology alone to the occurrence of double recalescence. For example, similar internal dendritic structures are exhibited at dendrite cores in Figure 10(b)

and (c), which solidified without and with double recalescence, respectively. In addition, internal structures fade away as initial undercooling increases while double recalescence is distinct.

Solute profiles, on the other hand, are relevant to the occurrence of double recalescence. Figure 17 plots the patterns of the solute profiles on the "nucleation phase diagram". In the samples analyzed, it is seen that cores of the dendrites are enriched in Cr but depleted in Ni when they are in the bcc nucleation region, while cores of the dendrites are enriched in both Cr and Ni when the initial undercooling is in the fcc nucleation region. The former profiles, i.e., high Cr and low Ni at dendrite cores, are exactly what is expected in the bcc phase from the partition ratios of Cr and Ni during bcc solidification and subsequent bcc-to-fcc transformation.[10,13] The latter behavior, i.e., high Cr and high Ni at dendrite cores, must be explained by partitionless solidification.[8]

4.3 Growth during the First Recalescence

Dendrite growth velocities were evaluated from recalescence time data, and compared with velocities determined assuming the BCT (Boettinger-Coriell-Trivedi) model[11]. A time for the first recalescence, Δt_{R1}, is converted to a velocity, V, by the following equation in the present study:

$$V = 4.4\,(I_S)^{-0.5}\,(\Delta t_{R1})^{-1.5} \qquad (1)$$

where I_S is the critical nucleation rate and is assumed to be 10^7 ($m^{-2}\,s^{-1}$) as mentioned in the previous chapter. Assumptions for the conversion and the application of the BCT model to the present alloys were described in the previous chapter. The details of the model itself are found in refs. [4,11]. Numerical data used for the calculation are listed in Table 2.

Figures 18 and 19 compare the estimated velocities and calculated velocities from the BCT model for Fe-16Cr-14Ni and Fe-

15Cr-15Ni, respectively. The calculated results demonstrate that the growth of fcc is faster than that of bcc for the entire undercooling range of interest in both alloys. Nevertheless, experimental observation indicates that primary bcc solidification is favored from the melts undercooled by more than a certain level. This means that the process governing the primary phase selection is not growth but nucleation in the present situation of solidification.

Although the growth phase can not be specified from the comparison due to data scatter, velocities estimated from experimental data follow the calculated temperature-velocity relationship well. This indicates that the first recalescence is essentially governed by normal dendritic growth, i.e. steady-state growth controlled by thermal and solute diffusion, in both alloys. It may be interesting that there is a stay in plots of experimentally estimated velocities around 1640 K in Figure 19, which seems to indicate change in the growth phase from fcc to bcc. Another concern is that estimated velocities are likely to be larger than the model results at higher undercoolings (i.e., lower temperatures). This may imply that the assumption of nucleation-growth control for deriving Eq. (1) is not reasonable at undercoolings higher than approximately 170 K.

4.4 Formation of Fcc after Bcc Solidification

In the preceding sections, it has been shown that the first recalescence in these alloys is a result of metastable bcc solidification. Thus, the subsequent plateau time can be characterized as the incubation time for secondary recalescence, i.e., the formation of fcc. Figure 9 indicates two features of the plateau time data: a large scatter at lower undercooling levels in Fe-16Cr-14Ni alloy, and composition-dependent characteristics. Plateau times observed in Fe-16Cr-14Ni are approximately five times longer than those in Fe-15Cr-15Ni; initial undercooling does not seem to influence the times.

In Figure 20, the data of Figure 9 are re-plotted versus calculated fraction solid after recalescence. Assuming bcc solidification during the first recalescence, the fraction solid, f_S, is given by

$$f_S = \frac{\Delta H_f}{C_{pL}} (T_R - T_N) \qquad (2)$$

where ΔH_f is the latent heat of fusion of bcc, C_{pL} is the specific heat of the liquid, T_R is the recalescence temperature, and T_N is the original undercooled temperature. Since the freezing temperature range of bcc is not very large, the liquidus temperature of bcc can be taken as T_R for convenience. It is seen in Figure 20 that most of the scatter occurs at fraction solid less than approximately 0.4. In other words, the plateau times become rather stable when the fraction solid is greater than 0.4. Perhaps fcc formation (or nucleation) needs a certain fraction of bcc solid in the liquid for its stable occurrence.

Figure 21 shows calculated results of the effect of heterogeneous nucleation site on the nucleation temperature of fcc in the presence of the liquid and bcc. The situations considered are: (1) spherical homogeneous nucleation in bcc, (2) heterogeneous nucleation on planar catalytic bcc with a spherical fcc cap in the liquid, (3) heterogeneous nucleation at the bcc/liquid interface with a spherical fcc cap in bcc, (4) heterogeneous nucleation at the bcc/liquid interface with two abutting spherical fcc caps, and (5) heterogeneous nucleation on the bcc/bcc grain boundary with two abutting symmetric spherical caps of fcc. The critical free energy for nucleation, ΔG^*, was calculated for each geometry, and nucleation temperature, T_N, was determined simply from $\Delta G^* = 60kT_N$[14,21]. Details of the calculation and data used for the calculation are given in the Appendix. Results are obtained as a function of the bcc/fcc interfacial energy since it is not well known and can vary widely between coherent and incoherent bcc/fcc interfaces.

Regarding the nucleation of fcc from the liquid, bcc is not a strong catalyst. This is because of the difference of solid/liquid interfacial energies between fcc and bcc. In the case of fcc nucleation on planar bcc, for example, even if the fcc/bcc interface is highly coherent, the calculation indicates that the nucleation still needs more than 100 K undercooling. Smaller undercoolings were observed for double recalescence in this study. Consequently, in order for fcc to nucleate at the plateau temperature, the nucleation of fcc on a bcc/bcc boundary is realistically the most probable among the five cases investigated, while fcc nucleation within bcc requires very high coherency.

The above calculation considers rather simple cases of fcc nucleation, and there are other complicated candidates for fcc nucleation sites such as edges and corners of combinations of the liquid and bcc. However, the results of the calculation are suggestive that when a sufficiently high fraction solid is reached, grain boundaries may form as a result of coalescence, collisions, or strains from a cohesive network, leading to fcc nucleation. Therefore, the tendency of plateau times seen in Figure 20 is explained by the effect of fraction solid on the formation of bcc/bcc grain boundaries for fcc nucleation.

4.5 Incubation Time of Fcc Formation

In the expression of time-dependent nucleation, the duration of the transient, τ, is given to an order of magnitude by[14]

$$\tau = \frac{n_c^2}{D_c} = \frac{n_c^2}{q_0 A_c} \qquad (3)$$

where n_c is the number of atoms in a nucleus of critical size, q_0 is the probability per unit area and unit time of an atom adding itself to an embryo, and A_c is the surface area of a nucleus of critical size. In an ideal situation, the time will be inversely proportional to $(\Delta G)^4$, where ΔG is the thermodynamic driving force for formation. The

driving force for fcc formation at the liquidus temperature of bcc is estimated as 136 J/mol for Fe-16Cr-14Ni and 200 J/mol for Fe-15Cr-15Ni. Therefore, the incubation time for steady state nucleation of fcc in Fe-16Cr-14Ni is about 5 times longer than that in Fe-15Cr-15Ni ($\approx (200/136)^4$). This appears to be comparable with experimental observation. In summary, the composition-dependent plateau time is interpreted as an incubation time for the nucleation of fcc.

4.6 Growth of Fcc during the Second Recalescence

Once the growth of fcc starts after some incubation time, it should proceed into both the liquid and the bcc simultaneously during the second recalescence. This growth is relatively fast for its undercooling level. As shown in Figures 7 and 8, undercooling before the second recalescence is roughly 30 to 40 K with respect to the fcc liquidus temperature. Times for the first recalescence corresponding to this undercooling are more than 10 ms in Figure 5, but actual times for the second recalescence are less than 10 ms as shown in Figure 6. Growth into the liquid is controlled by relatively fast solute transport through the liquid. The solid-state bcc-to-fcc transformation could also be fast since bcc is completely unstable at likely transformation temperatures, and therefore, it could be massive-like (composition-invariant). In addition, the driving force for the bcc-to-fcc transformation is almost twice as large as that for the liquid-to-fcc transformation at the likely transformation temperatures (i.e., plateau temperatures).

Since the growth of fcc into the liquid continues even after the second recalescence, the second recalescence may be essentially attributed to the solid-state bcc-to-fcc transformation. As initial undercooling increases, the fraction of bcc formed during the first recalescence is increased, and eventually coalescence occurs. This tendency is demonstrated in Figure 13 (c) and (d). Nevertheless, the recalescence time tends to decrease with increasing undercooling, as shown in Figure 6. Therefore, this may indicate the necessity of the

massive-like transformation from bcc to fcc at higher fraction solid of bcc.

4.7 Formation of Core Structures

When the recalescence was single and the solidification was primary fcc, both Cr and Ni were found to be enriched at dendrite cores as shown in Figure 14. Those profiles were probably detected as core structures in etched microstructures. The solute enrichments are believed to be attained by increased partition ratios during rapid solidification.[8,12] According to non-equilibrium interface kinetics,[15] partition ratios are expected to change noticeably when the growth velocity is around 1 m/s or more. Based on relations between initial undercooling and velocity in Figure 18 and 19, the assumption of increased partition ratios seems reasonable. The solute-rich crosses were observed even when the initial undercooling was 12 K, but actual solute enrichments with respect to the surroundings were found to be small, compared with other samples with higher undercoolings.

In contrast, Cr enrichment and Ni depletion were observed at dendrite cores when the solidification was primary bcc and there was an accompanying double recalescence. However, bcc was not retained even in quenched microstructures, as shown in Figure 12(a), and only solute profiles corresponding to bcc were retained; core structures within dendrites probably reflect these solute profiles. Both core structures and solute profiles were recognized only when initial undercooling was relatively low, and both of them were found to fade away as undercooling increased. In bcc solidification at relatively small undercooling levels, Ni is depleted in the growing bcc solid, while the partitioning of Cr is insignificant. In order for dendrite cores to be depleted in Ni and enriched in Cr, additional solute redistribution is necessary, and this will occur in the diffusional bcc-to-fcc transformation. Then, the transformation proceeds from the external surface of the dendrite to the core, and the last part to transform to fcc will be depleted in Ni and enriched

in Cr, since the partition ratio for Ni is more than unity and that for Cr is less than unity during the bcc-to-fcc transformation.

When the initial undercooling is relatively large, the resultant fraction of solid bcc is rather high after the first recalescence, and dendrites are more likely to coalesce. Solute partitioning becomes insignificant as the partition ratio is increased with increasing undercooling, and the bcc-to-fcc transformation tends to become massive. The possibility of massive-like bcc-to-fcc transformation is thermodynamically high in this situation. Consequently, both core structure and specific solute profiles at dendrite cores are less likely to remain in quenched structures.

5. Conclusions

Rapid solidification of two Fe-Cr-Ni alloys, Fe-16Cr-14Ni and Fe-15Cr-15Ni, was investigated using a levitation technique. Both alloys are fully fcc upon equilibrium solidification. Bulk samples were melted, then rapidly solidified from variously undercooled conditions, and quenched into an In-Ga liquid metal bath immediately after recalescence. Conclusions obtained in the present study are as follows:

(1) Double recalescence occurs in both alloys when the initial undercooling is greater than a certain level specific to each alloy composition. The undercooling level inducing double recalescence corresponds to that causing metastable bcc solidification in a calculated "nucleation phase diagram". It is concluded that the first recalescence results from metastable bcc solidification. This is consistent with the other evidence: recalescence temperatures, solute profiles and X-ray diffraction analysis.

(2) The second recalescence is attributed to subsequent fcc formation, and the isothermal inter-recalescence plateau is attributed to the incubation for the fcc nucleation. Incubation times decrease and vary less as initial undercooling increases, which suggests that nucleation of fcc is enhanced by the presence of a high fraction of bcc solid. The second recalescence is primarily controlled by the bcc-to-fcc transformation, and the growth of fcc is likely to be massive when the initial undercooling is large.

(3) Within each quenched dendrite, another internal dendritic structure was observed. These core structures result from either fcc solidification with non-equilibrium partitioning or from metastable bcc solidification. Dendrite cores are enriched in both Cr and Ni when recalescence was single, while they are enriched in Cr but depleted with Ni when recalescence is double. The former core profiles are the result of improved partition ratios in fcc solidification, and the latter result from bcc solidification and subsequent bcc-to-fcc transformation.

Appendix

Models for fcc nucleation in the mixture of the liquid and bcc

Regarding the nucleation of fcc solid in the mixture of the liquid and bcc solid, many combinations of nucleation site and critical nucleus morphology are possible. In the present study, the following five simple cases were considered in order to evaluate the feasibility of the nucleation of fcc:

(1) Homogeneous nucleation of fcc in bcc with spherical morphology of critical nucleus, where coherency and accompanying strain between fcc and bcc were ignored. The free energy of activation for the critical nucleus formation, ΔG^*, is:

$$\Delta G^* = \frac{16\pi (\gamma_{fcc/bcc})^3}{3 (\Delta G_{v,\ bcc\ to\ fcc})^2} \qquad (A\text{-}1)$$

(2) Heterogeneous nucleation of fcc on planar bcc with a spherical cap into the liquid. ΔG^* is:

$$\Delta G^* = \frac{16\pi (\gamma_{liq/fcc})^3}{3 (\Delta G_{v,\ liq\ to\ fcc})^2} f(\theta) \qquad (A\text{-}2)$$

where θ is a wetting (or contact) angle between fcc and bcc substrate, and $f(\theta)$ is given by a function of $\cos\theta$:

$$f(\theta) = \frac{(2 + \cos\theta)(1 - \cos\theta)^2}{4} \qquad (A\text{-}3)$$

$$\cos\theta = \frac{\gamma_{liq/bcc} - \gamma_{fcc/bcc}}{\gamma_{liq/fcc}} \qquad (A\text{-}4)$$

(3) Heterogeneous nucleation of fcc at the liquid/bcc interface with a spherical cap in bcc. Coherency between fcc and bcc was ignored. ΔG^* and $\cos\theta$ are:

$$\Delta G^* = \frac{16\pi (\gamma_{fcc/bcc})^3}{3 (\Delta G_{v,\ bcc\ to\ fcc})^2} f(\theta) \qquad (A\text{-}5)$$

$$\cos\theta = \frac{\gamma_{liq/bcc} - \gamma_{liq/fcc}}{\gamma_{fcc/bcc}} \qquad (A\text{-}6)$$

(4) Heterogeneous nucleation at the liquid/bcc interface with two abutting spherical caps with different radii (i.e., different wetting angles). Let θ_1 be the wetting angle between the liquid-side fcc cap and the liquid/bcc interface, and θ_2 be the wetting angle between the bcc-side cap and the interface. Then ΔG^*, $\cos\theta_1$ and $\cos\theta_2$ are[16]:

$$\Delta G^* = \frac{16\pi (\gamma_{fcc/bcc})^3}{3 (\Delta G_{v,\ bcc\ to\ fcc})^2} \left(f(\theta_1) + \left(\frac{\gamma_{fcc/bcc}}{\gamma_{liq/fcc}}\right)^3 f(\theta_2) \right) \qquad (A\text{-}7)$$

$$\cos\theta_1 = \frac{\gamma_{liq/bcc}^2 + \gamma_{liq/fcc}^2 - \gamma_{fcc/bcc}^2}{2\gamma_{liq/bcc}\gamma_{liq/fcc}} \quad \text{(A-8)}$$

$$\cos\theta_2 = \frac{\gamma_{liq/bcc}^2 - \gamma_{liq/fcc}^2 + \gamma_{fcc/bcc}^2}{2\gamma_{liq/bcc}\gamma_{fcc/bcc}} \quad \text{(A-9)}$$

(5) Heterogeneous nucleation at planar disordered bcc/bcc boundary with two abutting (symmetrical) spherical caps. Coherency between fcc and bcc was ignored. ΔG^* and $\cos\theta$ are:

$$\Delta G^* = \frac{16\pi (\gamma_{fcc/bcc})^3}{3 (\Delta G_{v,\ bcc\ to\ fcc})^2} \frac{f(\theta)}{2} \quad \text{(A-10)}$$

$$\cos\theta = \frac{\gamma_{bcc/bcc}}{2\gamma_{fcc/bcc}} \quad \text{(A-11)}$$

In the calculation of ΔG^*, volume free energy changes, ΔG_v, (J m^{-3}) were estimated by enthalpy changes, and given as a function of temperature, T (K):

$$\Delta G_{v,\ liq\ to\ fcc} = \frac{\Delta H_f(T_L - T)}{V_m T_L} = 1.50\times10^9 - 8.64\times10^5 T \quad \text{(A-12)}$$

$$\Delta G_{v,\ bcc\ to\ fcc} = \frac{\Delta H_{bcc/fcc}(T_{bcc/fcc} - T)}{V_m T_{bcc/fcc}} = 4.02\times10^8 - 2.11\times10^5 T \quad \text{(A-13)}$$

where $T_{bcc/fcc}$ is the hypothetical bcc solvus temperature (1904.13 K) and $\Delta H_{bcc/fcc}$ is the enthalpy change for the change from bcc to fcc at $T_{bcc/fcc}$ (3,094 J mol^{-1}). Definition and value of the other parameters in Eqs. (A-12) and (A-13) are given in Table 2. Interfacial energies, $\gamma_{liq/fcc}$, $\gamma_{liq/bcc}$, and $\gamma_{bcc/bcc}$, were assumed to be constant for the simplicity and taken as 0.3, 0.2, and 0.47[17] (J m^{-2}), respectively.

Nucleation temperature of fcc, T_N, was determined so as to satisfy $\Delta G^* = 60kT_N$, where k is the Boltzmann constant. The nucleation

temperature was calculated as a function of interfacial energy between fcc and bcc, $\gamma_{fcc/bcc}$, and plotted in Figure 21.

References

1. Y. Wu, T. J. Piccone, Y. Shiohara, and M. C. Flemings: *Metall Trans. A*, 1987, vol. 18A, p. 915
2. T. J. Piccone, Y. Wu, Y. Shiohara, and M. C. Flemings: *Metall Trans. A*, 1987, vol. 18A, p. 925
3. Q. Zhao, T. J. Piccone, Y. Shiohara, and M. C. Flemings: *MRS Int'l. Mtg. on Adv. Mats.*, 1989, vol. 3, p. 597
4. M. Suzuki, T. J. Piccone, M. C. Flemings, and H. D. Brody: *Metall. Trans. A*, 1991, vol. 22A, p. 2761
5. E. Scleip, R. Willnecker, D. M. Herlach, and G. P. Görler: *Mater. Sci. Eng.*, 1988, vol. 98, p. 39
6. D. M. Herlach, B. Feuerbacher, and E. Schleip: *Mater. Sci. Eng.*, 1991, vol. A133, p. 795
7. T. Piccone: Sc. D. Thesis, MIT, 1990
8. A. Munitz and G. J. Abbaschian: *Adv. Materials & Manufacturing Processes*, 1988, vol. 3, p. 419
9. I. Taguchi and H. Hamada: *Analytical Sci.*, 1985, vol. 1, p. 119
10. B. Sundman, B. Jansson, and J.-O. Andersson: *CALPHAD*, 1985, vol. 9, p. 153
11. W. J. Boettinger, S. R. Coriell, and R. Trivedi: *Rapid Solidification Processing: Principles and Technologies IV*, R. Mehrabian and P. A. Parrish, eds., Claitor's Publ. Div., Baton Rouge, LA., 1988, p. 13
12. T. Z. Kattamis: *Z. Metallkde*, 1970, vol. 61, p. 856
13. J. A. Brooks, J. C. Williams, and A. W. Thompson: *Metall. Trans.* A, 1983, vol. 14A, p. 1271
14. J. W. Christian: *Theory of Transformation in Metals and Alloys*, Pergamon Press, Oxford, 1975, p. 442
15. M. J. Aziz: *Mater. Sci. and Eng.*, 1988, vol. 98, p. 369

16. W. C. Johnson, C. L. White, P. E. Marth, P. K. Ruf, S. M. Tuominen, W. D. Wade, K. C. Russell, and H. I. Aaronson: *Metall. Trans. A*, 1975, vol. 6A, p. 911
17. L. E. Murr: *Interfacial Phenomena in Metals and Alloys*, Addison-Wesley Publ. Co., MA, 1975, p. 131
18. Y. Ono: *The Properties of Liquid Metals*, S. Takeuchi, ed., Taylor and Francis, London, 1973, p. 543
19. M. Bobadilla, J. Lacaze, and G. Lesoult: *J. Cryst. Growth*, 1988, vol. 89, p. 531
20. W. J. Boettinger, S. R. Coriel, and R. F. Sekerka: *Mater. Sci. Eng.*, 1984, vol. 65, p.27
21. M. R. Plichta, W. A. T. Clark, and H. I. Aaronson: *Metall. Trans. A*, 1984, vol. 15A, p. 427

Table 1. Chemical Compositions of alloys used (wt%)

	Fe-16Cr-14Ni	Fe-15Cr-15Ni
Cr	15.9	15.0
Ni	14.3	15.0
C	0.012	0.018
Si	0.02	0.01
Mn	0.03	0.03
N	0.002	0.001
O	0.014	0.009
Fe	bal	bal

Table 2: Parameter values used for the calculations involving the dendrite tip model.

parameter			value		ref.
			15Cr/15Ni	16Cr/14Ni	
T_L	liquidus temperature (K)	(fcc)	1733.81	1731.10	
		(bcc)	1704.44	1708.52	
ΔH_f	enthalpy of fusion (J mol^{-1})	(fcc)	11643.31	11532.89	
		(bcc)	8901.91	8885.15	
ΔS_f	entropy of fusion (J $mol^{-1}K^{-1}$)	(fcc)	6.7753	6.6983	
		(bcc)	5.7775	5.7354	
k_{Cr}	partition ratio of Cr	(liq/fcc)	0.8790	0.8743	
k_{Ni}	partition ratio of Ni	(liq/bcc)	0.7625	0.7641	
m_L	slope of liquidus (K $wt\%^{-1}$)	(fcc)	-3.5352	-3.7150	
		(bcc)	-7.0625	-6.9588	
C_{pL}	specific heat of liqiud (J $mol^{-1}K^{-1}$)		43.8785	43.832	
$\overline{V}$	molar volume (m^3 mol^{-1})	(liq)	7.71×10^{-6}		
		(fcc)	7.71×10^{-6}		
		(bcc)	7.71×10^{-6}		
D_{Cr}	diffusivity of Cr in liquid (m^2 s^{-1})				
	D_0 diffusion constant (m^2 s^{-1})		2.67×10^{-7}		[18]
	Q activation energy (J mol^{-1})		6.69×10^4		[18]
D_{Ni}	diffusivity of Ni in liquid (m^2 s^{-1})				
	D_0 diffusion constant (m^2 s^{-1})		4.92×10^{-7}		[18]
	Q activation energy (J mol^{-1})		6.77×10^4		[18]
α	thermal diffusivity in liquid (m^2 s^{-1})		5.4×10^{-6}		[19]
V_0	sound velocity in liquid (m s^{-1})		2000		[11]
a_0	interatomic distance in liquid (m)		1×10^{-9}		[20]

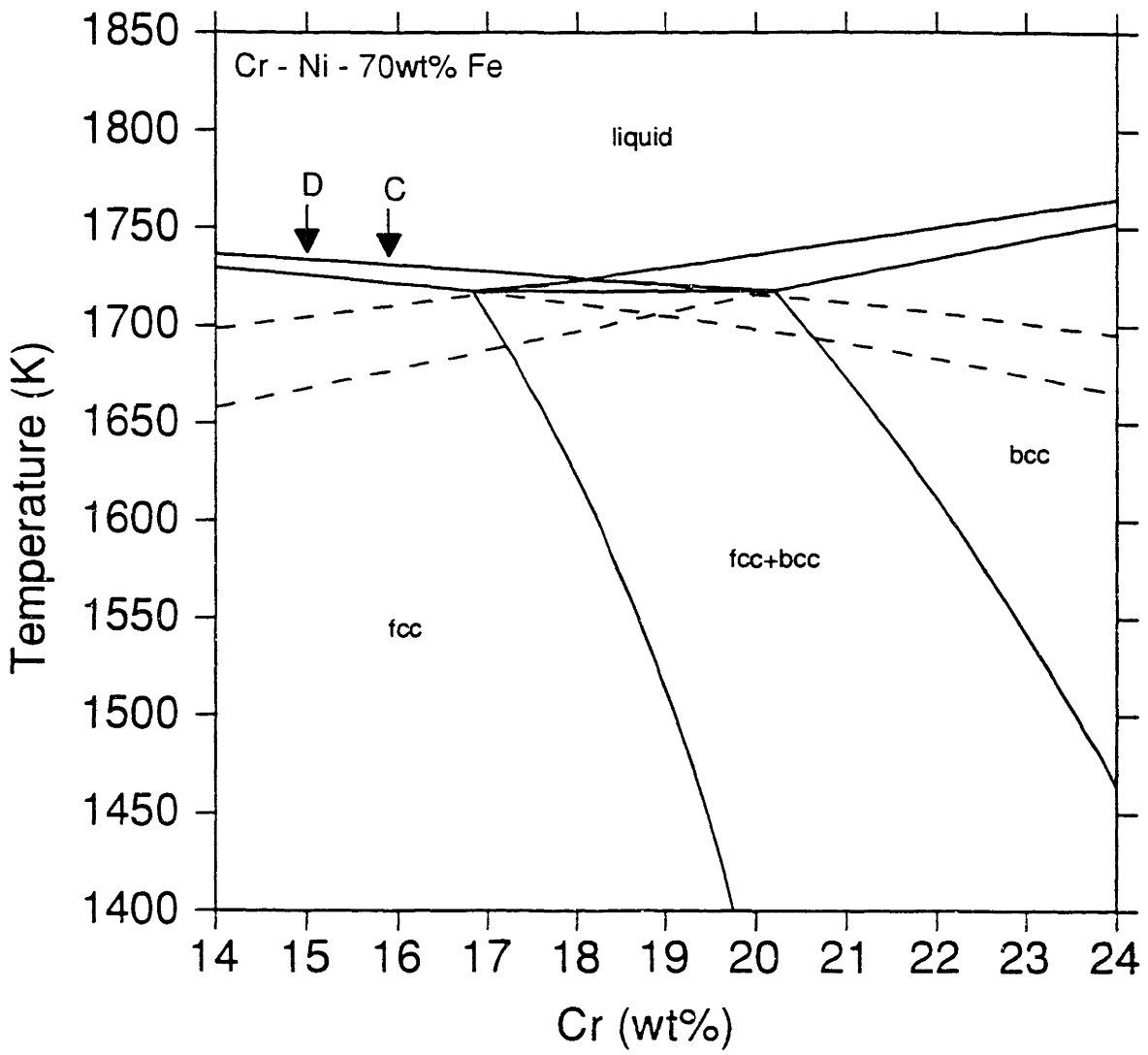

Figure 1 - Pseudo-binary phase diagram of the Fe-Cr-Ni alloy system at 70 wt pct Fe calculated using Thermo Calc[10], and locations of the two alloy compositions used in the present study. Dashed lines are the extension of liquidus and solidus lines.

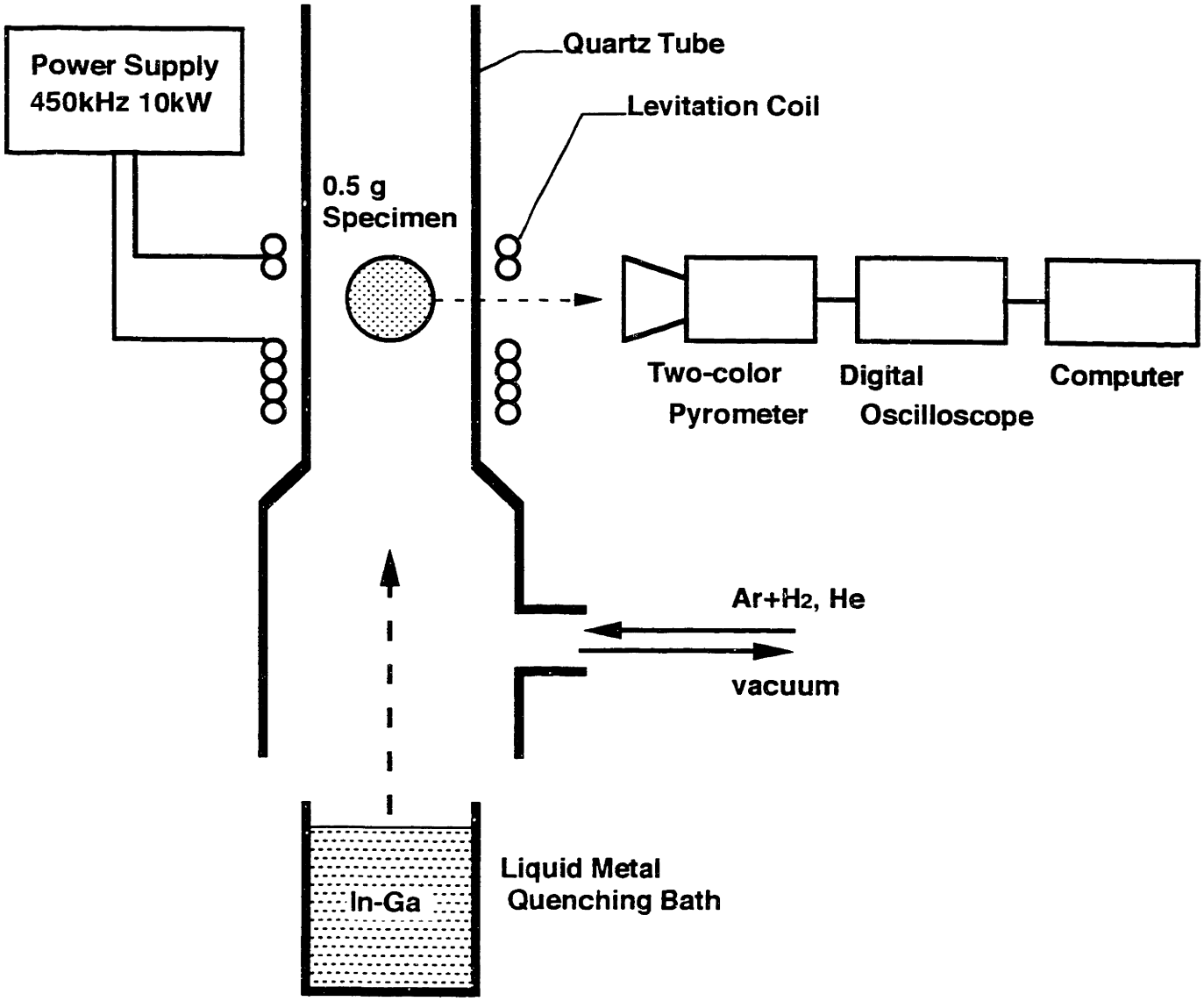

Figure 2 - Schematic diagram of apparatus for levitation melting and undercooling experiments.

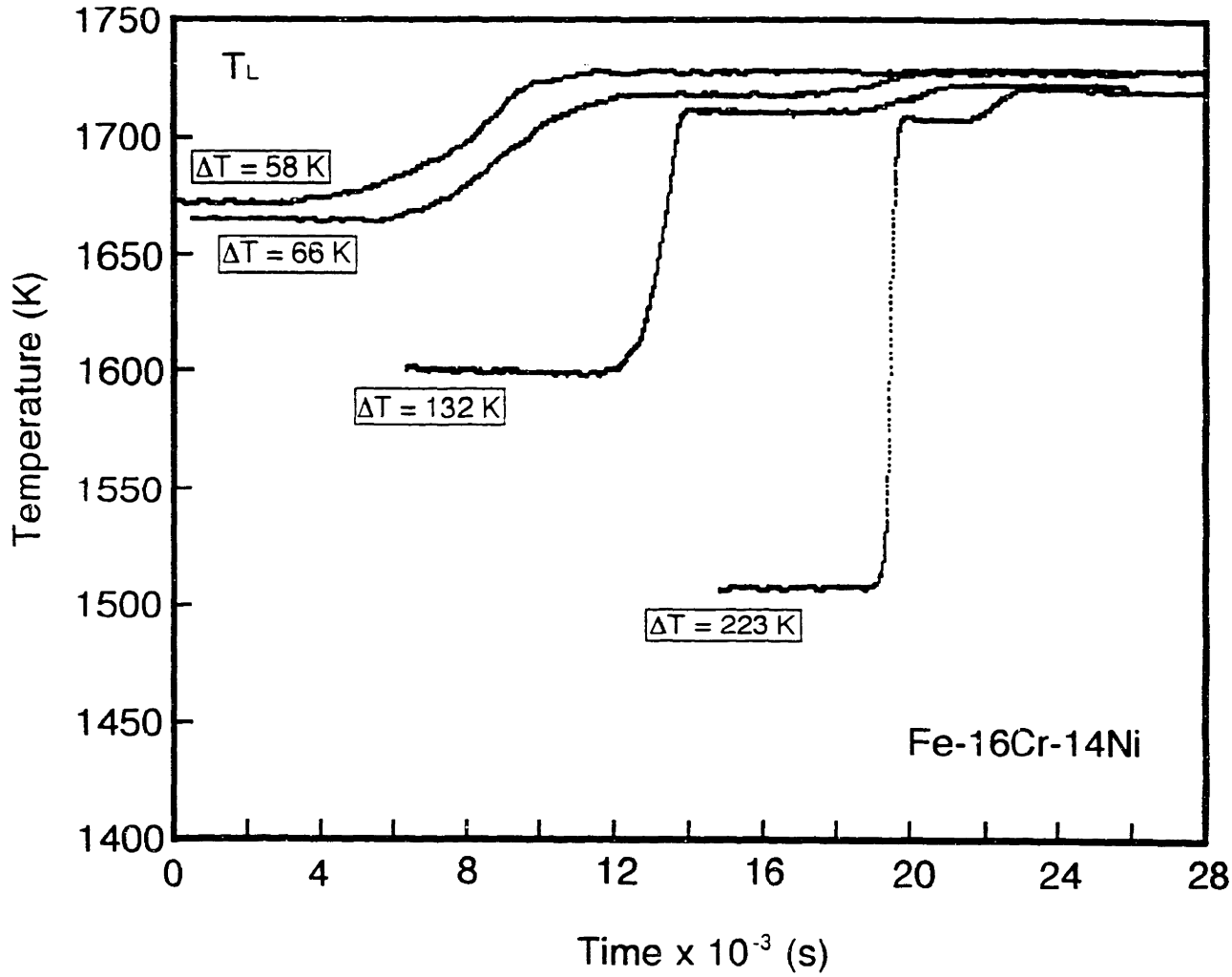

Figure 3 - Typical recalescence curves observed in the solidification of Fe-16Cr-14Ni alloy with different initial undercooling. Transition from single to double recalescence was found at an initial undercooling of about 60 K.

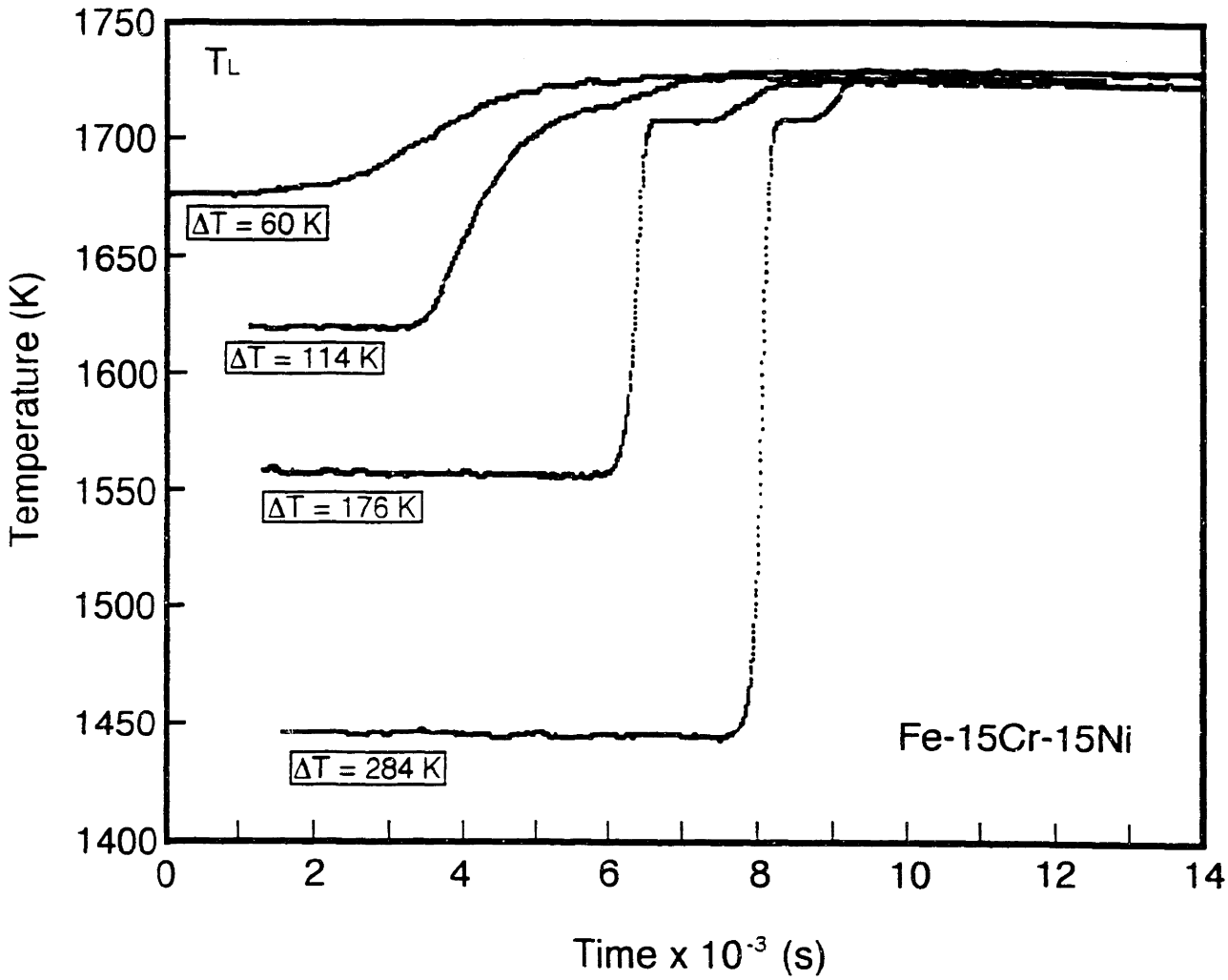

Figure 4 - Typical recalescence curves observed in the solidification of Fe-15Cr-15Ni alloy with different initial undercooling. Transition from single to double recalescence was found at an initial undercooling of about 100 K

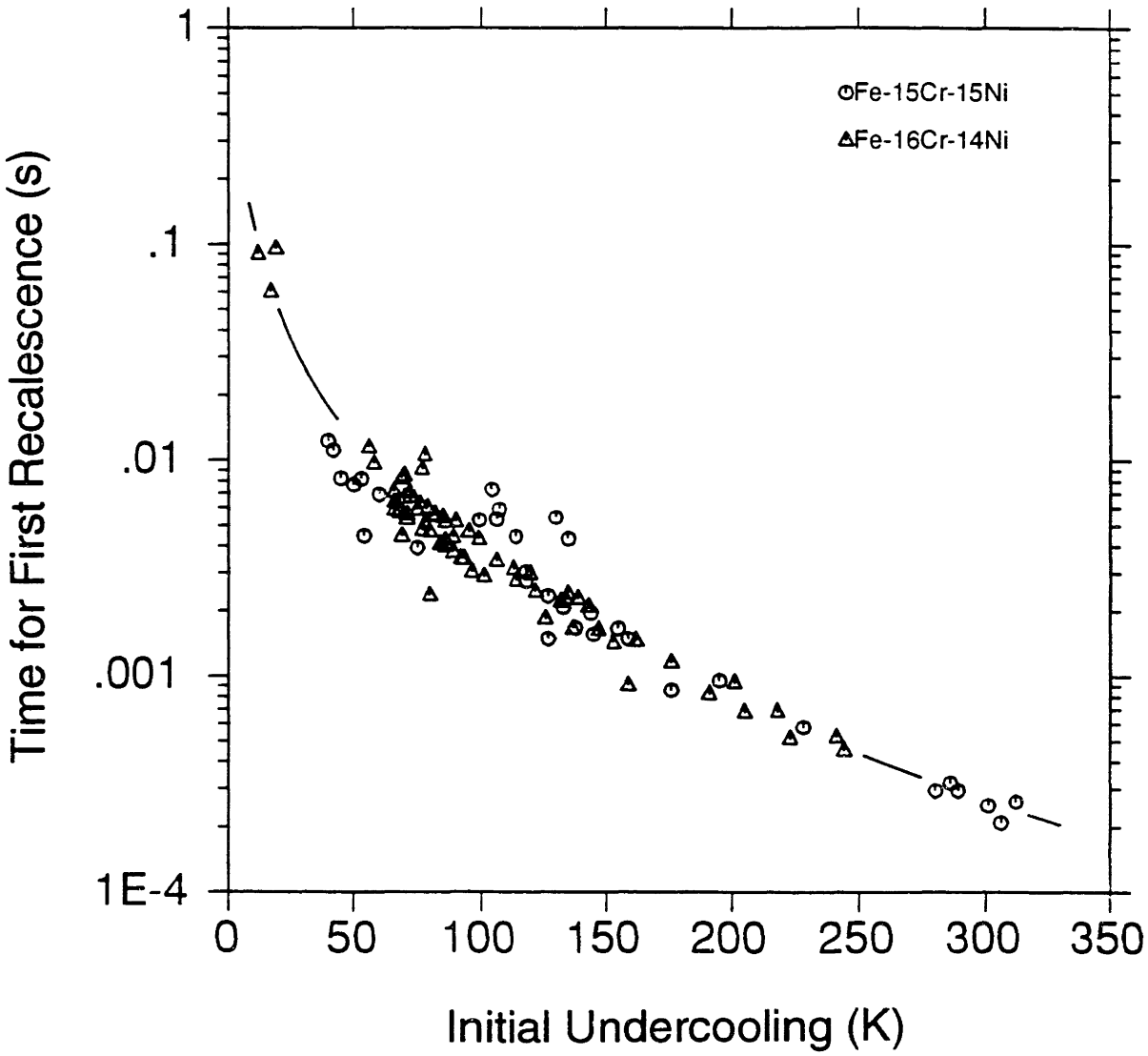

Figure 5 - Effect of initial undercooling on time for the first recalescence in Fe-16Cr-14Ni and Fe-15Cr-15Ni alloys.

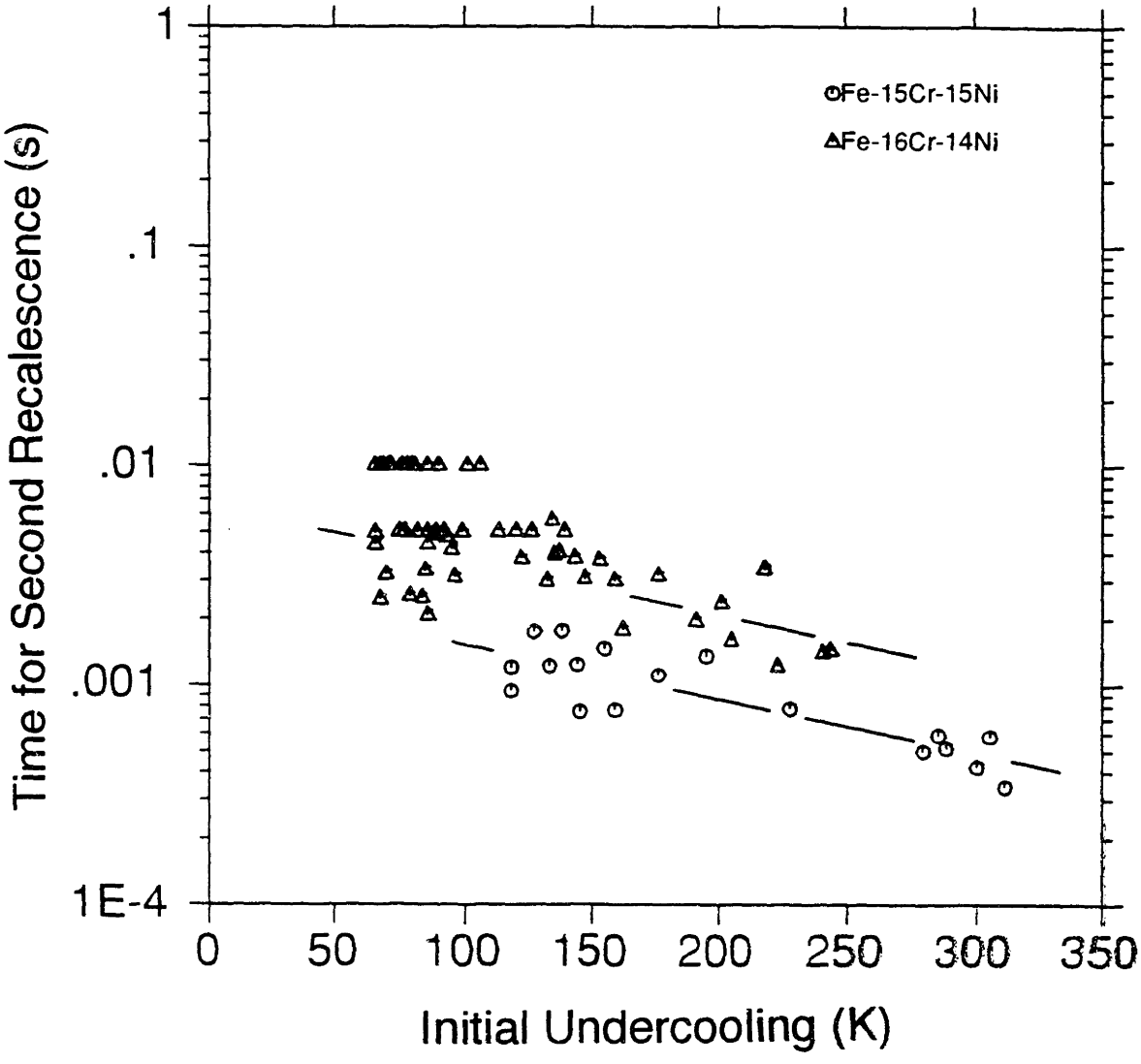

Figure 6 - Effect of initial undercooling on time for the second recalescence in Fe-16Cr-14Ni and Fe-15Cr-15Ni alloys.

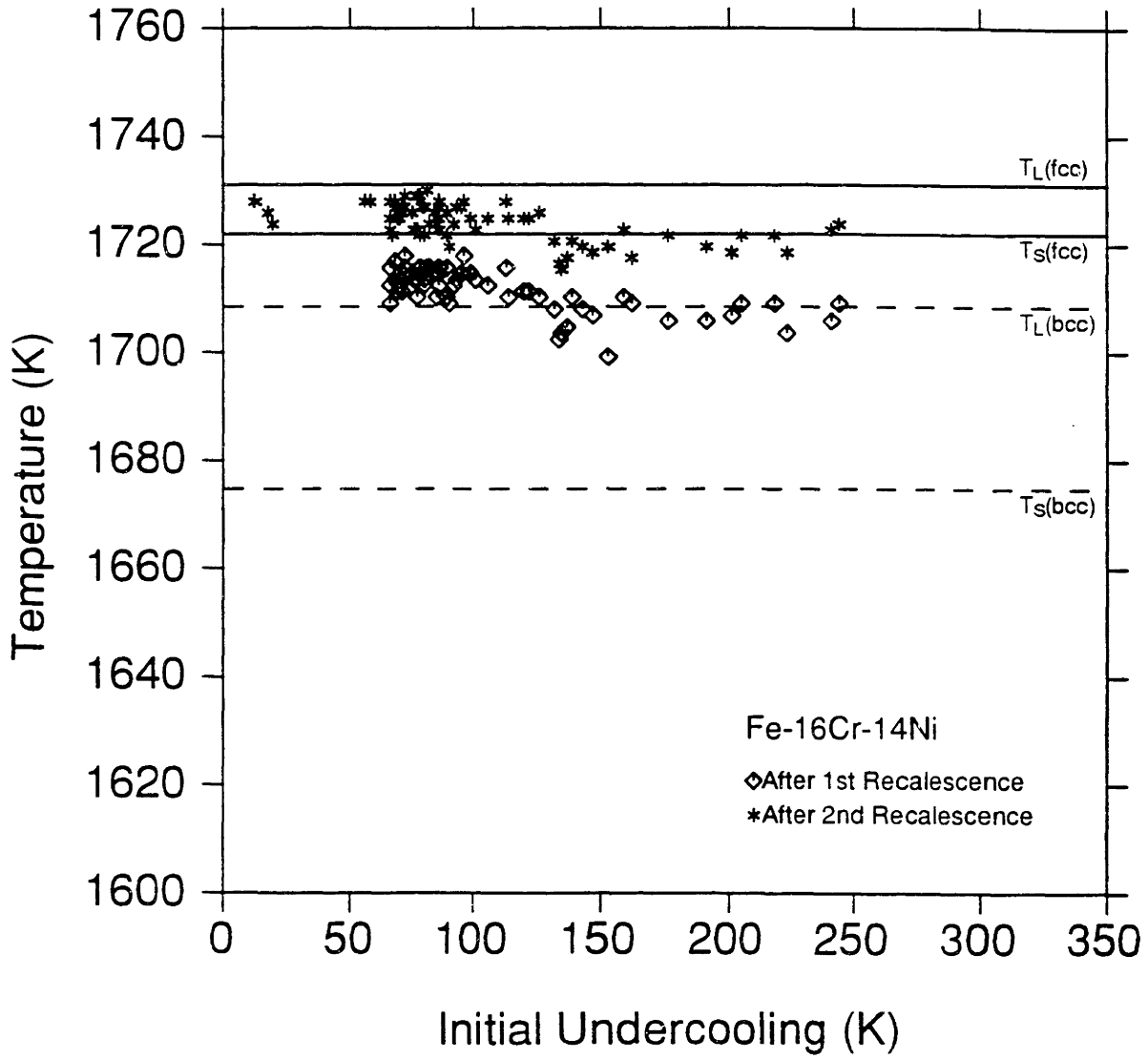

Figure 7 - Temperatures after the first recalescence and second recalescence in the solidification of Fe-16Cr-14Ni alloy

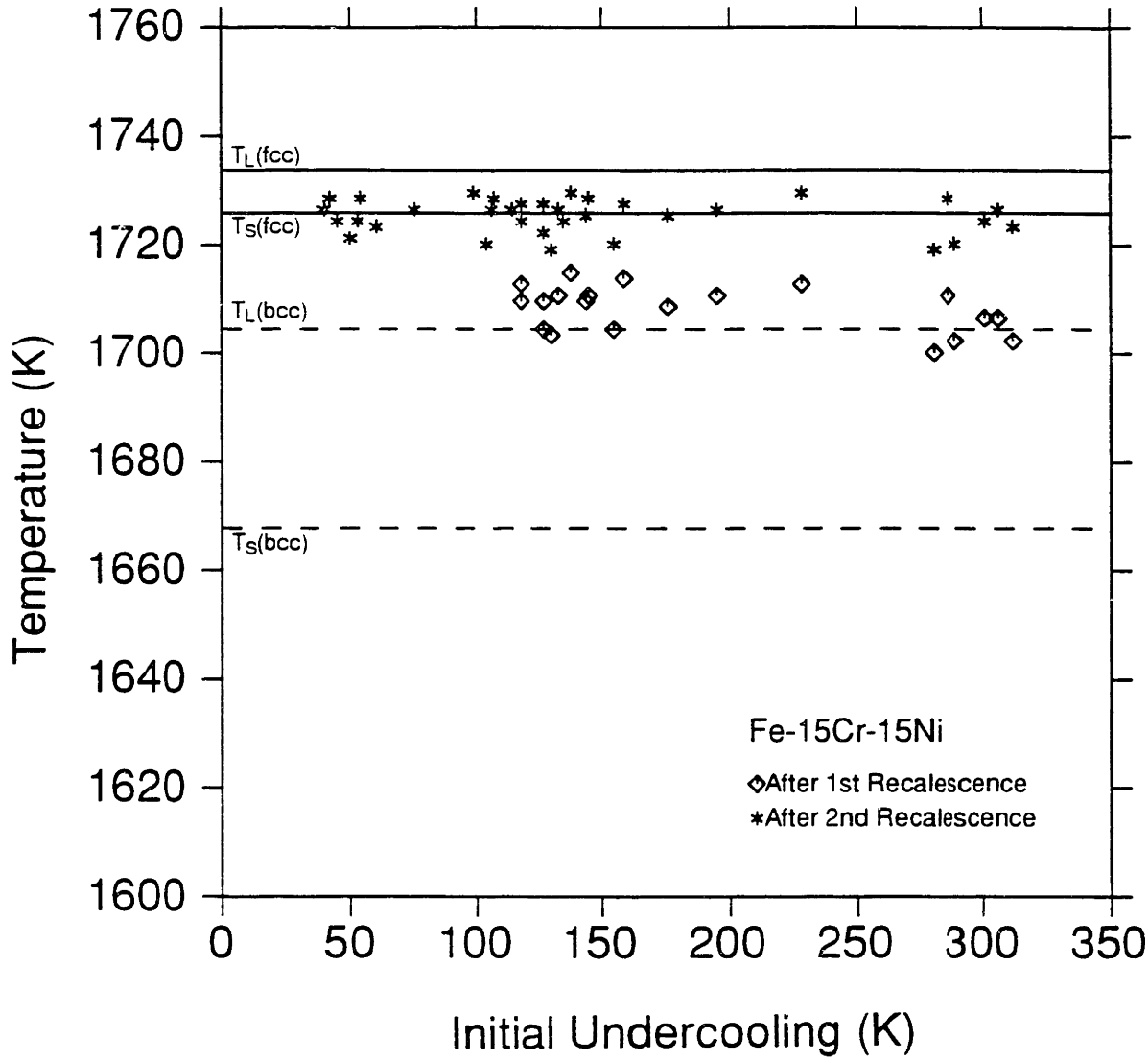

Figure 8 - Temperatures after the first recalescence and second recalescence in the solidification of Fe-15Cr-15Ni alloy

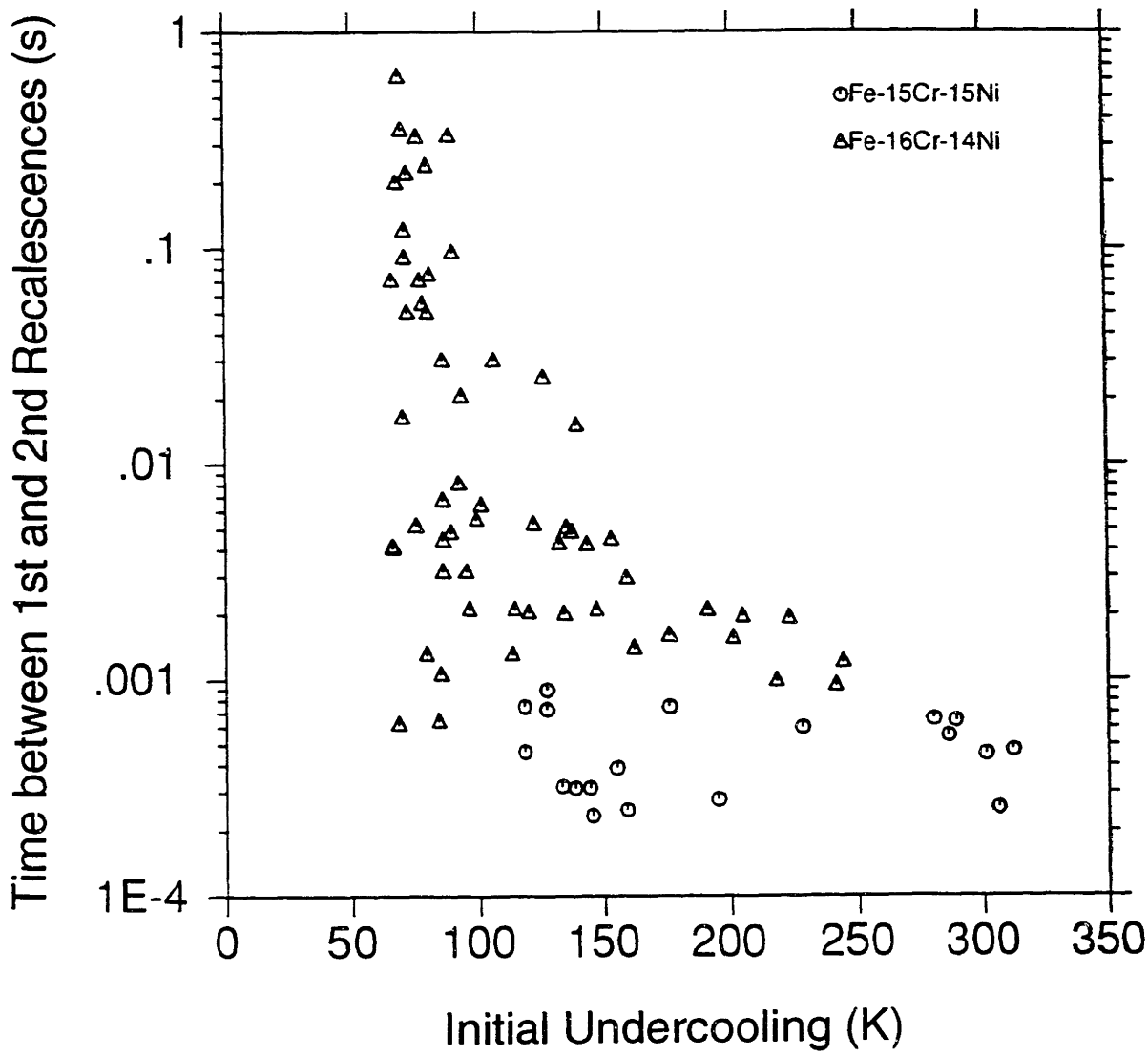

Figure 9 - Effect of initial undercooling and alloy composition on time between the first recalescence and second recalescence.

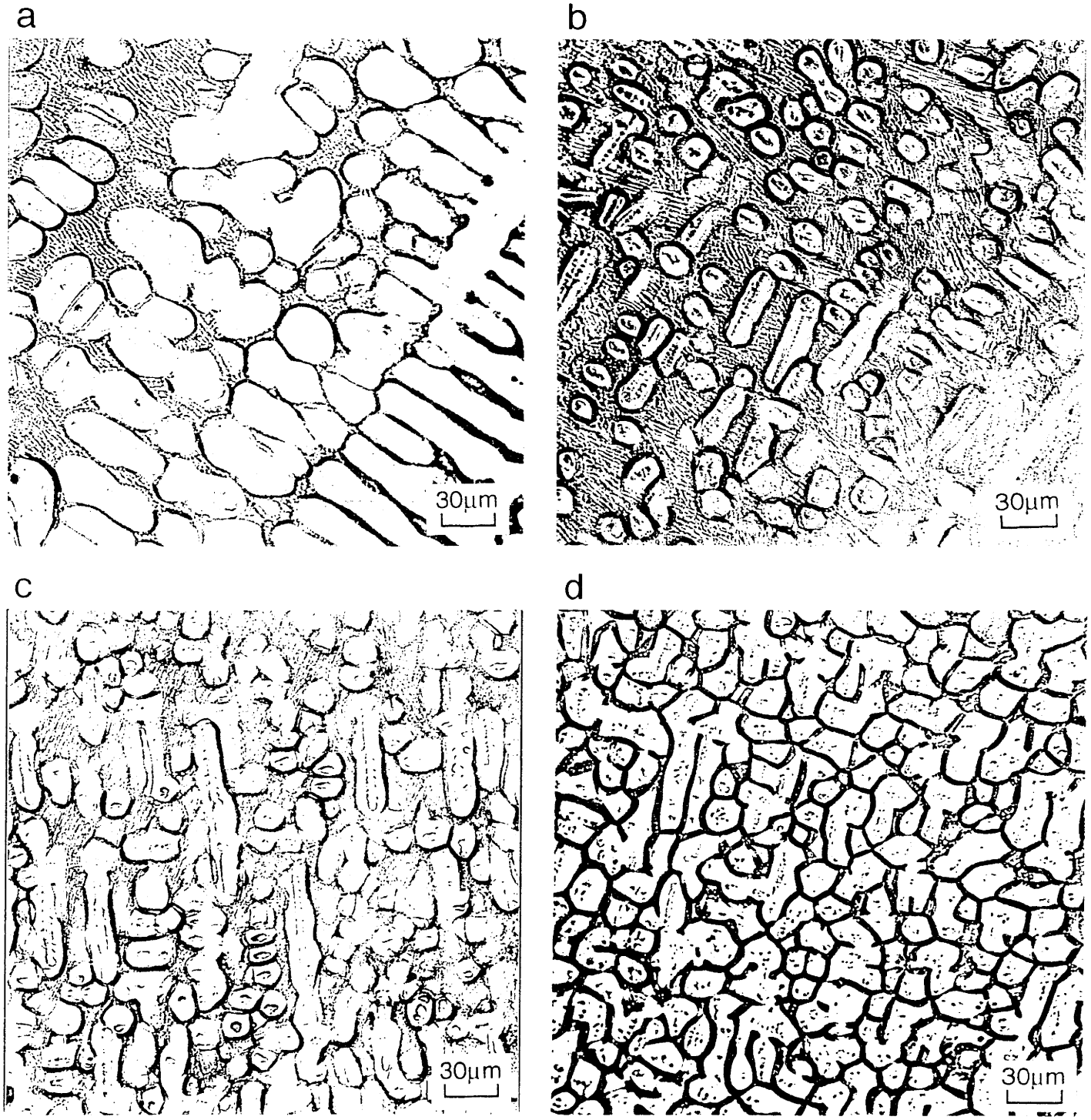

Figure 10 - Typical microstructures of Fe-16Cr-14Ni which were solidified with different initial undercooling (ΔT) and quenched into In-Ga liquid bath immediately after recalescence. (a) ΔT =12 K, (b) ΔT = 58 K, (c) ΔT = 101 K, and (d) ΔT = 176 K.

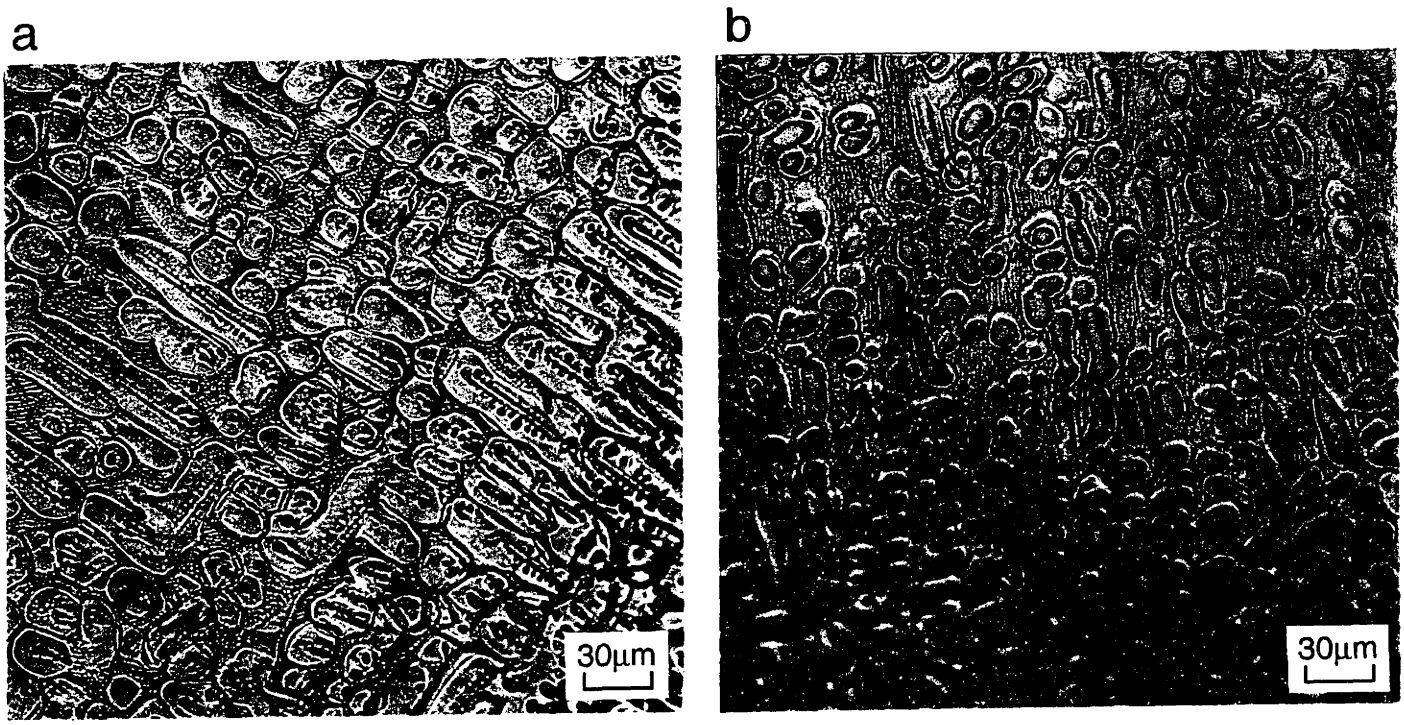

Figure 11 - Microstructures of Fe-16Cr-14Ni which were solidified with similar initial undercooling but with different plateau time, and quenched into an In-Ga bath immediately after the second recalescence. (a) ΔT = 66 K with a plateau time of 4 ms, and (b) ΔT = 70 K with a plateau time of 350 ms.

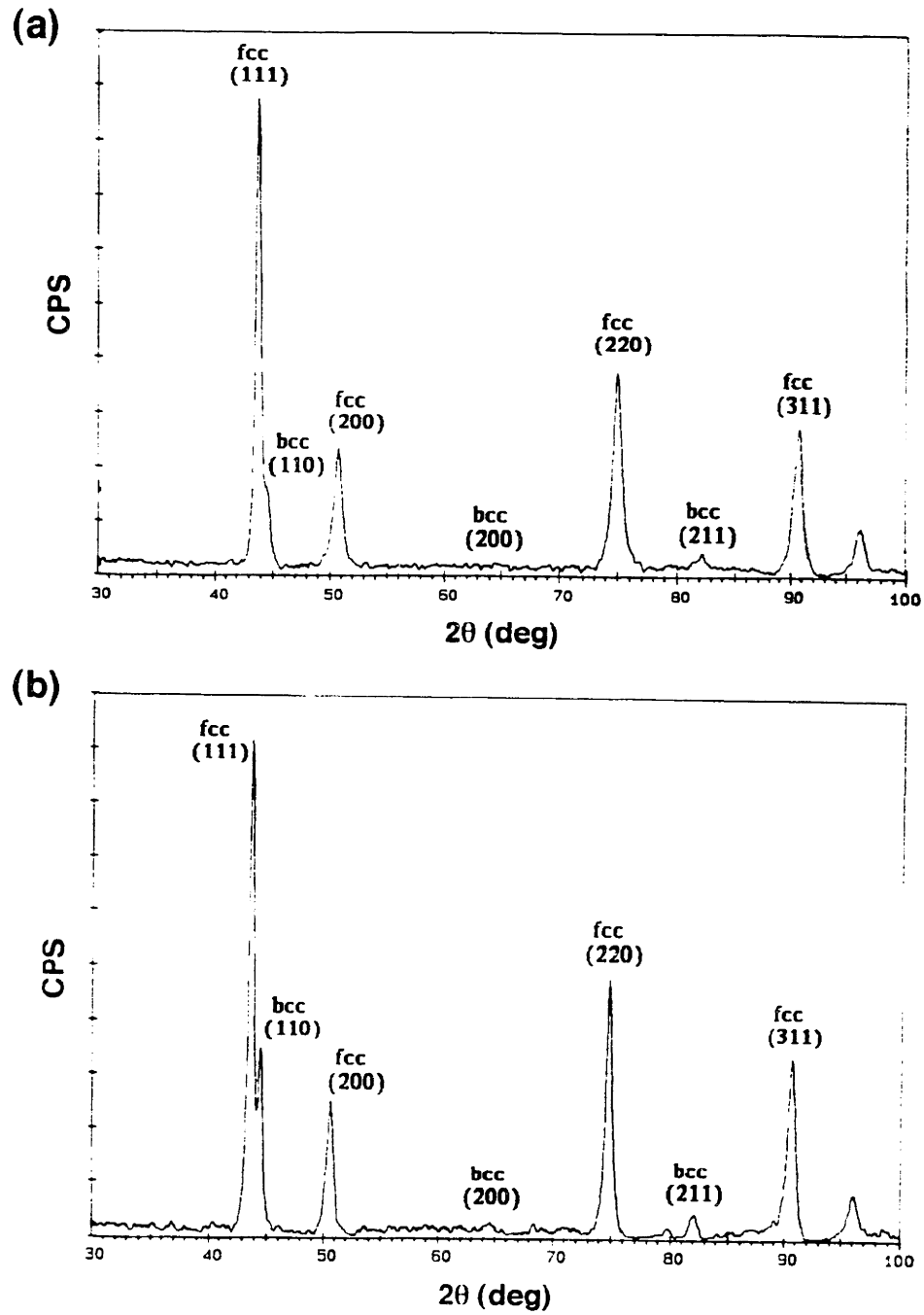

Figure 12 - X-ray diffraction results from specimens shown in Figure 11 (a) and (b). (a) ΔT = 66 K with a plateau time of 4 ms, and (b) ΔT = 70 K with a plateau time of 350 ms.

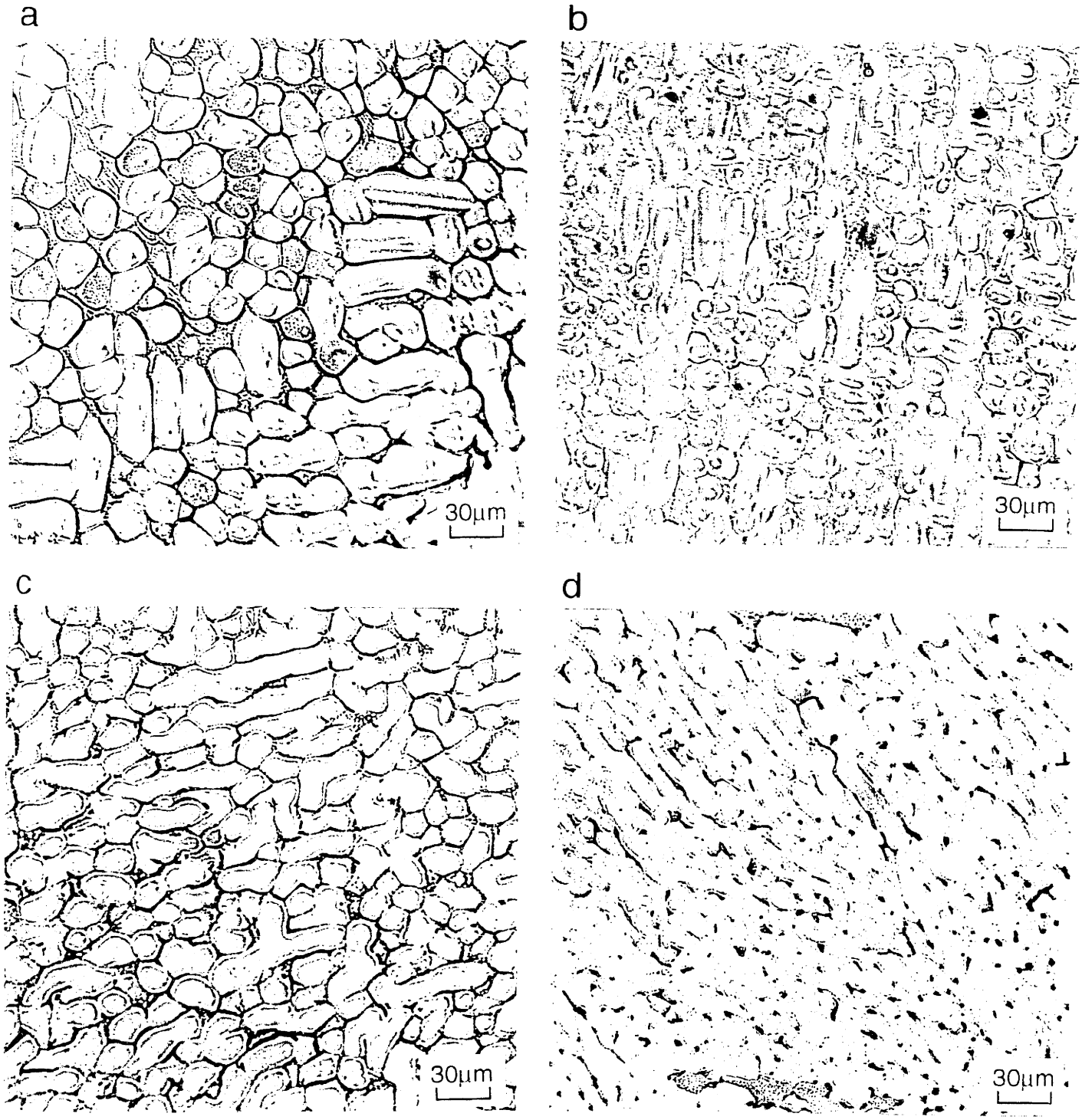

Figure 13 - Typical microstructures of Fe-15Cr-15Ni which were solidified with different initial undercooling (ΔT) and quenched into an In-Ga liquid bath immediately after recalescence. (a) ΔT = 60 K, (b) ΔT = 104 K, (c) ΔT = 205 K, and (d) ΔT = 306 K.

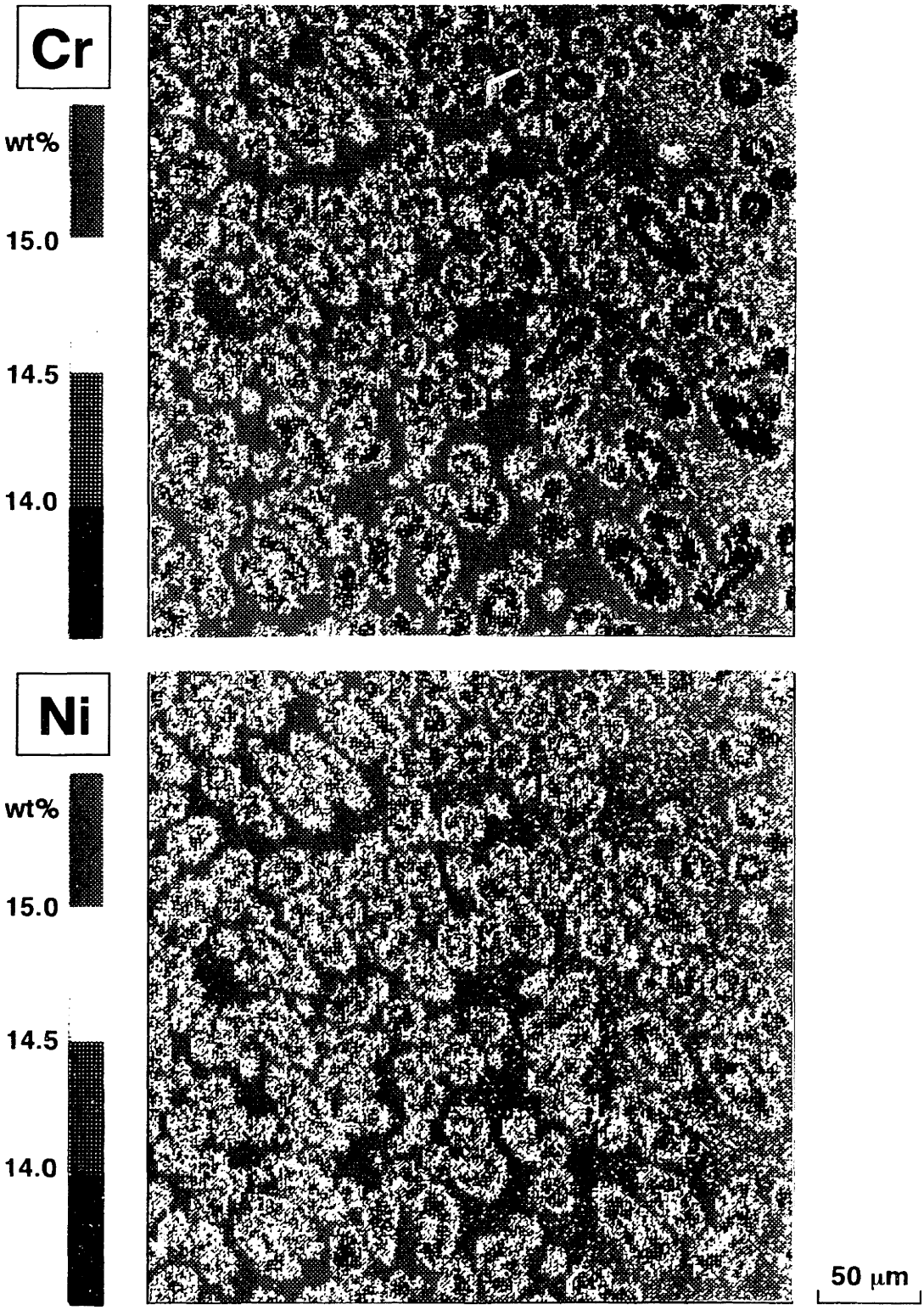

Figure 14 - Concentration profiles of Cr and Ni in a microstructure of Fe-15Cr-15Ni which was solidified with an initial undercooling of 60 K, and quenched after recalescence.

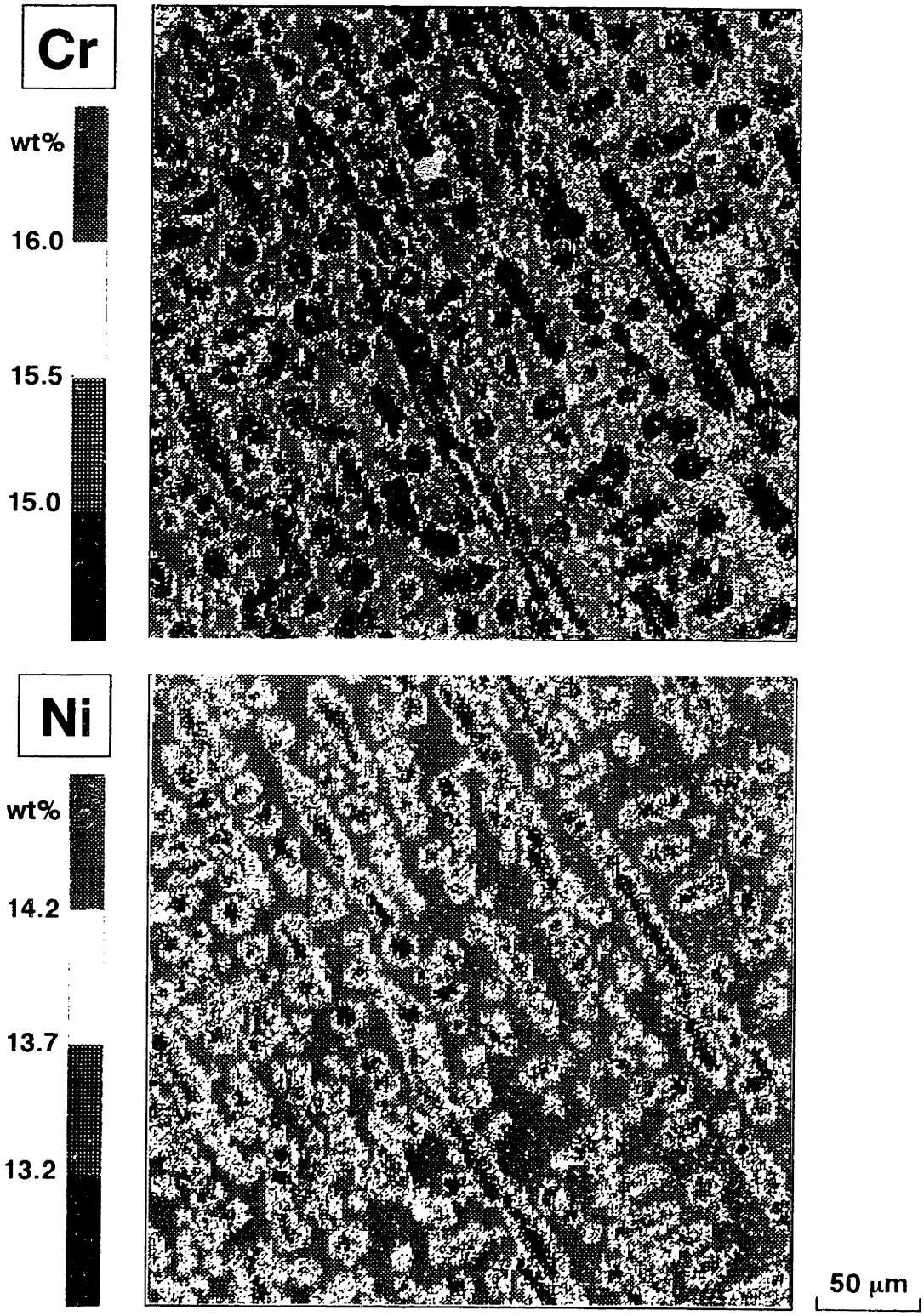

Figure 15 - Concentration profiles of Cr and Ni in a microstructure of Fe-16Cr-14Ni which was solidified with an initial undercooling of 101 K, and quenched after recalescence.

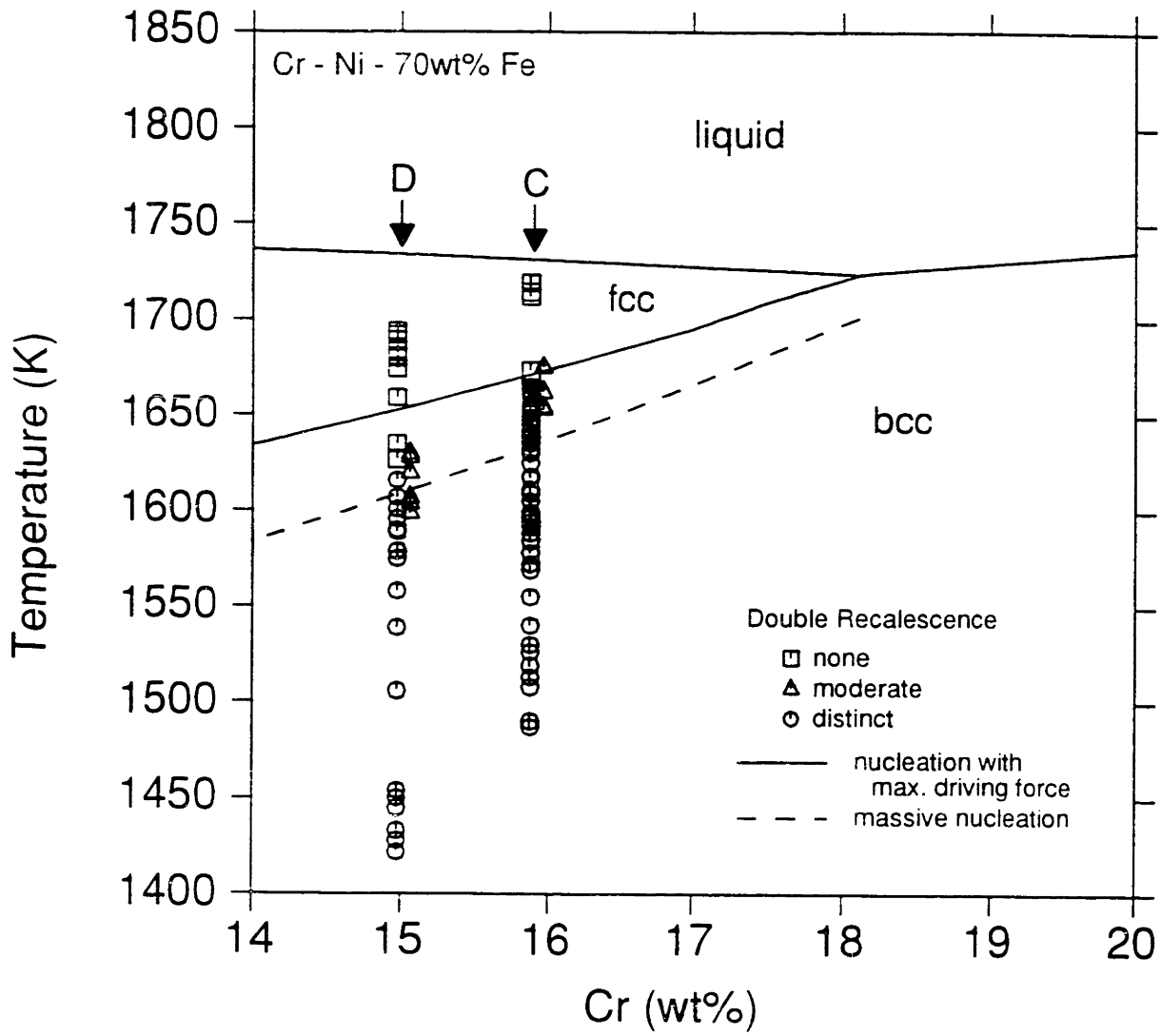

Figure 16 - Effect of composition and initial undercooling on the occurrence of double recalescence. The comparison of the effect with the nucleation diagram suggests that double recalescence is related to metastable bcc solidification.

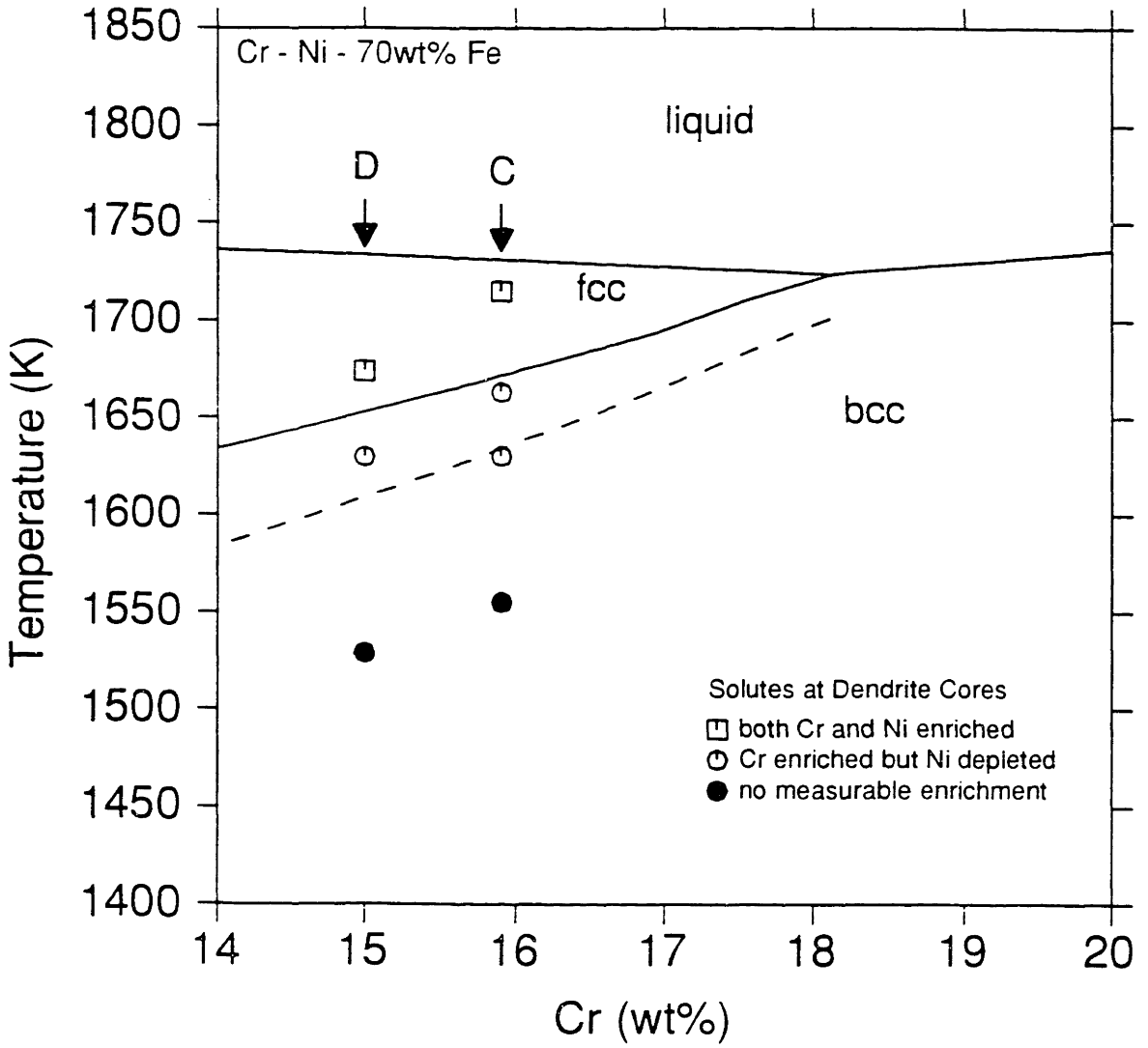

Figure 17 - Effect of initial undercooling on solute profiles at dendrite cores plotted on the nucleation diagram.

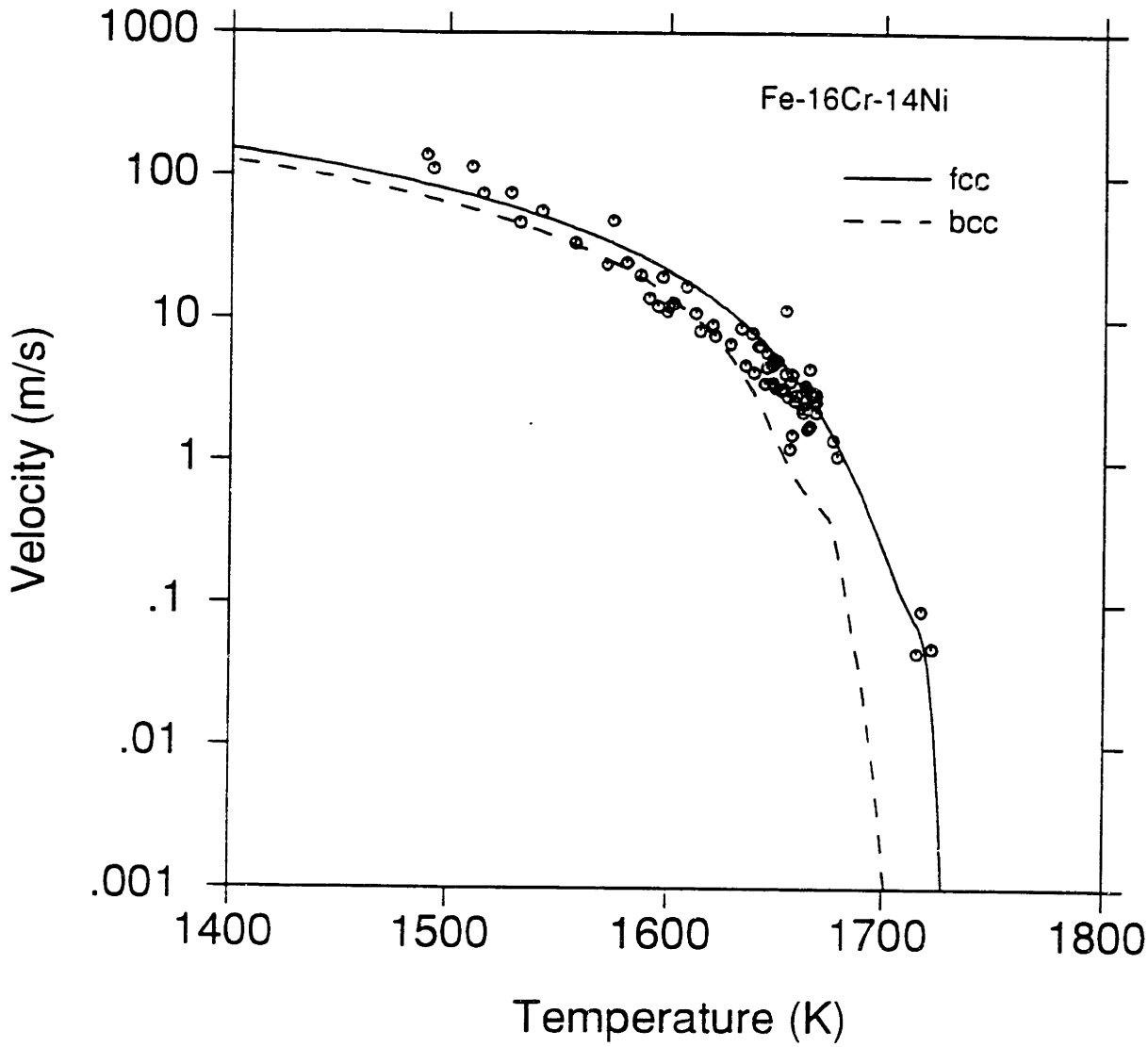

Figure 18 - Growth velocities of fcc and bcc dendrites calculated as a function of melt temperature using the BCT model[11], and comparison of experimentally estimated velocities with the model results for Fe-16Cr-14Ni alloy.

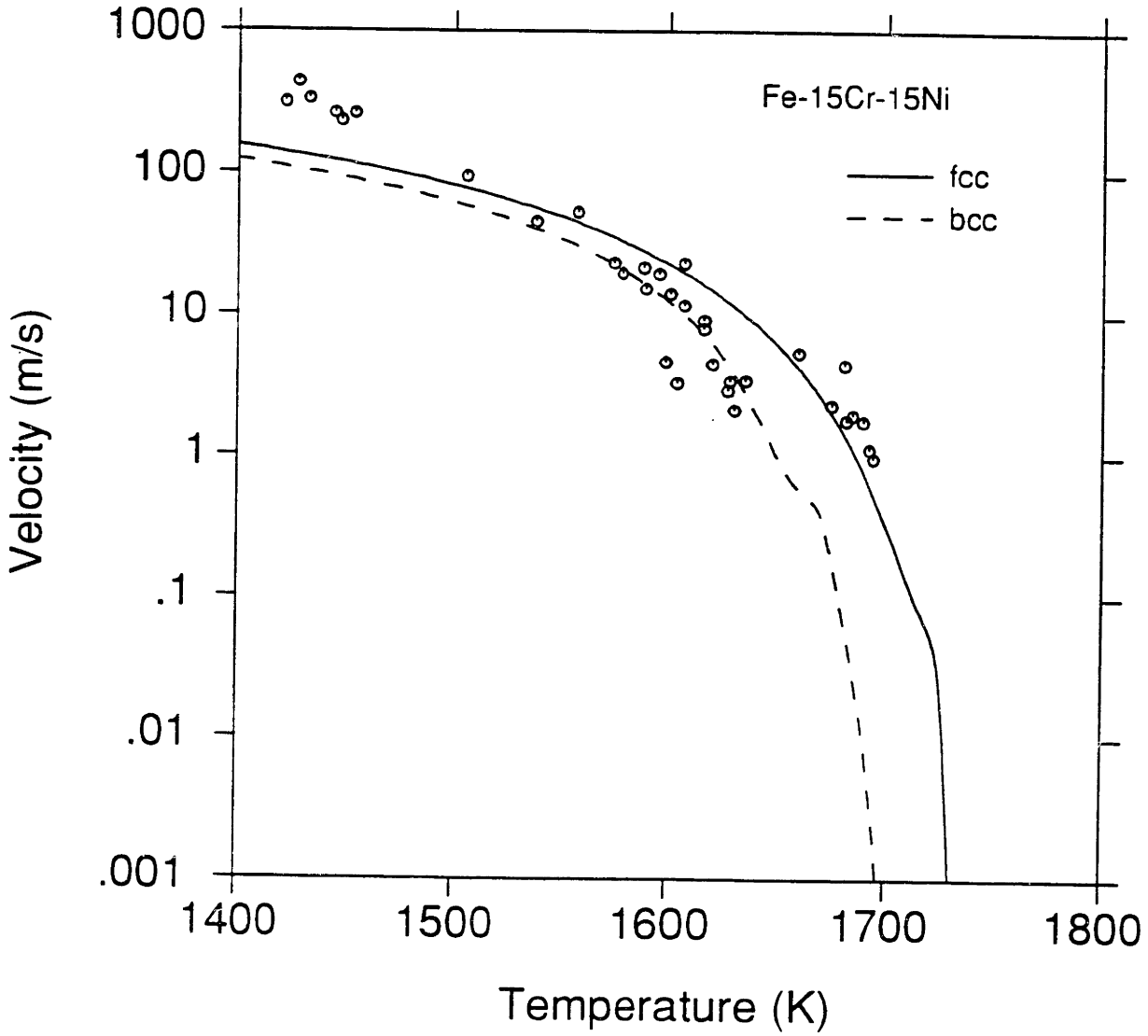

Figure 19 - Growth velocities of fcc and bcc dendrites calculated as a function of melt temperature using the BCT model[11], and comparison of experimentally estimated velocities with the model results for Fe-15Cr-15Ni alloy.

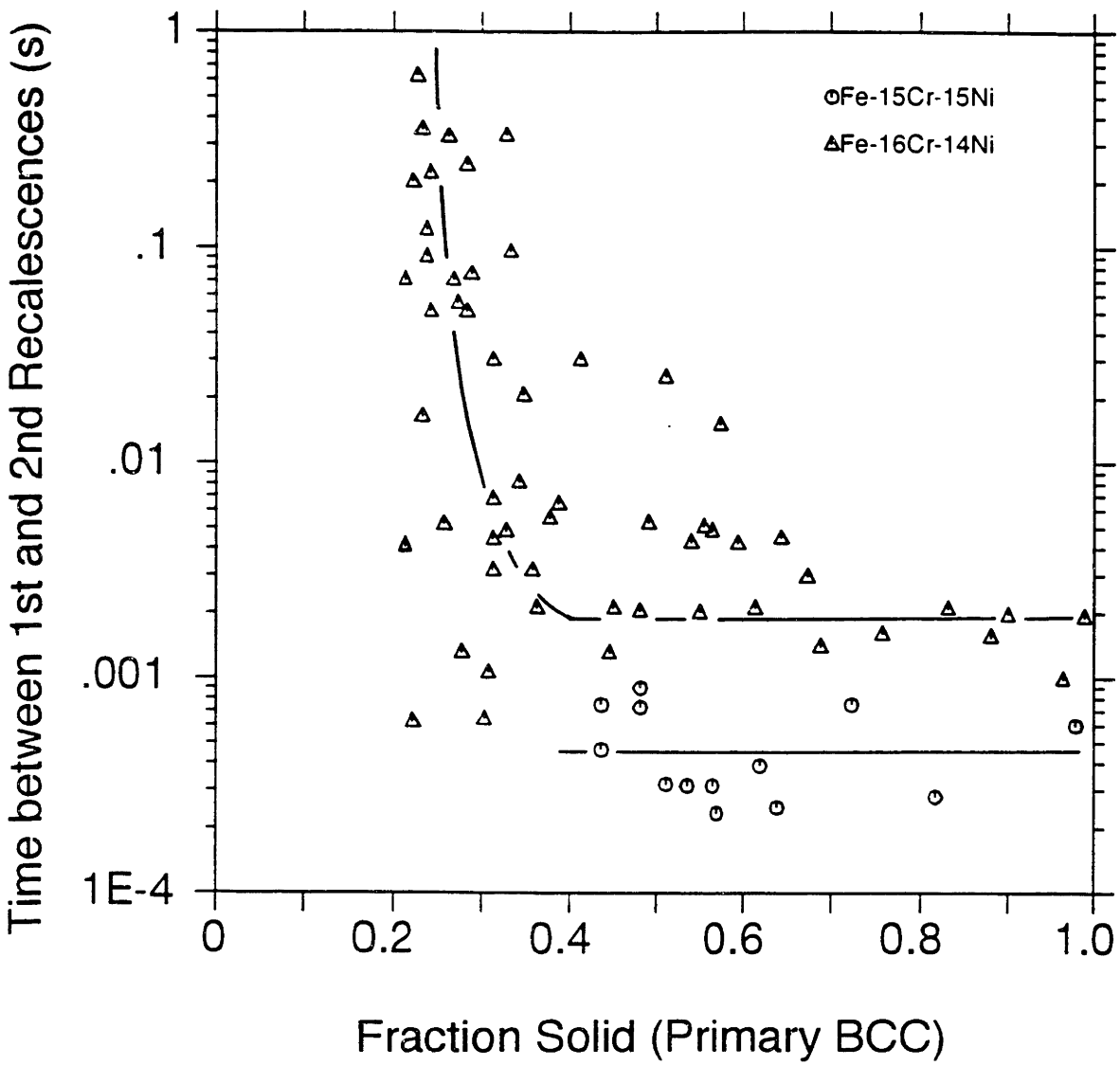

Figure 20 - Effect of fraction solid after the first recalescence on the plateau time. It is suggested that plateau times are stable and composition-dependent when the fraction solid is more than 0.4.

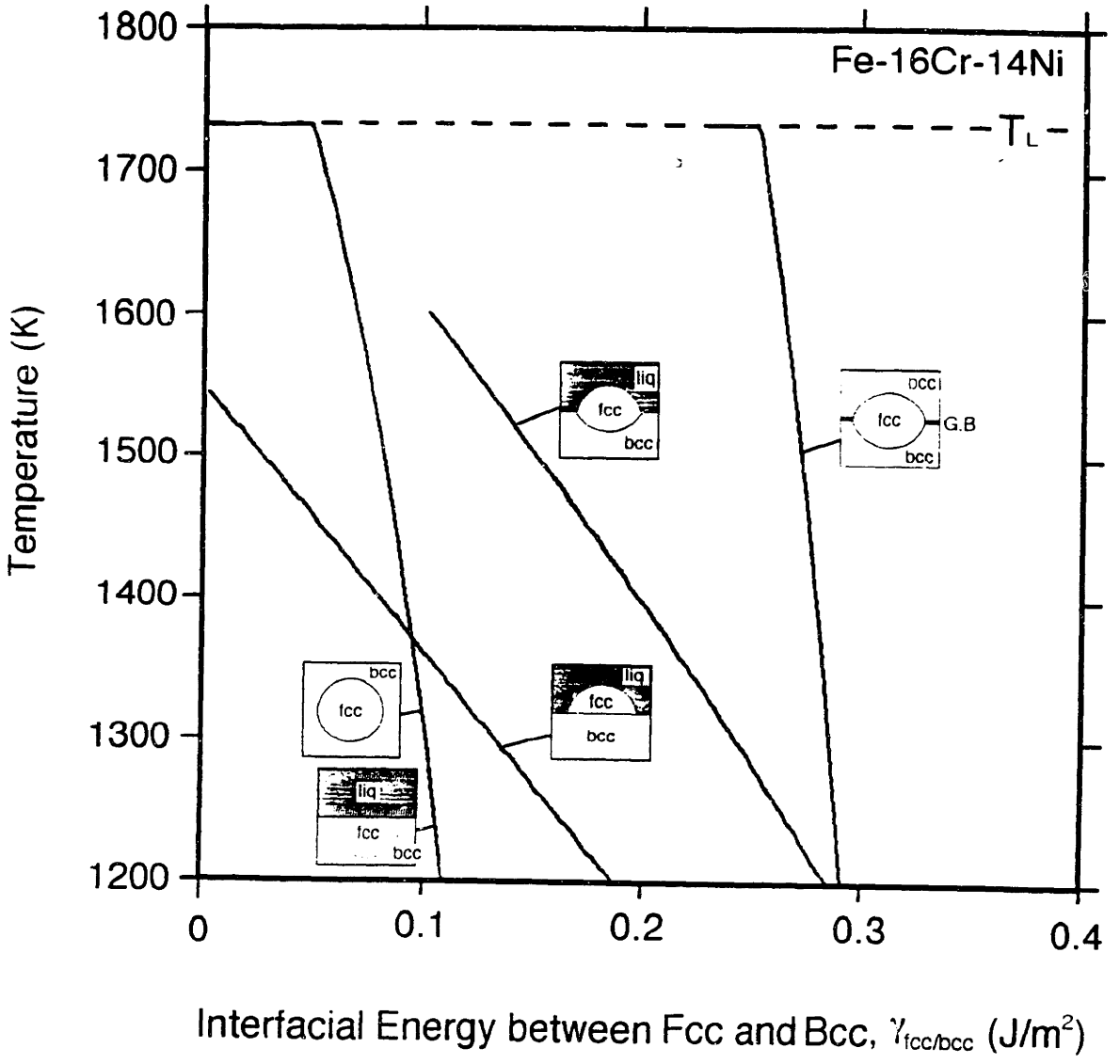

Figure 21 - Calculation results of the nucleation temperature of fcc at various nucleation sites in the presence of the liquid and bcc.

Chapter IV - Effect of Heat Extraction Rate on Dendrite Growth into Undercooled Melt in Fe-Cr-Ni Alloys

Abstract

The rapid solidification behavior of two Fe-Cr-Ni alloys was investigated: one, Fe-17.5Cr-12.2Ni (alloy A), has fcc as its equilibrium primary phase and the other, Fe-18.5Cr-11.3Ni (alloy B), has bcc. Phase selection during chill casting of the undercooled melt was examined using different chill materials. The predominant phase to solidify is fcc in alloy A and metastable fcc in alloy B; this is in contrast to the preferential bcc solidification found in the gas-cooled solidification of both alloys. Nearly concurrent nucleation of bcc and fcc is suggested by tiny bcc dendrites intermittently present at the chill surface. The heat extractive capacity of the chill material exerts a major influence on the nucleation and selective growth of fcc.

1. Introduction

In the foregoing chapters, using a levitation melting and undercooling method, the occurrence of metastable bcc solidification was demonstrated in primary fcc Fe-Cr-Ni alloys. It was concluded that the phase selection of primary bcc was determined by nucleation. The nucleation of bcc was favored over the nucleation of fcc in the undercooled melt, and preferential nucleation determined the overall solidification structure.

In contrast to the above, some solidification processes have produced preferential fcc solidification in similar alloy compositions. Vitek *et al.*[1,2] investigated the solidification of several commercial stainless steels using a laser beam melting and splat quenching techniques. They found that primary fcc solidification became favored over primary bcc solidification as the cooling rate increased. Elmer *et al.*[3] examined the effect of solidification rate on the solidification of Fe-25wt% Cr-Ni ternary alloys using an electron beam melting technique, and confirmed the above results. They also showed that fcc dendrites selectively grew from the "matching substrate" even if the "substrate" consisted of fcc-bcc duplex structure. A similar tendency was observed in laser beam surface melting[4,5] and in capacitor discharge welding.[6] Mizukami *et al.* [7] investigated the casting of Type 304 stainless steel on copper chill, and found metastable fcc primary solidification to occur near the chill surface. The prevalence of fcc solidification in chill casting and substrate quenching was also reported in Fe-Ni alloys.[8,9]

In the case of laser and electron beam welding, it is obvious that the phase selection is controlled by growth, since nucleation is not required. Vitek *et al.*[1] considered that metastable fcc growth resulted from larger undercoolings at high growth rates. Bobadilla *et al.*[4] attempted to explain the preferential fcc solidification by the use of the KGT (Kurz-Giovanola-Trivedi[10]) model, a dendrite growth model for constrained growth. The tip temperature of an fcc dendrite was calculated to be higher than that of a bcc dendrite at the higher

growth rate even in a primary bcc alloy composition. They therefore concluded that fcc growth is dominant over bcc growth in the presence of a positive temperature gradient ahead of the growing dendrites. However, the mechanism of fcc growth is still controversial.[11]

The case of chill casting is different from that of welding in that nucleation is required, and so some degree of undercooling can be anticipated before solidification begins. Mizukami *et al.*[7] measured the melt temperature of a chill cast stainless steel by embedding a photo-diode at the chill surface, and found that the melt was substantially undercooled at the chill interface prior to solidification. Numerical analyses also demonstrated the existence of undercooling ahead of the advancing solidification front during chill casting, assuming planar growth.[12-14] In such cases, the temperature gradient is negative from the advancing front to the undercooled liquid, whereas it is positive in the solid toward the chill.

The mechanism of phase selection in chill casting is still unclear. There is a nucleation barrier at the chill interface, which leads to undercooling at the chill prior to solidification. Once solidification starts, growth proceeds into undercooled melt. In this respect, chill casting is similar to gas-cooled solidification by the levitation technique described in the previous chapters. Conditions unique to chill casting are the presence of the chill/metal interface which may act as a preferred nucleation site, and the presence of heat flow through the solid to the chill. Therefore, one or both of these two factors may cause different phase selection in chill casting from that in gas-cooled solidification. However, few investigations have been conducted on the phase selection behavior of Fe-Cr-Ni alloys during chill casting.

In this chapter, rapid solidification of two Fe-Cr-Ni alloys via chill casting is investigated. Upon equilibrium solidification, one of the alloys used is primary fcc, and the other is primary bcc. The phase selection of these alloys in chill casting is presented, and

compared with those in gas-cooled solidification by a levitation technique. Effects of nucleation and growth on phase selection in chill casting are discussed.

2. Experimental

Two Fe-Cr-Ni alloys were used: Fe-17.5Cr-12.2Ni (alloy A) and Fe-18.5Cr-11.3Ni (alloy B). The locations of both alloy compositions are indicated on the pseudo-binary phase diagram of the Fe-Cr-Ni system at 70 wt pct Fe shown in Figure 1, where the diagram was calculated using Thermo Calc[15]. Alloy A is primary fcc on equilibrium solidification and alloy B primary bcc as seen in the figure; this was also verified by zone melting. The purity of these ternary alloys is more than 99.95 wt pct; impurities are carbon, silicon, manganese, nitrogen, and oxygen, and the concentration of each impurity is less than 0.01 wt pct. The preparation of these alloys was described in the previous chapter.

Figure 2 shows a schematic diagram of the apparatus for the levitation experiment. An alloy sample of mass 0.5 g (±0.05g) was electro-magnetically levitated and induction-melted in an atmosphere of argon and 4% hydrogen. Then the melt was cooled by flowing high-purity helium. During the cooling, the melt sample was dropped onto a solid chill substrate or quenched into an In-Ga liquid metal chill bath at an appropriate undercooling level before nucleation.

Solid chill substrates were made from various materials: copper, fully ferritic stainless steel (AISI 444, Fe-19Cr-2Mo), fully austenitic stainless steel (AISI 310, Fe-25Cr-20Ni), pure alumina (Al_2O_3) and pure zirconia (Zr_2O_3). The volume ratio of a chill substrate to an alloy sample was approximately 12:1. The surface of the chill substrate was polished with a 600-grit SiC paper, and the chill was placed 50 mm below the levitated sample.

During levitation, the thermal history was measured by using high-speed pyrometry, as described in previous chapters. In chill casting, the temperature measurement was valid until the sample started to fall, but the sample must have been further undercooled during the fall and after reaching the chill. The increase in undercooling during the fall was estimated from the cooling rate before the fall and the time necessary for the free fall to the chill surface. This undercooling increase was approximately 10 K, and was added to the undercooling measured before the fall; therefore, undercooling values reported in this chapter are the sum of these two undercoolings. However, because of an additional increase in undercooling after the sample impacts upon the chill, the final undercooling prior to nucleation was not determined. The undercooling measurement during levitation was useful to assure a minimum undercooling of the melt droplet before casting. In addition, a CCD camera capable of 60 frames per second was used during each experiment to verify that nucleation did not occur during the fall.

Table 1 lists the number of samples cast on each chill successfully (i.e., without nucleation during the fall), and the undercoolings of those samples. Chill casting using copper and In-Ga liquid metal bath were extensively conducted, and various undercooling levels were attained, up to approximately 100 K. For other chill materials, a few samples were made for each. For a given undercooling and chill material, some variation in structure was obtained from sample to sample, apparently depending on metal/chill contact (and hence heat transfer coefficient). Results described in the following section represent results typical of each of the methods of solidification, and illustrate the trends observed. The effect of undercooling prior to casting on structure was not as clear as the effect of chill material. Using the copper chill, samples were chill cast from different undercooling levels, but the change in microstructure was not consistent with increasing undercooling prior to casting. Therefore, in this chapter, the effect of chill material is

mainly described using samples which were similarly undercooled prior to chill casting.

Optical microscopy was used to observe the microstructures. Samples were cut perpendicular to the chill surface, and regions near the chill interface on the cross-section were closely examined. The microstructure was revealed by electrolytic etching in an aqueous solution of 10 vol pct sulfuric acid at 4 V for 5 to 10 s. Concentration distributions of Cr and Ni were measured using computer-aided microprobe analysis (CMA)[16]. Two-dimensional profiles were obtained by step-scanning over the area of interest on the as-polished cross-section of a sample. Operating conditions of the CMA were: an acceleration voltage of 15 kV, a beam current of 1 μA, a beam size (also the distance of each step scan) of 1 μm, and a beam irradiation time of 20 ms per point.

3. Results

3.1 Solidification of Alloy A

Figure 3(a) shows the microstructure of a sample which was undercooled by 51 K and then solidified while levitated (gas-cooled solidification). In this solidification process, the primary phase to solidify from the undercooled melt is metastable bcc. The equilibrium solidification mode of alloy A is primary fcc followed by eutectic bcc plus fcc formation in interdendritic regions (AF mode). In the microstructure of the levitated sample, bcc (dark) is located at dendrite cores and has a skeletal morphology indicating primary bcc solidification. Also, as shown in Chapter III, the primary bcc was confirmed by the solute distribution in a mushy zone and by secondary recalescence for fcc formation. The metastable bcc solidification was obtained for undercoolings greater than 20 K.

When a levitated droplet of alloy A was undercooled and then chill cast before recalescence, a different structure resulted. Figures 3(b), 3(c) and 3(d) show structures of samples cast onto chill substrates of copper, ferritic stainless steel, and alumina, respectively. The micrographs near the chill show a clear contrast to the gas-cooled solidification sample. Fcc grows from the chill; primary fcc solidification is evident throughout the sample for all chills used. However, close examination reveals that tiny bcc dendrites appear sparsely at the interface; some are seen as separate dendrites and others as clusters of cells as shown in Figure 4. They are certainly dissimilar to the surrounding matrix, and some of them exhibit Ni depletion in the measurement of solute distribution as an indication of bcc solidification. These bcc dendrites cease to grow within twenty microns of the interface. They are longer and more numerous in the samples cast against the alumina and stainless steel chills and less in the samples cast against the copper chill. In the vicinity of the chill, some fully fcc regions without any eutectic bcc are observed; in this region of some samples, there is a layer right at the chill which seems to be non-dendritic or featureless as shown in Figure 5. Beyond this zone, solidification becomes dendritic, and the structures change gradually from fully fcc to fcc with interdendritic eutectic bcc. Casting on the austenitic stainless steel chill resulted in a similar structure to that obtained using a ferritic stainless steel chill, while casting on zirconia resulted in a structure similar to that obtained with an alumina chill.

3.2 Solidification of Alloy B

Figure 6(a) shows the solidification structure of alloy B obtained by gas-cooled solidification with an initial undercooling of 60 K. In this solidification process, the primary phase is bcc; the equilibrium primary phase is favored even in an undercooled condition. The microstructure is similar to that in Figure 3(a), showing skeletal bcc (dark) at dendrite cores. The primary bcc was stable at all undercooling levels investigated (up to 190 K).

Figures 6(b), 6(c) and 6(d) are chill cast structures; samples were undercooled by levitation and then cast against a copper, ferritic stainless steel, and alumina chills, respectively. In contrast to gas-cooled solidification, metastable fcc solidification is extensively observed in the vicinity of the chill for all chill materials used. Fcc dendrites (bright) are found to grow from the chill surface for some distance; beyond these, dendrites of primary bcc (dark) are formed in an equiaxed manner. The region of metastable fcc is a few hundred microns for the copper chill, and less for other chills. Formation of bcc dendrites at the chill surface is more distinct than in the case of alloy A; they are seen between fcc dendrites at the copper and ferritic stainless chills. In some parts of the sample surface cast against the alumina chill (normally, at the center of the chilled face), growth is first of bcc, then changes to fcc solidification, and finally back to bcc solidification again. The bcc-fcc-bcc sandwich structure is seen in Figure 6(d).

3.3 Solute Profiles in Samples cast on Solid Chills

Figure 7 shows the distributions of Cr and Ni in an alloy A sample cast on a copper chill. The partition of both Cr and Ni are not significant up to approximately 100 μm from the chill surface, and become more noticeable beyond this zone. Beyond 100 μm, both Cr and Ni are generally depleted at dendrite cores, the degree of partitioning being greater for Cr. Some dendrites reveal the enrichment of both solutes at the center of the solute-depleted dendrites; the solute-rich cores are also visible in cast structures of both alloy A and B as shown in Figure 8. As discussed in the previous chapter, the solute-rich cores result from the rapid solidification of primary fcc with accompanying non-equilibrium solute partition ratios.

Figure 9 shows the distributions of Cr and Ni in the chill cast structure of alloy B; the sample was cast onto a copper chill. The region of primary metastable fcc is clearly identified in the profile of Ni; the partitioning of Ni in this region is insignificant. On the other

hand, the partitioning of Cr is also insignificant up to about 50 μm from the chill, but beyond that, dendrites in this region are depleted in Cr, which is typical of fcc solidification[17,18]. Solute-rich cores are observed in the fcc dendrites in the microstructure, as shown in Figure 8(b), but corresponding solute enrichment is not clearly identified in the profiles shown. Within the region of the primary bcc solidification, dendrites are enriched in Cr and depleted in Ni; the concentration of Ni is increased in interdendritic regions. The profiles in this region are typical of conventional primary bcc solidification (FA mode)[18,19].

3.4 Structures of Samples Quenched in the Liquid In-Ga Chill Bath

Figure 10 shows microstructures of alloys A and B which were quenched into the In-Ga liquid bath from the undercooled liquid state. The cooling rate, i.e., the rate of heat extraction, is much higher than that attained in chill casting processes. Figure 10(a), which is for alloy A with an initial undercooling of 27 K, reveals a fully fcc structure consisting of very fine cells. No trace of ferrite growth can be identified at the surface, and even the cellular structure of fcc is unclear up to 30 μm from the surface; this region probably results from either planar growth or partitionless growth. Figure 10(b), which is of alloy B with an initial undercooling of 28 K, shows a fully fcc region about 100 μm from the surface. Similar to Figure 10(a), no trace of ferrite growth is visible at the surface. The growth morphology of fcc is fine cellular, but this becomes unclear in the vicinity of the surface. Coarse bcc dendrites were found to originate between fcc cells and then grow inward. It is interesting to note that the coarse bcc dendrites have well-developed branches in contrast to fine fcc cells at their roots.

When the initial melt undercooling was larger (i.e., approximately 100 K) prior to quenching into an In-Ga liquid bath, a region of bcc dendrites and a region of fcc dendrites were both found in one specimen. This was observed in both alloy A and alloy B, as shown in Figures 11(a) and 11(b), respectively. Each region is clearly

defined; the dark region is for bcc dendrites and the bright region for fcc dendrites. High magnification micrographs of each region is shown in Figures 11(c) and 11(d). Bcc dendrites have very well-developed fine branches (Figure 11(c)), and they do not seem to be either thickened or ripened significantly. In contrast, fcc dendrites look cellular-dendritic where side branches are limited or coarsened already (Figure 11(d)). These structural features are observed in both alloy A and alloy B. It is interesting to note that both macro- and microscopically similar structures were obtained in the two alloys which have different equilibrium primary phases. The evolution processes of the structures are not clear; it is possible that both phases form concurrently or one forms epitaxially on the other phase. Micrographs of the boundary between the two regions are shown in Figure 12. Fcc dendrites are aligned in a certain direction, and macroscopically bcc dendrites also seem to be aligned, displaying columnar patterns (Figure 12(a)). The boundary, on the other hand, seems to be rough, and does not show any particular relationship between the two phases.

4. Discussion

Table 2 summarizes the phase selection behavior of alloy A and alloy B. The equilibrium primary phases of alloy A and alloy B are fcc and bcc, respectively. In gas-cooled solidification, the primary phase of alloy A was bcc for initial undercoolings greater than 20 K, while the primary phase of alloy B was always bcc regardless of undercooling. On the other hand, chill casting of alloy A from the undercooled liquid produced an fcc structure, and chill casting of alloy B produced a predominantly fcc structure near the chill and bcc in the rest of the sample.

The dominance of fcc solidification in chill casting is obvious in both alloys, which is in contrast to the dominant bcc solidification in the case of gas-cooled solidification. Alloys cast against solid chills

contained small amounts of tiny bcc dendrites at the chill. This indicates that bcc exists concurrently with fcc at the nucleation stage and during the early stages of growth. Then, after growth competition, fcc dominates the growth behavior.

The heat extractive capacity of the chill material appears to play a role in phase selection. There is no indication from these results that the crystal structure of the chill material affects epitaxial selection. Preferential fcc solidification was consistently observed in both alloy A and B at the chill regardless of the crystal structure of the solid chill material. The thickness of the metastable fcc region in chill cast alloy B was greater for the copper chill than for stainless steel or alumina chills, and the amount of retained tiny bcc dendrites was less at the copper chill. Bcc dendrites were observed in samples cast against the fcc stainless steel chill as well as against the bcc stainless steel chill. No trace of bcc growth was observed at the surface of samples cast in the In-Ga liquid chill, but bcc nuclei or small bcc dendrites may have been present in sections not observed. The results obtained herein are fully consistent with the conclusion that it is the heat extraction capacity of the chill materials that determines the structural difference observed.

The rate of heat extraction from the growth front by the chill decreases with time after the melt impacts upon the chill substrate.[20,21] Therefore, the influence of high heat extraction rate is most significant for the nucleation and the initial stages of growth. This is the unique feature of chill casting in determining the phase selection as compared with gas-cooled solidification. The nucleation of bcc and fcc can be made more nearly simultaneous due to rapid cooling in chill casting, even though the nucleation of bcc is preferred from the undercooled melts of both alloys. High heat extraction rates probably change the contributions of thermal and kinetic effects on the growth, and as a result, may enable fcc to grow selectively. The mechanism of phase selection during chill casting is to be discussed further in a different chapter.

When fcc grows selectively from the chill, the growth morphology is sometimes unclear. For example, a region up to 20 μm from the chill interface seems featureless, as shown in Figure 5. Another example is shown in Figure 13, where a sample of alloy A was cast onto a copper chill from the slightly undercooled liquid state ($\Delta T \approx 7$ K). The structure seems featureless up to a few tens of microns from the chill, then changes to fine cells as it goes inward, and finally changes to dendrites with bcc in the interdendritic regions. These changes are apparently caused by the decreasing rate of heat extraction from the growth front as the increasing distance from the chill. On the other hand, even directly at the chill, "featureless" regions of bcc have not been observed. Bcc is observed to have well-developed dendrites with branches even at the chill, as shown in Figure 4(a).

Another typical contrast between fcc and bcc can be seen in Figure 10(b). While fcc has a cellular morphology, bcc has a dendrite morphology in the same region. The tendency is consistent in Figure 11(c) and Figure 11(d). Bcc dendrites exhibit well-developed side branches, while fcc dendrites are cellular-dendritic. These clear morphology differences were not observed even when both phases coexisted during gas-cooled solidification.

5. Conclusions

Phase selection in the chill casting of two Fe-Cr-Ni alloys was investigated: one is primary fcc (alloy A: Fe-17.5Cr-12.2Ni) and the other is primary bcc (alloy B: Fe-18.5Cr-11.3Ni). Undercooled melt samples were cast onto different chills such as copper, stainless steels, and ceramics, or into a liquid metal chill, and the phase selection results were compared with those obtained during gas-cooled solidification of the same alloys. The conclusions obtained in the present study are:

(1) In chill casting, the dominant phase to solidify is fcc throughout the sample in alloy A, and metastable fcc near the chill in alloy B. The phase selection is in contrast to the preferential bcc solidification observed in gas-cooled solidification of both alloys.

(2) Preferential fcc solidification is found in all chilled samples. In alloy B, the region of metastable fcc growth tends to be greatest in samples cast in the liquid metal and against the copper chill, and least at the ceramic chills. Small dispersed bcc dendrites are observed in samples cast against all of the solid chills, suggesting nearly concurrent nucleation of bcc and fcc. The length and amount of these bcc dendrites are least at the copper chill and largest at the ceramic chills. No retained bcc dendrites were observed in samples quenched into In-Ga liquid, but they may exist in small quantities. Preferential fcc solidification and its priority are not affected by the crystal structure of the chill material, but by the heat extraction rate produced by the chill. Based on these results it is concluded that both fcc and bcc nuclei exist on chill casting in quenched samples but that fcc growth is favored over bcc by heat extraction of the chill material.

(3) Growth morphology of fcc is likely to be fine cellular or sometimes featureless in the vicinity of the chill, while bcc tends to exhibit a well-developed dendritic morphology. Solute partitioning is insignificant for both Cr and Ni near the chill surface.

References

1. J. M. Vitek, A. Dasgupta, and S. A. David: *Metall. Trans. A*, 1983, vol. 14A, p. 1833
2. S. A. David, J. M. Vitek, and T. L. Hebble: *Weld. J.*, 1987, vol. 66, p. 289s
3. J. W. Elmer, S. M. Allen, and T. W. Eagar: *Metall. Trans. A*, 1989, vol. 20A, p. 2117

4. M. Bobadilla, J. Lacaze, and G. Lesoult: *J. Cryst. Growth*, 1988, vol. 89, p. 531
5. Y. Nakao, K. Nishimoto, and W.-P. Zhang: *Proc. 4th Int'l. Colloq. on Welding and Melting by Electron and Laser Beams*, eds. M. Contré and M. Kuncevic, French Inst. of Welding, 1988, p. 673
6. S. Venkataraman and J. H. Devletian: *Weld. J.*, 1988, vol. 67, p. 111s
7. H. Mizukami, T. Suzuki, and T. Umeda: *Tetsu-to-Hagane*, 1991, vol. 77, p. 134
8. T. Z. Kattamis, W. F. Brower, and R. Mehrabian: *J. Cryst. Growth*, 1973, vol. 19, p.229
9. C. Hayzelden, J. J. Rayment, and B. Cantor: *Acta metall.*, 1983, vol. 31, p. 379
10. W. Kurz, B. Giovanola and R. Trivedi: *Acta metall.*, 1986, vol. 34, p. 823
11. J. M. Vitek and S. A. David: to be published
12. T. W. Clyne: *Metall. Trans. B*, 1984, vol. 15B, p. 369
13. G.-X. Wang and E. F. Matthys: *Int'l J. Rapid Solidification*, 1991, vol. 6, p.297
14. X. Zhang and A. Atrens: *JOM*, 1994, vol. 46(1), p. 48
15. B. Sundman, B. Jansson, and J.-O. Andersson: *CALPHAD*, 1985, vol. 9, p. 153
16. I. Taguchi and H. Hamada: *Analytical Sci.*, 1985, vol. 1, p. 119
17. J. A. Brooks, J. C. Williams, and A. W. Thompson: *Metall. Trans. A*, 1983, vol. 14A, p. 23
18. T. Koseki, T. Matsumiya, W. Yamada, and T. Ogawa: To be published in *Metall. Trans. A*
19. J. A. Brooks, J. C. Williams, and A. W. Thompson: *Metall. Trans.* A, 1983, vol. 14A, p. 1271
20. K. Takeshita and P. H. Shingu: *Trans. Japan Inst. Metals*, 1986, vol. 27, p. 454
21. H. Mühlbach, G. Stephani, R. Sellger, and H. Fiedler: *Int'l J. Rapid Solidification*, 1987, vol. 3, p. 83

Table 1: The number of samples cast against each chill and the undercoolings (ΔT) attained in those samples. Note that ΔT is the undercooling prior to casting which is the sum of the measured undercooling during levitation and the estimated undercooling during falling onto the chill. The sample must have been additionally undercooled after reaching the chill prior to nucleation.

Alloy	Chill	# of Samples made	Undercoolings (ΔT) prior to casting (K)
Alloy A	Copper	8	7, 30, 46, 50, 71, 74, 94, 102
	Ferritic S.S.	2	39, 50
	Austenitic S.S.	2	62, 65
	Alumina	2	64,74
	Zirconia	1	66
	In-Ga bath	5	0, 27, 50, 105, 110
Alloy B	Copper	8	3, 50, 50, 73, 75, 78, 81, 106
	Ferritic S.S.	3	37, 49, 53
	Austenitic S.S.	1	40
	Alumina	3	41, 58, 64
	Zirconia	4	67, 71, 87, 89
	In-Ga bath	3	28, 98, 100

Table 2 - Preferred Growth Structure of Two Fe-Cr-Ni Alloys

	Alloy A Fe-17.5Cr-12.2Ni	Alloy B Fe-18.5Cr-11.3Ni
Equilibrium	fcc	bcc
Free Levitation	bcc ($\Delta T \geq 20K$) mixed ($\Delta T < 20K$)	bcc
Chill Casting	fcc	fcc (near chill)

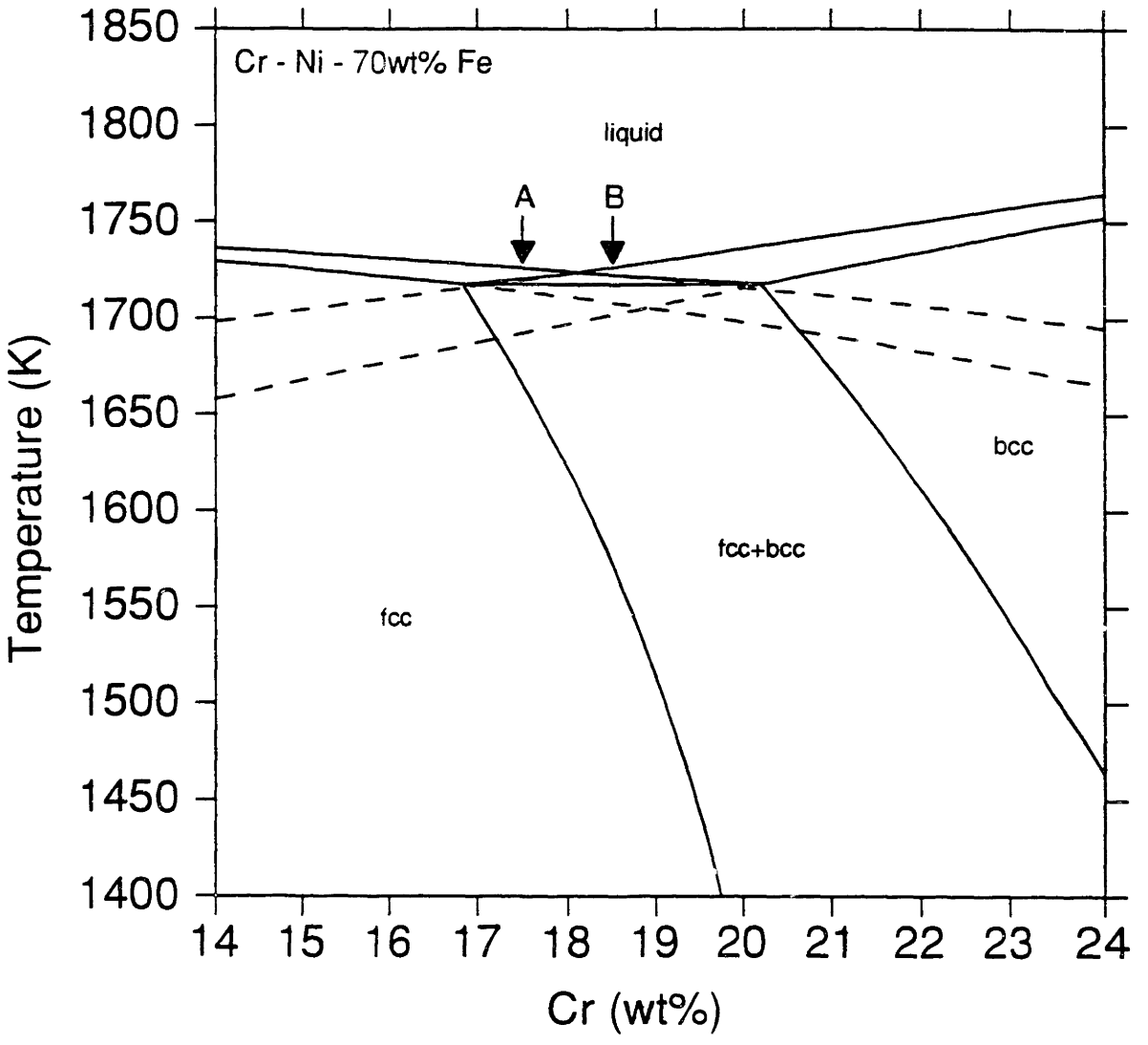

Figure 1 - Pseudo-binary phase diagram of the Fe-Cr-Ni alloy system at 70 wt pct Fe calculated using Thermo Calc[10]. The locations of the two alloy compositions, A and B, used in the present study are indicated in the figure.

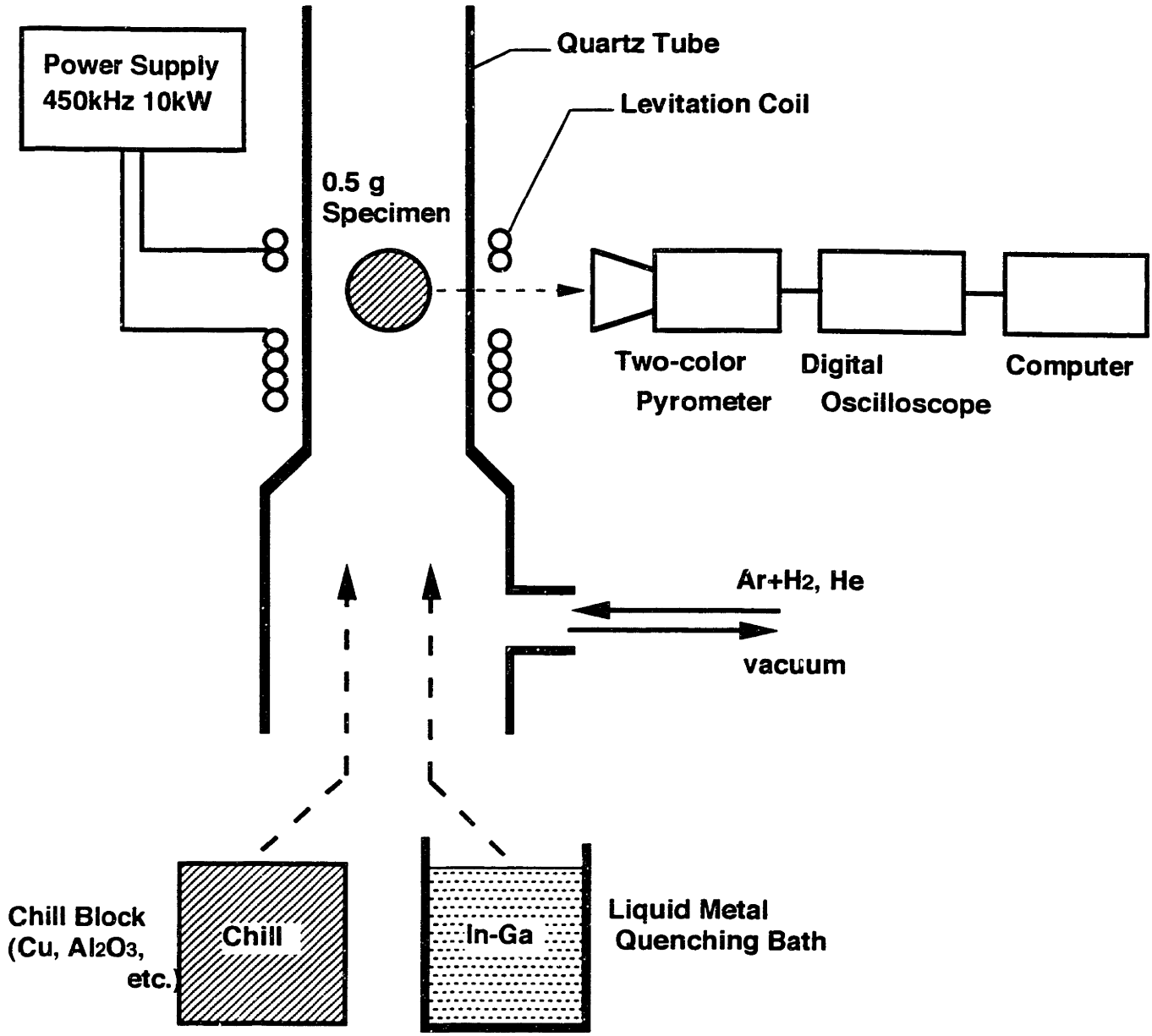

Figure 2 - Schematic diagram of apparatus for levitation melting. Undercooled melt samples were either solidified while levitated (gas-cooled solidification), or cast on a chill block made of various materials, or quenched into the liquid In-Ga bath.

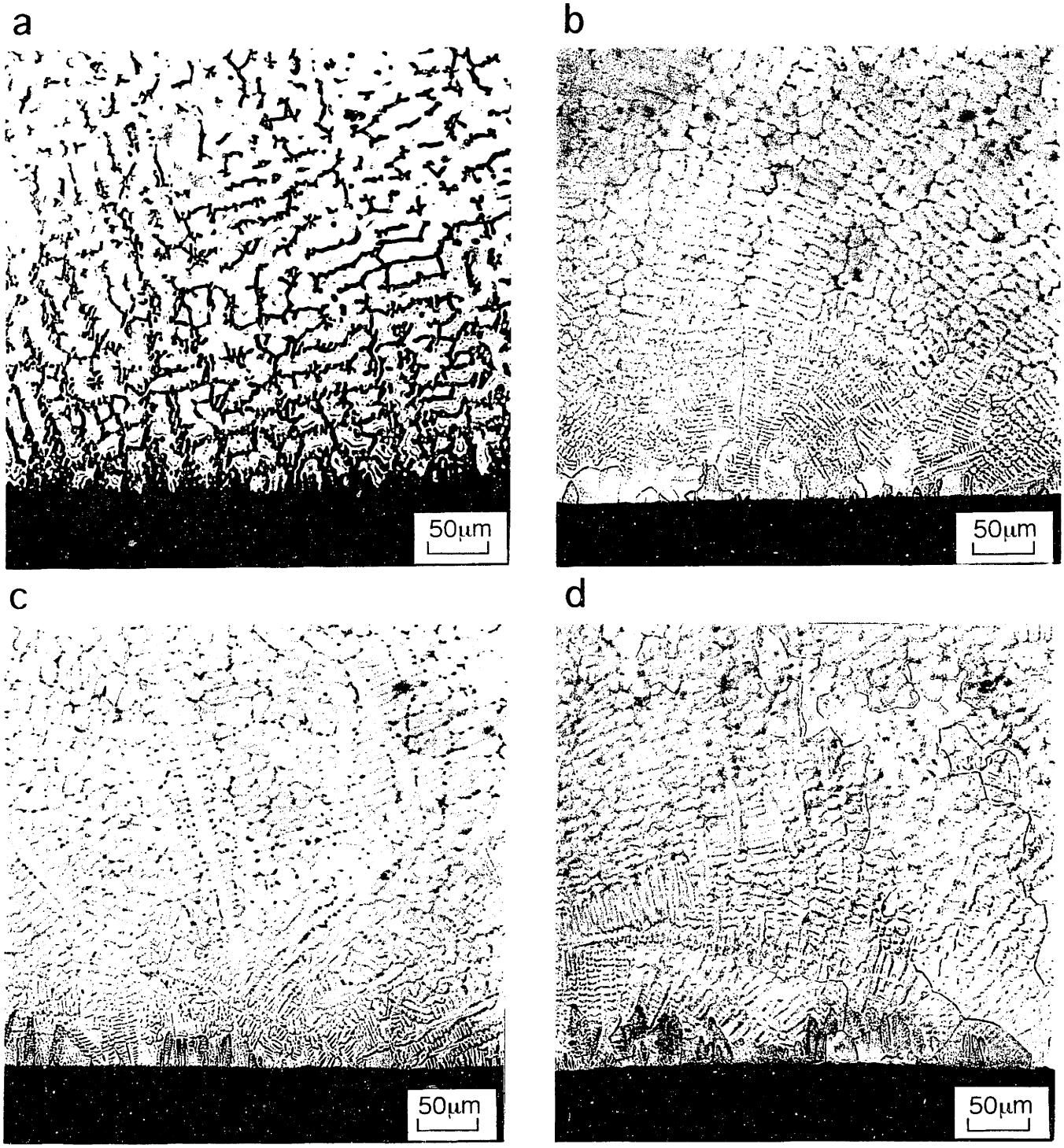

Figure 3 - Solidification structures of alloy A (Fe-17.5Cr-12.2Ni): (a) developed by gas-cooled solidification with an initial undercooling of 51 K, (b) chill cast onto a copper substrate (ΔT= 71 K), (c) chill cast onto a ferritic stainless steel substrate (ΔT= 39 K), and (d) chill cast onto an alumina substrate (ΔT= 64 K).

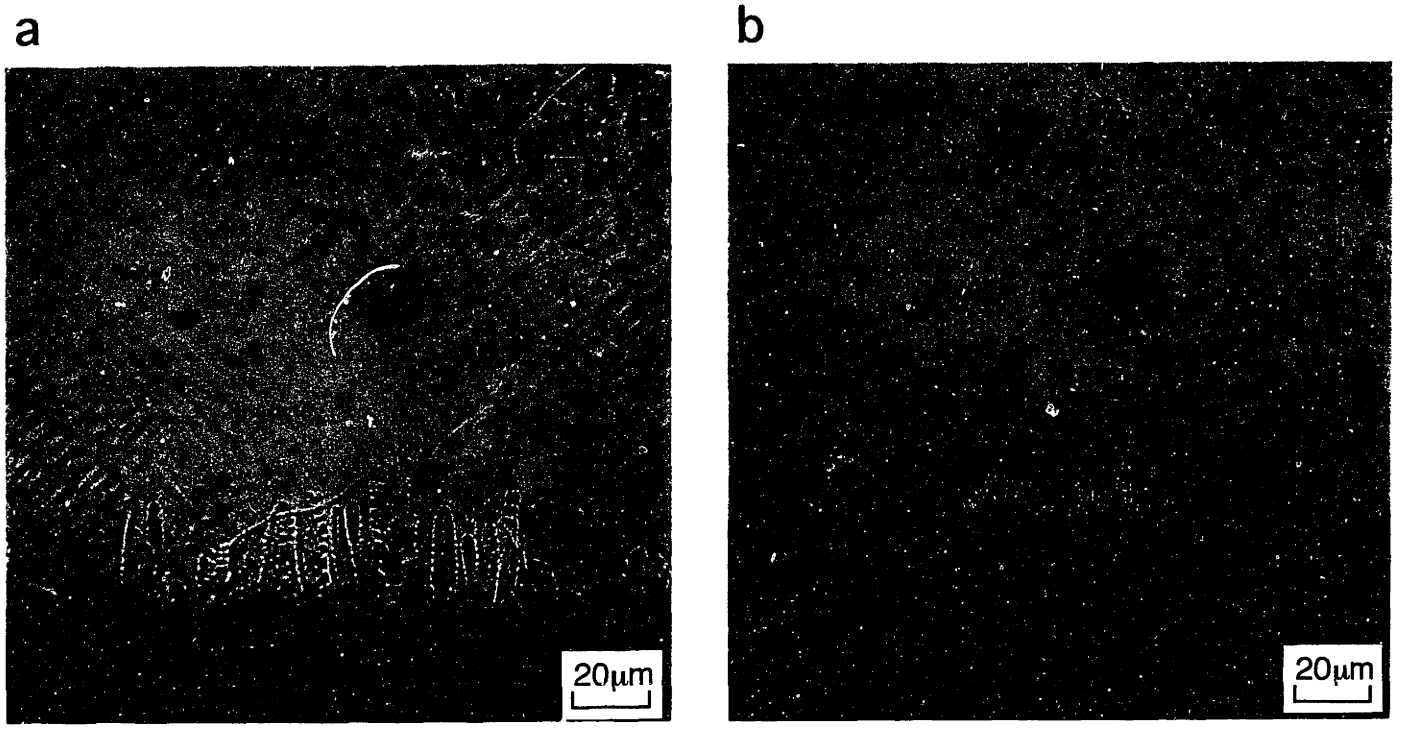

Figure 4 - Bcc dendrites observed at the chill surface in the cast structure of alloy A: (a) cast onto an alumina substrate ($\Delta T = 64$ K), and (b) cast onto a copper substrate ($\Delta T = 71$ K).

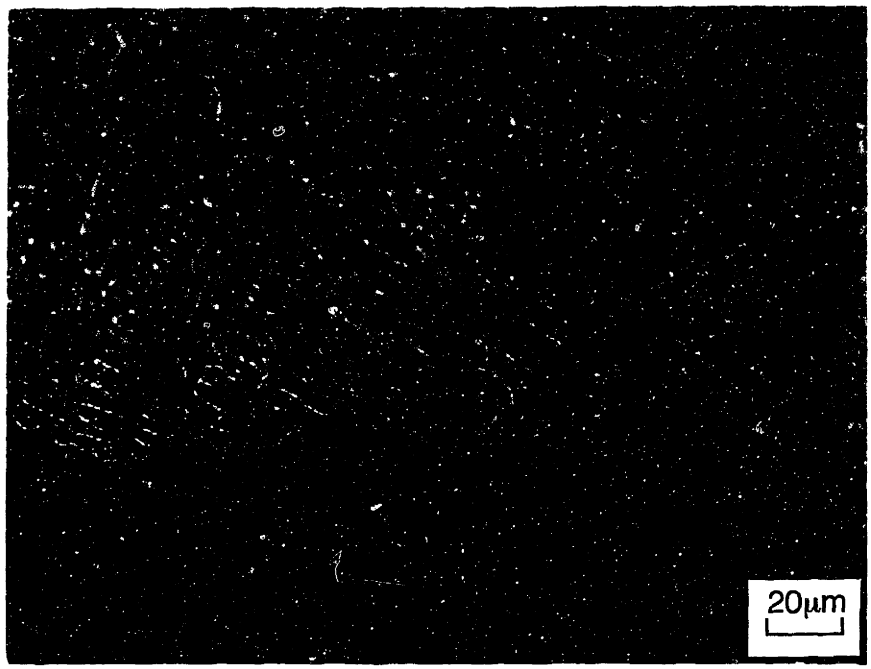

Figure 5 - Microstructure of alloy A cast onto copper chill (ΔT= 71 K). The sporadic thin layer of bcc dendrites is followed by a region which seems non-dendritic in 20 μm from the chill.

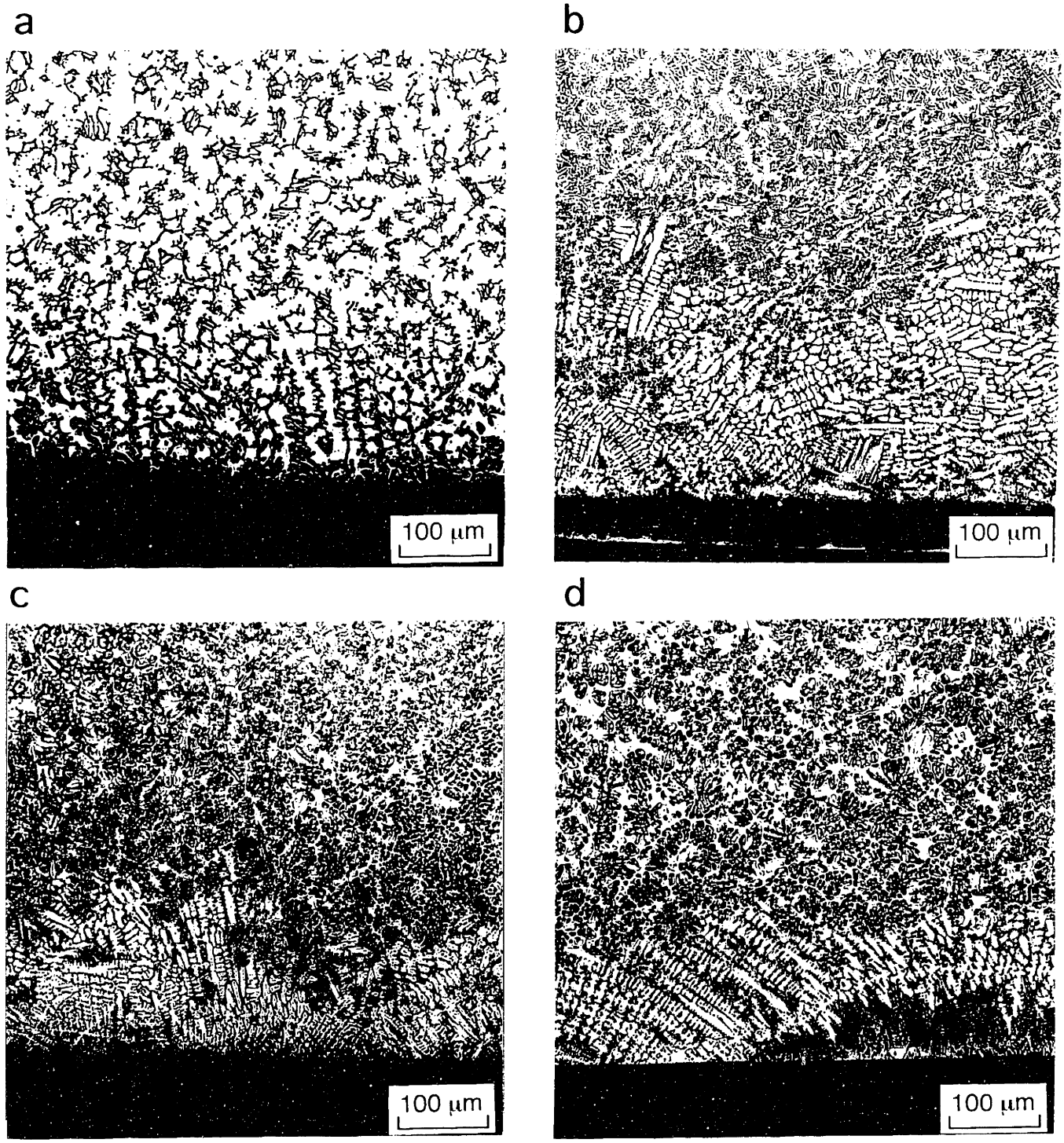

Figure 6 - Solidification structures of alloy B (Fe-18.5Cr-11.3Ni): (a) developed by gas-cooled solidification with an initial undercooling of 60 K, (b) chill cast onto a copper substrate (ΔT= 78K), (c) chill cast onto a ferritic stainless steel substrate (ΔT= 49 K), and (d) chill cast onto an alumina substrate (ΔT= 64 K).

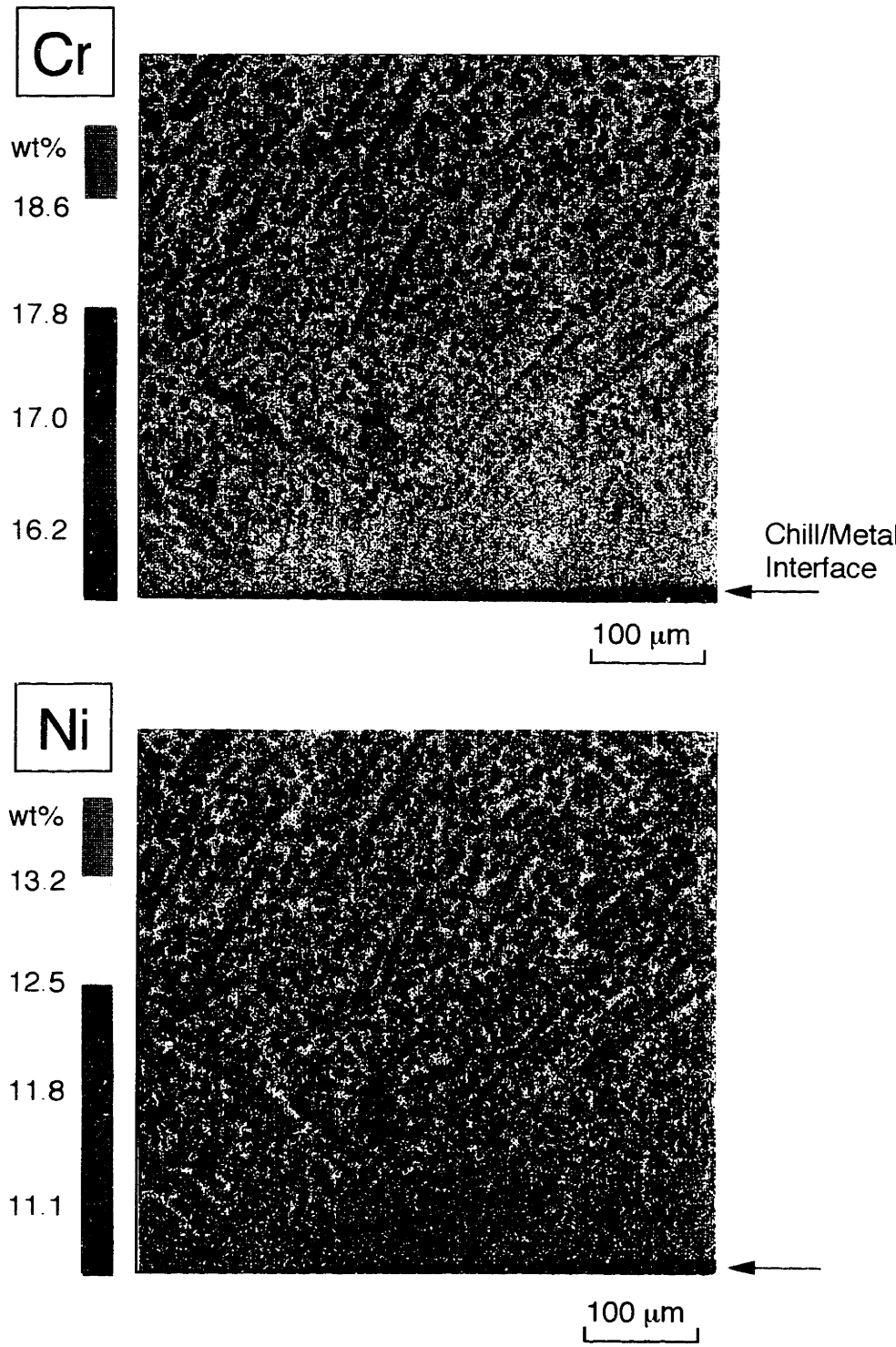

Figure 7 - Distributions of Cr and Ni in a solidification structure of alloy A cast onto copper chill (ΔT= 71 K).

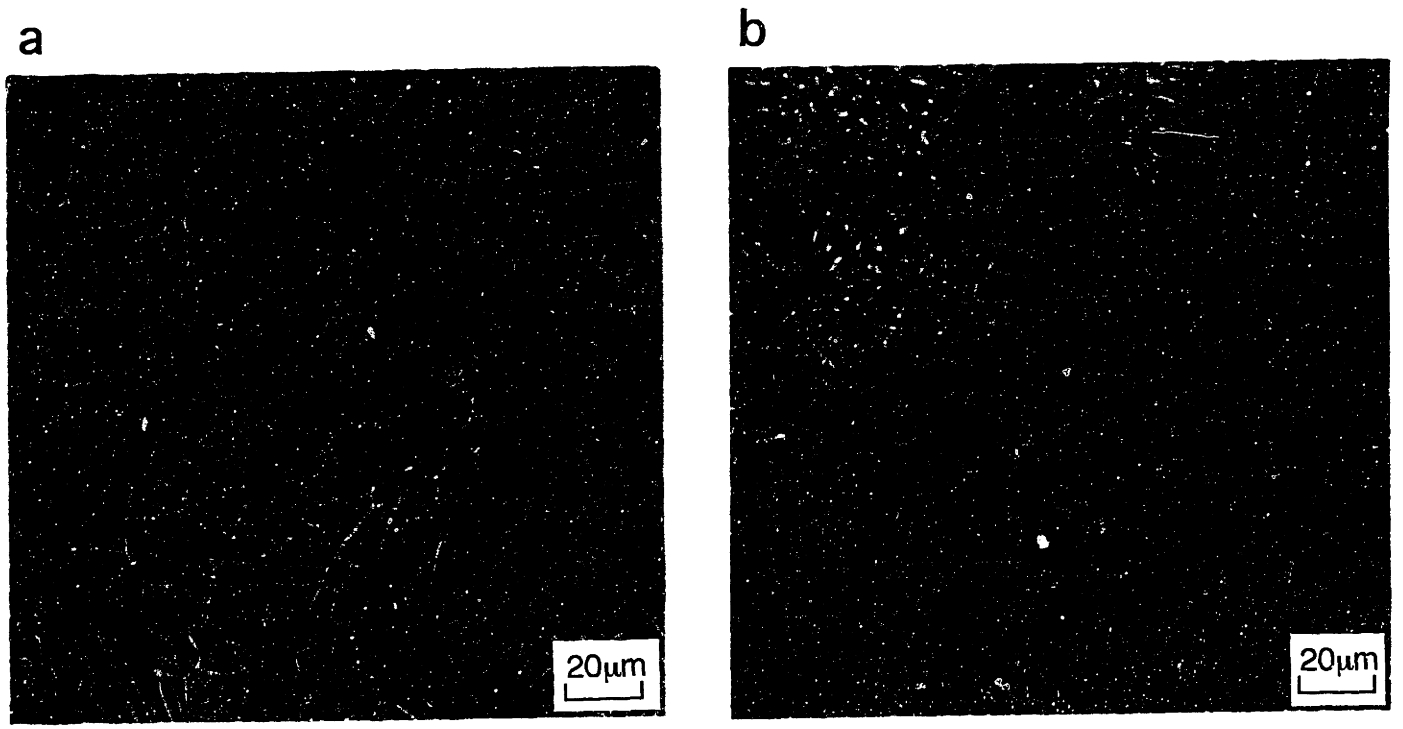

Figure 8 - Solute-rich cores seen in fcc dendrites in the form of crosses: (a) alloy A cast onto a copper chill (ΔT= 71 K), and (b) alloy B cast onto a copper chill (ΔT= 78 K).

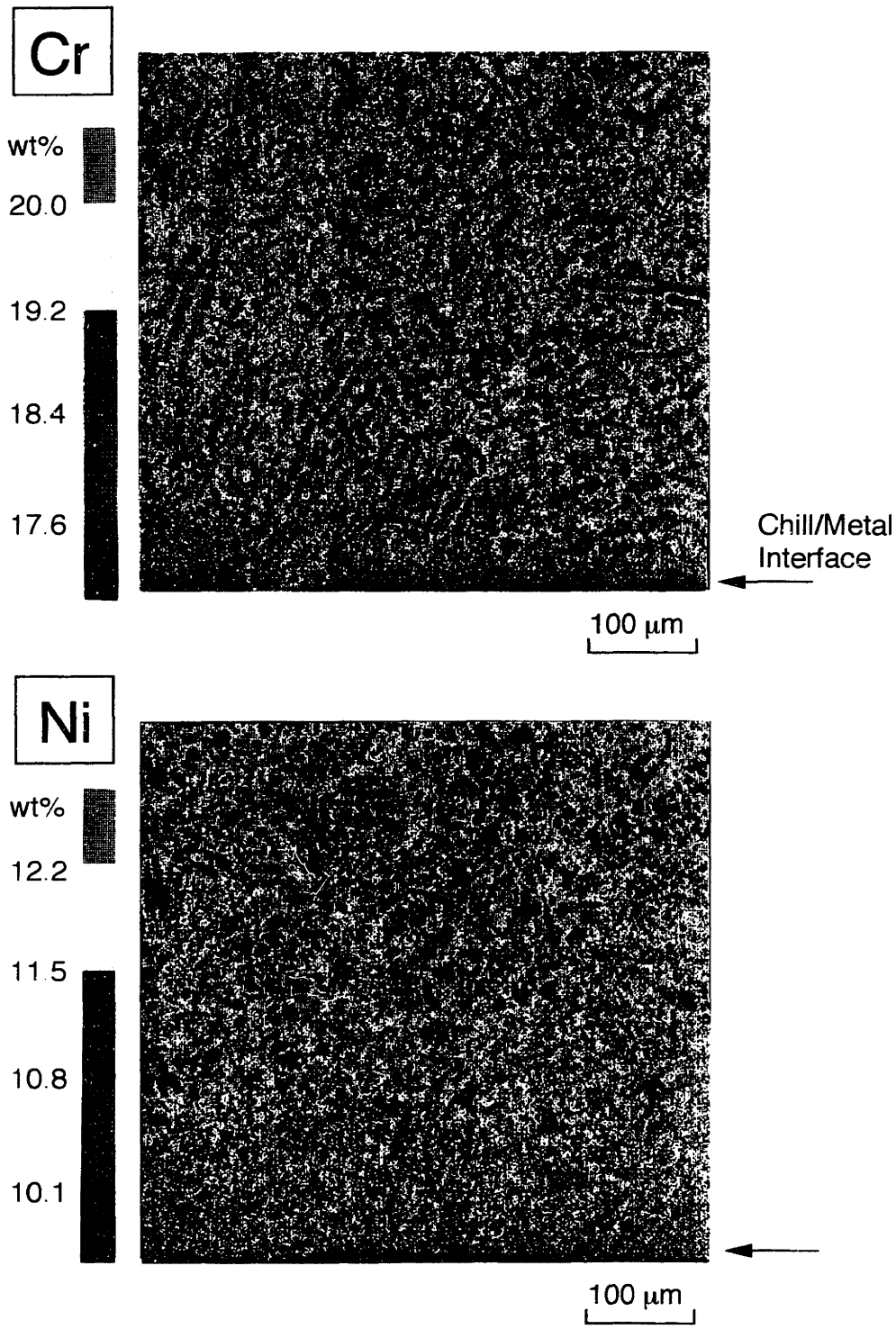

Figure 9 - Distributions of Cr and Ni in the solidification structure of alloy B cast onto a copper chill (ΔT= 78 K).

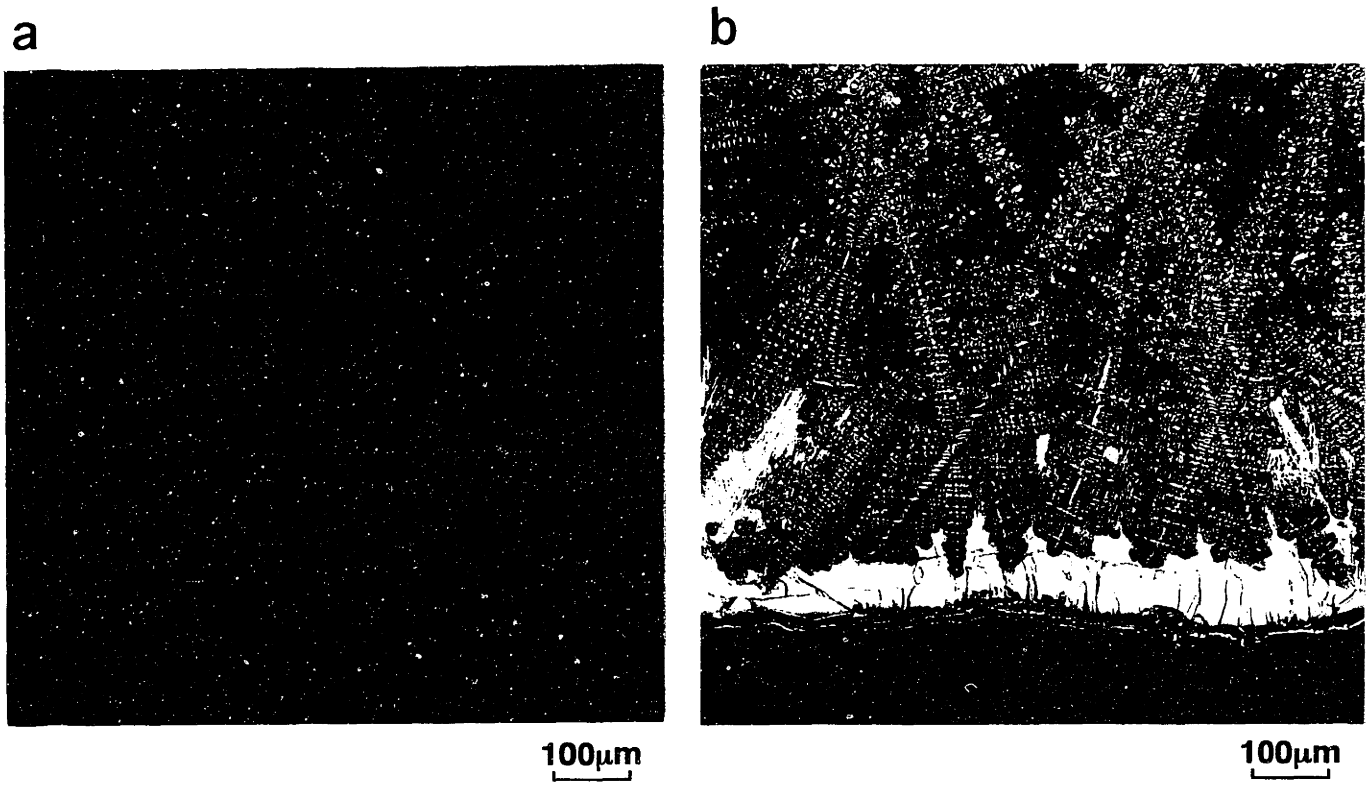

Figure 10 - Microstructure of specimens quenched into an In-Ga liquid bath from the undercooled liquid state: (a) alloy A (ΔT= 27 K), showing a fully fcc, fine cellular structure, and (b) alloy B (ΔT= 28 K), showing a fully fcc zone (bright) for about 100 μm from the surface, and an adjacent region of coarse bcc dendrites (dark).

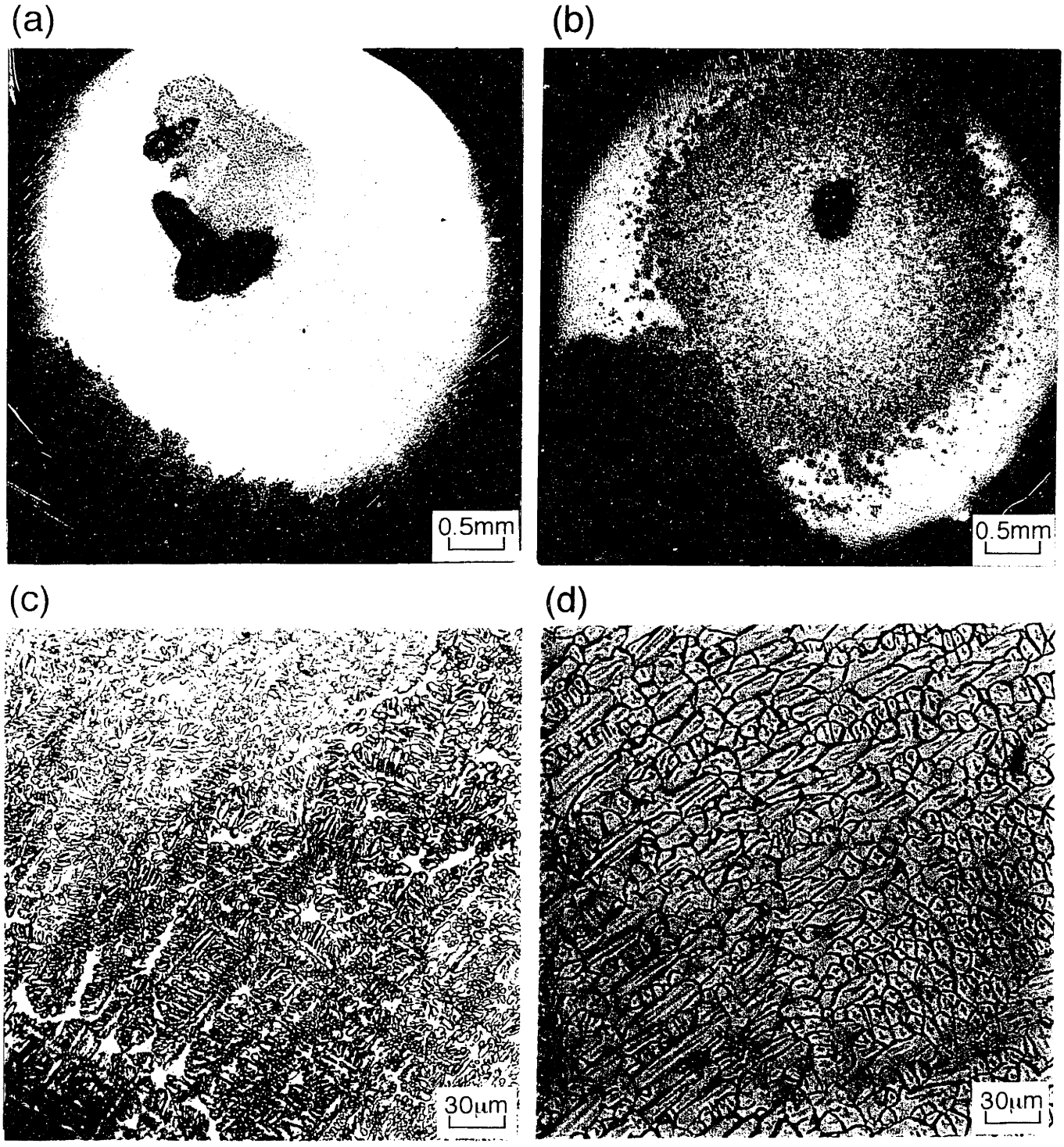

Figure 11 - Structures of samples quenched into an In-Ga chill bath from the undercooled liquid state: (a) alloy A, ΔT= 105 K, (b) alloy B, ΔT= 98 K, (c) a typical structure of the region of bcc dendrites (alloy A, ΔT= 105 K), and (d) a typical structure of the region of fcc dendrites (alloy A, ΔT= 105 K).

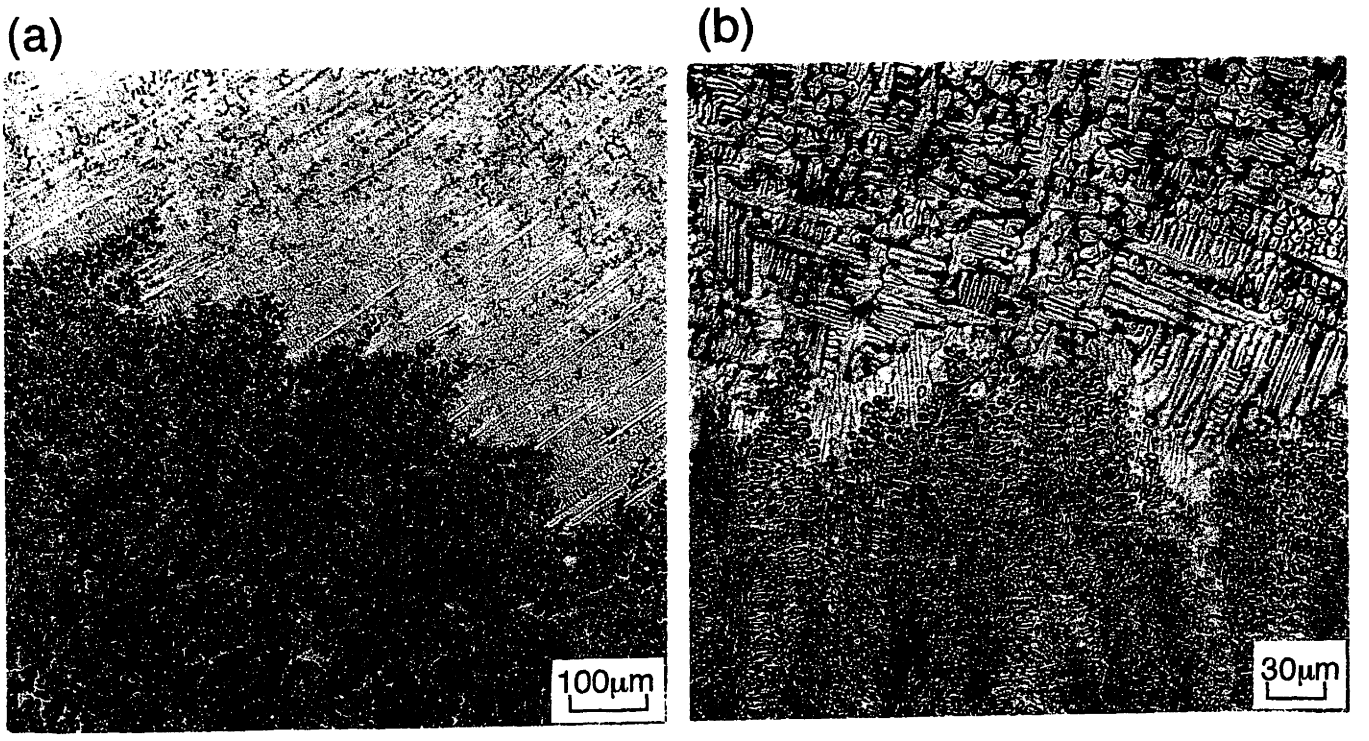

Figure 12 - Boundary structure between the regions of bcc dendrites and fcc dendrites: (a) at low magnification and (b) at high magnification.

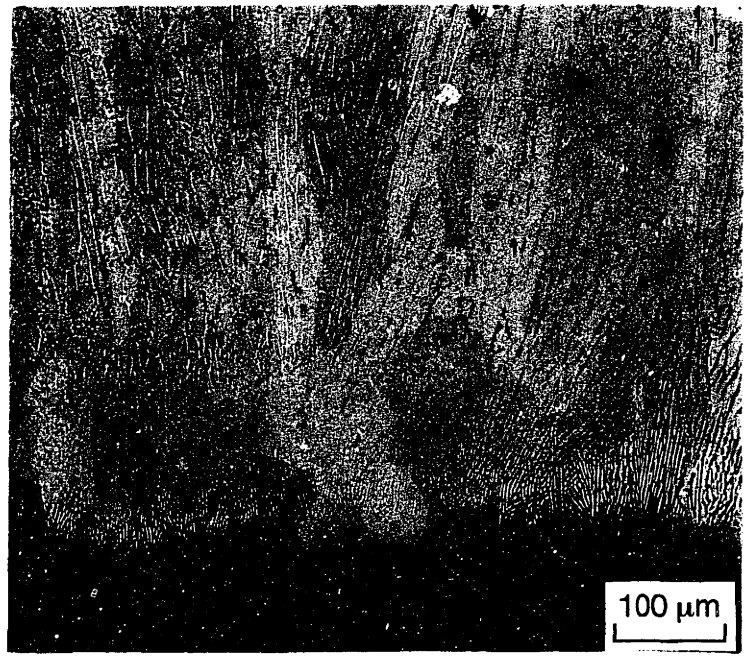

Figure 13 - Structure of an alloy A sample which cast onto a copper chill from the slightly undercooled liquid state ($\Delta T \approx 7K$).

Chapter V - Rapid Dendrite Growth during Chill Casting

Abstract

A dendrite growth model is derived for solidification during chill casting, based on existing models of dendrite growth and stability. The model involves the combined effects of the undercooled melt and the chill as effective heat sinks. The situation considered is commonly encountered in rapid solidification processes. The significance of the proposed dendrite model and the stability of dendrite growth in such situations are discussed.

1. Introduction

The important features of chill casting are the presence of high heat extraction rate by the chill and the presence of substantial undercooling in the liquid. This situation is common in solidification processes including strip casting, melt spinning, splat cooling, spray coating and so on. In these processes, very high heat transfer coefficients between the melt and the chill substrate, often more than 10^6 W $m^{-2}K^{-1}$, were estimated.[1-3] Therefore, high rates of heat extraction from the melt can be achieved by the chill. On the other hand, temperature measurements of melts at chill surfaces have indicated that the melt can be substantially undercooled prior to solidification, often more than 200 K.[4] Numerical analyses assuming planar growth have also demonstrated the existence of undercooling ahead of the advancing solidification front during chill casting.[5-7] Therefore, both chill substrate and undercooled melt can be effective sinks for the latent heat when crystallization occurs from a chill.

The dendrite is the most common morphology of solidification in the above rapid solidification processes. However, dendrite growth resulting from chill casting has not previously been modeled adequately. Dendrite growth models have been developed in two categories thus far. The LKT (Lipton-Kurz-Trivedi) model[8] and the BCT (Boettinger-Coriell-Trivedi) model[9] are both for free dendrite growth into the undercooled melt. They assume a negative temperature gradient in the liquid and no gradient in the solid. Thus, all the latent heat released at the interface is assumed to be removed by the undercooled melt, and adiabatic conditions are maintained overall. On the other hand, the KGT (Kurz-Giovanola-Trivedi) model[10] is for constrained growth, and assumes a positive temperature gradient in both the liquid and the solid. Thus, all the latent heat is assumed to be extracted by the solid, but the exact heat balance is not taken into account because of the constrained temperature gradient assumption. The thermal field in chill casting does not match any of the existing models, but is a hybrid of the above two categories. The dendrite tip will grow into the undercooled

melt, and heat evolution at the dendrite tip occurs both into the undercooled melt and through the growing solid towards the chill. Consequently, the temperature gradient is negative in the liquid and positive in the solid. A dendrite model which considers the combined effects of both temperature gradients needs to be developed based on the existing models.

In this chapter, a dendrite growth model for chill casting is derived using an approach analogous to that of the existing models[8-11]. Thermal balance and the stability of growth morphology are modeled taking into account the combined effects of the negative temperature gradient in the liquid and positive gradient in the solid. The effect of the external heat extraction rate and the stability of dendrite growth in the chill casting situation are discussed.

2. Model: Dendrite Growth with Heat Extraction

2.1 Dendrite Tip Undercooling in the Presence of Heat Extraction

A dendrite growth model for chill casting was developed based on the LKT[8] and BCT[9] models. Heat extraction from a growing dendrite tip through the solid has been incorporated. Therefore, terms related to thermal diffusion and the stability criterion were modified. Assumptions relevant to the present model are:

- an isolated dendrite growing into an undercooled melt
- steady-state growth with a constant velocity, V
- dendrite tip has the shape of a paraboloid of revolution
- isothermal solid/liquid interface
- diffusion controlled heat transfer in the liquid
- heat extraction from the tip along the growth direction into the solid with a constant rate of J (per unit area and unit time)

Other assumptions related to mass transport and various undercooling effects are identical to those of the above models. Schematics of the dendrite tip and corresponding temperature distribution are shown in Figure 1 (symbols in the figure are explained below).

The governing equation for the temperature field in the liquid is written as the following for a coordinate system moving at the velocity of V:

$$\nabla^2 T - \left(\frac{V}{\alpha_L}\right)\frac{\partial T}{\partial z} = 0 \qquad (1)$$

where T is the absolute temperature, V is a tip velocity, and α_L is the thermal diffusivity in the liquid. When the variables λ and r are defined as $\lambda = z + r$, and $r = \sqrt{x^2+y^2+z^2}$, then Eq. (1) can be rewritten as[12,13]

$$\frac{d^2T}{d\lambda^2} + \left(\frac{1}{\lambda} + \frac{V}{2\alpha_L}\right)\frac{dT}{d\lambda} = 0 \qquad (2)$$

Note that $\lambda = \rho$ represents the surface of the paraboloid of revolution,

$$z = \frac{\rho}{2} - \frac{(x^2+y^2)}{2\rho} \qquad (3)$$

The boundary condition at the solid/liquid interface is given by

$$-k_L\left(\frac{\partial T}{\partial n}\right)_{\lambda=\rho} = \Delta H_f \vec{V}\cdot\vec{n} + \vec{J}\cdot\vec{n} \qquad (4)$$

where k_L is the thermal conductivity of the liquid, ΔH_f is the latent heat of fusion per unit volume, $\vec{V}$ is a vector for the growth velocity (i.e., $|\vec{V}| = V$) directed to the positive z-axis, $\vec{J}$ is a vector for the heat extraction (i.e., $|\vec{J}| = J$) directed to the negative z-axis, and $\vec{n}$ is a unit vector normal to the solid/liquid surface and directed into the liquid. The second term of the right-hand side (RHS) in Eq. (4) is the heat

extraction effect in chill casting. Using the variable λ, Eq. (4) is rewritten as[12,14]

$$\left(\frac{\partial T}{\partial \lambda}\right)_{\lambda=\rho} = -\frac{1}{2k_L}(V\Delta H_f - J) \qquad (5)$$

Eqs. (2) and (5) yield

$$T_\rho - T_\infty = \frac{\Delta H_f}{C_{pL}} \frac{V\rho}{2\alpha_L} \exp(\frac{V\rho}{2\alpha_L}) E_1(\frac{V\rho}{2\alpha_L}) - \frac{J\rho}{2k_L} \exp(\frac{V\rho}{2\alpha_L}) E_1(\frac{V\rho}{2\alpha_L}) \qquad (6)$$

where T_ρ is the dendrite surface temperature, T_∞ is the melt temperature, C_{pL} is the specific heat of the liquid per unit volume, and $E_1(u)$ is the exponential integral function defined by

$$E_1(u) = \int_u^\infty \frac{e^{-u}}{u} du \qquad (7)$$

Letting R and T_{tip} be the dendrite tip radius (=ρ) and tip temperature (=T_ρ), respectively, and using the thermal Péclet number P_t (=$VR/2\alpha_L$) and the Ivantsov function, $I_v(P)= P \exp(P) E_1(P)$,[13] Eq. (6) is finally written in the form of a thermal undercooling at the tip:

$$T_{tip} - T_\infty = \frac{1}{C_{pL}}(\Delta H_f - \frac{J}{V}) I_v(P_t) \qquad (8)$$

The solution (Eq. (8)) is intuitively understandable as compared with the existing expression of the thermal undercooling[8,9,11]. That is, in the presence of external heat extraction, the heat (ΔH_f) which is generated at the tip and expected to diffuse into the undercooled melt is reduced by the heat extraction, J/V.

2.2 Stability of Dendritic Growth

The transport analysis can only specify a product of V and R; therefore, a stability criterion is necessary as the second equation to

determine unique values for V and R. The stability criterion of Mullins and Sekerka[15] was extended to high thermal-Péclet-number regimes by Trivedi and Kurz[16]. They introduced thermal stability parameters: ξ_L and ξ_S for the liquid and solid, respectively, in addition to the solutal stability parameter ξ_C from Mullins and Sekerka. According to their result with a relationship, $R=\lambda$[28], the marginal stability criterion is[16]

$$-\Gamma\omega^2 - [\bar{k}_L G_L \xi_L + \bar{k}_S G_S \xi_S] + m_L G_c \xi_c = 0 \qquad (9)$$

where
Γ = Gibbs-Thomson parameter ($= \gamma/\Delta S_f$)
γ = solid/liquid interfacial energy
ΔS_f = entropy of fusion
ω = wave number ($= 2\pi/\lambda$)
λ = wavelength
$\bar{k}_L$ = weighted conductivity of the liquid ($= k_L/(k_L+k_S)$)
$\bar{k}_S$ = weighted conductivity of the solid ($= k_S/(k_L+k_S)$)
G_L = temperature gradient in the liquid
G_S = temperature gradient in the solid
G_C = concentration gradient in the liquid
m_L = slope of the liquidus line

The liquid and solid have different thermophysical properties, and even two possible solid phases differ in thermophysical properties. Therefore, full expression of thermal stability parameters ξ_L and ξ_S is employed in the present study; they are written as

$$\xi_L = \frac{(1+\kappa)\left(-1+\sqrt{1+\frac{1}{\sigma^* P_t^2}}\right)}{\kappa\left(1+\sqrt{1+\frac{1}{\sigma^* P_t^2}}\right)+\left(-\beta+\sqrt{\beta^2+\frac{1}{\sigma^* P_t^2}}\right)} \qquad (10)$$

$$\xi_S = \frac{(1+\kappa)\left(\beta+\sqrt{\beta^2+\frac{1}{\sigma^* P_t^2}}\right)}{\kappa\left(1+\sqrt{1+\frac{1}{\sigma^* P_t^2}}\right)+\left(-\beta+\sqrt{\beta^2+\frac{1}{\sigma^* P_t^2}}\right)} \qquad (11)$$

where κ is the ratio of thermal conductivity of the liquid to that of the solid ($= k_L/k_S$) and β is the ratio of the thermal diffusivity in the liquid to that in the solid ($= \alpha_L/\alpha_S$). σ^* is the stability constant ($= 1/4\pi^2 \approx 0.025$)[8,17]. The solutal stability parameter, ξ_C, is given as

$$\xi_C = 1 + \frac{2k}{1 - 2k - \sqrt{1 + \frac{1}{\sigma^* P_c^2}}} \tag{12}$$

where k is the partition ratio at the solid/liquid interface, P_C is the solutal Péclet number ($=VR/2D$), and D is the solutal diffusivity in the liquid.

From the above thermal analysis, G_L and G_S are defined as follows:

$$G_L = -\frac{2P_t}{C_{pL}R}\left(\Delta H_f - \frac{J}{V}\right) \tag{13}$$

$$G_S = \frac{J}{k_S} \tag{14}$$

The definition of the concentration gradient, G_C, is identical to that in the earlier work[8,11]. That is,

$$G_c = \frac{-2C_0P_c(1-k)}{R\,(1-(1-k)Iv(P_c))} \tag{15}$$

where C_0 is the nominal solute concentration.

Substituting G_L, G_S, and G_C into Eq. (9) yields a quadratic equation:

$$AV^2 - BV + C = 0 \tag{16-1}$$

where the coefficients A, B, and C are:

$$A = \frac{\Gamma}{4\sigma^* \alpha_L^2 P_t^2} \tag{16-2}$$

$$B = \frac{\kappa \Delta H_f}{k_L(1+\kappa)} \xi_L + \frac{m_L C_0(k-1)}{D(1-(1-k)I_v(P_c))} \xi_c \tag{16-3}$$

$$C = \frac{\kappa J}{k_L(1+\kappa)} (\xi_L + \xi_S) \tag{16-4}$$

By solving the quadratic equation, the velocity V is obtained. Then the tip radius R is determined, and the contribution of each undercooling and the total undercooling, ΔT_{total}, are also determined, where

$$\Delta T_{total} = \Delta T_t + \Delta T_c + \Delta T_r + \Delta T_k \tag{17}$$

Terms in the RHS: ΔT_t, ΔT_c, ΔT_r, and ΔT_k, are the thermal undercooling, solutal undercooling, curvature undercooling, and kinetic undercooling, respectively. The thermal undercooling is given in Eq. (8). Definitions of the other undercoolings are:

$$\Delta T_c = m_L C_0 \left(1 - \frac{m'_L/m_L}{1-(1-k)Iv(P_C)} \right) \tag{18}$$

$$\Delta T_r = \frac{2\Gamma}{R} \tag{19}$$

$$\Delta T_k = \frac{V}{\mu} \tag{20}$$

where m'_L is a liquidus slope taking into account the deviation from the equilibrium due to high growth rate, and defined by[9]

$$m'_L = m_L \left(1 + \frac{k_e - k(1-\ln(k/k_e))}{1-k_e} \right) \tag{21}$$

In the above equation, k_e is the equilibrium partition ratio, and k is a partition ratio which is dependent on the velocity of the solid/liquid interface. The latter, k, is formulated by Aziz[18] as

$$k = \frac{k_e + (a_0 V / D)}{1 + (a_0 V / D)} \qquad (22)$$

where a_0 is a characteristic length on the order of the interatomic distance in the liquid.[18,19] In the expression of kinetic undercooling in Eq. (20), μ is the kinetic coefficient and given by

$$\mu = \frac{\Delta H_f V_S}{R_g T_L^2} \qquad (23)$$

where V_S is the speed of sound in the liquid[9,20], and R_g is the universal gas constant.

2.3 Calculation using the Model

Calculations were carried out for Fe-18.5Cr-11.3Ni alloy and different heat extraction rates. Although bcc is the equilibrium primary phase in the Fe-18.5Cr-11.3Ni alloy, the calculations were conducted for both bcc and fcc in order to examine the effect of solidifying phase. Numerical data used for the calculations are listed in Table 1. Thermodynamic data were obtained using Thermo Calc[21] version J with SGTE database. Although some parameters inherently involve uncertainties about their values,[22] effects of these parameters are not described in this chapter; parameters affecting heat extraction effects, such as heat extraction rate and thermal conductivity (and therefore, thermal diffusivity), are mainly examined in the present analysis. Various heat extraction rates, such as 10^6 to 10^{11} (W m^{-2}), were applied to the calculations, because a wide range of heat transfer coefficients at the chill/metal interface were reported.[1-7]

3. Results

3.1 Growth Morphology

The stability of dendritic growth is the most important issue in modeling the growth behavior. A sufficiently high positive temperature gradient in the solid which is caused by heat extraction toward the chill prevents stable growth of dendrites. This is implied by Eq. (9).

Figure 2 shows the tip velocity of a bcc dendrite calculated as a function of melt temperature for two heat extraction conditions: one is for no heat extraction (J=0) and the other for a heat extraction rate J of 10^9 W m^{-2}. When no heat is extracted through the solid, which is the case assumed by the BCT model[9], the tip velocity can be determined for almost the entire relevant temperature range: from the liquidus down to the absolute stability limit for thermal diffusion. The lower limit may be achieved at extremely low melt temperatures. On the other hand, when J=10^9 W m^{-2}, the dendrite tip velocities are determined at melt temperatures below approximately 1670 K; dendritic growth is not feasible above the temperature. In other words, in the presence of heat extraction thorough the solid, plane-front growth is preferential when the melt temperature is relatively high (T_L to 1670 K), and the growth morphology changes to dendritic when the melt temperature is below the critical temperature. Plane front growth in this situation is discussed further in the next chapter.

Since Eq. (16) for determining the tip velocity is quadratic, two velocities are simultaneously obtained for a given condition, as shown by the solid and dashed lines in the figure; the solid line is used. Compared with the case of J=0, the presence of heat extraction increases tip velocities (up to 50 % in this case) at temperatures near the plane-front/dendrite transition, while it does not affect the velocities at low melt temperatures (or high melt undercoolings).

Figure 3 shows the tip radius of a bcc dendrite calculated as a function of melt undercooling for various heat extraction conditions. As mentioned above, dendritic growth at small undercoolings becomes infeasible as the heat extraction rate increases. For example, when $J=10^9$ W m^{-2}, the tip radius is determined for undercoolings more than approximately 60 K, and planar growth is expected for undercoolings smaller than this. At the transition, the tip radius tends to increase sharply. It is obvious from the figure that the undercooling necessary for the transition from planar to dendritic growth increases as the heat extraction rate increases.

Figure 4 summarizes the effect of heat extraction rate on the transition temperature between planar and dendritic growth, where the solid line is for the fcc phase and the dashed line for the bcc phase. When the heat extraction rate is small, i.e., from J=0 to 10^7 W m^{-2}, dendritic growth is always suitable for both phases. When the heat extraction rate is between 10^8 and 10^9 W m^{-2}, the stability of dendrites is abruptly lost, and the transition temperature decreases by 30 to 50 K. In this regime, bcc is more resistant to the transition from dendrite to plane front than fcc at a given melt temperature. Then, as the heat extraction rate further increases to more than 10^9 W m^{-2}, the transition temperature decreases drastically. In this regime, fcc dendrites are slightly more stable than bcc ones against an increase in the heat extraction rate at a given temperature.

The relationship between dendrite velocity and heat extraction rate giving the dendritic/planar morphological transition is plotted in Figure 5. The coordinates used in the figures can be reduced to G (temperature gradient) versus V (growth rate) which is often used for illustrating the morphological stability of solidification products[23,24]. Figure 5(a) is determined by the present model, and Figure 5(b) by the KGT model[10] for comparison. The difference between the two models is that the present model for chill casting considers the thermal balance between heat generation and thermal diffusion so as to allow thermal undercooling in the liquid; on the

other hand, the KGT model only assumes a given positive temperature gradient without considering the above mentioned thermal balance. While Figure 5(b) defines the region of dendritic solidification in the portion which has relatively low heat extraction rate and growth velocity, Figure 5(a) shows the region expanding to higher heat extraction rates and growth velocities. In Figure 5(a), fcc dendrites change to plane-front at relatively lower heat extraction rates than bcc dendrites at a given velocity in the low-velocity regime; the difference is significant at growth velocities of 0.1 to 1 m/s. On the contrary, bcc dendrites change to plane front at slightly lower heat extraction rates than fcc in the high-velocity regime. In the case of constrained growth in Figure 5(b), the absolute stability limit is caused by solute diffusion for both fcc and bcc at velocities of 0.1 to 1 m/s; the transition of fcc dendritic to plane front morphology occurs at a lower velocity than for bcc. Beyond the stability limit, only planar growth is stable.

3.2 Effect of Heat Extraction Rate on Dendritic Growth

Figure 6 shows the effect of heat extraction rate on the tip velocity of fcc and bcc dendrites at various melt temperatures: 1650 K (ΔT= 77 K), 1600 K (ΔT= 127 K), and 1500 K (ΔT= 227 K). It is clear that dendrites growing into relatively higher-temperature melts (e.g., 1650 K) undergo the transition to plane front at relatively lower heat extraction rates than those growing into lower temperature melts. Heat extraction rate does not exert a significant influence on the tip velocity until it approaches the critical rate causing the morphological change. Near the transition to planar growth, dendrites grow at higher velocities with increasing heat extraction; this is more obvious at 1650 K than at 1500 K. Tip velocities of bcc are higher than those of fcc at all three of the melt temperatures; the relative difference in velocity between the two phases becomes smaller as the melt temperature decreases.

The effect of heat extraction rate on the tip radius of fcc and bcc dendrites at the given melt temperatures is shown in Figure 7.

The tip radius noticeably increases only near the transition from the dendrite to plane front at all three of the melt temperatures. Fcc dendrites have larger tip radii than bcc ones when growth occurs into relatively high temperature melts, but the difference becomes smaller as the melt temperature decreases.

Figure 8 shows the effect of heat extraction rate on the tip temperature of fcc and bcc dendrites at the given melt temperatures. The tip temperature decreases with increasing heat extraction rate near the morphological transition. In general, fcc dendrites have higher tip temperature than bcc dendrites, and the difference becomes larger as the melt temperature decreases; the difference seems to be independent of heat extraction rate.

Figure 9 depicts the relationship between the tip velocity of a bcc dendrite and the thermal Péclet number for various heat extraction conditions. When heat extraction through the solid is not present, i.e., J=0, tip velocity and thermal Péclet number show a one-to-one correspondence; as tip velocity increases, thermal Péclet increases monotonously, and vice-versa. This is the case at positive heat extraction rates up to 10^8 W m^{-2}. In fact, effects of heat extraction are not observed at these heat extraction rates in Figures 6 to 9. When heat extraction rate is 10^9 W m^{-2} or more, the correspondence between tip velocity and thermal Péclet is no longer one-to-one. Thermal Péclet number demonstrates a minimum at a certain tip velocity in this regime. Both the minimum Péclet number and corresponding tip velocity increase as the heat extraction rate increases. Similar results were obtained for fcc dendrites, but a given tip velocity corresponds to a slightly higher Péclet value in the case of fcc because the tip radius of fcc is likely to be larger than that of bcc.

3.3 Effect of Thermal Conductivity

In the above calculations, thermal conductivity of the liquid, fcc-solid, and bcc-solid: k_L, k_{fcc}, and k_{bcc}, respectively, are assumed

to be the same for simplicity. This may be true for some systems[16], but the difference between these values of thermal conductivity may be large in other systems. The liquid usually has a much lower conductivity than the solid.[5,6] Figure 10 compares the effect of thermal conductivity of the liquid on tip velocity. Two different values of k_L, 10 and 35 W $m^{-1}K^{-1}$ were tried while k_{fcc} and k_{bcc} were unchanged. Thermal diffusivity in the liquid, α_L, is correspondingly changed. It is apparent that a decrease in the liquid thermal conductivity reduces the tip velocity of both fcc and bcc dendrites; the effect is more pronounced for fcc.

4. Discussion

4.1 Stability of Dendrite Growth

The results of the model indicate that the stability of dendrite growth is reduced by the presence of a high external heat extraction rate. As the heat extraction rate increases, planar growth becomes more stable and higher undercooling is needed for dendritic growth to be feasible. Figure 4 illustrates this tendency.

From Eq. (9), it is obvious that a planar interface is stable (or dendritic growth becomes unstable) when

$$-(\bar{k}_L G_L \xi_L + \bar{k}_S G_S \xi_S) + m'_L G_c \xi_c < 0 \qquad (24)$$

The transition from dendritic to planar growth in Figure 4 is caused by two mechanisms. One applies in small undercooling regime, and the other in the large undercooling regime. When the melt undercooling is small, the temperature gradient in the liquid, G_L, is not important since the thermal Péclet number is small. Therefore, the criterion for the transition (Eq. (24)) is determined by the competition of the temperature gradient in the solid, G_S, and the gradient caused by the liquid concentration gradient, $m_L G_C$. G_S is given by dividing the heat flux through the solid, J, by the solid

thermal conductivity k_S. At a certain value of G_S, the condition given in Eq. (24) holds, and planar growth then becomes stable at any temperature between the liquidus and the solidus since $m_L G_L$ is approximately constant in this undercooling range. This results in the abrupt change in transition temperature at small undercoolings in Figure 4. Because $m_L G_C$ for the bcc phase is larger than that for the fcc phase, the transition from dendritic to planar growth in bcc occurs at higher heat extraction rate than that in fcc.

When the melt undercooling becomes large, the concentration gradient G_C becomes insignificant due to the solute trapping effect defined by Eq. (22). Then the criterion of stability is determined by G_L (<0) and G_S (>0). As the heat extraction rate is increased, G_L approaches zero while G_S increases, and eventually planar growth becomes stable at a certain heat extraction rate. Since the latent heat of bcc is smaller than that of fcc, G_L goes toward zero at a relatively lower heat extraction rate when bcc solidifies, and therefore, the transition from dendritic to planar growth occurs in bcc at a relatively lower heat extraction rate than in fcc.

The effect of growth velocity on the transition shown in Figure 5 can be similarly interpreted. At the plateau observed at growth velocities of 0.1 to 1 m/s, the morphological transition is independent of the velocity. When the growth velocity is less than 0.1 m/s, the effect of velocity and the heat extraction rate on the morphological transition in Figure 5(a) is almost identical to that in Figure 5(b). These indicate that the transition is mainly controlled by G_S and $m_L G_C$, and G_L is not apparently involved up to a velocity of 1 m/s. Bcc dendrites are stable up to higher heat extraction rates than fcc dendrites at a given growth velocity up to 1 m/s in Figure 5 (a).

When the growth velocity is more than 1 m/s, higher heat extraction rates are necessary for the morphological transition to occur. At the same time, G_L increases with increasing thermal Péclet number, while G_C approaches zero by the solute trapping effect. The effect of growth velocity on the transition in this regime can be

estimated from $\bar{k}_L G_L + \bar{k}_S G_S = 0$ assuming $G_C=0$ in Eq. (24). Combining Eqs. (13) and (14), one can obtain at the transition:

$$V = \frac{2J}{\Delta H_f} \qquad (25)$$

This indicates that tip velocity and heat extraction rate which define the morphological transition, have a linear relationship. In fact, the transition lines at velocities greater than approximately 1 m/s shown in Figure 5(a) exhibit the same relationship. It is obvious from the above equation that bcc changes from dendritic to plane front at relatively smaller heat extraction rates than does fcc at a given growth velocity, since the latent heat of bcc is smaller.

In summary, stability of growth morphology in chill casting is discussed in terms of heat extraction rate through the solid, melt undercooling, and growth velocity. It is shown that the morphological transition in chill casting behaves similarly to that in constrained growth as predicted by the KGT model when the growth velocity is less than 0.1 m/s. As the melt undercooling increases, increasing growth velocity causes an abrupt increase in the stability of a plane front interface; then, the transition is determined mainly by competition between the thermal gradient in the solid and that in the liquid. It should be noted that the latter case, i.e., the stability under high heat extraction rate and growth velocity fields, is characteristic of chill casting situations. Another finding to be noted is that, because of the difference in thermodynamic properties, fcc is more likely to be planar than bcc at small to medium undercoolings while bcc is more likely to be planar at large undercoolings.

4.2 Effect of Heat Extraction Rate on Dendritic Growth

Although heat extraction through the solid apparently affects growth morphology, it does not modify the tip velocity, tip radius, and tip temperature of dendrites significantly until the rate of heat extraction comes close to a certain level. The tendency is depicted in

Figures 6 to 8. The effect of heat extraction rate on these quantities only becomes noticeable when the ratio of the heat extraction rate to the growth rate, i.e., J/V, becomes comparable in magnitude to the latent heat, as suggested by Eq. (8). For instance, since the latent heat (ΔH_f) is around 10^9 J m^{-3}, heat extraction rate needs to be also around 10^9 W m^{-2} to be influential to the properties of a dendrite growing at 1 m/s. When J/V and ΔH_f are comparable, the morphology transition is likely to occur, as suggested by Eq. (25). Therefore, the effect of heat extraction on the properties of a dendrite may be exerted within only a small range of heat extraction rate; the tendency observed in Figures 6 to 8 is quite understandable. Among these results, it should be noted that the tip temperature tends to decrease as the heat extraction rate increases, especially at low melt temperatures (or high undercoolings). This indicates that thermal undercooling decreases but kinetic undercooling increases with increasing heat extraction rate.

Regarding the thermal Péclet number, the following relationship is obtained from Eqs. (16), assuming $\kappa = \beta = \xi_L = \xi_S = 1$ for simplicity:

$$P_t \geq \sqrt{\frac{4k_L\Gamma}{\sigma^* \alpha_L^2 \Delta H_f^2}}\sqrt{J} \qquad (26)$$

where solutal undercooling (ΔT_c) is neglected since it is very small at high growth rates due to solute trapping[18]. The above equation indicates that the minimum Péclet number for dendritic growth increases in proportion to $\sqrt{J}$ in chill casting. For example, P_t needs to be equal to or greater than approximately 0.1 when $J=10^9$ W m^{-2}, which is very large compared to conventional casting practices. In other words, dendritic solidification in a substrate-quenching process can only proceed at high growth velocity and thermal Péclet number. On the other hand, it is obvious that free dendrite growth (i.e., J=0) is always feasible at any thermal Péclet number.

4.3 On the Growth Model Incorporating Heat Extraction Effects

As emphasized already, the thermal field in chill casting results from a large heat extraction by the chill and a substantial undercooling in the liquid ahead of the chill. Figures 11(a) to (c) compare the thermal field at a dendrite tip in three different growth situations. The dendritic growth considered in the present model has thermal characteristics which are hybrids of those in free growth and the constrained growth. In fact, Eqs. (8) and (16) in this model are identical to those predicted by the LKT and BCT models[8,9] when the heat extraction rate J is equal to zero. On the other hand, Eqs. (16) can be reduced to the KGT model[10] if the thermal effect is neglected. In other words, the present model for chill casting can encompass those existing dendrite models as limiting cases.

The dendrite model for chill casting also demonstrates correlation between free dendrite growth (LKT and BCT) and plane front growth limited by interface kinetics[24] as a function of heat extraction rate. Temperature fields for free growth, the current study, and the plane front case are shown in Figure 11(a), 11(c) and 11(d), respectively. As the heat extraction rate increases, heat diffusing into the liquid is reduced, and thermal undercooling (ΔT_t) therefore decreases. However, the kinetic undercooling (ΔT_k) increases for a given melt undercooling. In the extreme case, a plane front interface with full kinetic undercooling is favored over a dendritic one at sufficiently high heat extraction rates.

5. Conclusions

(1) A dendrite model is proposed for chill casting situations. The model combines the effects of heat extraction through the solid with the BCT model[9] of free growth into an undercooled melt. The corresponding stability criterion is also modified.

(2) As the heat extraction rate increases, dendritic growth becomes infeasible and changes to planar growth. When the melt undercooling is small, the morphological transition occurs at relatively lower heat extraction rate and is governed by the competition between the thermal gradient in the solid caused by heat extraction and that caused by solute concentration gradient. This behavior is similar to that in the KGT model[10]. When the melt undercooling is large, dendritic growth is stable up to high heat extraction rates, and the morphological transition is governed by the competition between the thermal gradient in the solid and that in the liquid.

(3) When the melt undercooling is small, an fcc dendrite changes to plane front at a relatively lower heat extraction rate than a bcc dendrite because fcc maintains smaller solutal undercooling than bcc during its growth. When the melt undercooling is large, on the other hand, a bcc dendrite changes to plane front at relatively lower heat extraction rate than an fcc dendrite because bcc possesses relatively smaller thermal undercooling effect.

(4) The effect of heat extraction on the properties of a dendrite becomes noticeable only when the heat extraction rate approaches the value causing the morphological transition. Within this narrow range, increased heat extraction increases both tip velocity and tip radius, and decreases the tip temperature.

(5) Dendritic solidification during the substrate-quenching process is shown to proceed at high growth velocity and high thermal Péclet number when large amounts of heat are extracted through the solid by the substrate.

(6) Decreased thermal conductivity of the liquid reduces the tip velocity of both fcc and bcc dendrites.

(7) The proposed dendrite model for chill casting is a hybrid of the models for free dendrite growth and constrained growth; therefore, it includes the existing models as its extreme cases. It also gives a

physical correlation between free dendrite growth and plane front growth limited by interface kinetics.

References

1. H. Mühlbach, G. Stephani, R. Sellger, and H. Fiedler: *Int'l J. Rapid Solidification*, 1987, vol. 3, p. 83
2. K. Takeshita and P. H. Shingu: *Trans. Japan Inst. Metals*, 1986, vol. 27, p. 454
3. M. J. Tenwick and H. A. Davies, *Rapidly Quenched Metals V*, eds. S. Steeb and H. Warlimont, Elsevier Publishers B. V., NY, 1985, p. 67
4. H. Mizukami, T. Suzuki, and T. Umeda: *Tetsu-to-Hagane*, 1991, vol. 77, p. 134
5. T. W. Clyne: *Metall. Trans. B*, 1984, vol. 15B, p. 369
6. G.-X. Wang and E. F. Matthys: *Int'l J. Rapid Solidification*, 1991, vol. 6, p. 297
7. X. Zhang and A. Atrens: *Int'l J. Rapid Solidification*, 1993, vol. 8, p. 1
8. J. Lipton, W. Kurz, and R. Trivedi: *Acta metall.*, 1987, vol. 35, p. 957
9. W. J. Boettinger, S. R. Coriell, and R. Trivedi: *Rapid Solidification Processing: Principles and Technologies*, eds. R. Mehrabian and P. A. Parrish, Claitor's Publ. Div., 1988, p. 13
10. W. Kurz, B. Giovanola and R. Trivedi: *Acta metall.*, 1986, vol. 34, p. 823
11. J. Lipton, M. E. Glicksman, and W. Kurz: *Mater. Sci. Eng.*, 1984, vol. 65, p. 57
12. R. F. Sekerka, R. G. Seisensticker, D. R. Hamilton, and J. D. Harrison: *Investigation of Desalination by Freezing*, WRL Report No. 319, Westinghouse Research Laboratories, 1968, Chapter 3
13. G. P. Ivantsov: *Dokl. Akad. Nauk S.S.S.R.*, 58, 1947, p. 567
14. G. Horvay and J. W. Cahn: *Acta metall.*, 1961, vol. 9, p. 695

15. W. W. Mullins and R. F. Sekerka: *J. Appl. Phys.*, 1964, vol. 35, p. 444
16. R. Trivedi and W. Kurz: *Acta metall.*, 1986, vol. 34, p. 1663
17. H. Müller-Krumbhaar and J. S. Langer: *Acta metall.*, 1978, vol. 26, p. 1697
18. M. J. Aziz: *J. Appl. Phys.*, 1982, vol. 53, p. 1158
19. W. J. Boettinger, S. R. Coriel, and R. F. Sekerka: *Mater. Sci. Eng.*, 1984, vol. 65, p.27
20. D. Turnbull: *Metall. Trans. A*, 1981, vol. 12A, p. 695
21. B. Sundman, B. Jansson, and J.-O. Andersson: *CALPHAD*, 1985, vol. 9, p. 153
22. M. Suzuki, T. J. Piccone, M. C. Flemings, and H. D. Brody: *Metall. Trans. A*, 1991, vol. 22A, p. 2761
23. R. Mehrabian: Int'l Met. Rev., 1982, vol. 27, p. 185
24. W. Kurz and D. J. Fisher: *Fundamentals of Solidification*, 3rd ed., Trans Tech Publ., 1989, p. 140
25. Y. Ono: *The Properties of Liquid Metals*, S. Takeuchi, ed., Taylor and Francis, London, 1973, p. 543
26. B. Lally, L. Biegler, and H. Henein: *Metall. Trans. B*, 1990, vol. 21B, p. 761
27. W. J. Boettinger, S. R. Coriel, and R. F. Sekerka: *Mater. Sci. Eng.*, 1984, vol. 65, p.27
28. J. S. Langer and H. Müller-Krumbhaar: *J. Cryst. Growth*, 1977, vol. 42, p. 11

Table 1: Parameter values for Fe-18.5Cr-11.3Ni used for the dendrite tip model.

parameter			value	ref.
			Fe-18.5Cr-11.3Ni	
T_L	liquidus temperature (K)	(fcc)	1722.40	
		(bcc)	1727.61	
ΔH_f	enthalpy of fusion (J mol^{-1})	(fcc)	11209.61	
		(bcc)	8943.64	
ΔS_f	entropy of fusion (J $mol^{-1}K^{-1}$)	(fcc)	6.4678	
		(bcc)	5.6388	
k_{Cr}	partition ratio of Cr	(liq/fcc)	0.8578	
k_{Ni}	partition ratio of Ni	(liq/bcc)	0.7710	
m_L	slope of liquidus (K $wt\%^{-1}$)	(fcc)	-4.3439	
		(bcc)	-6.4793	
C_{pL}	specific heat of liqiud (J $mol^{-1}K^{-1}$)		43.789	
$\overline{V}$	molar volume (m^3 mol^{-1})	(liq)	7.71×10^{-6}	
		(fcc)	7.71×10^{-6}	
		(bcc)	7.71×10^{-6}	
D_{Cr}	diffusivity of Cr in liquid (m^2 s^{-1})			
	D_0 diffusion constant (m^2 s^{-1})		2.67×10^{-7}	[25]
	Q activation energy (J mol^{-1})		6.69×10^4	[25]
D_{Ni}	diffusivity of Ni in liquid (m^2 s^{-1})			
	D_0 diffusion constant (m^2 s^{-1})		4.92×10^{-7}	[25]
	Q activation energy (J mol^{-1})		6.77×10^4	[25]
k_L	thermal conductivity of liquid (W $m^{-1}K^{-1}$)		35	[26]
k_{fcc}	thermal conductivity of fcc (W $m^{-1}K^{-1}$)		35	
k_{bcc}	thermal conductivity of bcc (W $m^{-1}K^{-1}$)		35	
V_S	sound velocity in liquid (m s^{-1})		2000	[9]
a_0	interatomic distance in liquid (m)		1×10^{-9}	[27]

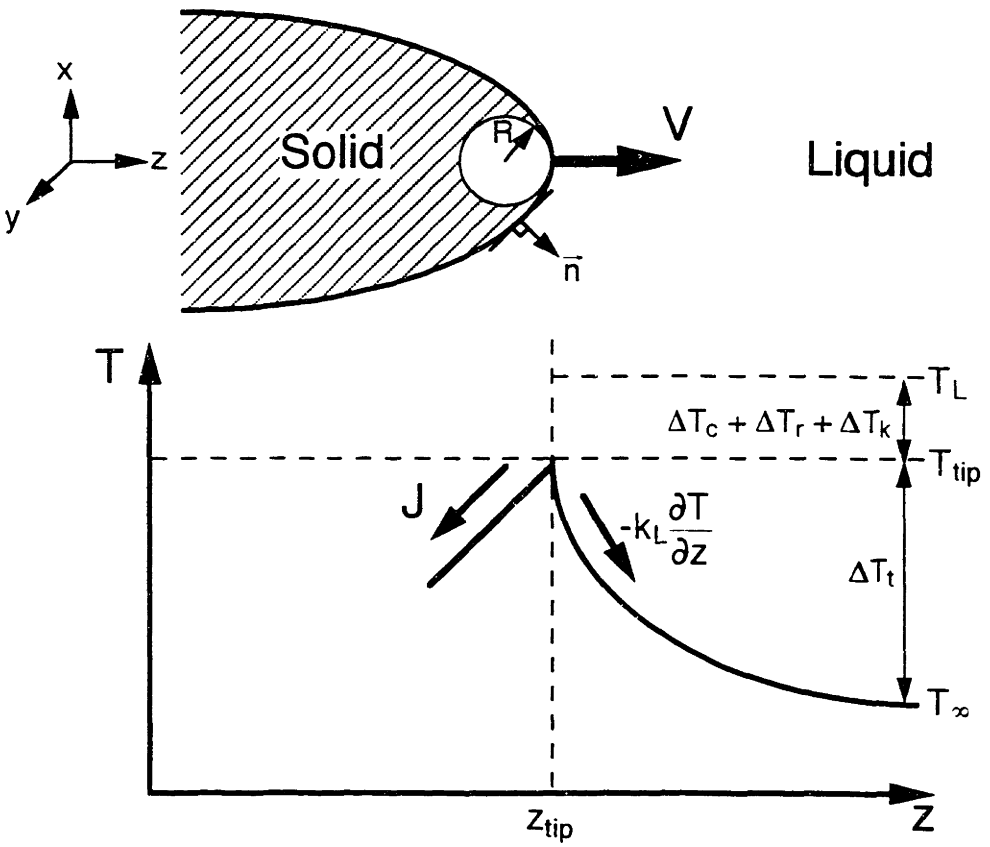

Figure 1 - Schematic of the thermal field around a dendrite tip growing into an undercooled melt during chill casting

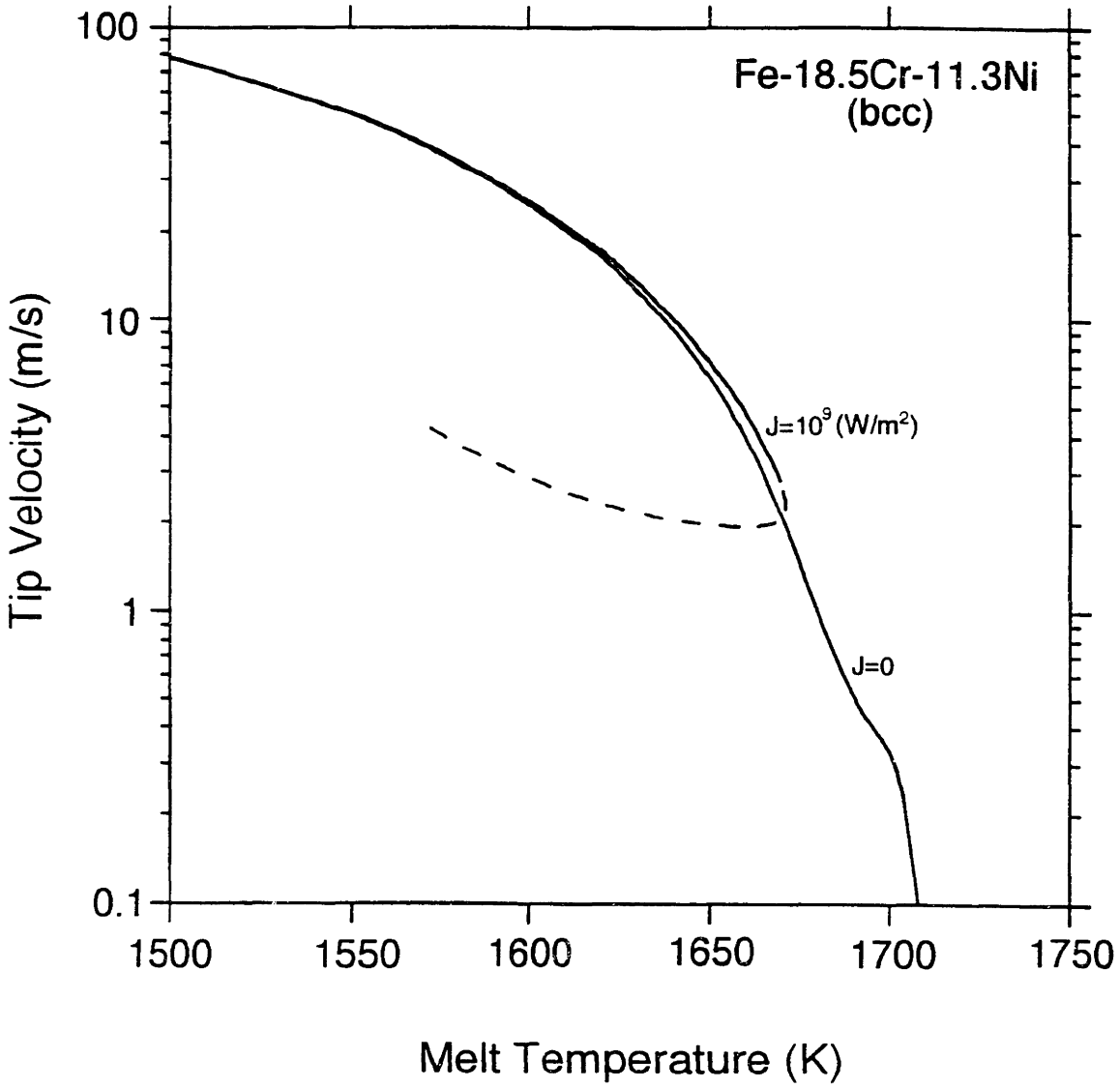

Figure 2 - Effect of melt temperature on the tip velocity of a bcc dendrite for two heat extraction conditions: no heat extraction (J=0) and a heat extraction rate J of 10^9 W m^{-2}.

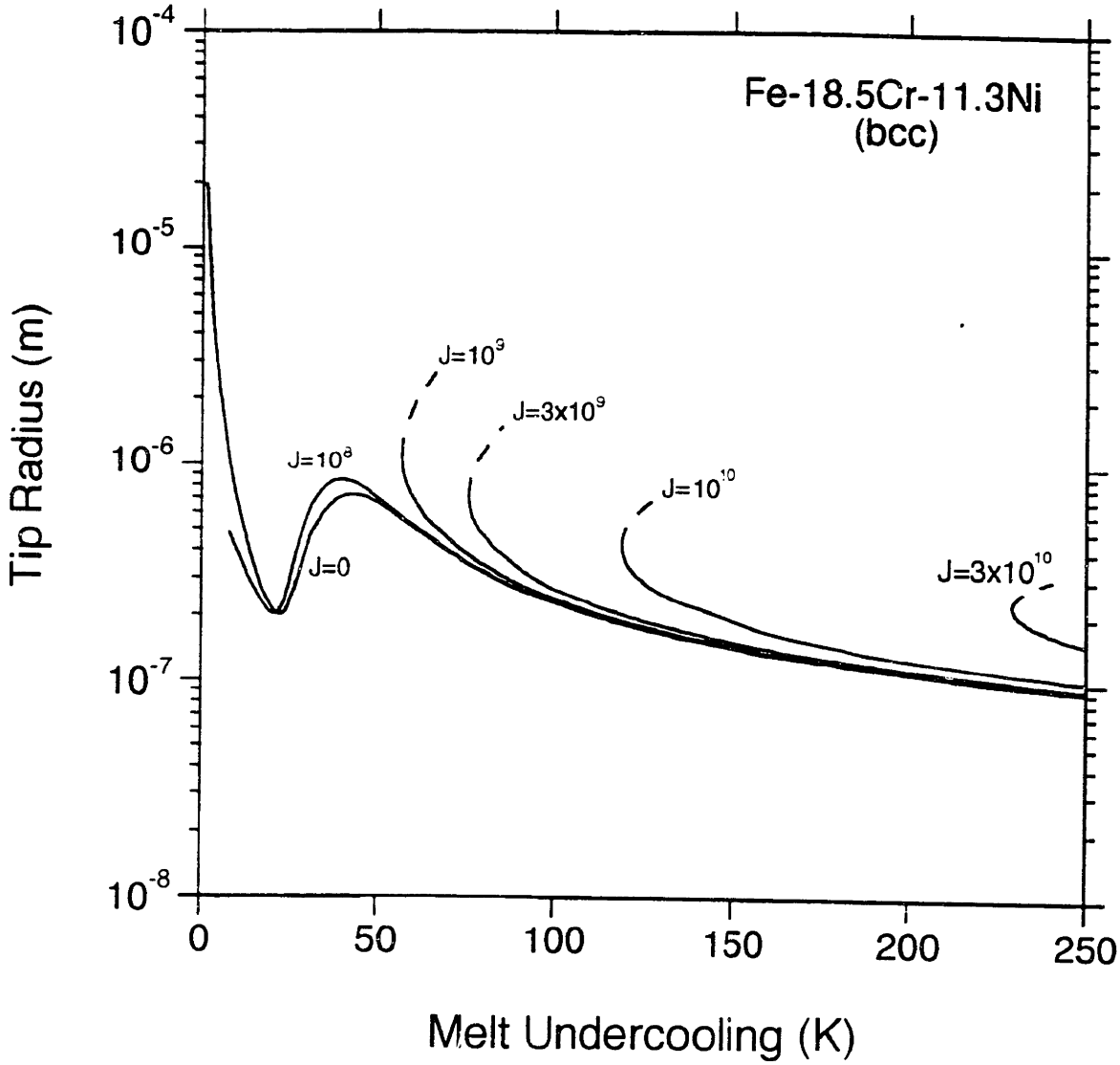

Figure 3 - Effect of melt temperature on the tip radius of a bcc dendrite for different heat extraction conditions. Heat extraction rate J is varied from 0 to $3x10^{10}$ W m^{-2}.

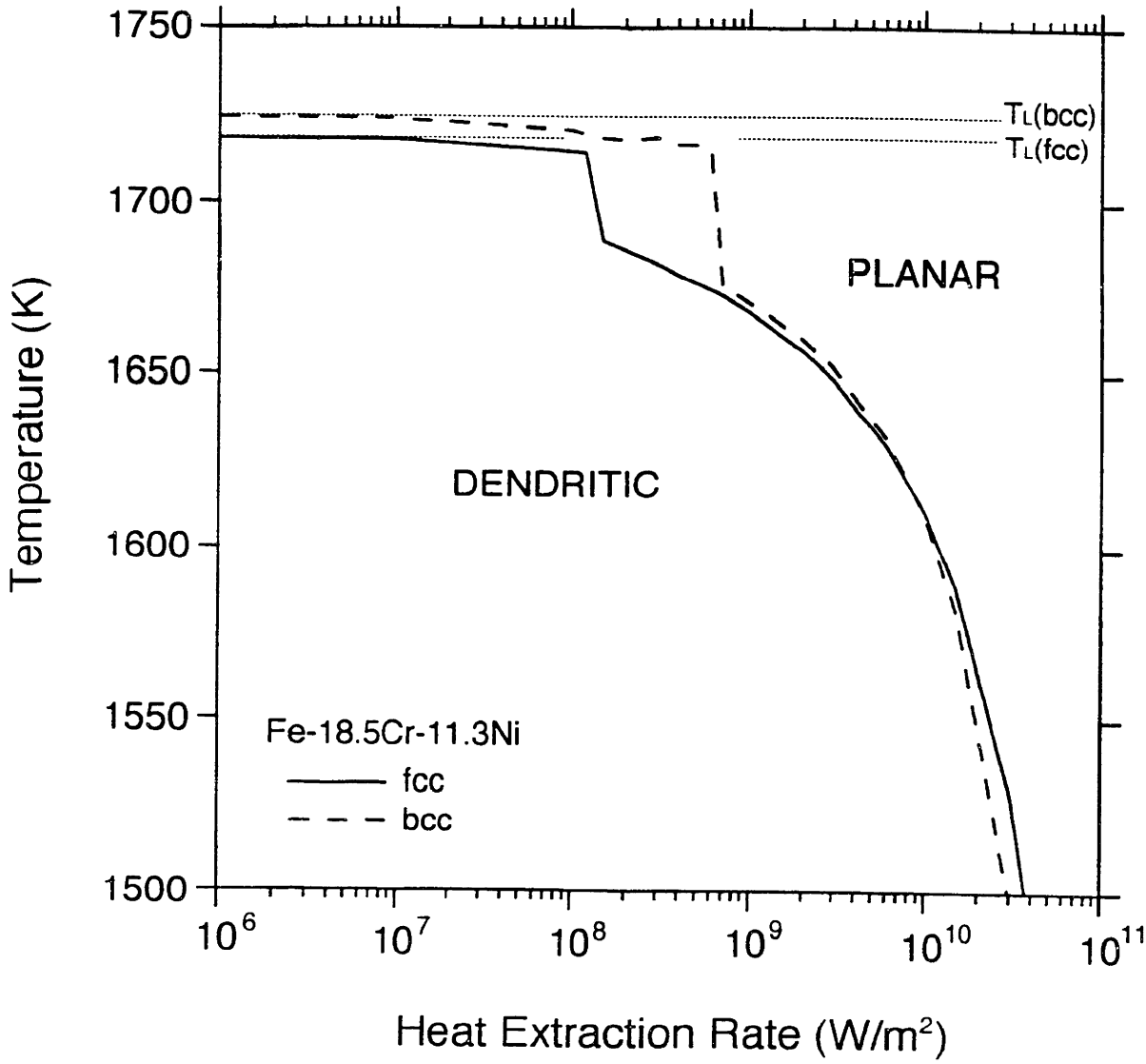

Figure 4 - Effect of heat extraction rate and melt temperature on the growth morphology of fcc and bcc.

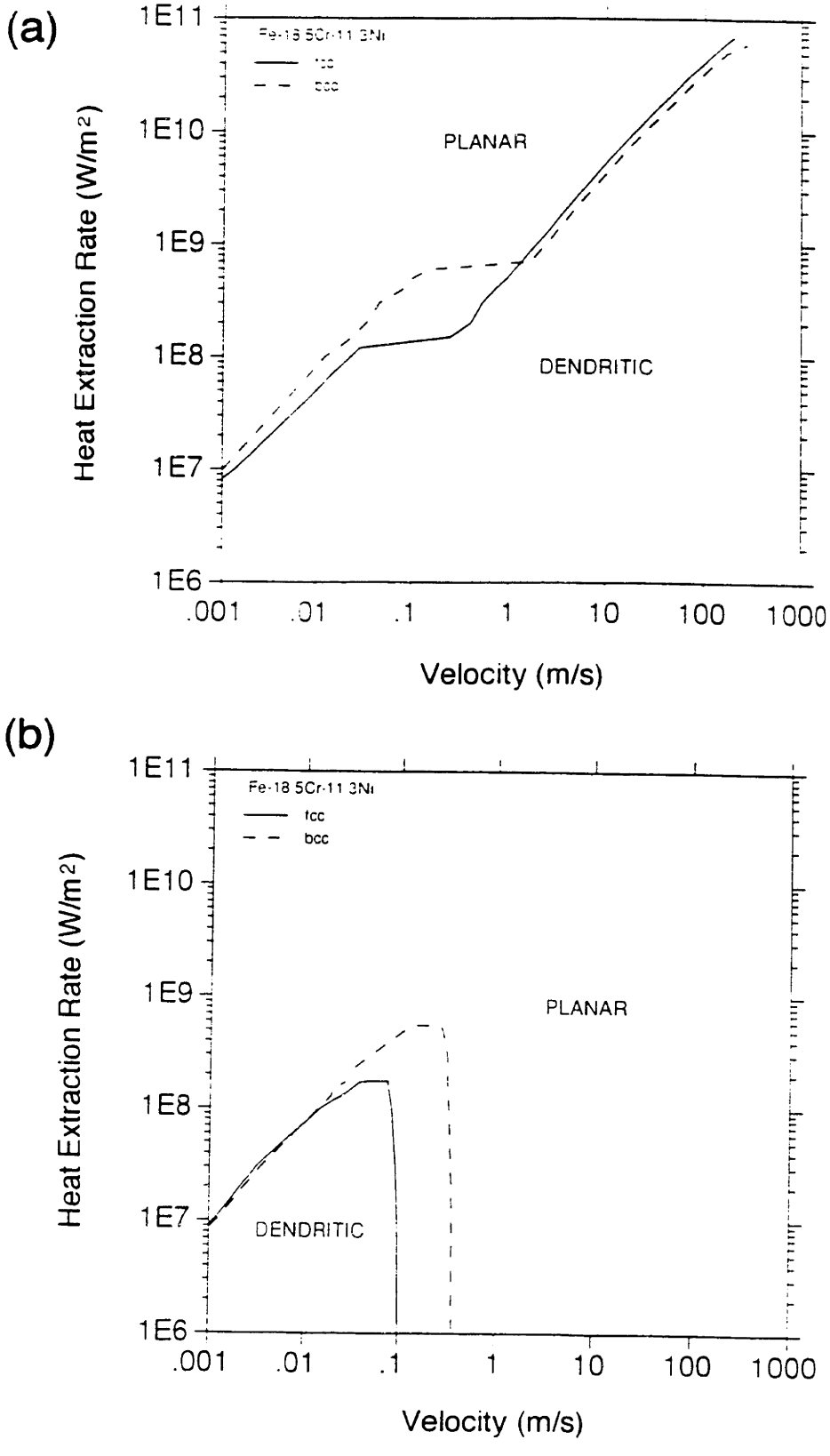

Figure 5 - Effect of heat extraction rate and growth velocity on the growth morphology of fcc and bcc, (a) evaluated by the present model, and (b) evaluated by the KGT model[10]

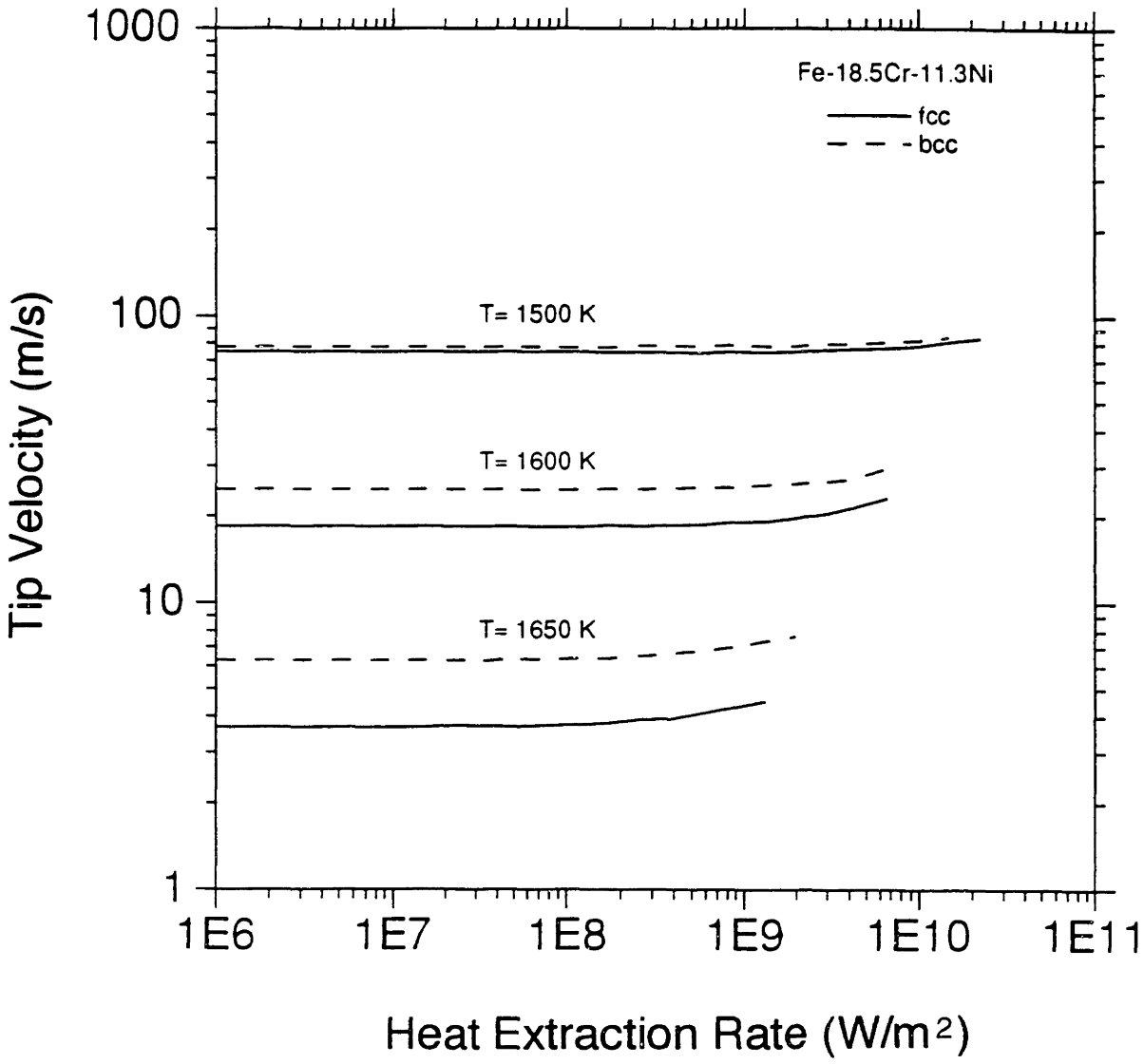

Figure 6 - Effect of heat extraction rate on the tip velocity of fcc and bcc dendrites at a given melt temperature: 1500 K, 1600 K, and 1650 K.

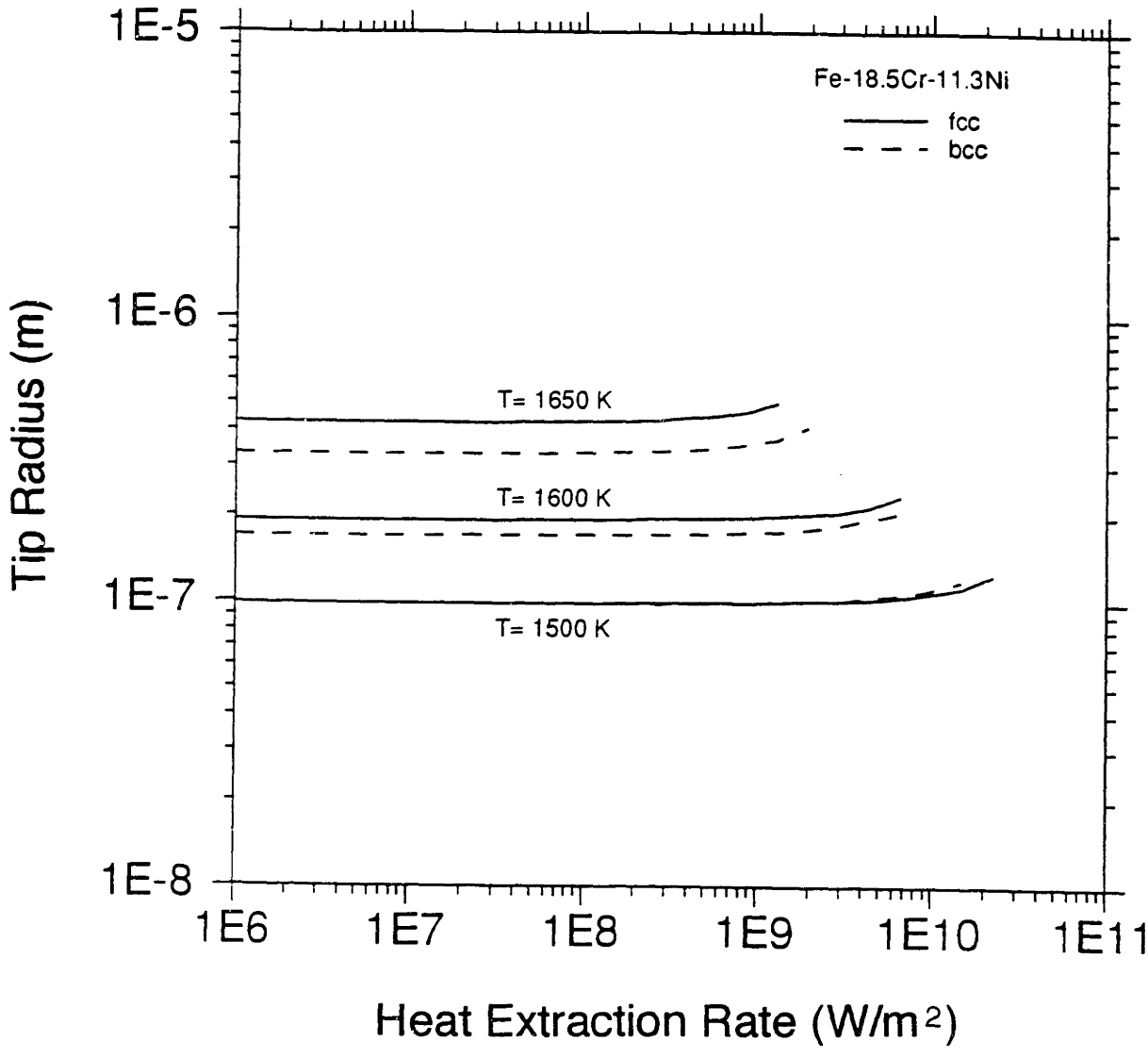

Figure 7 - Effect of heat extraction rate on the tip radius of fcc and bcc dendrites at a given melt temperature: 1500 K, 1600 K, and 1650 K.

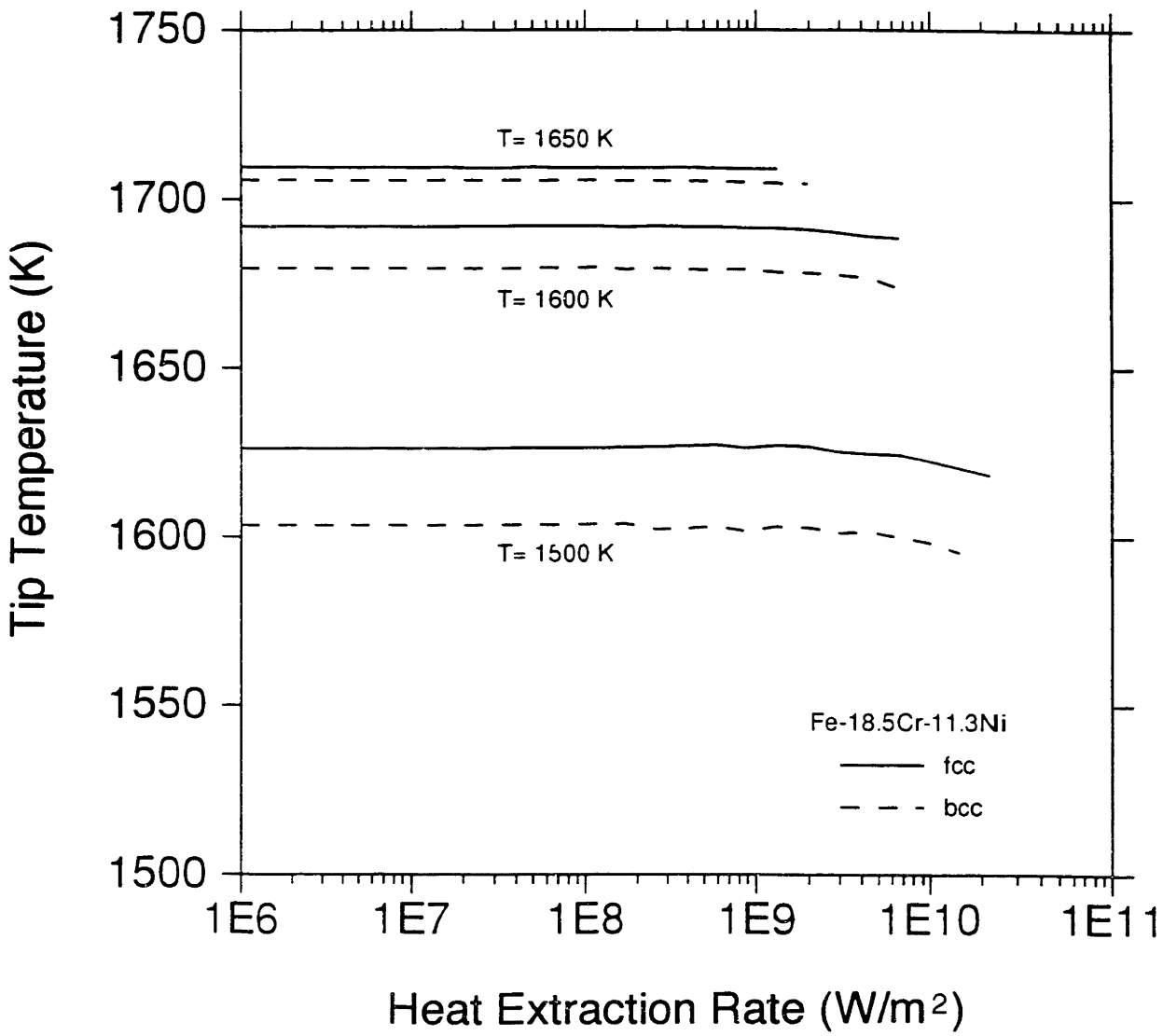

Figure 8 - Effect of heat extraction rate on the tip temperature of fcc and bcc dendrites at a given melt temperature: 1500 K, 1600 K, and 1650 K.

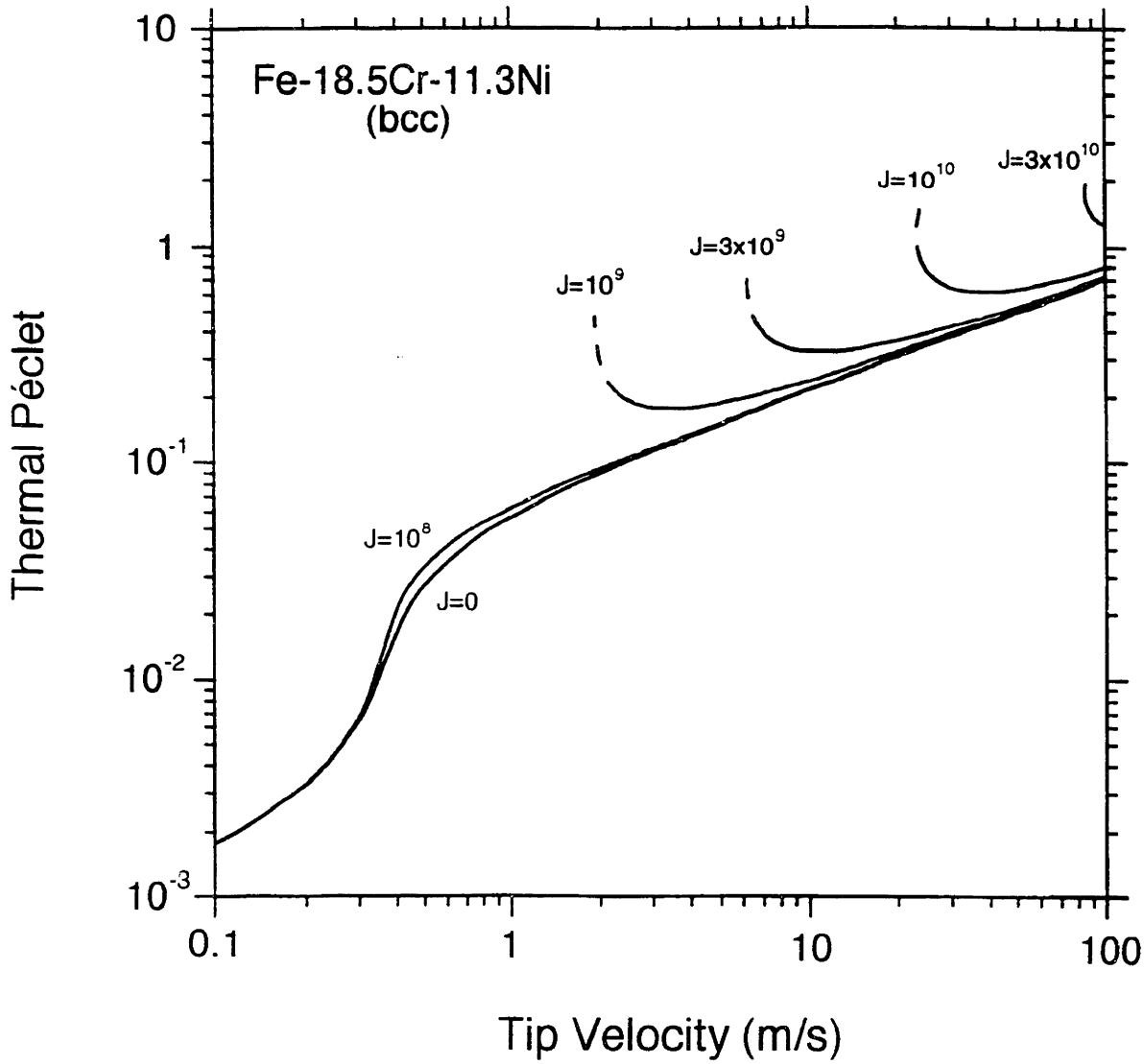

Figure 9 - Relationship between the tip velocity of a bcc dendrite and thermal Péclet number for different heat extraction conditions. Heat extraction rate J is varied from 0 to $3x10^{10}$ W m^{-2}.

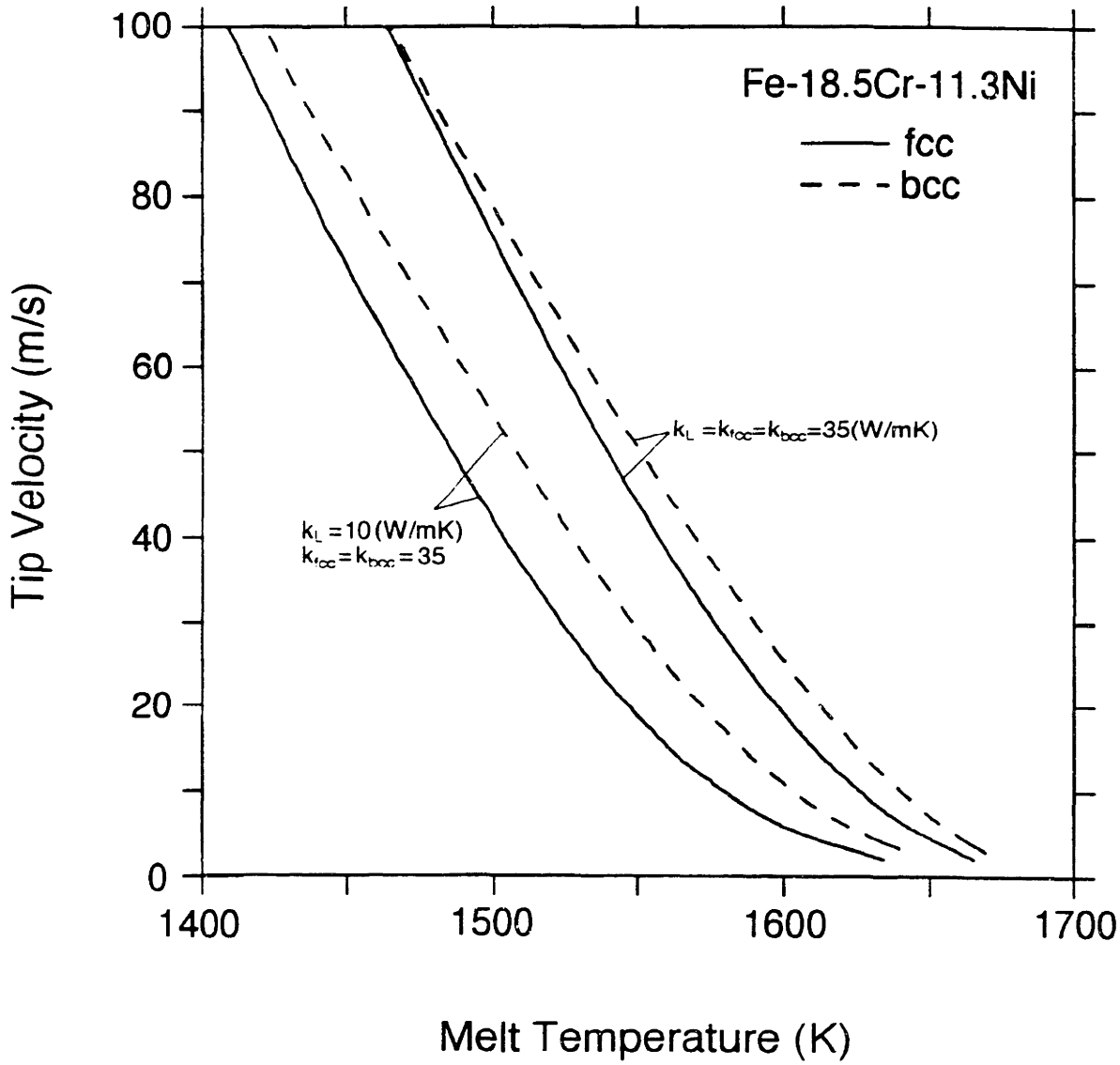

Figure 10 - Effect of the thermal conductivity of the liquid on the tip velocity of fcc and bcc dendrites

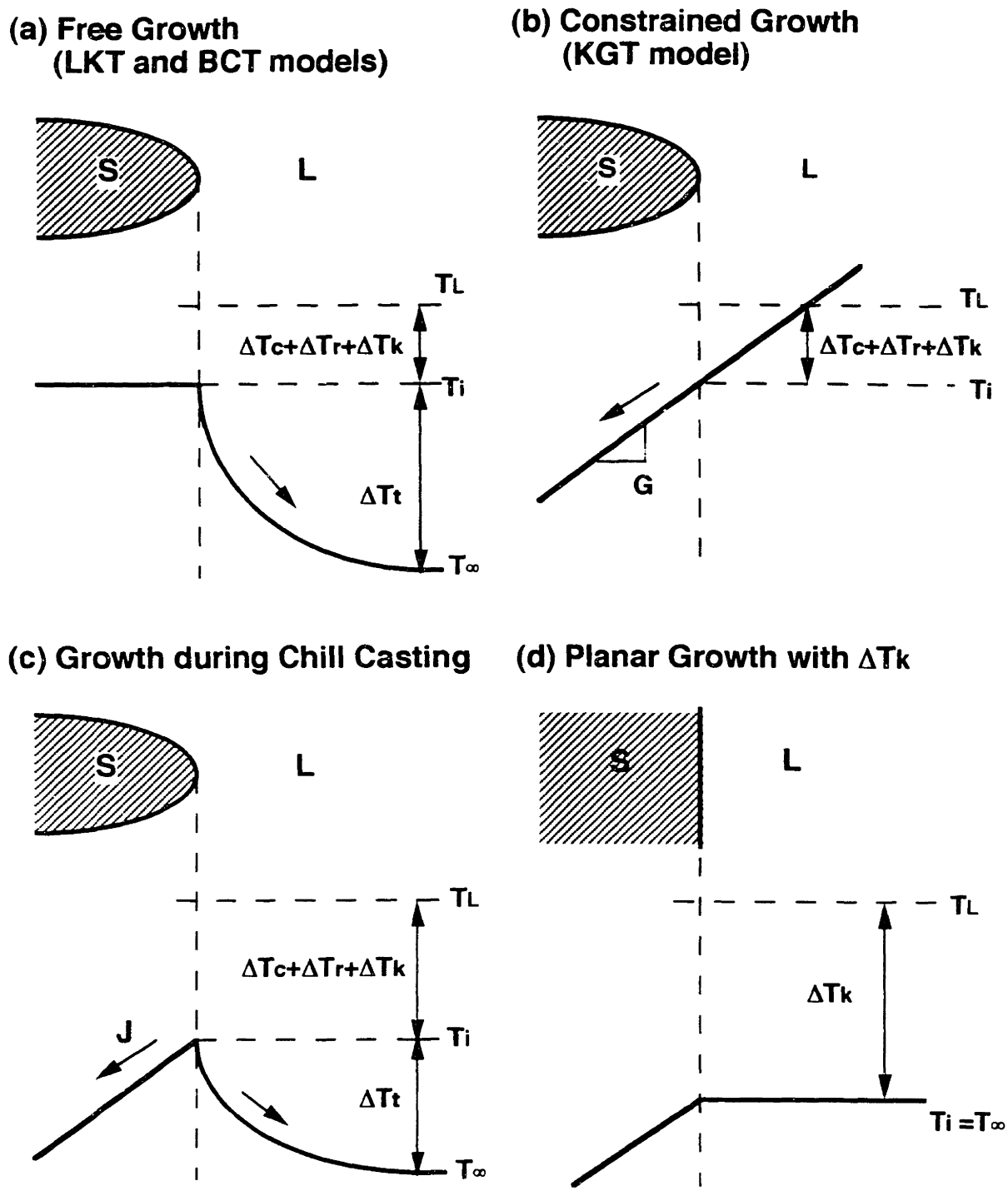

Figure 11 - Schematics of the thermal field around a dendrite tip and the solid/liquid interface for different growth situations.

Chapter VI - Preferential Fcc Solidification in Fe-Cr-Ni Alloys during Chill Casting

Abstract

The mechanism of preferential fcc solidification which was observed in the chill casting of the undercooled Fe-Cr-Ni alloy melts is discussed from standpoints of nucleation and growth. It is suggested that rapid cooling of the melt at the chill can cause nucleation of bcc and fcc which is nearly simultaneous. An explanation for selective fcc growth from the coexisting two phases is proposed.

1. Introduction

In Chapter IV, fcc solidification was found to be dominant in the chill casting of undercooled Fe-Cr-Ni alloy melts. Primary fcc solidification was observed throughout a chill-cast Fe-17.5Cr-12.2Ni sample, and metastable fcc solidification was dominant in the vicinity of the chill substrate in Fe-18.5Cr-11.3Ni alloy. These results are in contrast to the fact that both alloys solidified as primary bcc when gas-cooled using a levitation technique. Small bcc dendrites were found to be retained at the chill/metal interface, which suggests that bcc and fcc nucleated nearly concurrently, and that fcc grows preferentially out of the coexistence of the both phases. The amount of retained small bcc dendrites increased as the heat extractive capacity of the chill decreased. The fcc often seemed featureless up to several tens of microns from the chill/metal interface, and in fact, distributions of solutes were nearly uniform in that region. The difference of morphology between fcc and bcc in the vicinity of the chill/metal interface was observed in many samples.

Despite extensive work on chill casting and substrate quenching of many kinds of alloys, the solidification behavior during these processes has not been analyzed thoroughly. The features of these solidification conditions are:

- the melt is undercooled especially in the vicinity of the chill/metal interface
- a large amount of heat is extracted from the solidification front by the chill, especially during the initial stages

Dendritic growth under these conditions was modeled in the previous chapter. Since a specific crystallographic relationship between the chill and the cast metal was not clearly observed in the experiment, the above thermal features are assumed to determine the solidification products.

Regarding the preferential fcc growth found in chill casting, the mechanism is still poorly understood. Recently, Mizukami et al.[1] stated that fcc is preferred over bcc because the tip temperature of an fcc dendrite is higher than that of a bcc dendrite in the highly undercooled condition. This statement is based on results from the modeling of free dendrite growth; it does not reflect the chill casting condition. It is still unclear why fcc growth is favored in chill casting. Moreover, there is also the matter of the nucleation event prior to growth to be considered. In undercooled melts of Fe-Cr-Ni alloys, nucleation of bcc is preferred, as indicated by experiments using gas-cooled solidification. This being the case, the primary issues to be addressed in interpreting the chill casting results are: (1) why does fcc nucleate at all?, and (2) why does it grow preferentially to bcc?

This chapter discusses these issues, i.e., the mechanism of the process which cause preferential fcc solidification. Both nucleation and growth stages are examined using nucleation theory and the proposed dendrite model for chill casting, respectively. In addition, models of plane-front growth are also employed to the latter discussion.

2. Models

2.1 Nucleation Temperatures during Continuous Cooling

In chill casting, the melt is rapidly supercooled after it impacts upon the chill.[2] The cooling rate is probably on the order of 10^6 K/s or more.[2-6] Nucleation is assumed to occur heterogeneously at the chill/metal interface. Thus, the nucleation temperature of fcc and bcc can be calculated as a function of cooling rate as follows, if a contact angle is assumed.

Following classical nucleation theory[7-9], surface nucleation rate, I_s, is given by

$$I_s = \frac{k_s}{\eta} \exp\left[- \frac{\Delta G^*}{kT} \right] \qquad (1)$$

where k_s is the kinetic parameter for heterogeneous nucleation (= 1×10^{29} N m^{-4})[7,9], η is the viscosity of the liquid, and ΔG^* is the critical free energy of formation of a nucleus. η is estimated by[26,27]

$$\eta = 10^{-4.3} \exp\left[\frac{3.34}{T_r - T_{rg}} \right] \text{ (N s } m^{-2}) \qquad (2)$$

where T_r is a reduced temperature ($=T/T_L$), T_L is the liquidus temperature, and T_{rg} is the reduced glass transition temperature ($=0.25$)[8]. In the case of planar catalytic sites and incoherent nuclei, the critical free energy ΔG^* is given by

$$\Delta G^* = \frac{16\pi}{3} \frac{\gamma_{S/L}^3}{\Delta G_v^2} f(\theta) \qquad (3)$$

where $\gamma_{S/L}$ is the interfacial energy between the solid and the liquid and ΔG_v is the free energy of formation of the solid from the liquid (per unit volume). $f(\theta)$ is a catalytic potency factor which is a function of the wetting angle θ between the nucleus and the substrate, and is given as $f(\theta)=(2-3\cos\theta+\cos^3\theta)/4$. In the present study, calculations were made assuming contact angles of 30°, 45°, and 60°.

ΔG_v can be estimated from the latent heat of fusion, ΔH_f:

$$\Delta G_v = \frac{\Delta H_f (T_L - T)}{\overline{V} T_L} \qquad (4)$$

where $\overline{V}$ is the molar volume of the solid phase. The interfacial energy between solid and liquid, $\gamma_{S/L}$, is estimated by the following equation[10]:

$$\gamma_{S/L} = \frac{\alpha_{S/L}\,\Delta H_f}{(N\overline{V}^2)^{1/3}} \qquad (5)$$

where $\alpha_{S/L}$ is a dimensionless interfacial energy parameter ($\alpha_{fcc/liq}$ = 0.86, $\alpha_{bcc/liq}$ = 0.71)[11,12] and N is Avogadro's number.

When a value of θ is assumed, the nucleation rate I_S becomes a function of temperature alone; therefore, nucleation temperature T_N can be obtained by integrating the nucleation rate with respect to temperature[9]:

$$\int_{T_N(\theta)}^{T_L} \frac{I_S S}{dT/dt}\,dT = 1 \qquad (6)$$

where S is the metal/substrate surface area, and is assumed to be 2.5 x 10^{-5} m^2. dT/dt is the cooling rate of the specimen.

2.2 Dendritic Growth during Chill Casting

The dendrite model for chill casting has already been described in the previous chapter. The model assumes that heat evolved at the solidification front is transferred into both the undercooled melt and the solid. Figure 1 shows a schematic of the thermal field around a dendrite tip during chill casting.

2.3 Planar Growth during Chill Casting

As mentioned in the previous chapter, planar growth becomes more likely in chill casting as the heat extraction rate increases. Dendrite growth models can be reduced to the model of planar growth by allowing the tip radius to go to infinity ($R\rightarrow\infty$). Plane front is assumed to advance into the undercooled melt with thermal undercooling. A schematic of the thermal field is shown in Figure 2. The total undercooling, ΔT_{total}, is given by

$$\Delta T_{total} = \Delta T_t + \Delta T_c + \Delta T_k \qquad (7)$$

where ΔT_t, ΔT_c, and ΔT_k, are the thermal undercooling, solutal undercooling, and kinetic undercooling, respectively. ΔT_t is defined as

$$\Delta T_t = \frac{1}{C_{pL}} (\Delta H_f - \frac{J}{V}) \qquad (8)$$

where C_{pL} is the specific heat of the liquid, J is the heat extraction rate through the solid, and V is the growth velocity. Note that ΔT_t can be not only positive but negative or zero depending on the magnitudes of J and V. ΔT_C is given by

$$\Delta T_c = m_L C_0 (1 - \frac{m'_L/m_L}{k}) \qquad (9)$$

where m_L is the slope of the equilibrium liquidus, C_0 is the nominal solute concentration, and m'_L is the slope of the liquidus taking into account the deviation from equilibrium due to the high growth rate. It is determined by[13]

$$m'_L = m_L (1 + \frac{k_e - k(1-\ln(k/k_e))}{1-k_e}) \qquad (10)$$

where k_e and k are the equilibrium and non-equilibrium partition ratio at the solid/liquid interface, respectively. These are linked by[14]

$$k = \frac{k_e + (a_0 V / D)}{1 + (a_0 V / D)} \qquad (11)$$

where D is the solute diffusivity in the liquid and a_0 is a characteristic length on the order of the interatomic distance in the liquid.[14,15] Finally, the kinetic undercooling ΔT_k is determined by[10,13]

$$\Delta T_k = \frac{V}{\mu} \qquad (12)$$

The kinetic coefficient μ is defined as

$$\mu = \frac{\Delta H_f V_S}{R_g T_L^2} \qquad (13)$$

where V_S is the speed of sound in the liquid, and R_g is the universal gas constant.

The stability of plane-front growth is given by the thermal gradient in the liquid (G_L), thermal gradient in the solid (G_S), and the temperature gradient induced by the concentration gradient ($m'_L G_C$):

$$G_L = -\frac{V}{\alpha}\Delta T_t \qquad (14)$$

$$G_S = \frac{J}{k_S} \qquad (15)$$

and

$$G_c = \frac{-(1-k)\, V\, C_0}{k\, D} \qquad (16)$$

Plane-front growth is stable when[16]

$$-(\bar{k}_L G_L + \bar{k}_S G_S) + m'_L G_c < 0 \qquad (17)$$

where $\bar{k}_L$ and $\bar{k}_S$ are the weighted conductivities of the liquid and the solid, respectively.

2.4 Numerical Calculations

The above models were implemented numerically. Two alloy compositions which were used in the chill casting experiments, Fe-17.5Cr-12.2Ni and Fe-18.5Cr-11.3Ni were employed. Thermodynamic data necessary for the calculation were obtained using Thermo-Calc[17]. The thermodynamic data and thermophysical data used are listed in Table 1.

3. Results and Discussion

3.1 Nucleation in Chill Casting

Figure 3 shows calculated nucleation temperatures for fcc and bcc in Fe-17.5Cr-12.2Ni during continuous cooling. In the calculation, the contact angle between the solid nucleus and the substrate was assumed to be the same for bcc and fcc, and angles of 30°, 45° and 60° were used. In the figure, the intersection of one of the calculated curves with a given cooling curve is defined as the nucleation temperature of the phase of interest for that cooling rate and wetting angle. The results indicate that bcc nucleation always takes place earlier than fcc nucleation during continuous cooling even at cooling rates as high as 10^6 K/s. The nucleation temperature of bcc can be up to a hundred degrees higher than that of fcc, depending on the contact angle. However, the difference seems to be unchanged by cooling rate. Results were similar for Fe-18.5Cr-11.3Ni.

The occurrence of the nucleation of bcc and fcc can be made more nearly simultaneous by increasing cooling rate. Therefore, coexistence of fcc nucleation with bcc nucleation may be possible in the rapid quenching situation. In general, when a melt reaches its nucleation temperature, the subsequent temperature increase (recalescence) is determined by the competition between external heat extraction and internal heat evolution by crystallization. If the external heat extraction rate is sufficiently high, the melt can be further supercooled (or hyper-cooled) in spite of the solid (bcc) formation. Suppose the cooling rate of the melt in gas-cooled solidification is 10^2 K/s and that in chill casting at the chill surface is 10^6 K/s[3,5,6]; it will take only 10^{-4} s to traverse the 100 K difference in nucleation temperature in chill casting, while it would take 1 s in the gas-cooled solidification process. In other words, at a sufficiently rapid cooling rate, the melt can reach the fcc nucleation temperature from the bcc nucleation temperature within a time interval

sufficiently short that the heat evolution by bcc crystallization remains small. This is schematically illustrated in Figure 4.

In addition, the possibility of fcc nucleation may be enhanced by the presence of bcc nuclei. It was shown in a previous chapter that a higher fraction of bcc in the liquid is amenable to subsequent fcc nucleation in an undercooled condition. This situation can be attained at the very beginning of solidification by the dense but thin layer of bcc at the chill interface in the presence of a steep temperature gradient. This was not confirmed in experiments of chill casting, however.

In summary, calculations and experiment suggest that bcc nucleation is favored over fcc in the two alloys studied, at both slow and rapid cooling rates. On the other hand, fcc nucleates nearly concurrently in the case of a rapid cooling rate, either from the rapid supercooling of the melt to the somewhat lower nucleation temperature of fcc, or through catalytic nucleation at the previously nucleated bcc, or a combination of both.

3.2 Possible Situations of Preferential Fcc Growth

Figure 5 shows the effect of heat extraction rate on the growth velocity of fcc and bcc dendrites in Fe-18.5Cr-11.3Ni at various melt temperatures (1650 K, 1600 K, and 1500 K). The results were calculated via the dendrite model for chill casting proposed in the previous chapter. It is apparent that the growth velocity of bcc dendrites is always higher than that of fcc dendrites at the melt temperatures examined. The difference in growth velocity becomes smaller as the heat extraction rate increases, and fcc would grow faster than bcc at melt temperatures lower than 1500 K. An important piece of information from the figure is that increasing heat extraction rate does not affect the ranking of growth velocities. In other words, as long as fcc and bcc grow with dendritic morphology, the advantage of bcc growth would be unchanged at small to medium undercooling levels regardless of heat extraction rate.

Since Fe-Cr-Ni alloys have narrow freezing temperature ranges, solute diffusion has an effect on the dendritic growth only at very small undercoolings, and growth into an undercooled melt is essentially controlled by thermal diffusion at small to medium undercoolings. The latent heat generated by fcc growth is approximately 20 % larger than that by bcc growth. Therefore, as long as the growth is thermally controlled, the growth of fcc may be slower than that of bcc. However, when the melt undercooling is sufficiently large, the kinetic effect becomes significant, and the growth velocity of fcc can become greater than that of bcc. As mentioned in the previous chapter, the effect of heat extraction becomes noticeable only when the ratio J/V is comparable to ΔH_f. However, dendritic growth becomes unstable when the ratio reaches $2\Delta H_f$. Therefore, the effect of heat extraction rate on growth velocity of dendrites is exerted only over a small range of heat extraction rates.

The above calculation of dendrite growth does not support the experimentally observed preferential growth of fcc from the coexistence of bcc and fcc nuclei. As shown in the previous chapter, the ranking of the tip temperature of fcc and bcc dendrites in Fe-18.5Cr-11.3Ni alloy is changed with increasing undercooling, but is not changed with increasing heat extraction. Therefore, tip temperature does not appear to explain the effect of chill casting on the preferential fcc growth alone despite the prediction by Mizukani et al[1]. The effects of parameters of the kinetic effect and solute-trapping effect were also investigated; kinetic coefficient μ was changed approximately from 0.05 to 3.0 m $s^{-1}K^{-1}$, and interatomic distance a_0 in Aziz's formula for solute trapping was changed from 10^{-10} to 10^{-8} m. However, the results are not strongly suggestive of the preferential fcc solidification during chill casting. On the other hand, experimental results are clear and reproducible, as shown in a previous chapter. Therefore, the actual situation may be more complex than growth competition between isolated dendrites of fcc

and bcc in normally expected chill casting conditions. Factors which may lead to preferential fcc growth are anticipated as follows:

- high heat extraction rate and high melt undercooling
- different growth morphology between fcc and bcc
- selective heat extraction through one phase either geometrically or due to conductivity difference
- an interaction between fcc and bcc dendrites
- strong fluid flow
- behavior controlled by non-steady state process

3.3 High Heat Extraction Rate and High Melt Undercooling

Tip velocities of fcc and bcc dendrites are calculated for Fe-17.5Cr-12.2Ni and Fe-18.5Cr-11.3Ni assuming a high heat extraction rate, 3×10^{10} W m^{-2}, and the results are shown in Figures 6 and 7, respectively. In both cases, dendritic growth of fcc and bcc is stable only at high undercoolings or low melt temperatures: up to approximately 1480 K for fcc and up to approximately 1410 K for bcc. The maximum temperature for dendritic growth for fcc is higher than that for bcc by approximately 70 K. Above the maximum temperature for dendritic growth, plane-front growth becomes stable. When the melt is undercooled sufficiently, an fcc dendrite has a higher velocity than bcc dendrites. In other words, whenever the growth morphology is dendritic, fcc growth is faster, which is consistent with observations of preferential fcc solidification.

In light of this result, the issue to be addressed is the attainability of the required heat extraction rate and undercooling. If heat transfer at the metal/chill interface is limiting, a heat extraction rate of 3×10^{10} W m^{-2} corresponds to a heat transfer coefficient greater than 2×10^{7} W $m^{-2}K^{-1}$. Mühlbach et al.[5] evaluated the heat transfer coefficient at a metal/substrate interface through the measurement of temperature during the melt spinning of steel on a CrAl-steel rotating wheel, and reported 10^{8} W m^{-2} for ideal metal/substrate contact. The heat transfer coefficient can initially be

very high after the melt impacts the wheel, but then decreases with time. Zhang and Atrens[18] also reported similar high heat transfer coefficients. Therefore, it is possible to attain very high heat extraction rates during nucleation and initial stages of growth even when using a solid chill. If the heat extraction rate is sufficiently high, then the melt is supercooled at a very high cooling rate, and a large undercooling can be also achieved. Mizukami et al.[2] measured melt undercoolings of more than 200 K in the chill casting of stainless steel. In the present study, the likelihood of required heat extraction rate is increased when the melt is cast into an In-Ga liquid chill bath. In fact, very fine cellular fcc was observed to grow from the chill/metal surface in both Fe-17.5Cr-12.2Ni and Fe-18.5Cr-11.3Ni when these alloys were quenched into the In-Ga bath from the undercooled liquid state. On the other hand, bcc growth was not observed within approximately 100 μm from the surface, although bcc nuclei were expected to coexist with fcc nuclei at the surface. This implies that only fcc grew with cell/dendrite morphology from the coexisting fcc and bcc nuclei.

3.4 Growth Competition between Different Growth Morphologies

The dendrite model proposed for chill casting suggests that instability of dendritic growth occurs in fcc at lower heat extraction rates than in bcc when the melt undercooling is small. Figure 8 shows the calculated tip velocities of fcc and bcc dendrites for Fe-18.5Cr-11.3Ni at the heat extraction rate of 3×10^8 W m^{-2}. The heat extraction rate corresponds to the heat transfer coefficient of 2×10^5 W $m^{-2}K^{-1}$, which is closer to values reported for chill casting processes[4,6,19]. For undercoolings up to approximately 50 K, fcc dendritic growth is infeasible, and therefore, bcc dendrites and/or fcc plane-front can grow into the undercooled melt. Although the undercooling level is small as compared to levels normally anticipated[2], the situation seems to be close to actual observations. That is, in microstructures of chill castings, small but well developed bcc dendrites were retained at the chill surface, while fcc appeared to be planar. Assuming the velocity of planar growth of fcc is higher

than that of bcc, the growth behavior may be as shown in Figure 9. Planar fcc and dendritic bcc coexist after nucleation and grow into the undercooled melt (Figure 9(a)). Then, since planar fcc grows faster, fcc eventually encompasses bcc dendrites and bcc can no longer grow. This also retards the ripening and coarsening of bcc dendrites due to the absence of the liquid, and branches of bcc dendrites are retained in the fcc matrix (Figure 9(b)). As the solidification front of planar fcc moves away from the chill, heat extraction rate decreases, and the plane-front interface of the fcc changes to dendritic one (Figure 9(c)). This sequence can explain the structure observed in Figures 3 to 5 in Chapter VI.

Then, the issue to be discussed is whether the planar growth of fcc can be faster than the dendritic growth. Figure 10 compares the tip velocity of dendrites and the growth velocity of planar fcc, where the melt temperatures of primary interest is about 1670 K to 1720 K at which the dendritic growth of fcc is infeasible. When the heat extraction rate is 3×10^8 W m^{-2} for both phases, the growth velocity of a bcc dendrite is higher than that of fcc plane-front except for very small undercooling levels. This is expected as long as the solidification is thermally controlled and the same amount of heat is extracted from each phase. Planar fcc can grow faster than dendritic bcc only when more amount of heat is selectively extracted from fcc than that from bcc, as also shown in Figure 10. As heat extraction through fcc increases, the growth velocity of planar fcc increases and a temperature range for preferential fcc growth expands. Note that, as heat extraction rate increases, planar fcc becomes more stable while dendritic fcc less. Therefore, the effect of selective heat extraction through fcc is beneficial only to the competition between planar fcc and dendritic bcc. Selective increase in heat extraction through fcc might be achieved either geometrically and/or due to conductivity difference. For example, locally better contact between the chill and the alloy melt is likely to enhance the nucleation of fcc and its planar growth, while locally insufficient contact results in low heat extraction rate leading to the preferential nucleation of bcc and its dendritic growth. In the previous chapters, it was shown that a

bcc dendrite tends to possess well-developed branches. The mixture of dendrite branches and interdendritic liquid reduces the apparent thermal conductivity of the mushy zone due to the low conductivity of the liquid, and therefore, the heat extraction rate from bcc is decreased.

3.5 Interaction between Fcc and Bcc

Although a dendrite tip model assumes an isolated dendrite, in reality growing dendrites may affect each other. In particular, when more than one phase coexists and grows, the thermal and solute fields in the liquid are likely to be distorted by the different characteristics of the dissimilar phases; the thermal field is more likely to be affected in the case of rapid solidification because of the longer diffusion distance.

Figure 11 shows the tip temperature of fcc and bcc dendrites calculated at a given temperature and as a function of heat extraction rate. It is obvious that the tip temperature of fcc is higher than that of bcc, and the difference becomes greater as the melt temperature decreases (i.e., the melt undercooling increases). The difference between the tip temperatures is almost constant regardless of heat extraction rate. Suppose fcc dendrites and bcc dendrites densely coexist; since fcc dendrites have higher interface temperatures than bcc dendrites, bcc dendrites may be heated by fcc dendrites so as to eliminate the temperature difference, which leads to a decrease in the growth velocity of bcc dendrites. Figure 12 shows the effect of dendrite tip temperature on the growth rate of fcc and bcc dendrites in Fe-18.5Cr-11.3Ni alloy. The calculation assumes a heat extraction rate of 1×10^9 W m^{-2}. If both phases have the same tip temperature, an fcc dendrite always grows faster than a bcc dendrite. In other words, the dendrite tip of bcc is more sensitive to fluctuations of the thermal field than that of fcc. In this case, the effect of chill casting is only to provide a competition between the two phases by the rapid cooling of the liquid through the nucleation temperatures. The

possibility of interaction between the two phases can also be applied to the competition between planar fcc and dendritic bcc.

3.6 Effect of Fluid Flow in the Melt

Significant fluid flow is expected to exist within the quenched drop when the melt impacts on the chill. This flow increases the effective thermal conductivity (and therefore, thermal diffusivity) of the liquid. As shown in Figure 10 of Chapter V, a higher conductivity of the liquid increases the growth velocity of fcc more effectively than that of bcc. On the other hand, the strong fluid flow may affect even the temperature field near the solid/liquid interface, and may decrease the difference of interface temperature between growing dendrites of bcc and fcc. Then, as seen in Figure 12, the growth of fcc may be favored.

4. Conclusions

The mechanism of preferential fcc solidification observed in the chill casting of Fe-Cr-Ni alloys is discussed. Models of nucleation, dendrite growth in the chill casting situation, and planar growth are applied to the discussion.

Calculations of nucleation temperature suggests that the nucleation of bcc is always favored from the undercooled melt regardless of the cooling rate. However, almost concurrent bcc and fcc nucleation can be achieved by rapid cooling of the melt at the chill. The formation of fcc nuclei is either from the rapid supercooling to the somewhat lower nucleation temperature of fcc, or through catalytic nucleation on previously nucleated bcc.

Several possibilities are suggested for the selective growth of fcc from the coexistence of fcc and bcc nuclei during chill casting. One is the case of high heat extraction rate and high undercooling. This

brings about higher growth rate for fcc dendrites than bcc dendrites, and may explain the structure of the sample quenched into an In-Ga chill bath. The second possibility is the growth competition between dendritic bcc and planar fcc, which is predicted by the proposed dendrite model for chill casting. This explains the structure observed in experiments very well. Selective heat extraction through fcc may assist the fcc in dominating the dendritic growth of bcc. The interaction between fcc and bcc dendrites is another possibility. The distortion of the thermal field in the liquid may heat bcc dendrites, causing dominant fcc growth. Strong fluid flow in the liquid also favors the growth of fcc, increasing the effective thermal conductivity of the liquid or agitating thermal field in the liquid. These factors may work individually or interactively; the phenomenon needs further experimental and theoretical investigation.

References

1. H. Mizukami, T. Suzuki, T. Umeda, and W. Kurz: *Mater. Sci. Eng.*, 1993, vol. A177, p. 361
2. H. Mizukami, T. Suzuki, and T. Umeda: *Tetsu-to-Hagane*, 1991, vol. 77, p. 134
3. J. M. Vitek, A. Dasgupta, and S. A. David: *Metall. Trans. A*, 1983, vol. 14A, p. 1833
4. T. W. Clyne: *Metall. Trans. B*, 1984, vol. 15B, p. 369
5. H. Mühlbach, G. Stephani, R. Sellger, and H. Fiedler: *Int'l J. Rapid Solidification*, 1987, vol. 3, p. 83
6. K. Takeshita and P. H. Shingu: *Trans. Japan Inst. Metals*, 1986, vol. 27, p. 454
7. D. Turnbull and J. C. Fisher: *J. Chem. Phys.*,1949, vol.17, p. 71
8. D. Turnbull: *Contemp. Phys.*, 1969, vol. 10, p.473
9. F. Spaepen and D. Turnbull: *Rapidly Quenched Metals II*, N. J. Grant and G. B. Giessen, eds., MIT Press, Cambridge, MA, 1976, p. 205

10. D. Turnbull: *Metall. Trans. A*, 1981, vol. 12A, p. 695
11. F. Spaepen and R. B. Meyer: *Scr. metall.*, 1976, vol. 10, p. 257
12. C. V. Thompson: Ph. D. Thesis, Harvard University, 1981
13. W. J. Boettinger, S. R. Coriell, and R. Trivedi: *Rapid Solidification Processing: Principles and Technologies*, eds. R. Mehrabian and P. A. Parrish, Claitor's Publ. Div., 1988, p. 13
14. M. J. Aziz: *J. Appl. Phys.*, 1982, vol. 53, p. 1158
15. W. J. Boettinger, S. R. Coriel, and R. F. Sekerka: *Mater. Sci. Eng.*, 1984, vol. 65, p.27
16. W. W. Mullins and R. F. Sekerka: *J. Appl. Phys.*, 1964, vol. 35, p. 444
17. B. Sundman, B. Jansson, and J.-O. Andersson: *CALPHAD*, 1985, vol. 9, p. 153
18. X. Zhang and A. Atrens: *JOM*, 1994, vol. 46, p. 48
19. H. A. Davies: *Rapidly Quenched Metals*, S. Steeb and H. Warlimont eds., Elsevier Science Publ., 1985, p. 101
20. Y. Ono: *The Properties of Liquid Metals*, S. Takeuchi, ed., Taylor and Francis, London, 1973, p. 543
21. B. Lally, L. Biegler, and H. Henein: *Metall. Trans. B*, 1990, vol. 21B, p. 761
22. W. J. Boettinger, S. R. Coriel, and R. F. Sekerka: *Mater. Sci. Eng.*, 1984, vol. 65, p.27

Table 1: Parameter values for Fe-17.5Cr-12.2Ni and Fe-18.5Cr-11.3Ni used for the calculations involving the dendrite tip model.

parameter			Fe-17.5Cr-12.2Ni	Fe-18.5Cr-11.3Ni	ref.
T_L	liquidus temperature (K)	(fcc)	1726.19	1722.40	
		(bcc)	1721.88	1727.61	
ΔH_f	enthalpy of fusion (J mol^{-1})	(fcc)	11332.44	11209.61	
		(bcc)	8947.16	8943.64	
ΔS_f	entropy of fusion (J mol^{-1}K^{-1})	(fcc)	6.5552	6.4678	
		(bcc)	5.6766	5.6388	
k_{Cr}	partition ratio of Cr	(liq/fcc)	0.8630	0.8578	
k_{Ni}	partition ratio of Ni	(liq/bcc)	0.7692	0.7710	
m_L	slope of liquidus (K wt%$^{-1}$)	(fcc)	-4.1248	-4.3439	
		(bcc)	-6.6132	-6.4793	
C_{pL}	specific heat of liqiud (J mol^{-1}K^{-1})		43.747	43.789	
$\overline{V}$	molar volume (m^3 mol^{-1})	(liq)	7.71×10^{-6}		
		(fcc)	7.71×10^{-6}		
		(bcc)	7.71×10^{-6}		
D_{Cr}	diffusivity of Cr in liquid (m^2 s^{-1})				
	D_0 diffusion constant (m^2 s^{-1})		2.67×10^{-7}		[20]
	Q activation energy (J mol^{-1})		6.69×10^{4}		[20]
D_{Ni}	diffusivity of Ni in liquid (m^2 s^{-1})				
	D_0 diffusion constant (m^2 s^{-1})		4.92×10^{-7}		[20]
	Q activation energy (J mol^{-1})		6.77×10^{4}		[20]
k_L	thermal conductivity of liquid (J m^{-1}K^{-1}s^{-1})		35		[21]
k_{fcc}	thermal conductivity of fcc (J m^{-1}K^{-1}s^{-1})		35		
k_{bcc}	thermal conductivity of bcc (J m^{-1}K^{-1}s^{-1})		35		
$\alpha_{liq/fcc}$	ratio of thermal diffusivity in liquid to in fcc (-)		1.4		
$\alpha_{liq/bcc}$	ratio of thermal diffusivity in liquid to in bcc (-)		1.0		
V_0	sound velocity in liquid (m s^{-1})		2000		[13]
a_0	interatomic distance in liquid (m)		1×10^{-9}		[22]

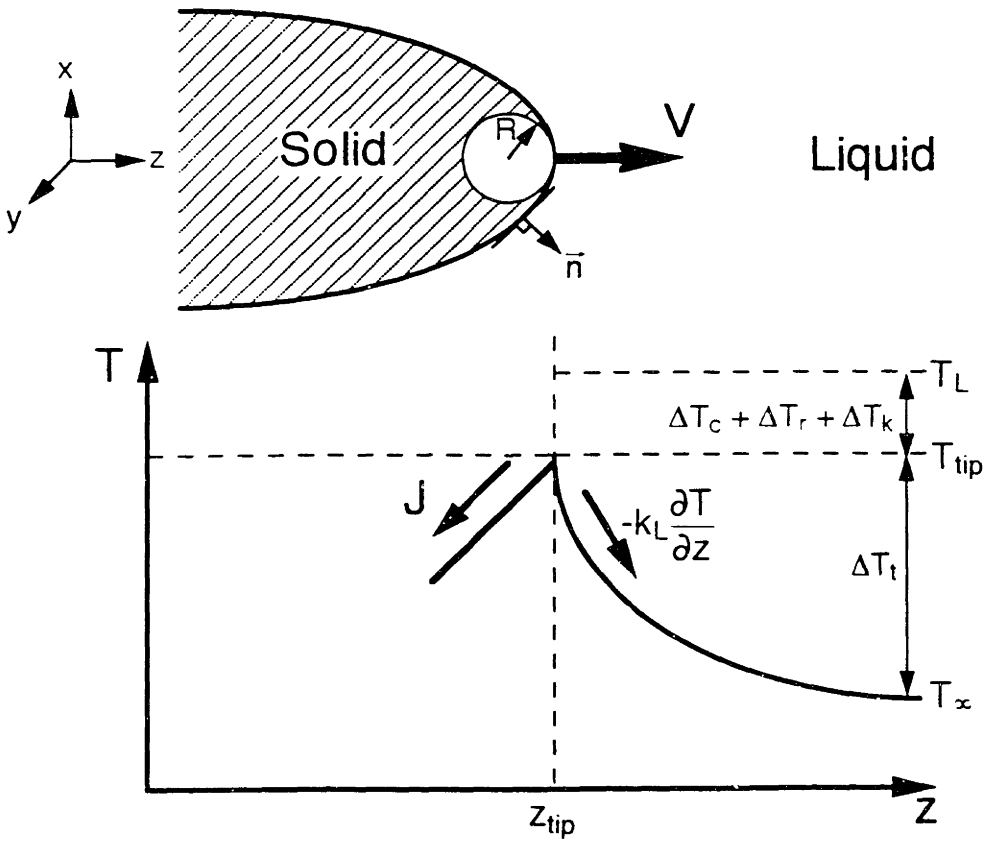

Figure 1 - Schematic of the thermal field around a dendrite tip growing into an undercooled melt during chill casting

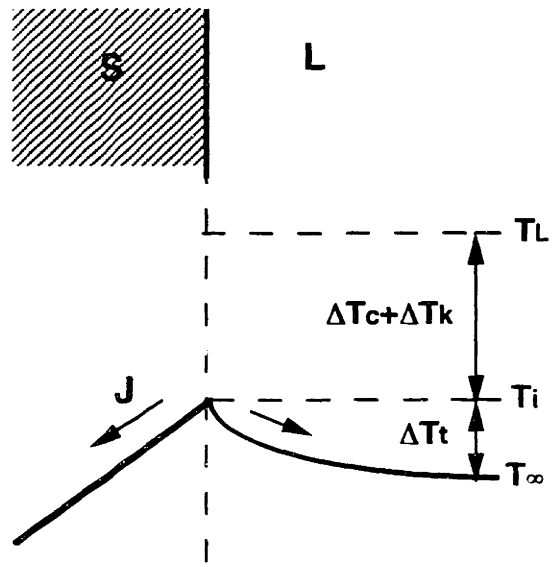

Figure 2 - Schematics of the thermal field around the solid/liquid interface during planar growth with the presence of thermal undercooling.

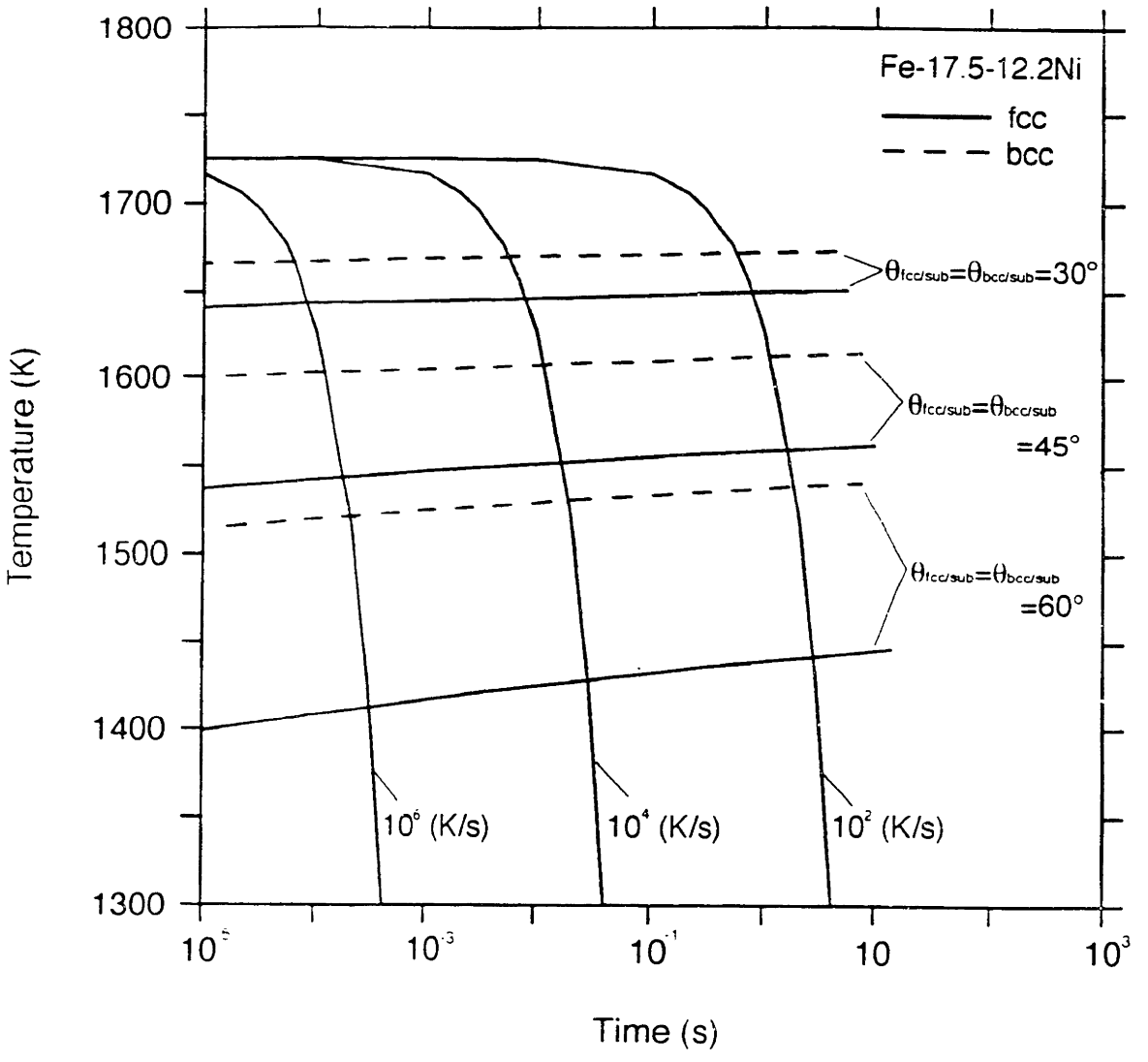

Figure 3 - Calculated nucleation temperatures of fcc and bcc during continuous cooling. Contact angles between fcc and the substrate ($\theta_{fcc/sub}$) and between bcc and the substrate ($\theta_{bcc/sub}$) were assumed to be equal, and calculations were made assuming contact angles of 30°, 45°, and 60°. The intersection of one of these calculated curves with a given cooling curve gives the nucleation temperature of the phase of interest for that particular situation.

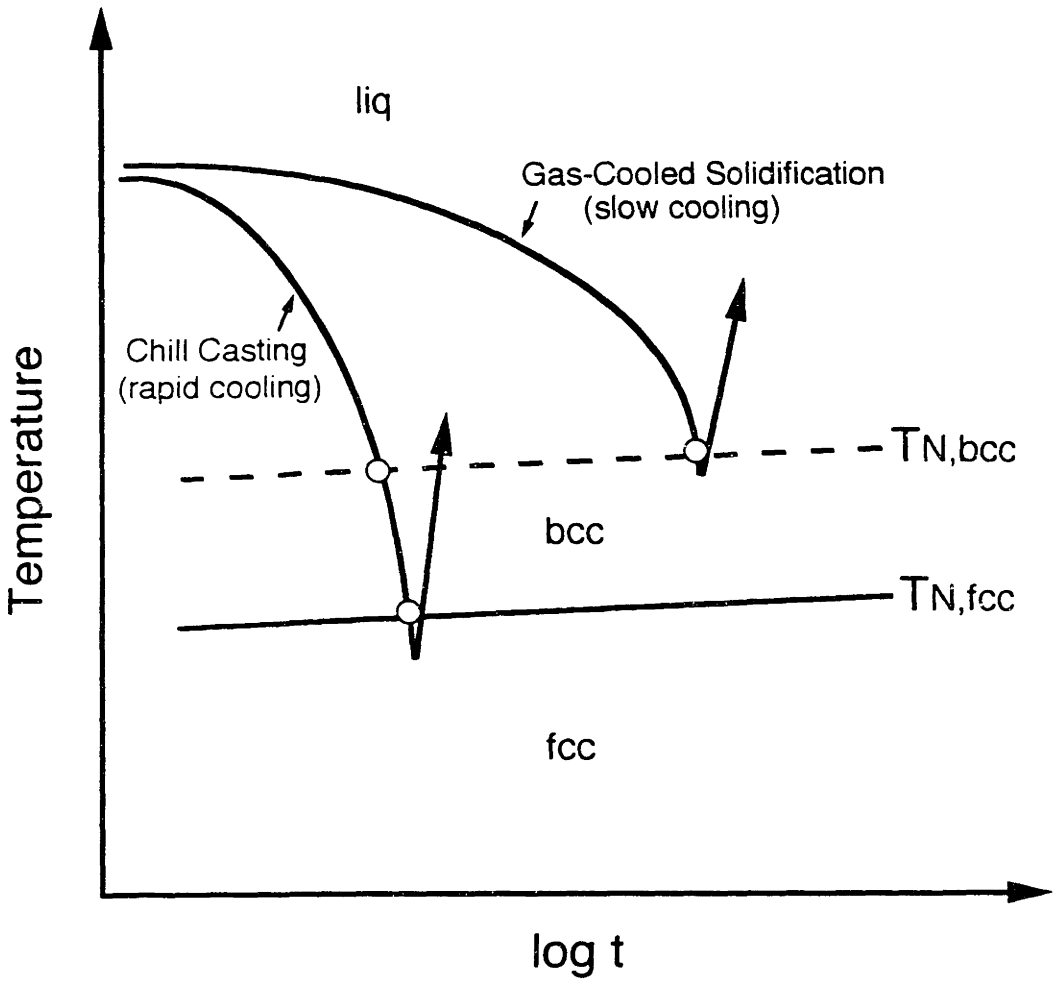

Figure 4 - Schematics of cooling curves at a high cooling rate and a low cooling rate. If the cooling rate is sufficiently high, the melt could be supercooled to the fcc nucleation temperature a very short time after the bcc nucleation temperature is reached.

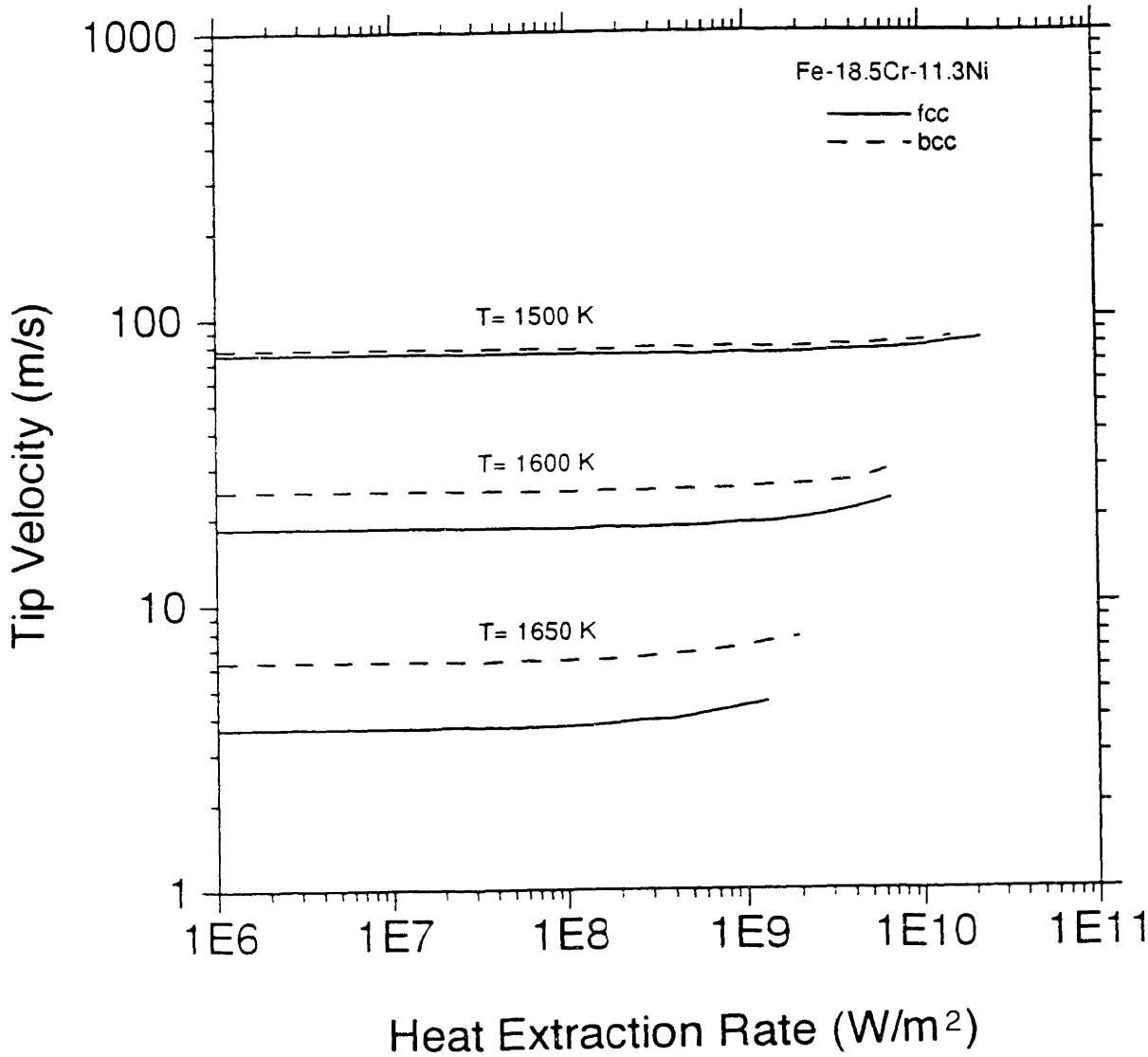

Figure 5 - The effect of heat extraction rate on tip velocities of fcc and bcc dendrites for Fe-18.5Cr-11.3Ni at various melt temperature: 1650 K, 1600 K, and 1500 K.

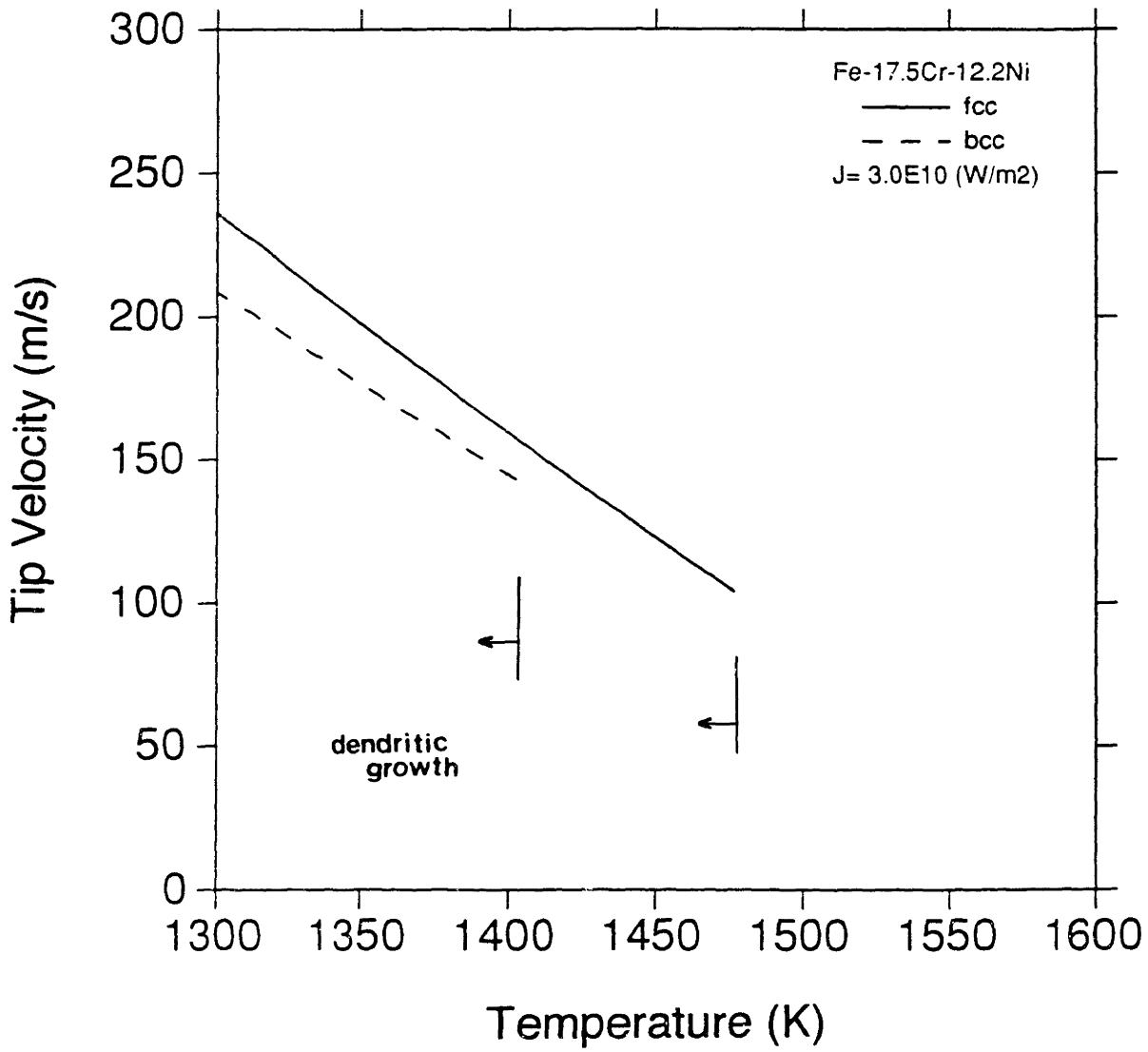

Figure 6 - The effect of melt temperature on tip velocities of fcc and bcc dendrites calculated for Fe-17.5Cr-12.2Ni at a heat extraction rate of 3×10^{10} W m^{-2}.

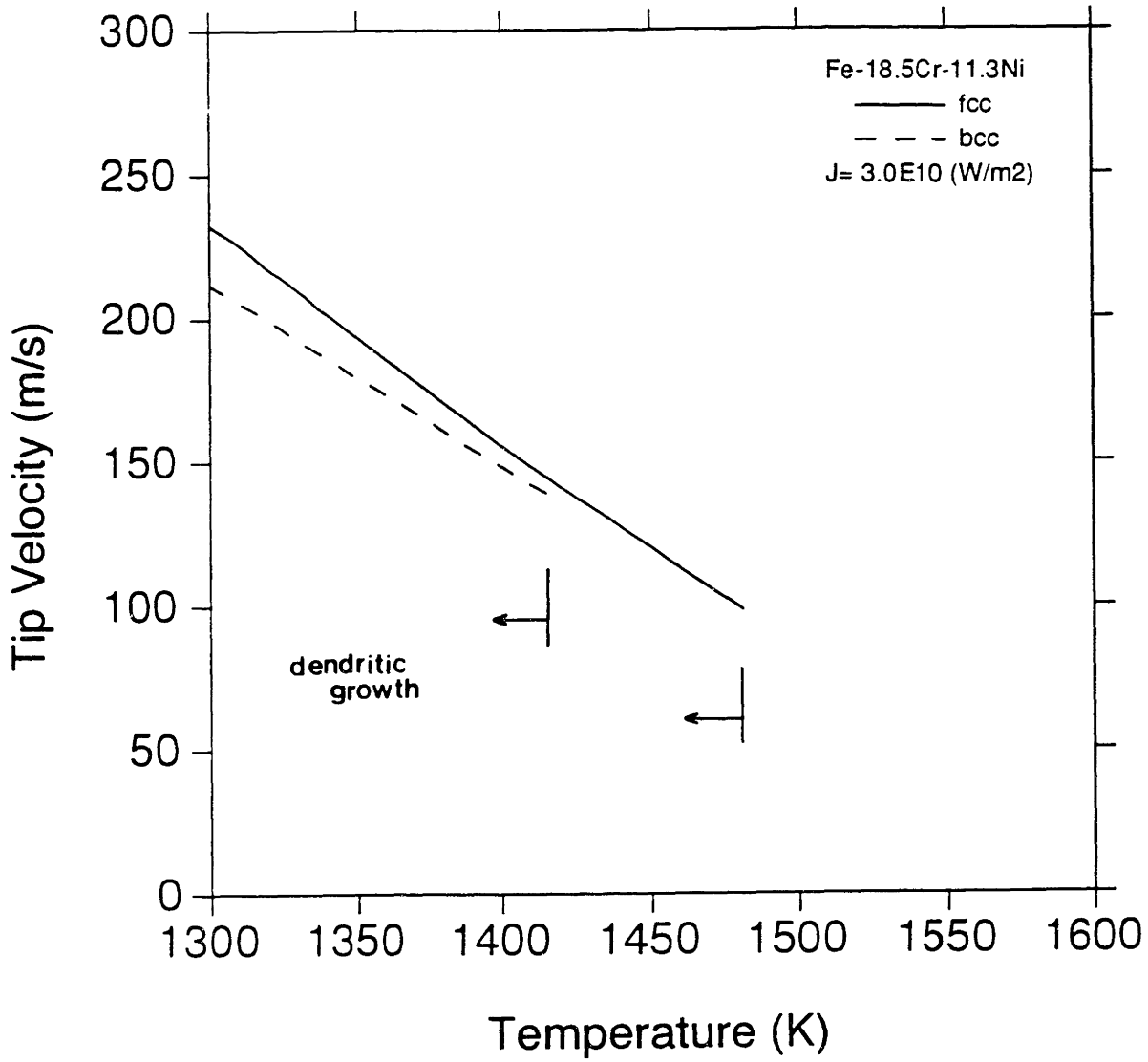

Figure 7 - The effect of melt temperature on tip velocities of fcc and bcc dendrites calculated for Fe-18.5Cr-11.3Ni at a heat extraction rate of 3×10^{10} W m^{-2}.

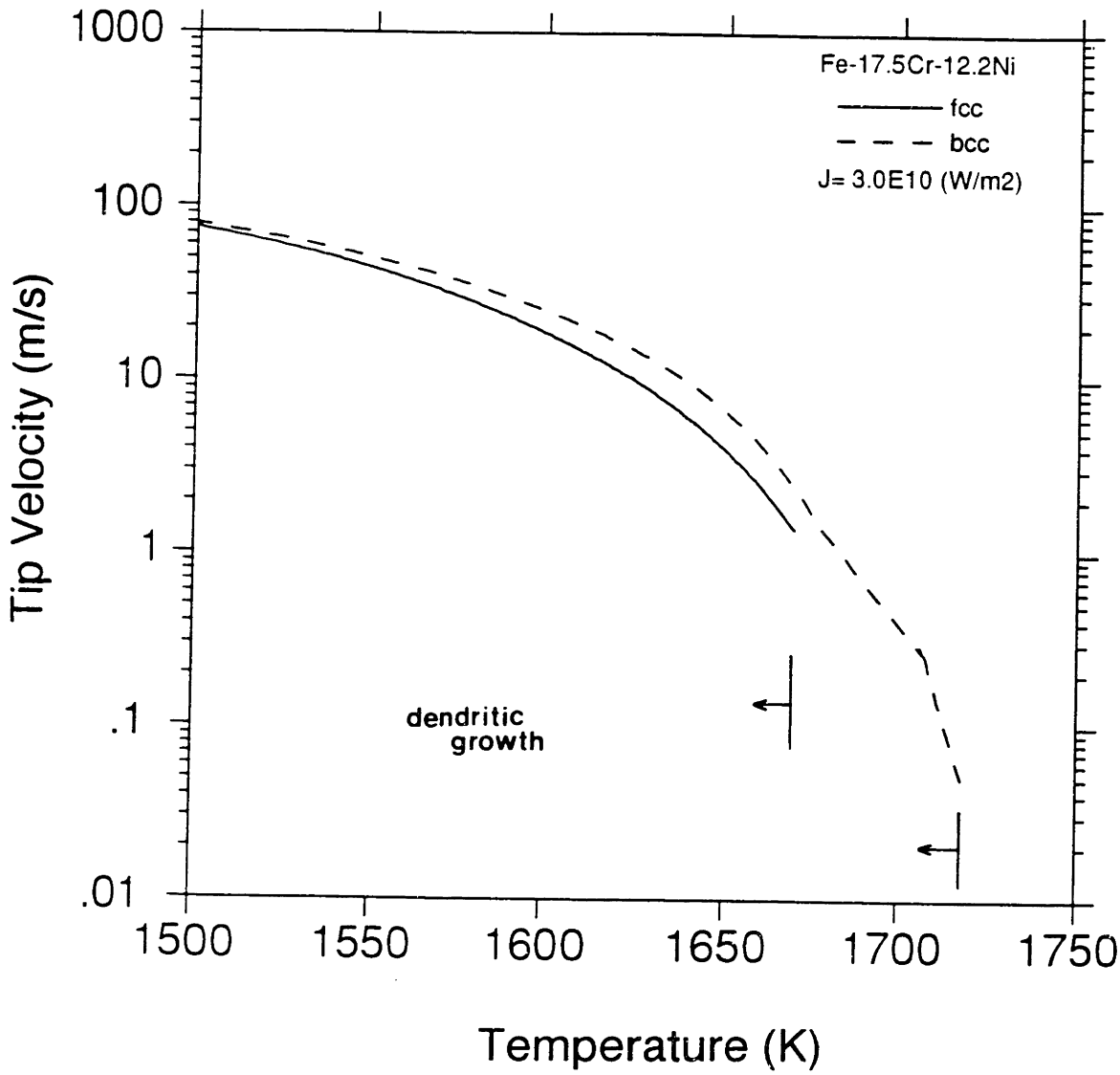

Figure 8 - The effect of melt temperature on tip velocities of fcc and bcc dendrites calculated for Fe-18.5Cr-11.3Ni at a heat extraction rate of 3×10^8 W m^{-2}, showing the instability of fcc dendritic growth at small undercoolings.

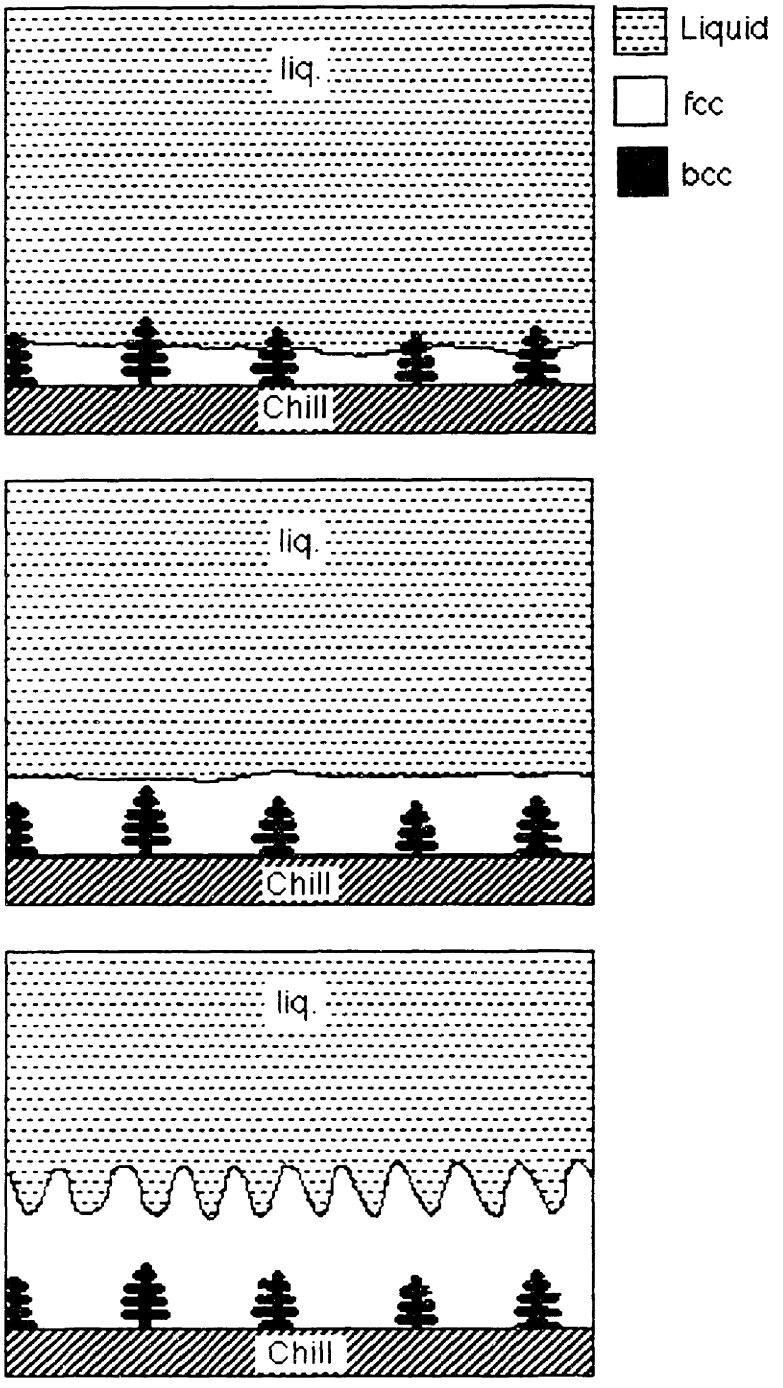

Figure 9 - Schematic illustration of the growth of planar fcc preferentially to dendritic bcc.

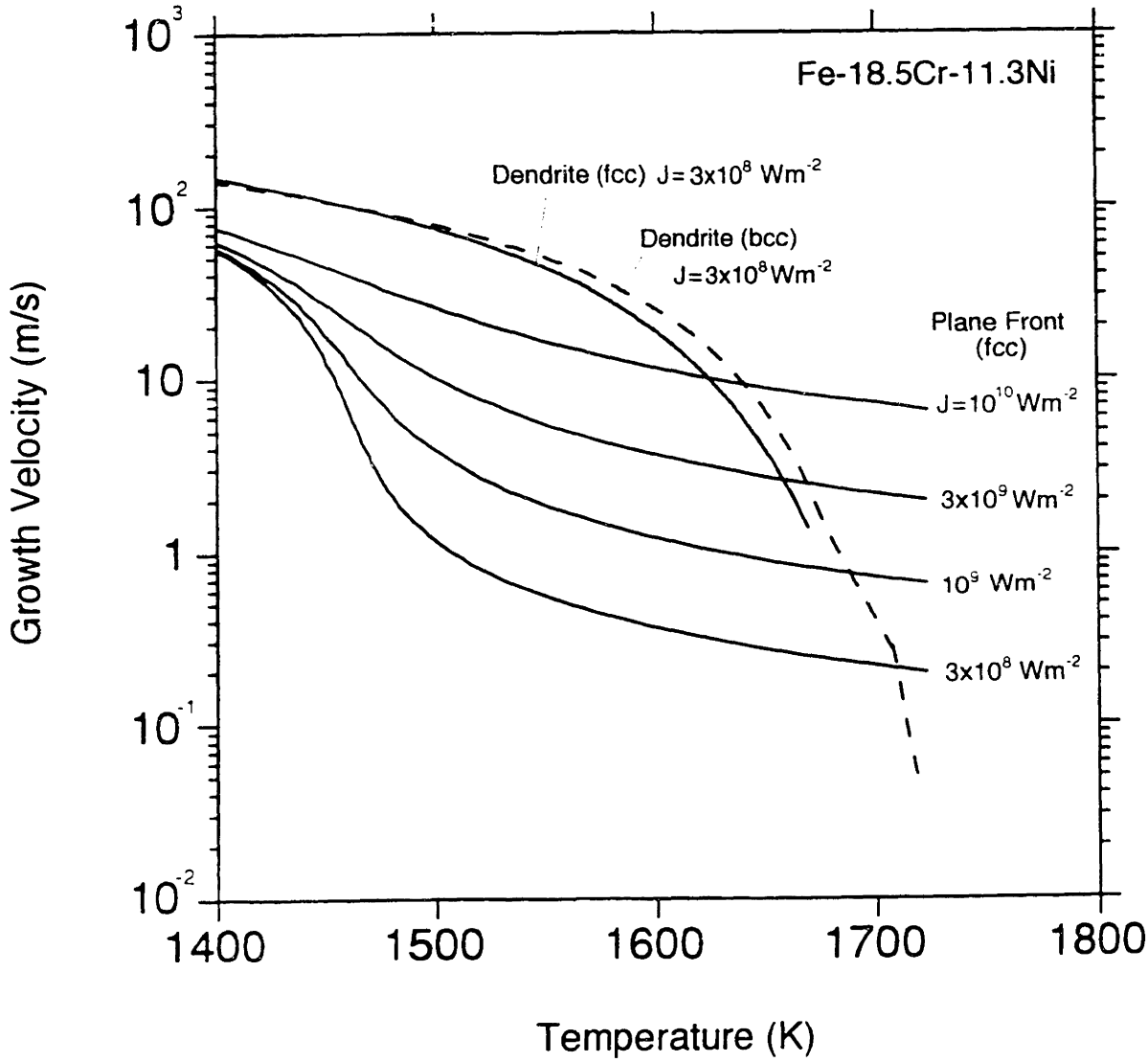

Figure 10 - Comparison of the growth velocity between a bcc dendrite and fcc plane front. Heat extraction rate through bcc is 3×10^8 W m^{-2}, while that through fcc is varied from 3×10^8 to 1×10^{10} W m^{-2}.

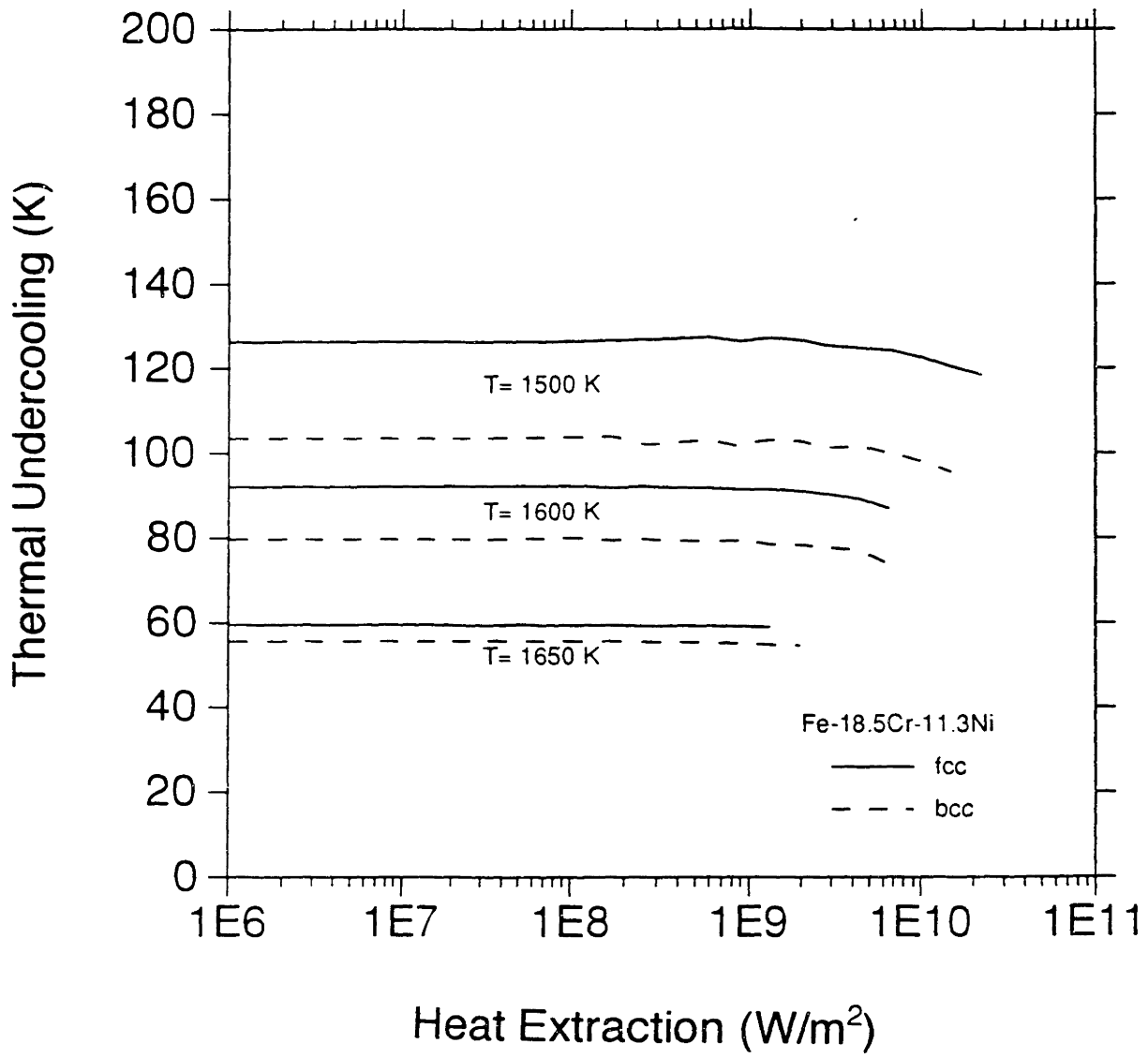

Figure 11 - The effect of heat extraction rate on thermal undercooling at the tip of fcc and bcc dendrites for Fe-18.5Cr-11.3Ni at various melt temperature: 1650 K, 1600 K, and 1500 K.

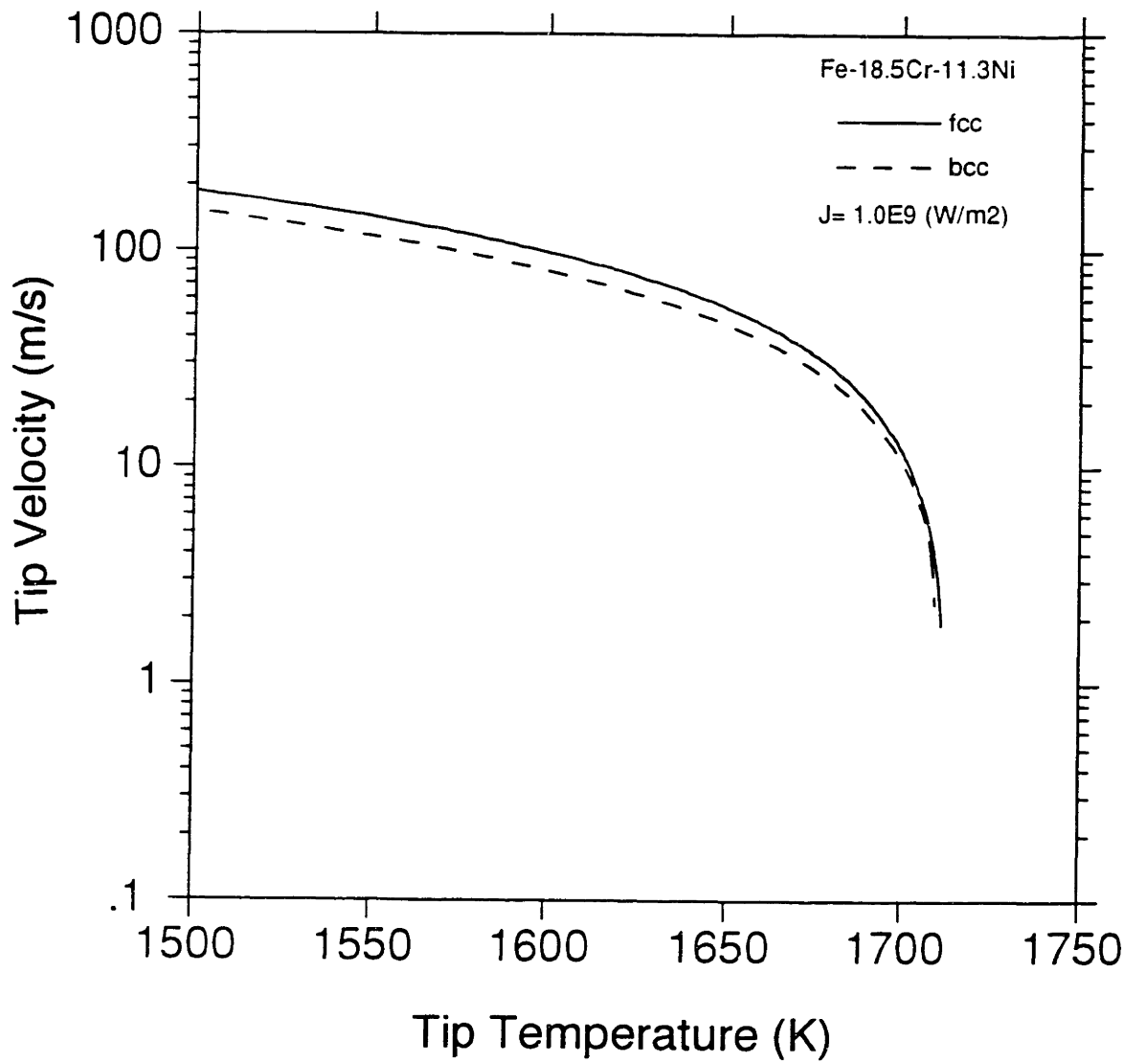

Figure 12 - The effect of dendrite tip temperature on the tip velocity of fcc and bcc dendrites at a heat extraction rate of 1 x 10^9 W m^{-2}.

Chapter VII - Bcc-to-Fcc Transformation after Rapid Solidification in Fe-Cr-Ni Alloys

Abstract

The bcc-to-fcc transformation after rapid solidification was investigated using a levitation melting and undercooling technique. Three different Fe-Cr-Ni alloy compositions close to the eutectic composition were examined. Massive transformation from bcc to fcc was found to occur in every composition when the initial undercooling is large. The metallographic features of massive fcc are presented, and the effect of rapid solidification on the transformation behavior is discussed.

1. Introduction

Primary bcc solidification of Fe-Cr-Ni alloys is often followed by the solid-state bcc-to-fcc transformation during subsequent cooling. When the alloy composition is sufficiently close to the eutectic composition, the transformation proceeds within dendrites even before solidification is completed. The primary bcc dendrites shrink, and at typical casting and welding cooling rates, the remaining bcc is retained at dendrite cores with skeletal or vermicular morphologies[1,2]. When the composition is not very close to the eutectic composition, solidification tends to be fully bcc, and the transformation is likely to occur after the completion of solidification. As a result, the transformation results in Widmanstätten fcc developing from bcc grain boundaries[1].

In the above cases, the bcc-to-fcc transformation is diffusional through the solid, and therefore, occurs via solute redistribution between bcc and fcc. Fcc is depleted in Cr and enriched in Ni, while bcc is depleted in Ni and enriched in Cr. Unless the alloy of interest contains a large amount of high-diffusivity solutes such as nitrogen, the partitioning of Cr and Ni between the two phases is distinct, and so phase identification from the solute profiles is possible.

At very high cooling rates, on the other hand, massive transformation from bcc to fcc can occur. Singh et al.[3] investigated the effect of cooling rate on the bcc-to-fcc transformation behavior from the fully bcc state in Fe-20Cr-10Ni. In their work, massive products started to replace the Widmanstätten products at a cooling rate of 100 K/s, and fully massive fcc was obtained at cooling rates of 7×10^3 K/s to 1.5×10^4 K/s. Elmer et al.[4] reported a massive transformation occurring in a Fe-26.4Cr-14.3Ni weld made by a high-speed electron beam. After solidifying as single phase bcc, the alloy transformed to massive fcc which was aligned perpendicular to the solidification direction and exhibited jagged appearance. Among four different primary bcc alloys investigated, only one alloy showed the

massive fcc despite the fact that these alloy compositions were very close to one another.

The massive transformation is defined as a composition-invariant plane-front transformation which occurs via short-range diffusion. However, there is still some controversy concerning the onset temperature of the transformation[5-8] and the mechanisms of nucleation and growth including the orientation-relationship between the parent and product phases[7,9-12]. Therefore, the massive phase is identified mainly through solute profiles and the microstructure. Although various morphologies of massive phases and their grain boundary configurations have been reported[13], structures formed by massive transformation still have appearances distinct from those formed by diffusional transformation[3,4]. Transformation temperature may also be an indication of the transformation type; it must be below the T_0 temperature for the massive transformation, where the T_0 is a temperature at which the free energy of fcc phase having the nominal composition is the same as that of bcc phase having the nominal composition.

This chapter describes the massive bcc-to-fcc transformation which was found to take place during gas-cooled solidification of Fe-Cr-Ni alloys. To the author's knowledge, research on the massive transformation of Fe-Cr-Ni alloys is very limited so far, and in particular, massive transformation from "as-solidified" bcc to fcc on post-solidification cooling has not been examined thoroughly[4]. Three Fe-Cr-Ni alloys were used; two alloys solidified as primary bcc regardless of undercooling level, and one alloy solidified as primary metastable bcc at undercoolings greater than about 20 K. Samples were melted and undercooled by a levitation technique, and solidified in flowing gas (gas-cooled solidification). Transformation of as-solidified bcc is discussed in terms of initial undercoolings and alloy compositions. The above disputed issue, nucleation and growth of the massive phase, will not be discussed in detail in the present study. The purpose is rather to investigate the effects of solidification

conditions and behavior on the subsequent occurrence of the massive bcc-to-fcc transformation in Fe-Cr-Ni alloys.

2. Experimental

Three Fe-Cr-Ni alloys were used for the present study: Fe-17.5Cr-12.2Ni (alloy A), Fe-18.5Cr-11.3Ni (alloy B), and Fe-19.7Cr-10.3Ni (alloy E). The locations of the three alloy compositions are indicated on the pseudo-binary phase diagram of the Fe-Cr-Ni system at 70 wt pct Fe shown in Figure 1. Alloy A solidifies as primary fcc on equilibrium solidification, but was observed to solidify as primary metastable bcc at melt undercoolings greater than 20 K. The alloys B and E are primary bcc on equilibrium solidification, which was unchanged for any undercooling level used in the present study. The purity of the alloys used was more than 99.96 wt pct as indicated by the chemical analyses listed in Table 1. The preparation of the starting materials was the same as described in the previous chapter.

An alloy specimen of mass 0.5 g (±0.05g) was electro-magnetically levitated and induction-melted in an atmosphere of argon and 4% hydrogen. After being superheated by approximately 100 K, the melt was then cooled by flowing high-purity helium; the melt was undercooled and finally solidified while being levitated in the flowing gas (gas-cooled solidification). Some samples were quenched into a Ga-25 pct In liquid bath immediately after the recalescence in order to "quench in" microstructural features. The thermal history of a levitated specimen was measured using high-speed pyrometry. Two different data sampling rates, 200 Hz and 200 kHz, were used to measure the whole thermal history and rapid recalescence event concurrently. The accuracy of the measured temperature difference (ΔT) from a fixed reference temperature (e.g., the liquidus temperature) was within ±7%. The cooling rate of specimens during gas-cooled solidification is about 100 to 150 K/s for both the fully liquid state and the fully solid state.

Microstructures were observed by optical microscopy. Samples (approximately 5 mm dia.) were cut into halves, and the cross-section was examined. Electrolytic etching was used to reveal the microstructure; the electrolyte was an aqueous solution of 10 vol pct sulfuric acid, and the etching was conducted at 4 V for 5 to 10 s. Concentration distributions of Cr and Ni in the microstructures were measured using computer-aided microprobe analysis (CMA). Two dimensional scanning was conducted by 1 μm steps over the area of interest on the as-polished cross-section of a sample. Operating conditions of the CMA were: an acceleration voltage of 15 kV, a beam current of 1 μA, a beam size of 1 μm, and a beam irradiation time of 20 ms per point. X-ray diffraction (XRD) analysis was employed to identify phases in the microstructures. Measurements were carried out on the as-polished cross section of a sample. The irradiation area was about 2 x 10^{-5} m^2. Operating conditions for XRD were: an acceleration voltage of 60 kV and a current of 300 mA for the X-ray source (Rigaku, RU-300) using a copper target , a divergence slit of 1° and a receiving slit of 0.3° for the diffractometer, and a diffraction angle, 2θ, varying from 30° to 100°. Phase identification in a small area was also attempted by using a micro-diffractometer (Rigaku, RAD-rA); the measured area is approximately 200 μm dia. (3 x 10^{-8} m^2) in this system. Operating conditions of the X-ray source (Rigaku, RU-200) were an acceleration voltage of 50 kV and a current of 160 mA using a copper target. Diffraction was with 2θ scanning from 85° to 40°.

3. Results

3.1 Structure of Fe-18.5Cr-11.3Ni Alloy (Alloy B) after Gas-Cooled Solidification

Figures 2(a) and 2(b) show microstructures of Fe-18.5Cr-11.3Ni (alloy B) which were solidified as primary bcc, with initial

undercoolings of 14 K and 150 K, respectively. In Figure 2(a), primary bcc dendrites (dark) are clearly identified in the fcc matrix; the lacy structure within each dendrite is a mixture of bcc and fcc resulting from the bcc-to-fcc transformation. This final microstructure is quite similar to the conventional stainless steel cast structure of primary bcc solidification (FA mode). When the initial undercooling is 150 K, the final microstructure contains coarse grains near the specimen surface, as shown in Figure 2(b). Substructures are not observed within these grains, but there is twinning which indicates that these grains are fcc. Some grain boundaries are fairly straight and parallel, while others are irregular. Lacy structures which are the mixtures of fcc and bcc are seen along some grain boundaries. These coarse-grained regions extend approximately 500 μm from the surface in the sample shown, and the thickness increases as the initial undercooling increases. The rest of the specimen, i.e., the core region, consists of well-aligned blocky fcc as well as lacy structures of an fcc-bcc mixture, as shown in Figure 3(a). Grain-boundary allotriomorphs and the formation of fcc platelets from them are also observed, as shown in Figure 3(b).

Figure 4 compares the X-ray diffraction results corresponding to the two structures shown above. Figure 4(a) is for the sample with an initial undercooling of 14 K. Intensity ratios of diffraction peaks are nearly in accordance with results expected for a powder diffraction for both fcc and bcc. Figure 4(b) is for the sample with an initial undercooling of 150 K. Relatively stronger (200) and (311) peaks of fcc were obtained. This indicates that the structure contains fcc with a preferred orientation. A relatively stronger fcc (111) peak was also obtained through diffraction from a sample which was solidified with similar initial undercooling.

Thermal histories of these samples are shown in Figure 5. The temperature decreases slowly after a rapid recalescence until the sample is completely solidified. The time which the sample spends in the semi-solid state depends on the initial undercooling; it becomes shorter as the initial undercooling becomes larger. After this period,

the sample is fully solid, and then the cooling rate increases to 100 to 150 K/s. In Figure 5, when the initial undercooling is 14 K, a temperature rise is observed while the sample is semi-solid (as indicated with an arrow). The fluctuations in the temperature measurements are due to sample vibrations. The temperature rise is probably caused by the bcc-to-fcc transformation as discussed in a previous chapter; the transformation starts in the semi-solid condition. When the initial undercooling is 150 K, the temperature rise corresponding to the bcc-to-fcc transformation is found after the completion of solidification, i.e., in the solid state (as indicated with an arrow). The onset temperature of the transformation is approximately 35 K below the liquidus temperature in the former case and approximately 90 K below the liquidus in the latter case. In summary, the bcc-to-fcc transformation proceeds in the semi-solid condition when the initial undercooling is small, while it occurs in the solid state when the undercooling is large.

Transformation temperatures of the samples tested were determined from cooling curves; the onset of the exothermic reaction or the change of the slope of a cooling curve was defined as the onset of the transformation, examples of which have been shown in Figure 5. The results for Fe-18.5Cr-11.3Ni (alloy B) are plotted versus initial undercooling in Figure 6. The liquidus and solidus temperatures, the T_0 temperature between fcc and bcc, and the fcc solvus temperature were calculated for the nominal composition using Thermo Calc[18], and are shown in the figure. For undercoolings up to approximately 60 K, the transformation temperature is around 1700 K, and for higher undercoolings, it is around 1650 K; overall the transformation temperature tends to decrease as the initial undercooling increases. All of the data points lie below the T_0 temperature.

3.2 Structure of Fe-19.7Cr-10.3Ni Alloy (Alloy E) after Gas-Cooled Solidification

Figures 7(a) and 7(b) show microstructures of another primary bcc alloy, Fe-19.7Cr-10.3Ni (alloy E), which were solidified with

initial undercoolings of 22 K and 128 K, respectively. When the initial undercooling was 22 K, most of the resulting structure is typical Widmanstätten fcc with grain-boundary allotriomorphs, as shown in Figure 7(a). Blocky fcc is also observed at both inter- and intragranular regions near the specimen surface, usually connected to fcc platelets. Figure 7(b) is of a sample with an initial undercooling of 128 K. The structure consists of blocky fcc grains which have an angular appearance. These grains seem to be aligned. The grain size is largest near the surface and becomes smaller towards the inside. Twinning was observed within some grains. Grain boundaries are rather straight and often contain the lacy structure signifying an fcc-bcc mixture. Islands of the lacy structure are also seen inside grains as if they were entrapped during the grain growth. The angular grain structures continue 1000 to 1500 μm from the surface, and then the structure changes to the lacy mixture of fcc and bcc in the core region of the sample.

When the initial undercooling was between 22 K and 128 K, the structure always consisted of a mixture of Widmanstätten fcc and blocky fcc. The size and amount of blocky fcc increased gradually with increasing initial undercooling. Structures similar to that shown in Figure 7(b) were found in several samples with different initial undercoolings more than 120 K.

Figures 8(a) and 8(b) show X-ray diffraction results from the structures shown in Figures 7(a) and 7(b), respectively. The comparison of these two diffraction results indicates relatively stronger fcc (200) and (311) peaks for the sample with the larger initial undercooling; this tendency is the same as in the case of alloy B. Also, some samples which were undercooled similarly showed a strong fcc (111) peak instead of the (200) and (311) peaks. The major structural difference between the two samples is the presence of coarse angular grains spreading from the surface toward the inside in the 128 K undercooled sample. Those grains are probably textured fcc causing the above difference. Micro X-ray diffraction results supported this, as shown in Figure 9; (a) was taken from a

lacy structure (i.e., a mixture of bcc and fcc), and (b) was taken from a single coarse grain in the 128 K undercooled sample of alloy E. The result indicates that those grains seen in Figure 7(b) are fcc, and probably aligned in a preferred orientation. It is noted that the scanning in the micro diffractometer was conducted from high angle to low angle, and the sensitivity of the diffraction detector increases at higher angles.

Distribution of Cr and Ni in the 128 K undercooled sample of alloy E is shown in Figure 10. Concentrations of Cr and Ni are uniform and approximately equal to nominal concentrations within each fcc grain near the surface. Inside the sample, fcc grains become smaller, and gradually enriched in Ni. Intergranular regions are slightly depleted in Cr and significantly depleted in Ni, which is probably the result of residual, intergranular lacy bcc. The partitioning of Ni between intra- and intergranular regions becomes distinct at the inside of the sample.

Figure 11 shows the thermal histories of the above samples with different initial undercoolings. Unlike alloy B, a temperature rise is not observed while the sample is in the semi-solid condition even when the initial undercooling is small. When the initial undercooling is 22 K, the onset of the bcc-to-fcc transformation is not clear; it may be defined as being at the place where the slope of the cooling curve changes (as indicated with an arrow). In contrast, when the initial undercooling is 128 K, the temperature change from the transformation is clearly defined. It can be concluded that the bcc-to-fcc transformation gradually proceeds over a relatively wide range of temperature in the solid state when the initial undercooling is small, whereas it occurs abruptly in the solid state when the initial undercooling is large.

Bcc-to-fcc transformation temperatures of this alloy are summarized in Figure 12 as a function of initial undercooling. In the figure, the temperatures of the liquidus, solidus, T_0 between bcc and fcc, and fcc solvus are included. The transformation temperatures are

all between the T_0 and fcc solvus temperatures, and decrease slightly with increasing initial undercooling.

Figures 13(a) and 13(b) show microstructures of samples quenched into an In-Ga liquid bath immediately after the recalescence from two different undercooled states: 25 K and 125 K, respectively. When the initial undercooling is 25 K, dendrites seem to be equiaxed and randomly dispersed in the liquid. It should be noted that the interdendritic regions were liquid prior to the quench. On the other hand, when the initial undercooling is 125 K, the fraction solid is high, and dendrites seem to be aligned in a certain direction. Coalescence of dendrites is already found to be proceeding near the surface at this point.

3.3 Structure of Fe-17.5Cr-12.2Ni Alloy (Alloy A) after Gas-Cooled Solidification

Figures 14(a) and 14(b) show microstructures of Fe-17.5Cr-12.2Ni alloy (alloy A) after gas-cooled solidification with initial undercoolings of 51 K and 155 K, respectively. The alloy is a primary fcc alloy upon equilibrium solidification. However, when the melt is undercooled by more than 20 K prior to solidification, it solidifies as primary metastable bcc, which was already described in a previous chapter. When the initial undercooling is 51 K, primary bcc is retained with a skeletal or lacy morphology in the final microstructure, as shown in Figure 14(a). Those morphologies of retained bcc are the remnants of the transformation from primary bcc to fcc, and they are therefore located at dendrite cores. When the initial undercooling is 155 K, the structure near the specimen surface becomes single phase as shown in Figure 14(b). It consists of coarse grains; the size of the grains is smaller in the vicinity of the surface than inside. Neither substructure nor retained bcc is observed within the grains, except for twinning. This single phase region extends up to approximately 1500 μm (out of 2500 μm sample radius), and then the structure changes to the mixture of fcc and retained bcc such as seen in Figure 14(a).

Figure 15 shows the X-ray diffraction results for the 155 K undercooled structure. A very strong fcc (200) peak was obtained, and the single phase region was assumed to be highly textured fcc. Solute distributions are completely uniform in the single phase region, and no concentration changes are clearly detected even at grain boundaries.

The thermal history of the 155 K undercooled sample is shown in Figure 16. A strong, rapid, exothermic reaction is seen approximately at the end of solidification; the temperature rise is more than 30 K. This is caused by the transformation from bcc to single phase fcc.

4. Discussion

The structures shown in Figures 2(b), 7(b), and 14(b) are obtained with relatively large undercoolings, and are quite different from those obtained with conventional solidification practices. They have common features as follows:

- coarse fcc grains occasionally with twinning inside
- uniform Cr and Ni distributions within each grain
- texture-like X-ray diffraction
- abrupt exothermic reaction after the solidification

In all cases, alloys solidify as primary bcc, and the bcc undergoes the bcc-to-fcc transformation. Since the above-mentioned coarse grains of fcc with uniform composition profiles could not have been obtained in a diffusional bcc-to-fcc transformation process, it may be concluded that they are massive fcc. The reasoning behind this conclusion becomes obvious when the bcc-to-fcc transformation process in those situation is considered, and compared with that in the cases of small undercoolings.

Regarding the alloy B, the structure in Figure 2(a) is typical of conventional cast structures produced by primary bcc solidification mode (FA mode)[1,2]. Since the alloy composition is close to the eutectic composition (Figure 1), primary bcc dendrites are subject to the bcc-to-fcc transformation even during the solidification. The thermal history in Figure 5 indicates this. As a result of typical diffusion controlled transformation, prior bcc dendrites change to a mixture of fcc and lacy bcc while keeping the same overall morphology. On the other hand, when the initial undercooling is large, solidification is likely to be fully bcc, which may be facilitated by the decreasing partitioning with a high rate of solidification. Then, the bcc-to-fcc transformation proceeds in the fully solid state, as the thermal history in Figure 5 indicates, and the resulting structure is either Widmanstätten fcc or massive fcc. In fact, the former structure was dominant in some samples with intermediate undercoolings, and massive-like fcc was found to increase at relatively larger undercoolings. Therefore, as the initial undercooling increases, the bcc-to-fcc transformation gradually changes from a diffusional transformation to a massive one.

The solidification of alloy E is fully bcc regardless of initial undercooling levels. When the initial undercooling is small, this fully bcc solidification mode results in the development of a typical Widmanstätten fcc structure. The corresponding cooling curve indicates that the bcc-to-fcc transformation does not proceed abruptly but gradually. On the other hand, when the massive transformation becomes dominant in samples with a large initial undercooling, a clear temperature change can be noted in the corresponding thermal history. In the microstructure shown in Figure 7(b), the edges of the angular grains of massive fcc clearly reveal a planar interface, and the alignment of those grains corresponds well to the XRD result of preferred orientation shown in Figures 7(b) and 8. Intraguranular dark spots in Figure 7(b), which are a lacy mixture of fcc and bcc, seem as if they were entrapped by the impingement of plane fronts. It should be noted that some blocky

fcc was also obtained in the 22 K undercooled specimen. This suggests that massive bcc-to-fcc transformation is feasible in this alloy composition even when the initial undercooling is small. The change in microstructure also indicates that the transition from a diffusional transformation to a massive one occurs gradually with increasing initial undercooling.

The solidification of alloy A from an undercooled melt occurs with metastable bcc, and therefore, a strong thermodynamic driving force for the bcc-to-fcc transformation always exists. When the initial undercooling is small, the transformation even starts before the solidification is complete, and the resultant structure (Figure 14(a)) is basically identical to that in Figure 2(a). When the initial undercooling is large, the sample solidifies as fully bcc, and therefore, the solid-state transformation can proceed massively to produce a uniform fcc phase, as shown in Figure 11(b). Solute profiles are completely uniform throughout the fcc single-phase region, and even grain boundaries are not clear in the solute profiles. The exothermic reaction is more significant and abrupt in this alloy than those in the other two alloys. The grain size of massive fcc is also the largest in this alloy. These observations agree with the fact that this alloy has the largest driving force for the bcc-to-fcc transformation among the three alloys investigated, and therefore the largest interface velocity.

It is clear that initial undercooling significantly affects the subsequent bcc-to-fcc transformation. When the initial undercooling is relatively small, samples are likely to undergo the diffusional transformation, either in the semi-solid condition or in the solid state, producing a Widmanstätten structure whereas, as the initial undercooling increases, the massive transformation becomes dominant. One of the important factors which changes with the initial undercooling and affects the subsequent transformation behavior is solute redistribution during solidification and the resultant solute profiles. In order for the massive transformation to occur, a high degree of solute-uniformity in the parent phase is necessary.[14,17] Solute microsegregation during solidification and following

homogenization prior to transformation may still be critical to determining the homogeneity (or heterogeneity) prior to transformation.

When the initial undercooling is small, partition ratios of the solutes are equal or close to the equilibrium values. For bcc solidification, the interdendritic region is enriched in Ni, and fcc becomes more favored as the solidification proceeds. Therefore, the exothermic reaction seen in Figure 5 and structures seen in Figures 2(a) and 14(a) are the result from the fcc formation from the interdendritic liquid and primary bcc solid. As the initial undercooling increases, the growth velocity increases and the partition ratios of solutes increase towards unity.[15,18] This reduces the microsegregation of solutes, and also enables solidification to be fully bcc without reaching the eutectic valley at the terminal stage. The bcc-to-fcc transformation occurs after the completion of solidification. Even in the solid state, chemical heterogeneity can facilitate the formation of the transformation product at higher temperature, while, if the homogeneity is high enough over a relatively wide region, the transformation can be retarded and is likely to be massive. In the latter case, initial undercooling needs to be large enough to bring about partition ratios close to unity. Figures 6 and 12 summarize the effect of initial undercooling on the transformation temperature, and show the tendency that transformation temperature decreases with increasing undercooling. Regarding the structure, when the initial undercooling is intermediate, i.e., roughly 80 to 120 K, Widmanstätten fcc or the mixture of blocky fcc and lacy bcc is dominant in the final structure, and massive fcc is obtained dominantly at higher initial undercooling.

Although transformation temperatures seem to be always below the T_0 temperature in Figures 6 and 12, this is not always true in practice. Because of the chemical heterogeneity produced by solidification, this critical temperature could vary locally. Therefore, diffusional transformation is locally facilitated in solute (Ni) enriched regions, and massive transformation in other regions, even if the

overall undercooling is large. A typical example may be seen in Figure 3, where the lacy bcc is the product of diffusional transformation while the blocky fcc is from the massive-like transformation. It is interesting to note that the structure appears to reflect the alignment of dendrites; lacy bcc probably corresponds to solute-enriched interdendritic region while blocky fcc to solute-depleted dendrite core region. As the homogeneity in the as-solidified condition increases, the comparison between the transformation temperature and the T_0 temperature for the overall composition may be reasonable.

Alignment of the original solidification structure may affect the subsequent transformation behavior. As seen in Figure 13, when the initial undercooling is small, the dendrites seem to be randomly oriented, but when the initial undercooling is large, the dendrites are aligned along a certain direction. These trends correspond to the final microstructures shown in Figure 7 and also to the X-ray diffraction results shown in Figure 8. In other words, aligned dendrites at the larger undercooling can facilitate the massive- like bcc-to-fcc transformation.

5. Conclusions

The bcc-to-fcc transformation after gas-cooled solidification was investigated using three different alloys which solidify as primary bcc. Conclusions obtained are:

(1) The bcc-to-fcc transformation of Fe-18.5Cr-11.3Ni (alloy B) is typical diffusional transformation leading to a lacy morphology of retained bcc when the initial undercooling is small. When the initial undercooling is large, the transformation occurs in the solid state, and becomes massive. The resultant structure consists of coarse fcc grains with a small amount of twinning inside and a preferred orientation.

(2) The bcc-to-fcc transformation of Fe-19.7Cr-10.3Ni proceeds in the solid state regardless of the initial undercooling. When the initial undercooling is small, Widmanstätten fcc is formed as the result of the transformation, while massive fcc becomes dominant when the initial undercooling is increased. The massive fcc has an angular morphology which is aligned in a certain direction with planar interfaces. The concentrations of Cr and Ni within each grain are uniform and approximately equal to the nominal concentrations.

(3) Fe-17.5Cr-12.2Ni solidifies as metastable bcc and undergoes a massive transformation to fcc when the initial undercooling is large. The grain size of massive fcc is the largest among the three alloys investigated. Massive fcc exhibits high uniformity of solute concentrations, and X-ray diffraction indicates microstructural texture.

(4) The occurrence of the massive transformation is clearly identified in the cooling curves of every alloy by an abrupt exothermic reaction.

(5) It is suggested that, as the initial undercooling increases, chemical homogeneity is increased even in the as solidified condition, and the massive transformation can occur provided the thermodynamic criterion is satisfied.

References

1. N. Suutala, T. Takalo, and T. Moisio: *Metall. Trans. A*, 1980, vol. 11A, p. 717
2. J. A. Brooks, J. C. Williams, and A. W. Thompson: *Metall. Trans.* A, 1983, vol. 14A, p. 1271

3. J. Singh, G. R. Purdy, and G. C. Weatherly: *Metall. Trans. A*, 1985, vol. 16A, 1363
4. J. W. Elmer, S. M. Allen, and T. W. Eagar: *Metall. Trans. A*, 1989, vol. 20A, p. 2117
5. D. A. Karlyn, J. W. Cahn, and M. Cohen: *Trans. TMS-AIME*, 1969, vol. 245, p. 197
6. T. B. Massalski, A. J. Perkins, and J. Jakrovsky: *Metall. Trans.*, 1972, vol. 3, p. 687
7. M. Hillert: *Metall. Trans. A*, 1984, vol. 15A, p. 411
8. B. Jönsson and J. Ågren: *Acta metall. mater.*, 1990, vol. 38, p. 433
9. T. B. Massalski: *Metall. Trans. A*, 1984, vol. 15A, p.421
10. M. R. Plichta, W. A. T. Clark, and H. I. Aaronson: *Metall. Trans. A*, vol. 15A, p. 427
11. J. H. Perepezko: *Metall. Trans. A*, 1984, vol. 15A, p. 437
12. E. S. K. Menon, M. R. Plichta, and H. I. Aaronson: *Acta metall.*, 1988, vol. 36, p. 321
13. C. S. Barrett and T. B. Massalski: *Structure of Metals*, 3rd ed., McGraw-Hill Book Co., New York, 1966, p. 507
14. T. B. Massalski, J. H. Perepezko, and J. Jaklovsky: *Mater. Sci. Eng.*, 1975, vol. 18, p. 193
15. M. J. Aziz: *J. Appl. Phys.*, 1982, vol. 53, p. 1158
16. W. J. Boettinger, S. R. Coriel, and R. F. Sekerka: *Mater. Sci. Eng.*, 1984, vol. 65, p.27
17. K. Hirano, M. Cohen, and B. L. Averbach: *Acta metall.*, 1961, vol. 9, p. 440
18. R. Trivedi, J. Lipton, and W. Kurz: *Acta metall.*, 1987, vol. 35, p. 965

Table 1 - Chemical compositions of Fe-Cr-Ni alloys used in the present study (in wt%).

	Alloy A	Alloy B	Alloy E
Cr	17.54	18.51	19.70
Ni	12.17	11.34	10.31
C	0.004	0.003	0.003
Si	<0.01	<0.01	<0.01
Mn	<0.01	<0.01	<0.01
P	<0.001	<0.001	<0.001
S	<0.001	<0.001	<0.001
N	0.001	0.001	0.001
O	0.009	0.008	0.010
Fe+Cr+Ni	>99.96	>99.96	>99.96

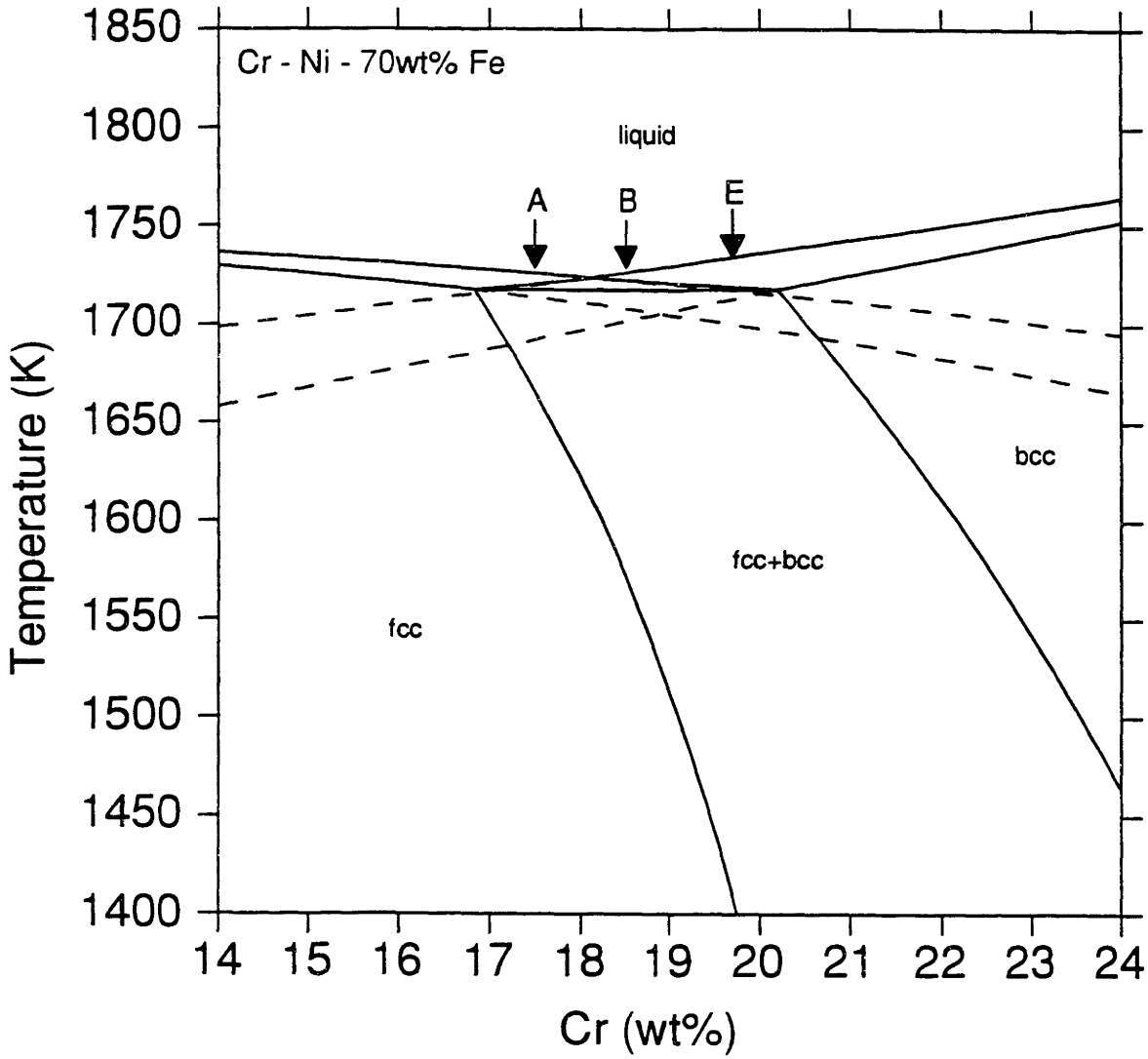

Figure 1 - Calculated pseudo-binary phase diagram of the Fe-Cr-Ni system at 70 wt pct Fe with the extension of liquidus lines and the locations of the alloy compositions: alloys A, B and E.

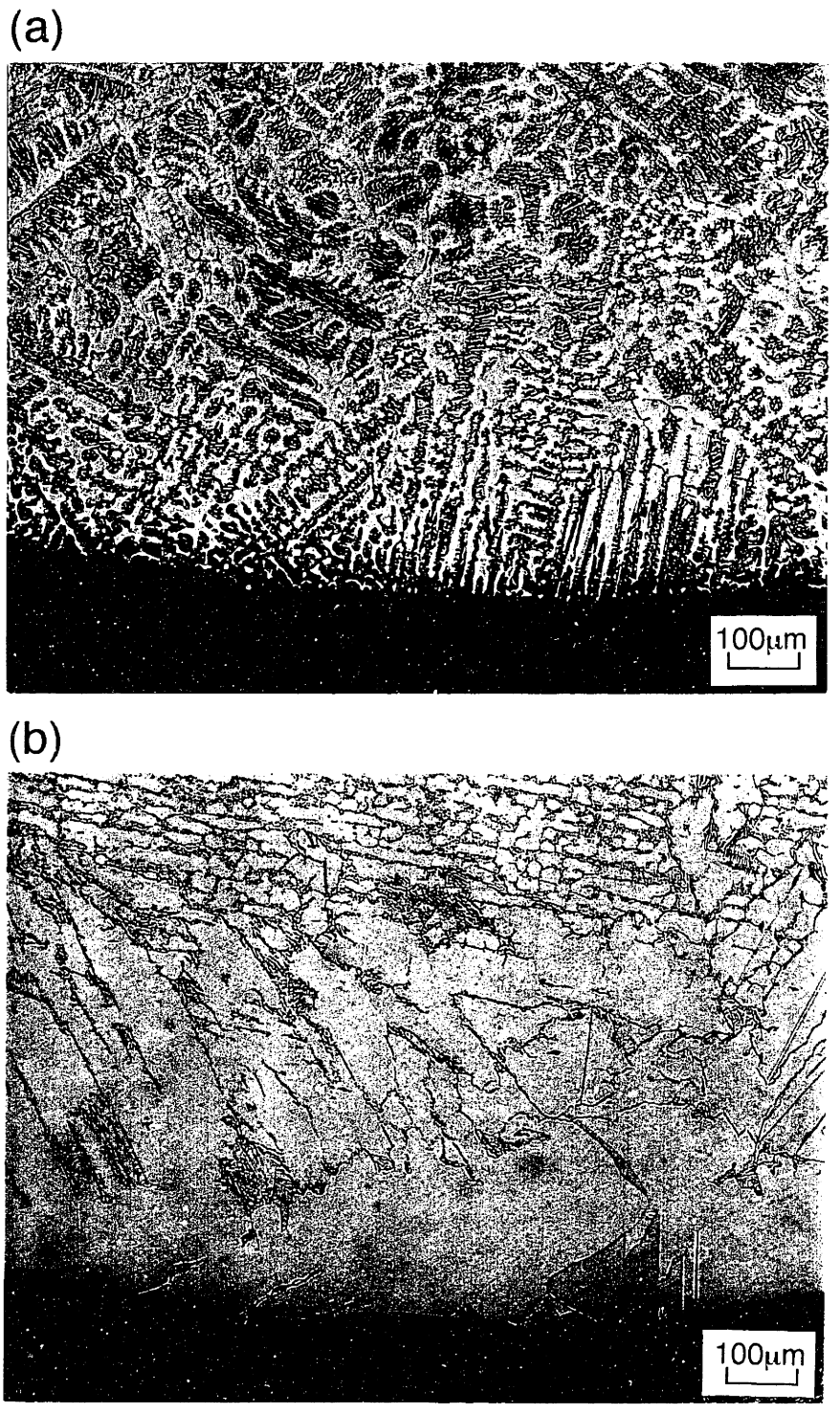

Figure 2 - Structure of Fe-18.5Cr-11.3Ni (alloy B) after gas-cooled solidification with an initial undercooling of (a) 14 K and (b) 150 K.

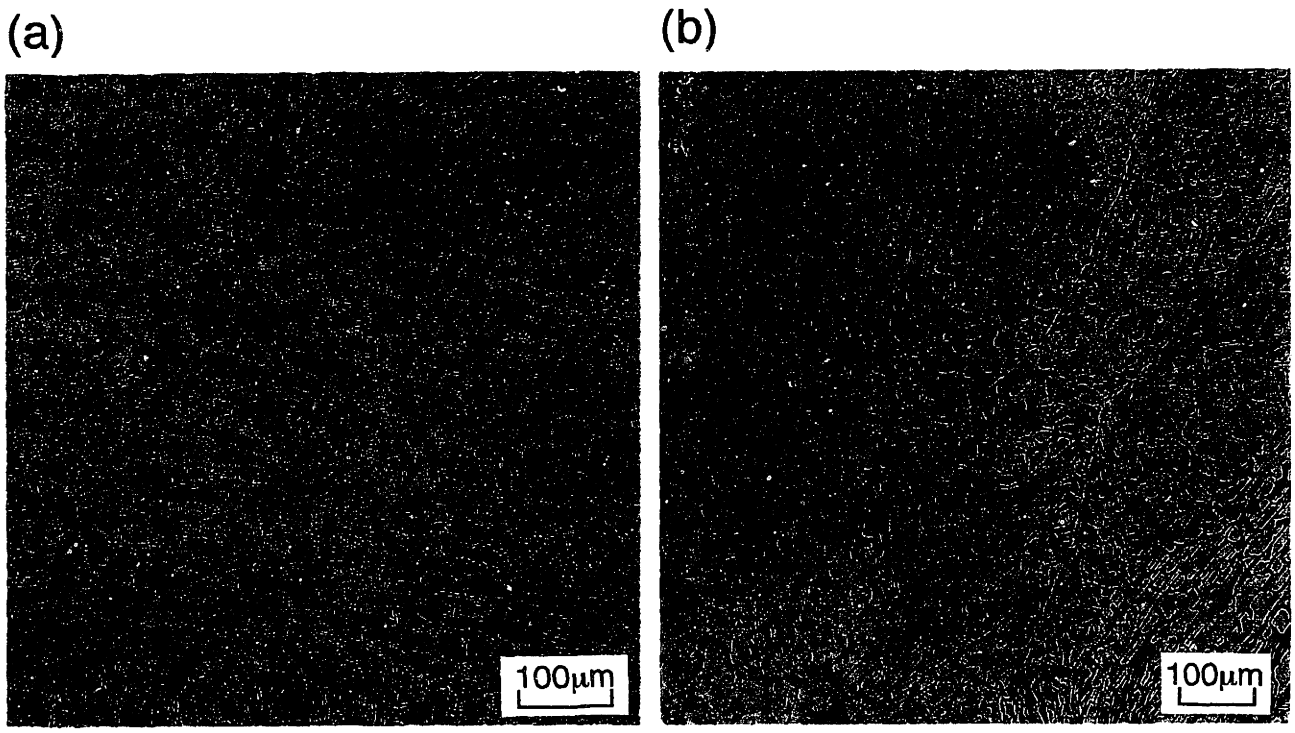

Figure 3 - Structures observed at the core region of the sample of Fe-18.5Cr-11.3Ni (alloy B) after gas-cooled solidification with an undercooling of 150 K: (a) aligned fcc blocks along lacy bcc, and (b) grain boundary allotriomorphs and platelets of fcc.

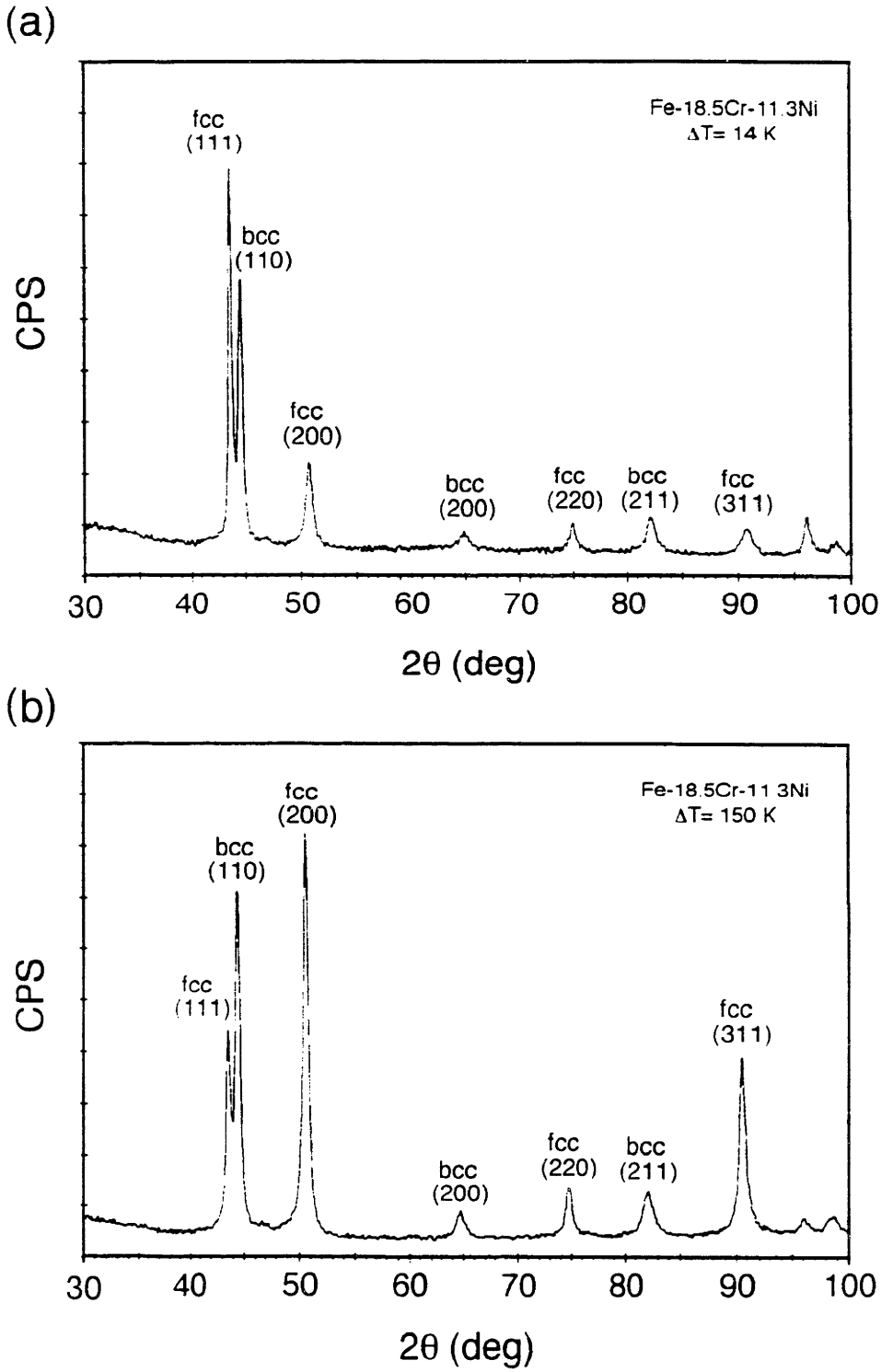

Figure 4 - X-ray diffraction results obtained from samples of Fe-18.5Cr-11.3Ni (alloy B) solidified with an initial undercooling of (a) 14 K and (b) 150 K, which correspond to the structures shown in Figures 2(a) and 2(b), respectively.

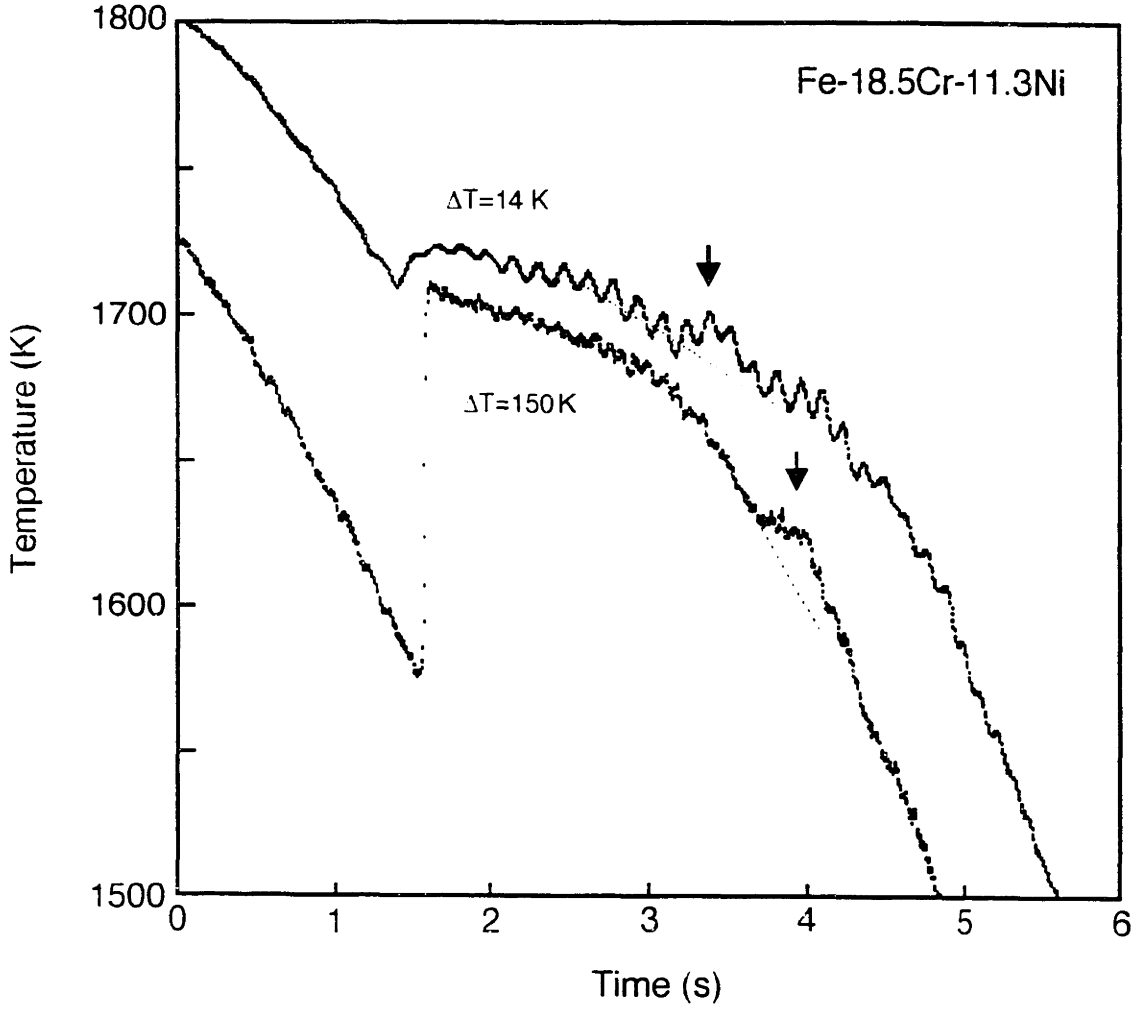

Figure 5 - Thermal histories of samples solidified with an initial undercooling of 14 K and 150 K, which correspond to the structures shown in Figures 2(a) and 2(b), respectively.

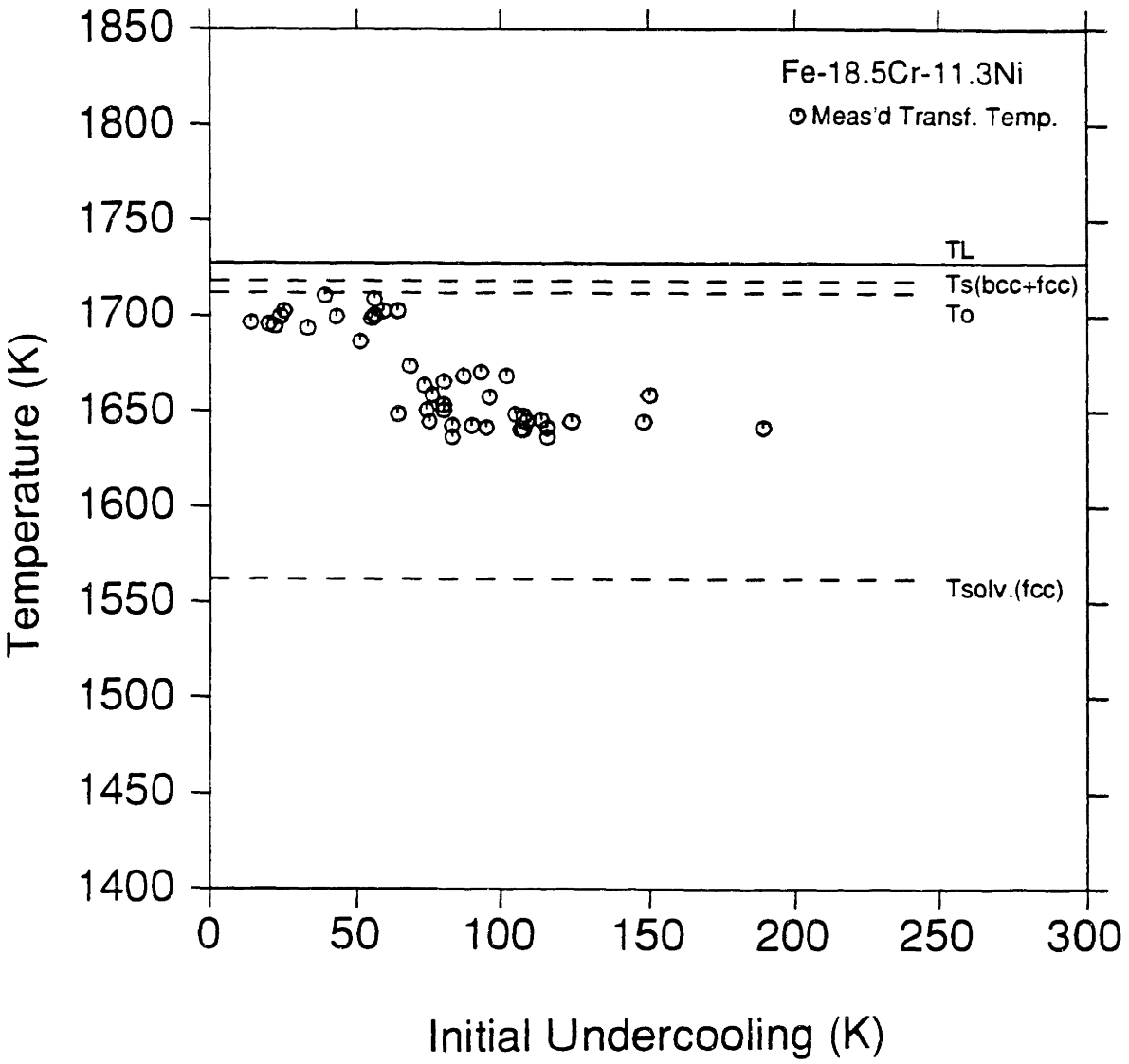

Figure 6 - Effect of initial undercooling on the onset temperature of the bcc-to-fcc transformation in a levitated Fe-18.5Cr-11.3Ni (alloy B). The transformation temperature was determined by the onset of the exothermic reaction or the change of the slope of the cooling curve.

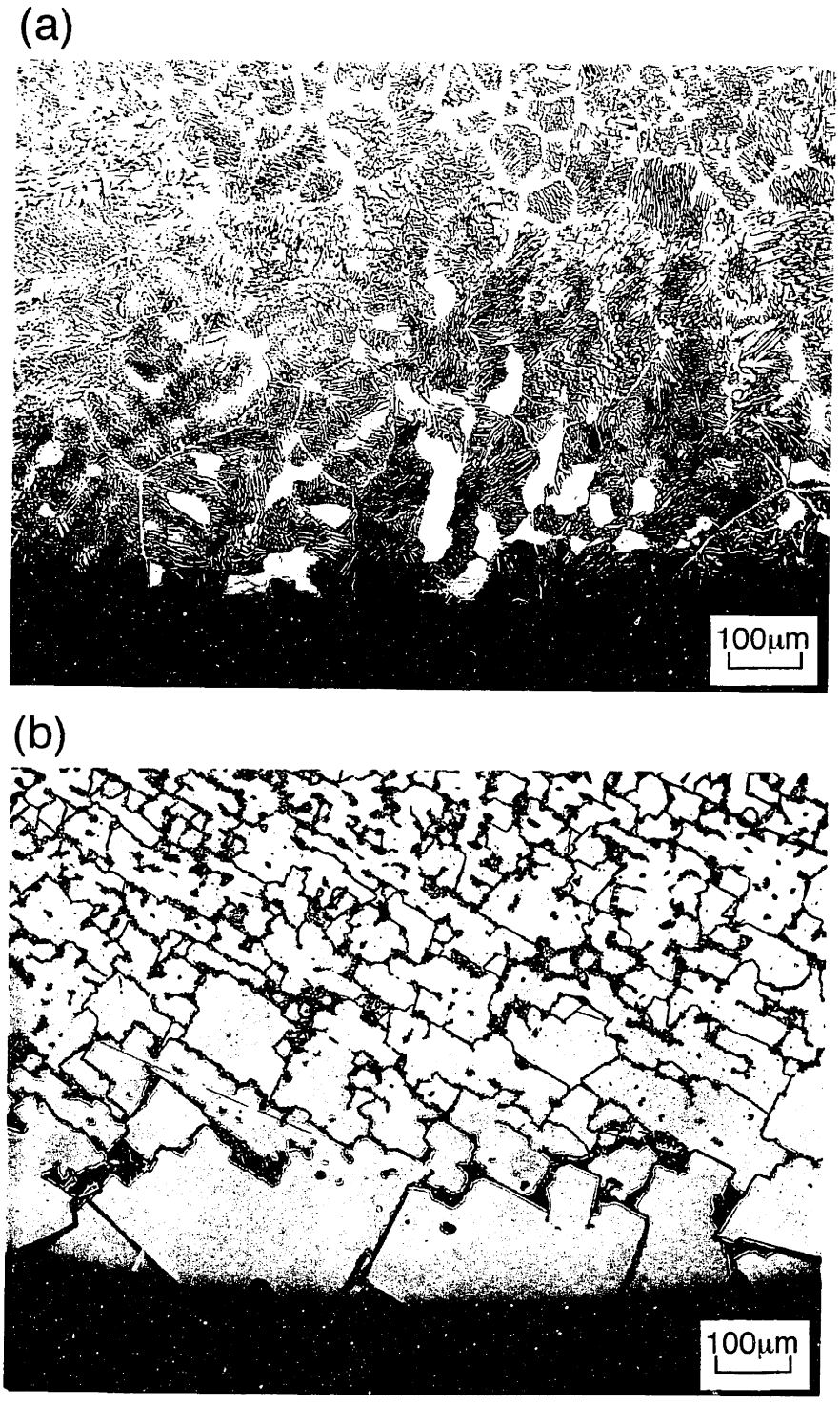

Figure 7 - Structure of Fe-19.7Cr-10.3Ni (alloy E) after gas-cooled solidification with an initial undercooling of (a) 22 K and (b) 128 K.

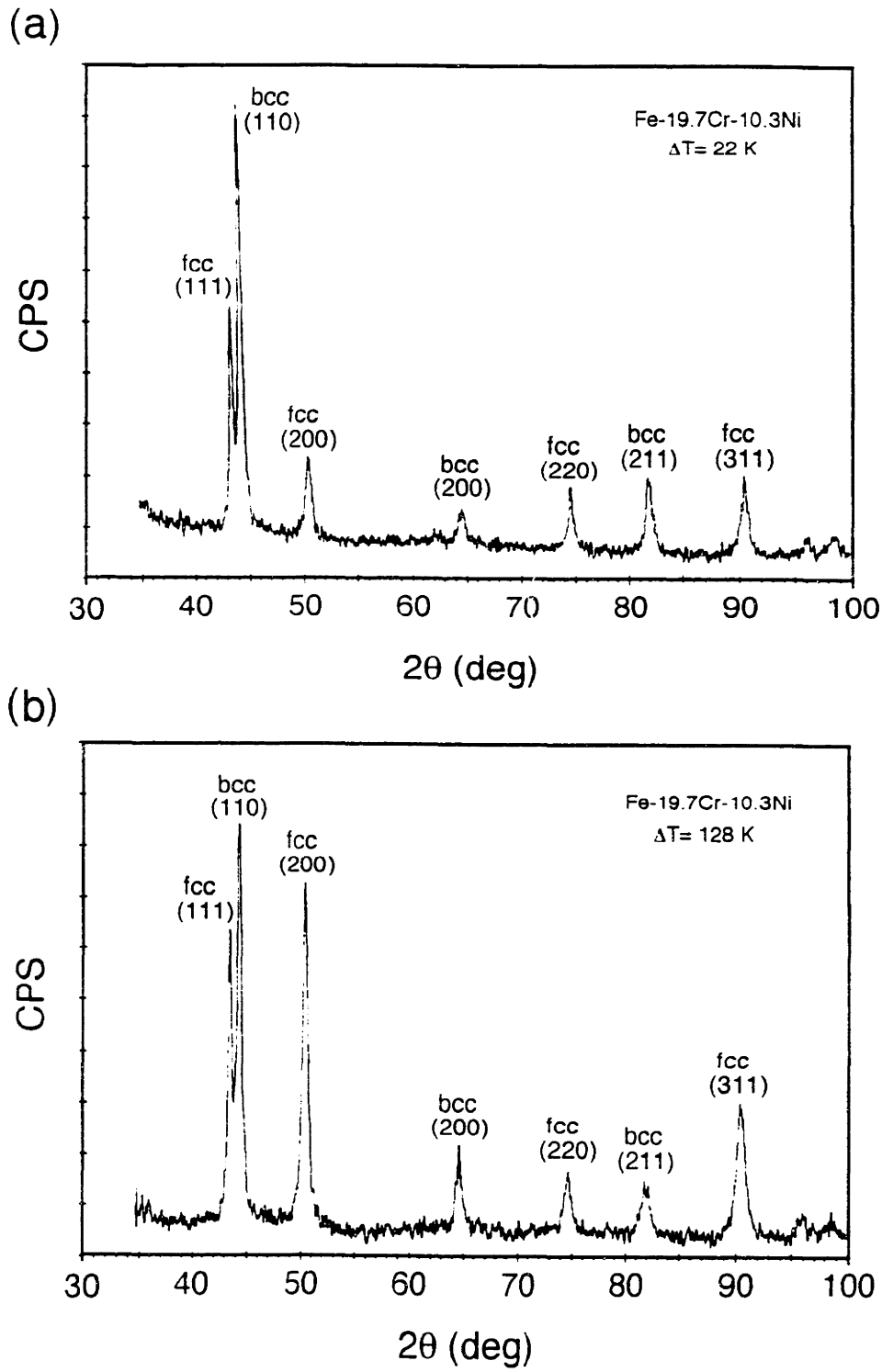

Figure 8 - X-ray diffraction results obtained from samples of Fe-19.7Cr-10.3Ni (alloy E) solidified with an initial undercooling of (a) 22 K and (b) 128 K, which correspond to the structures shown in Figures 7(a) and 7(b), respectively.

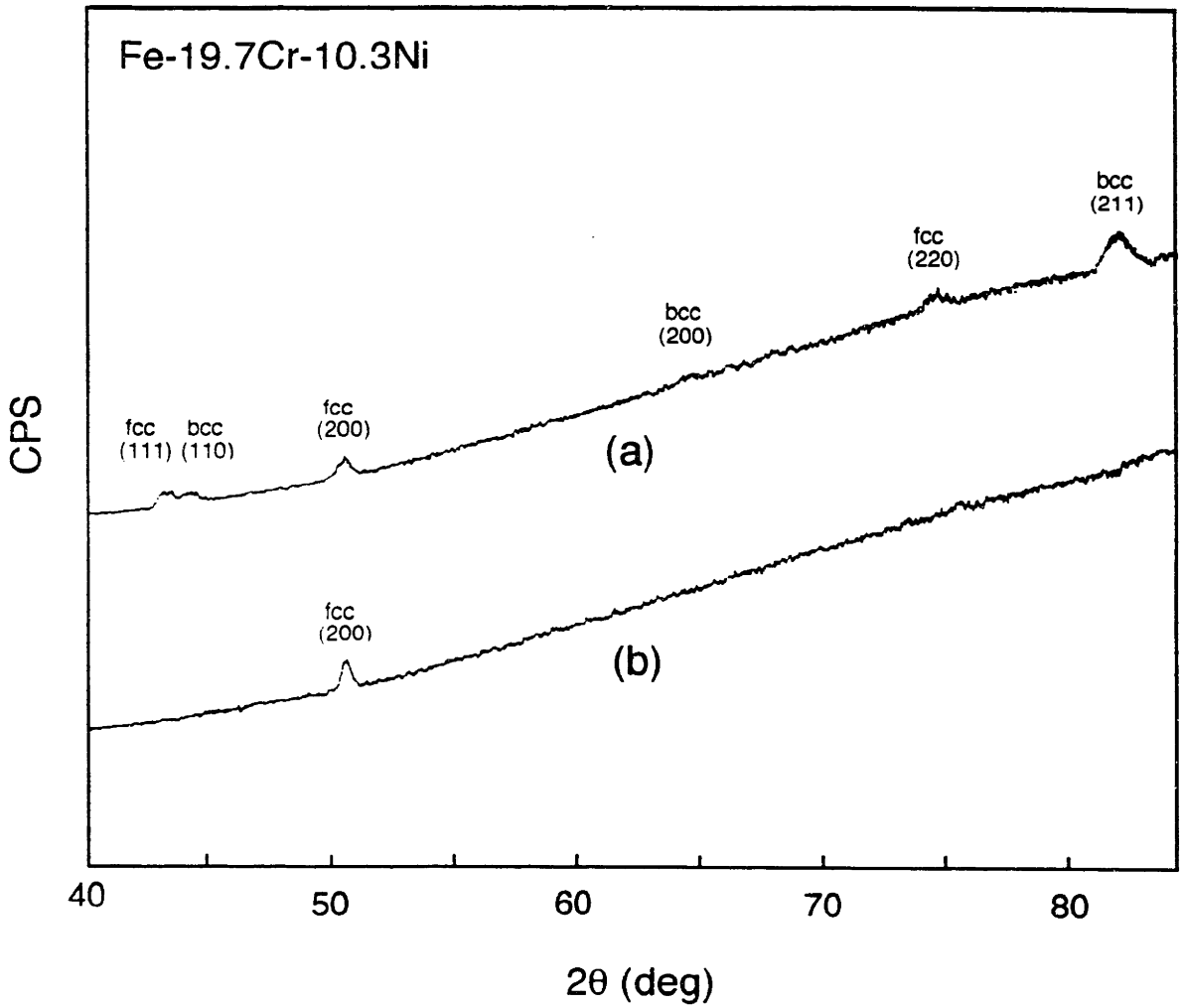

Figure 9 - Micro X-ray diffraction results obtained from (a) lacy bcc mixed with fcc and (b) a single coarse grain in the sample of Fe-19.7Cr-10.3Ni (alloy E) with an initial undercooling of 128 K.

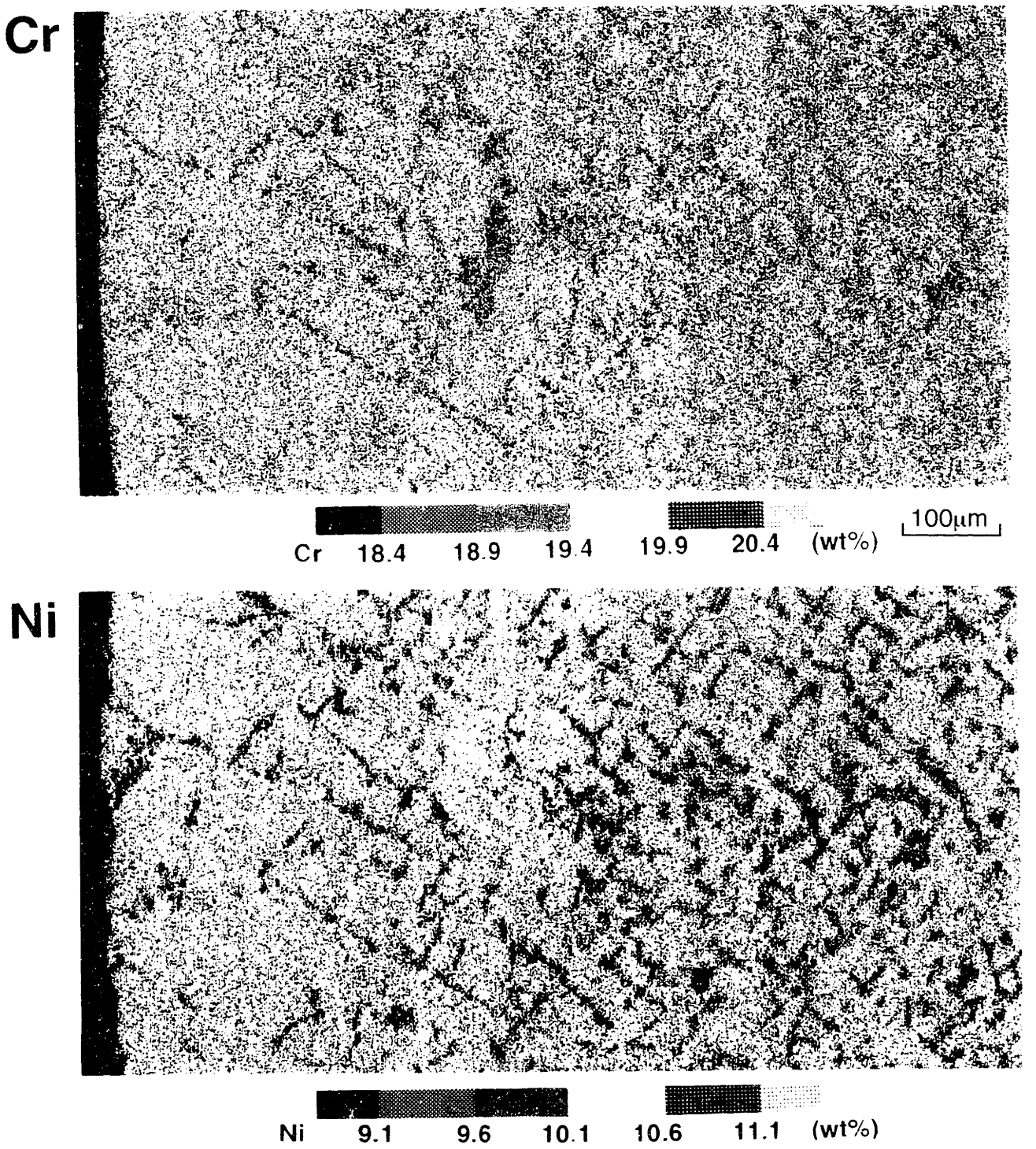

Figure 10 - Concentration profiles of Cr and Ni in the sample of Fe-19.7Cr-10.3Ni (alloy E) with an initial undercooling of 128 K.

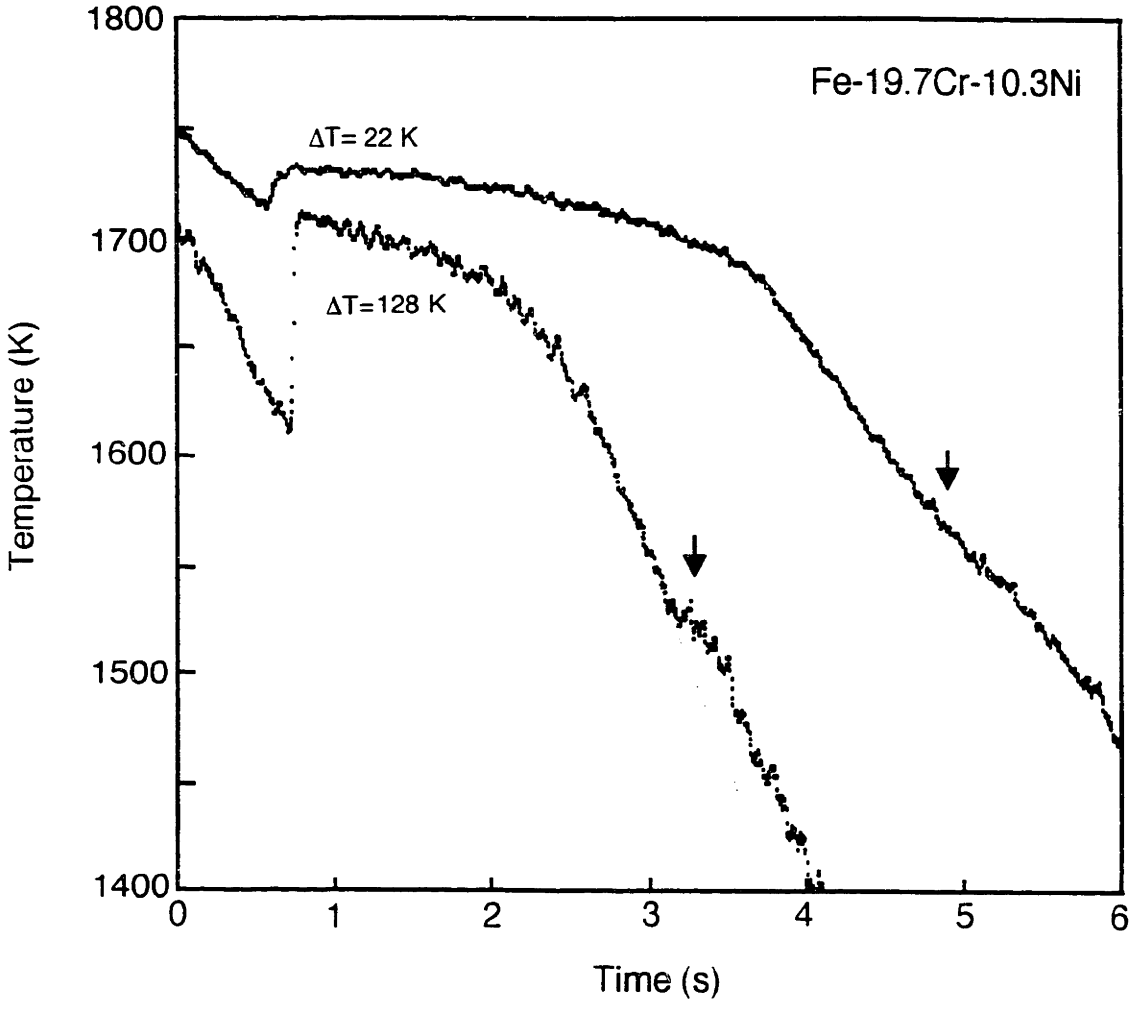

Figure 11 - Thermal histories of samples solidified with an initial undercooling of 22 K and 128 K, which correspond to the structures shown in Figures 7(a) and 7(b), respectively.

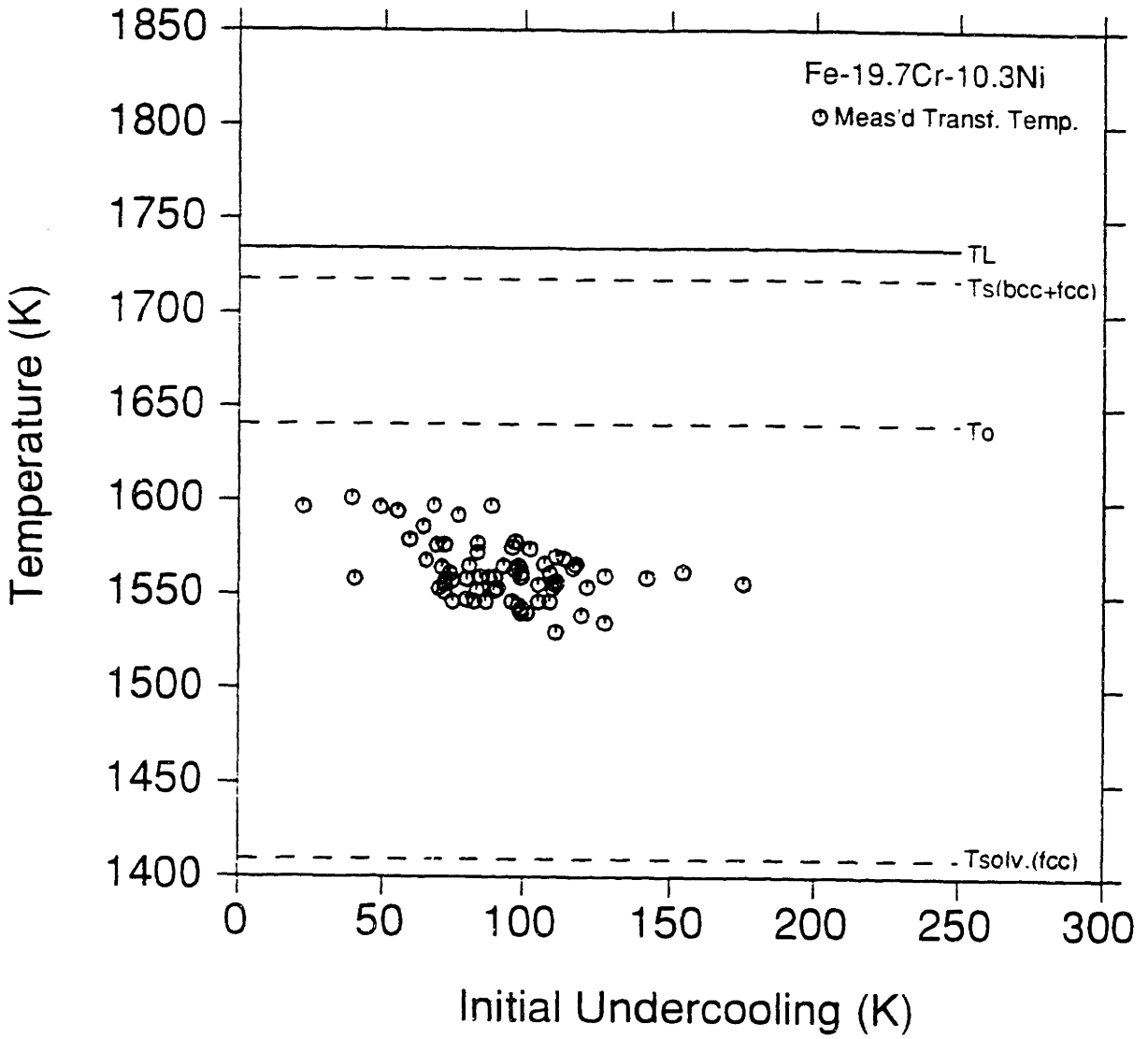

Figure 12 - Effect of initial undercooling on the onset temperature of the bcc-to-fcc transformation in a levitated Fe-19.7Cr-10.3Ni (alloy E).

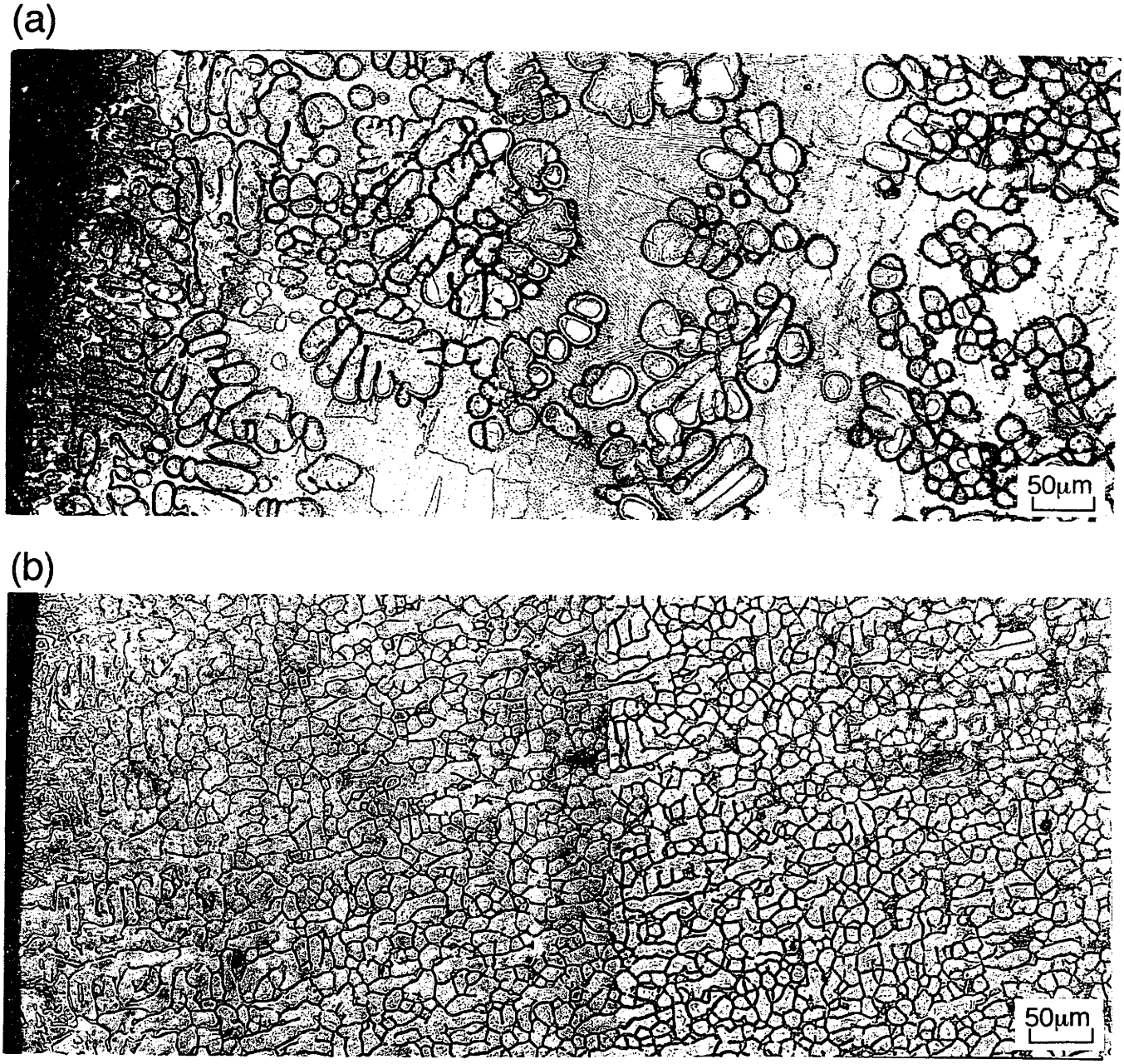

Figure 13 - Structures of samples of Fe-19.7Cr-10.3Ni (alloy E) which were quenched into In-Ga immediately after recalescence from different undercooling levels: (a) 25 K and (b) 125 K.

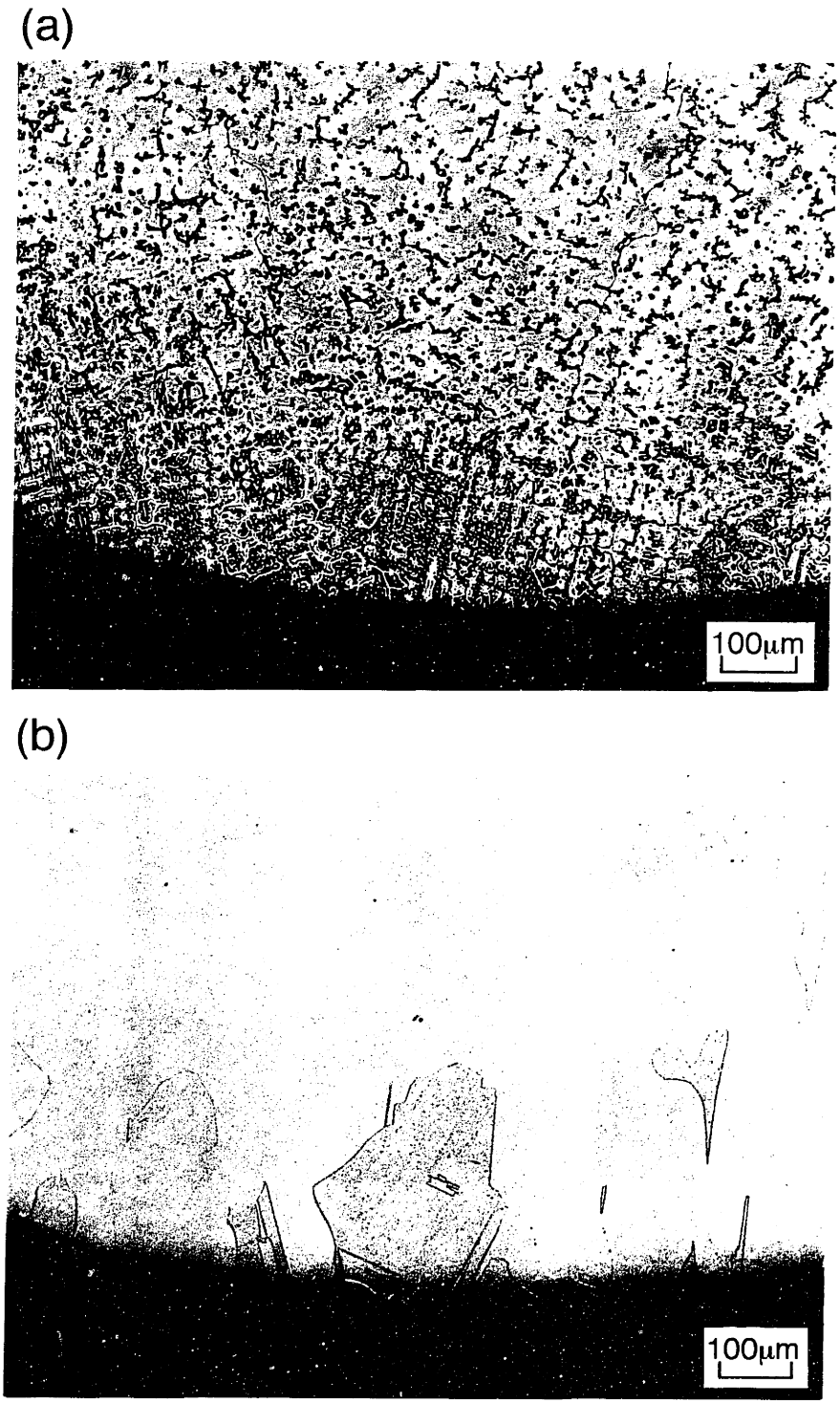

Figure 14 - Structure of Fe-17.5Cr-12.2Ni (alloy A) after gas-cooled solidification with an initial undercooling of (a) 51 K and (b) 155 K.

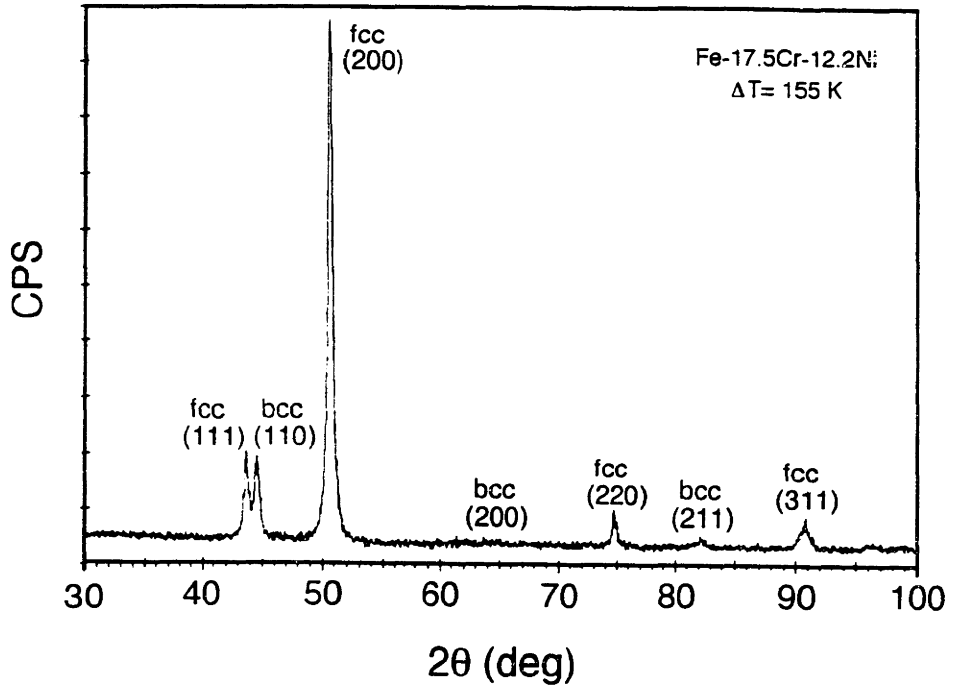

Figure 15 - X-ray diffraction obtained from samples of Fe-17.5Cr-12.2Ni (alloy A) solidified with an initial undercooling of 155 K, which corresponds to the structure shown in Figure 14(b).

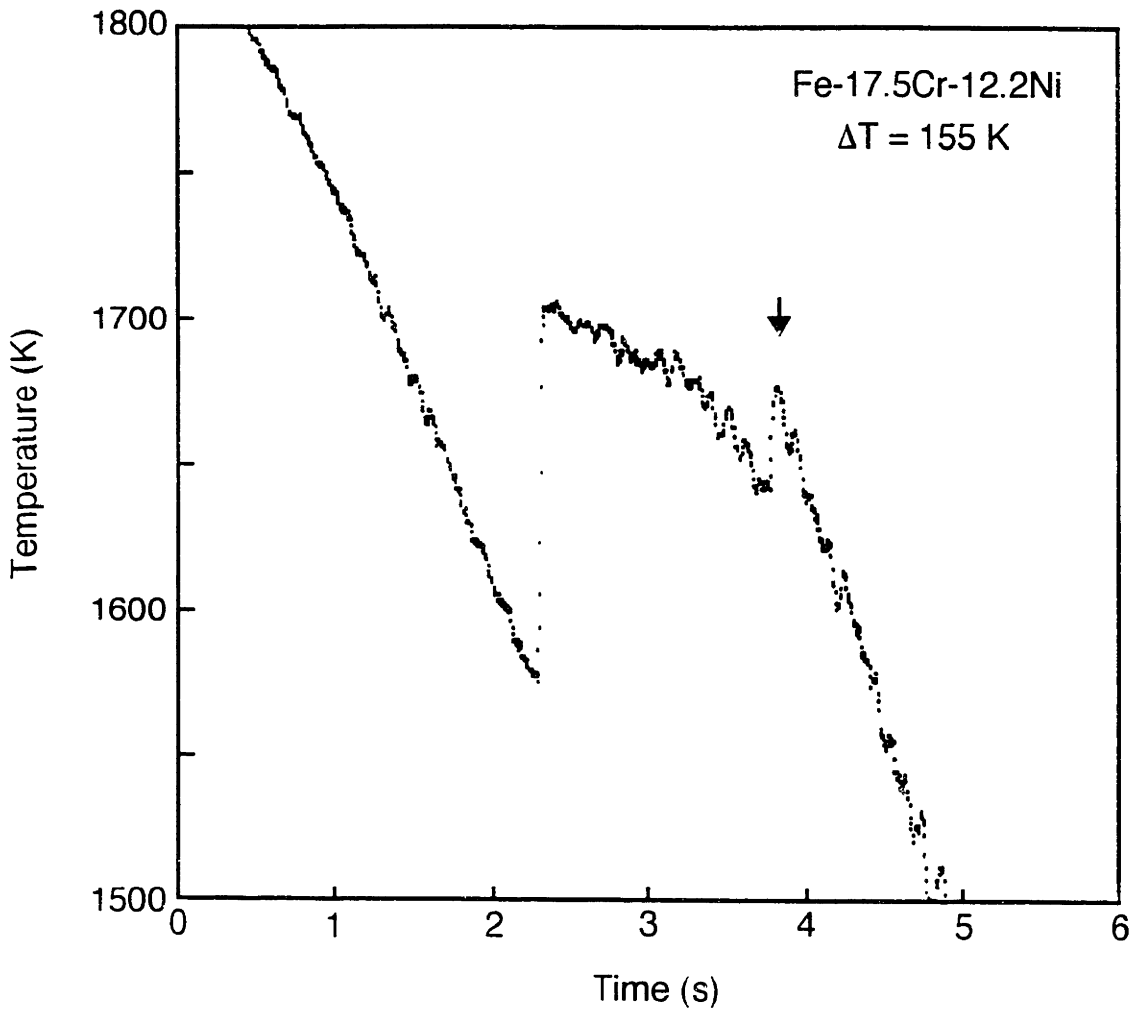

Figure 16 - Thermal history of the sample solidified with an initial undercooling of 155 K, which corresponds to the structure shown in Figure 14(b).

Chapter VIII - Suggestions for Future Work

1. Modeling of Solute Redistribution during Rapid Solidification of Multi-component Alloys

The partition ratio of solute at the solid/liquid interface approaches unity with increasing growth velocity[1,2], a phenomenon which is called solute trapping. The solute-rich core shown in Chapter II can probably be attributed to this effect. That is, as the melt undercooling becomes larger, the growth velocity of a dendrite tip increases and the composition approaches the nominal composition; therefore the dendrite core is enriched in solute. However, in the primary fcc solidification of Fe-Cr-Ni alloys, the partition ratio of Ni is inherently close to unity, and so a Ni-rich core would not be expected. Nevertheless, it is obviously present as shown in Figure 14 in Chapter II.

Various formulae have been proposed to predict the velocity-dependence of the partition ratio[3-7], but they have generally been developed assuming a binary alloy with retrograde liquidus and solidus lines. Therefore, the application of these formulae for solute trapping may not be appropriate in some multi-component alloy systems. The presence of the Ni-rich core in fcc solidification may suggest this. For example, from Aziz's model[5]:

$$k = \frac{k_e + (a_0 V / D)}{1 + (a_0 V / D)} \qquad (1)$$

where k is the velocity-dependent partition ratio of a solute at the solid/liquid interface, k_e is the equilibrium partition ratio, a_0 is a characteristic length on the order of the interatomic distance in the liquid, and D is the diffusivity of the solute in the liquid. Although

this relation is sometimes employed in discussing multi-component solidification, it was defined for a binary alloy.

The author believes that there is interaction between the partition ratios of solutes during the rapid solidification of multi-component alloys. In the fcc solidification of Fe-Cr-Ni alloy, the stability of fcc is decreased when the partition ratio of Cr approaches unity while that of Ni is fixed at unity. Therefore, the partition ratios of solutes in a multi-component alloy need to be linked in order to maintain a certain thermodynamic criterion even at high growth rates. Since solute trapping in multi-component alloy systems has not been well investigated, future theoretical and experimental investigation of this issue may be worthwhile.

2. Modeling of Overall Microsegregation during Rapid Solidification

In the interest of verifying the above theory, the modeling of microsegregation during rapid solidification would be of great importance. Such a model would have relevance to analyses of solute-rich core structures and massive bcc-to-fcc transformation. A successful model would predict solute enrichment at the cores of dendrites during fcc solidification and would determine the degree of homogeneity of the structure after bcc solidification which is necessary for the massive transformation. However, only a few models have been attempted[8-10,17], and some of them[8,17] are complicated numerical analyses.

The author proposes to divide rapid dendritic solidification into two regimes to simplify the phenomena: non-equilibrium and quasi-equilibrium. The former regime would encompass the region of the dendrite near the tip, where the interfacial growth velocity is relatively high and the curvature of the interface is also significant. In this regime, modeling a dendrite as a paraboloid of revolution and knowing the tip velocity from a dendrite tip model[11-13], one can geometrically determine the growth velocity of the interface as a function of position, and then determine a non-equilibrium partition

ratio.[10] Some correction due to curvature may be added.[14] Beyond this regime, growth of a cell/dendrite is characterized as lateral thickening where the curvature of the interface is insignificant. Since the temperature of this region is at or near the maximum recalescence temperature, homogenization by solid-state diffusion (so-called back diffusion) needs to be taken into account. This situation is basically identical to that modeled by Brody and Flemings[15]. Non-equilibrium effects in the first regime are required to account for the formation of solute-rich cores, while solid-state diffusion in the second regime is necessary to cause the homogenization required for massive transformation. The latter process may also explain the fact that solute-rich cores are not observed after bcc solidification but after fcc solidification.

3. Experiments with Needle-induced Nucleation

In chill casting experiments, it has been concluded that the selection of the fcc phase is caused by strong heat extraction by the chill substrate. Since this heat extraction effect is very large, the effect of the crystal structure of the chill substrate is unclear, if any. In gas-cooled solidification, on the other hand, the selection of solidifying phase is determined by nucleation. Therefore, it has not been determined which phase, bcc or fcc, can grow faster if nuclei of both phases are present and there is not any significant effect of heat extraction.

The use of a needle instead of a planar chill substrate can reduce the heat extraction effect and still induce nucleation. That is, a needle made of the material of interest is touched to or pierces an undercooled melt to become a heterogeneous nucleation site. Similar experiments were attempted by Herlach *et al.*[16] Successful experiments would bring about the controlled nucleation of a desired phase from the undercooled melt, which subsequently would make it possible to study the growth of the desired phase. They could also verify the nucleation behavior discussed in the present study.

References

1. C. W. White, B. R. Appleton, B. Stritzker, D. M. Zehner, and S. R. Wilson: *Mater. Res. Sym. Proc.*, 1981, vol. 1, p. 59
2. P. Baeri, G. Foti, J. M. Poate, S. U. Campisano, and A. G. Cullis: *Appl. Phys. Lett.*, 1981, vol. 38, p. 800
3. J. W. Cahn, S. R. Coriell, and W. J. Boettinger: *Laser and Electron Beam Processing of Materials*, C. W. White and P. S. Peercy, eds., Academic Press, New York, 1980, p. 89
4. R. F. Wood: *Appl. Phys. Lett.*, 1980, vol. 37, p. 302
5. M. J. Aziz: *J. Appl. Phys.*, 1982, vol. 53, p. 1158
6. M. J. Aziz: *Mater. Sci. Eng.*, 1988, vol. 98, p. 369
7. M. Hillert: *Conf. on In-situ Composites III*, J. L. Walter, ed., Ginn Custom Publ., Lexington MA, 1979, p. 1
8. J. D. Hunt: *Acta metall. mater.* 1990, vol. 38, p. 411
9. B. Giovanola and W. Kurz: *Metall. Trans. A*, 1990, vol. 21A, p. 260
10. T. M. Mackey and T. F. Kelly: *Acta metall.*, 1988, vol. 36, p. 2587
11. J. Lipton, W. Kurz, and R. Trivedi: *Acta metall.*, 1987, vol. 35, p. 957
12. W. J. Boettinger, S. R. Coriell, and R. Trivedi: *Rapid Solidification Processing: Principles and Technologies*, eds. R. Mehrabian and P. A. Parrish, Claitor's Publ. Div., 1988, p. 13
13. W. Kurz, B. Giovanola and R. Trivedi: *Acta metall.*, 1986, vol. 34, p. 823
14. D. E. Temkin: *Dokl. Akad. Nauk SSSR*, 1960, vol. 132, p. 1307
15. H. D. Brody and M. C. Flemings: *Trans. TMS-AIME*, 1966, vol. 236, p. 615
16. D. M. Herlach, B. Feuerbacher, and E. Schleip: *Mater. Sci. Eng.*, 1991, vol. A133, p. 795
17. J. D. Hunt and D. G. McCartney: *Acta metall.*, 1987, vol. 35, p. 89

Biographical Note

The author was born in Iwaki, Japan on May 2, 1958. He graduated from Iwaki High School in March, 1977, and entered the University of Tokyo in April of that same year. He graduated in March, 1981, with the degree of Bachelor of Engineering. He entered graduate school at the University of Tokyo in April of that year, and received the degree of Master of Engineering in March, 1983. Throughout his undergraduate and graduate studies, his major was metallurgy, and his master's thesis work was on the synthesis of ultrafine alloy powders by thermal plasma processing under the supervision of Professors Kazuo Akashi and Toyonobu Yoshida. The paper describing his thesis work won a Year's Best Paper Award from the Japan Institute of Metals in 1986. He joined Nippon Steel Corporation in April, 1983, and worked at the Welding and Joining Research Laboratory in R&D Laboratories-II, Sagamihara as a research metallurgist for seven years (1983-1990). He researched the solidification of stainless steel and nickel-based alloy welds and the microstructure, properties and performance of those alloy welds. In 1990, Nippon Steel Corporation gave him an opportunity to study abroad. He entered graduate school at MIT in September, 1990, and joined the Solidification Group under the supervision of Professor Merton C. Flemings.